TECHNISCHE UNIVERSITÄT
KAISERSLAUTERN

OPTIMAS

AG Magnetismus

Annual Report 2009

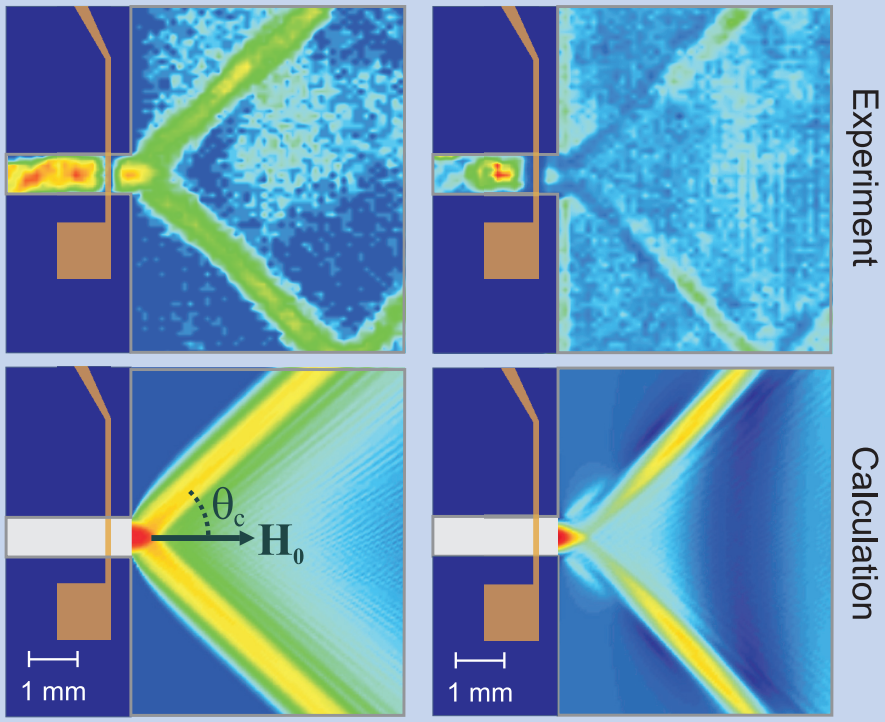

AG MAGNETISMUS
TU KAISERSLAUTERN

Front page: Space (left) and phase (right) resolved measurements (top row) and numerical calculations (bottom row) of diffractionless, sub-wavelength spin-wave beams (caustics). The beams are excited using a special narrow waveguide antenna. The space resolved measurement clearly confirms the existence and stability of the spin-wave caustic beams. The phase resolved measurement shows that the beam width is much smaller than the wavelength. For more details about this effect see Section 5.9 of this Report.

Annual Report 2009

Address:	Prof. Dr. Burkard Hillebrands Fachbereich Physik Landesforschungszentrum OPTIMAS Technische Universität Kaiserslautern Erwin-Schrödinger-Straße 56 67663 Kaiserslautern, Germany Tel.: +49-(0)631-205-4228 Fax.: +49-(0)631-205-4095
Postal address:	Postfach 3049 67653 Kaiserslautern, Germany
Internet:	http://www.physik.uni-kl.de/hillebrands/
E-Mail:	hilleb@physik.uni-kl.de

This Annual Report can be downloaded from:
http://www.physik.uni-kl.de/729.html

Our Group

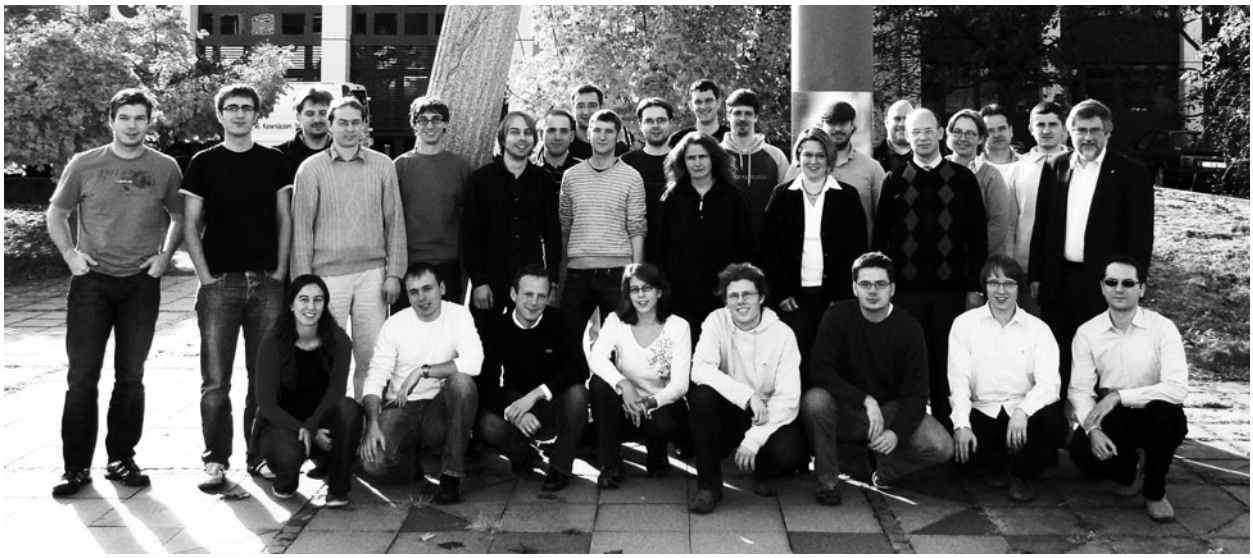

From left to right:

Helmut Schultheiss, Dr. Andrés Conca Parra, Ana Ruiz Calaforra,
Dr. Thomas Schneider, Dr. Jaroslav Hamrle, Dr. Andrii Chumak, Timo Neumann,
Benjamin Jungfleisch, Christian Sandweg, Sebastian Schäfer, Lukas Rist,
Thomas Sebastian, Katrin Vogt, Roland Neb, Sibylle Müller,
Sebastian Hermsdörfer, Peter Clausen, Thomas Brächer, Dr. Britta Leven,
Dr. Simon Trudel, Frederik Fohr, Oliver Hahn, Dr. Alexander Serga,
Dr. Isabel Sattler, Dieter Weller, Philipp Pirro, Dr. Vitaliy Vasyuchka,
Florin Ciubotaru, Prof. Dr. Burkard Hillebrands

Contents

Chapter 1: Preface

Dear Colleagues and Friends,

it is by now a good tradition in our group to present our results of the last year in an annual report. Here is the Annual Report 2009 covering the period of November 2008 to October 2009. We have made some modifications in the structure of this report to make it easier to read and to understand, and we introduced a new logo for our group. For our German speaking readers the introduction and some parts of the report now appear both in English and German language. We have also added introductory paragraphs for each section of reports to provide a short introduction into the respective field and to outline the relations between the individual reports.

Again, we feel this was a very successful year for us. A few highlights: In the field of magnon gases we studied the evolution of a parametrically driven spin-wave system and could reveal the interaction between a Bose-Einstein condensate of magnons and a condensate of parametrically injected magnon pairs. In the still new field of magnonic crystals we show that these new structures can be created fully functionally on the micrometer scale using Permalloy as the magnetic material. In our studies on spin-wave radiation from a point-like source into a two-dimensional film we found surprisingly narrow wave beams of sub-wavelength width. We investigated the reverse Doppler effect, which appears, when spin waves with negative group velocity are scattered from propagating sound waves. We continued to measure the exchange constant of many Heusler compounds with high spin polarization and achieved an understanding of the material dependence. In addition, we investigated the contribution of spin waves to the decrease of the tunnel magnetoresistance effect as a function of temperature.

The new setup for measurements of the quadratic Kerr effect is fully in operation and routinely used for scanning samples of Heusler compounds. Our Brillouin light scattering microscope has been amended by phase resolution, and first results of phase measurements of propagating spin wave in a narrow Permalloy stripe are reported.

Our group has grown this year. We are happy to welcome (in alphabetical order) Ana Ruiz Calaforra, Peter Clausen, Klaus-Peter Frohnhöfer (technician), Oliver Hahn (technician), Benjamin Jungfleisch, Volker Kegel, Philipp Pirro, Isabel Sattler (administration), Thomas Sebastian, and Katrin Vogt as new members of our group. Björn Obry and Ana Ruiz Calaforra started their Ph.D. research work, whereas Oksana Gaier and Thomas Schneider finished their Ph.D. successfully. Oksana already left our group for a postdoc at the RIKEN Quantum Nano-Scale Magnetics Lab with my dear colleague Yoshishika Otani. We also had to say good-bye to Abdelghani Laraoui, who left us for another postdoctoral stay at the City College of New York , and to Simon Trudel. Simon, who was a Humboldt fellow with our group, was appointed to an assistant professor position at the Department of Chemistry of the University of Calgary, Canada.

Another major event was the successful “Umhabilitiation” of Alexander Serga, i.e. the transfer of his degree of habilitation, obtained at the Taras Shevchenko National University of Kiev, to the University of Kaiserslautern.

At the end of July we were happy to welcome 50 participants at the beautiful Villa Denis (Diemerstein, near Kaiserslautern) for a joint workshop of the DFG Research Unit 559 and the JST Strategic Japanese-German Cooperative Program “Nanoelectronics”. This workshop that we jointly organized with our colleagues from the University of Mainz and Tohoku University (Sendai, Japan) further strengthened our very fruitful collaboration.

Our work would not have been possible without valuable collaborations with people all over the world. They are too many to list them here all. In particular we would like to thank, in alphabetical order, Yasuo Ando, Christian Back, Jozef Barnas, Gerrit Bauer, Hartmut Benner, Stanislav Chadov, John Chapman, Claude Chappert, Oksana Chubykalo-Fesenko, Darrell Comins, Russell Cowburn, Vladislav Demidov, Sergej Demokritov, Pallavi Dhagat, Bernard Dieny, Hajo Elmers, Jürgen Fassbender, Gerhard Fecher, Claudia Felser, Jacques Ferré, Albert Fert, Suzanna and Paulo Freitas, John Gregg, Dirk Grundler, Kouichiro Inomata, Gerhard Jakob, Albrecht Jander, Martin Jourdan, Boris Kalinikos, Sang-Koog Kim, Peter Kopietz, Mikhail Kostylev, Jürgen Kübler, Liesbet Lagae, Norbert Laube, Wolfram Maaß, Jan Marien, Roland Mattheis, Andrezj Maziewski, Gennadiy Melkov, Claudia and Tim Mewes, Jacques Miltat, Alexandra Mougin, Markus Münzenberg, Hans Nembach, Yoshichika Otani, Carl Patton, Dorothée Petit, Kamil Postava, Günter Reiss, Karsten Rott, John R. Sandercock, Rudi Schäfer, Gerd Schönhense, Justin Shaw, Andrei Slavin, Bob Stamps, Yoshishige Suzuki, Koki Takanashi, André Thiaville, Vasyl Tiberkevich, Stefan Visnovsky and Matsufumi Yamamoto for their interactions with us and their strong input to our work.

Collaborations within the Fachbereich Physik at the University of Kaiserslautern (in particular Martin Aeschlimann, James Anglin, Sebastian Eggert, Michael Fleischhauer, Hans-Christian Schneider, and Volker Schünemann and their groups), the Institut für Oberflächen- und Schichtanalytik, as well as the Nano+Bio Center have been very stimulating. We are very grateful to be a member of the State Research Center OPTIMAS that now became fully operational. OPTIMAS is dedicated to combine optics and material sciences research. It is one of two Research Centers at our University and was set-up as part of the Research Initiative 2008-2011 of the State of Rhineland Palatinate. Finally, I am much obliged to Peter Pesch and his team from the TZO GmbH for providing convenient general conditions for our work in Rheinbreitbach.

I would also like to thank all our sponsors, which are the Deutsche Forschungsgemeinschaft, the Bundesministerium für Bildung und Forschung, the Alexander von Humboldt Foundation, the Deutscher Akademischer Austauschdienst, the European Community, INTAS, the Carl Zeiss Foundation, the State of Rhineland Palatinate and the University of Kaiserslautern. My special thanks go to Andreas Beck, Isabel Sattler, and Sibylle Müller for their help in preparing this report and to Hubert Gerber from Photo-Repro-Druck, TU Kaiserslautern.

It is my special pleasure to greet all former group members. May this report help to stay in touch with each other. If you are interested in our work I would be happy to hear from you. If you have any questions, comments, suggestions, or any kind of criticism, please contact us.

With all my best wishes for Christmas, and a Happy New Year,

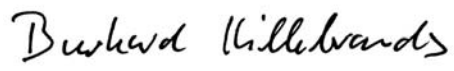

Kaiserslautern, November 2009

Vorwort

Liebe Kolleginnen und Kollegen und Freunde unserer Arbeitsgruppe,

inzwischen ist es schon eine gute Tradition in meiner Arbeitsgruppe geworden, jährlich die wichtigsten Resultate in Form eines Jahresberichtes vorzulegen. Hier ist nun der Jahresbericht 2009, der den Zeitraum November 2008 bis Oktober 2009 umfasst. Wir haben einige Modifikationen in der Struktur vorgenommen. Eine ist, wie Sie an dieser erstmalig auch in deutscher Sprache erscheinenden Einleitung schon bemerken können, die Zweisprachigkeit der Einleitung und der - ebenfalls neuen - Einführungen in die Forschungsgebiete. Auch wurde es Zeit für ein neues Gruppenlogo.

Das vergangene Jahr war wieder ein sehr erfolgreiches für uns. Einige "Highlights": Im Forschungsfeld der Magnonengase studierten wir die Entwicklung von parametrisch erzeugten Spinwellensystemen und konnten die Wechelwirkung zwischen einem Bose-Einstein-Kondensat von Magnonen und dem Kondensat von parametrisch injizierten Magnonenpaaren zeigen. Im noch recht neuen Feld der magnonischen Kristalle konnten wir nachweisen, dass diese Strukturen auch auf der Mikrometerskala funktionsfähig unter Verwendung von Permalloy als dem magnetischen Material erzeugt werden können. Wir untersuchten die Spinwellenabstrahlung von einer punktförmigen Quelle in einen zweidimensionalen Film und fanden erstaunlich schmale Spinwellenstrahlen mit einer Breite im Subwellenlängenbereich. Wir untersuchten den inversen Dopplereffekt, welcher auftritt, wenn Spinwellen mit negativer Gruppengeschwindigkeit an propagierenden Schallwellen gestreut werden. Wir haben die Austauschkonstanten vieler Heusler-Verbindungen mit hoher Spinpolarisation vermessen und erzielten ein gutes Verständnis dieser Größe als Funktion des Materials. Wir konnten hierbei auch zeigen, dass in einigen Materialien ein signifikanter Beitrag der Magnonen zur Temperaturabhängigkeit des Tunnelmagnetowiderstandseffektes besteht.

Der neue Aufbau zur Untersuchung des quadratischen Kerreffektes ist nun fertig gestellt und wird routinemäßig zur Untersuchung von Heusler Verbindungen eingesetzt. Unser Brillouin-Lichtstreumikroskop haben wir mit einem Phasenauflösungszusatz erweitert. Erste Messungen zur Phase von in einem Permalloystreifen propagierenden Spinwellen haben wir erfolgreich durchgeführt.

Die Gruppe ist dieses Jahr wieder gewachsen. Wir freuen uns dass wir als neue Gruppenmitglieder aufnehmen konnten (in alphabetischer Reihenfolge): Ana Ruiz Calaforra, Peter Clausen, Klaus-Peter Frohnhöfer (Techniker), Oliver Hahn (Techniker), Benjamin Jungfleisch, Volker Kegel, Philipp Pirro, Isabel Sattler (Management), Thomas Sebastian, und Katrin Vogt. Björn Obry und Ana Ruiz Calaforra starteten ihre Doktorarbeit, Oksana Gaier und Thomas Schneider schlossen ihren Promotionen erfolgreich ab. Oksana startete einen Postdoc-Aufenthalt am RIKEN Quantum Nano-Scal Magnetics Lab in der Gruppe von Yoshishika Otani. Wir verabschiedeten Abdelghani Laraoui, der einen weiteren Postdoc am City College of New York angetreten hat, und Simon Trudel, der bei uns durch die Humboldt-Stiftung gefördert wurde. Simon erhielt einen Ruf auf eine Assistant Professur am Department of Chemistry der University of Calgary in Kanada.

Ein weiteres wichtiges Ereignis war die erfolgreiche Umhabilitation von Alexander Serga von der Taras Shevchenko National University in Kiew zu unserer Universität.

Unsere Arbeit hätte nicht möglich sein können ohne die vielen wertvollen Zusammenarbeiten mit Forscherkollegen rund um die Welt. Beispielhaft möchten wir uns bedanken bei (in alphabetischer Reihenfolge) Yasuo Ando, Christian Back, Jozef Barnas, Gerrit Bauer, Hartmut Benner,

Stanislav Chadov, John Chapman, Claude Chappert, Oksana Chubykalo-Fesenko, Darrell Comins, Russell Cowburn, Vladislav Demidov, Sergej Demokritov, Pallavi Dhagat, Bernard Dieny, Hajo Elmers, Jürgen Fassbender, Gerhard Fecher, Claudia Felser, Jacques Ferré, Albert Fert, Suzanna and Paulo Freitas, John Gregg, Dirk Grundler, Kouichiro Inomata, Gerhard Jakob, Albrecht Jander, Martin Jourdan, Boris Kalinikos, Sang-Koog Kim, Peter Kopietz, Mikhail Kostylev, Jürgen Kübler, Liesbet Lagae, Norbert Laube, Wolfram Maaß, Jan Marien, Roland Mattheis, Andrezj Maziewski, Gennadiy Melkov, Claudia and Tim Mewes, Jacques Miltat, Alexandra Mougin, Markus Münzenberg, Hans Nembach, Yoshichika Otani, Carl Patton, Dorothée Petit, Kamil Postava, Günter Reiss, Karsten Rott, John R. Sandercock, Rudi Schäfer, Gerd Schönhense, Justin Shaw, Andrei Slavin, Bob Stamps, Yoshishige Suzuki, Koki Takanashi, André Thiaville, Vasyl Tiberkevich, Stefan Visnovsky und Matsufumi Yamamoto.

Einige unserer Kooperationspartner konnten wir Ende Juli zu einem gemeinsamen Workshop der DFG-Forschergruppe 559 und des deutsch-japanischen DFG-JST-geförderten Gemeinschaftsprojektes “Nanoelektronik” in der schönen Villa Denis in Diemerstein in der Nähe von Kaiserslautern begrüßen. Diesen Workshop organisierten wir gemeinsam mit unseren Kollegen von der Universität Mainz und der Tohoku-Universität Sendai/Japan.

Zusammenarbeiten im Fachbereich Physik an der Technischen Universität Kaiserslautern waren ebenfalls sehr wertvoll. Besonders bedanken möchten wir uns bei Martin Aeschlimann, James Anglin, Sebastian Eggert, Michael Fleischhauer, Hans-Christian Schneider, and Volker Schünemann und ihren Gruppen, wie auch beim Institut für Oberflächen- und Schichtanalytik und dem Nano+Bio Center. Wir sind dankbar für die Arbeitsmöglichkeiten im Landesforschungszentrum OPTIMAS welches seine Arbeit im Berichtszeitraum voll aufgenommen hat. Es ist eines der zwei Landesforschungszentren an der TU Kaiserslautern und wurde im Rahmen der Forschungsinitiative 2008 - 2011 des Landes Rheinland-Pfalz eingerichtet. Schließlich möchte ich mich bei Peter Pesch und seinem Team des Technologiezentrums Oberflächen (TZO GmbH) in Rheinbreitbach für die dortigen Arbeitsmöglichkeiten bedanken.

Unsere Arbeit wäre nicht ohne die finanziellen Unterstützungen möglich gewesen. Wir danken der Deutschen Forschungsgemeinschaft, dem Bundesministerium für Bildung und Forschung, der Alexander von Humboldt-Stiftung, dem Deutschen Akademischen Austauschdienst, der Europäischen Gemeinschaft, INTAS, der Carl Zeiss-Stiftung, dem Land Rheinland-Pfalz und der TU Kaiserslautern. Mein spezieller Dank geht an Andreas Beck, Isabel Sattler und Sibylle Müller für ihre Hilfe in der Erstellung dieses Berichtes, sowie an Hubert Gerber von der Photo-Repro-Druck, TU Kaiserslautern.

Es ist meine besondere Freude, an dieser Stelle alle früheren Gruppenmitglieder zu grüßen. Vielleicht hilft dieser Bericht ein wenig, Kontakt zu halten. Wenn Sie an unserer Arbeit interessiert sind, würden wir uns freuen von Ihnen zu hören. Falls Sie Fragen, Kommentare oder Anregungen haben freuen wir uns, wenn Sie mit uns in Kontakt treten.

Mit den besten Wünschen für ein frohes Weihnachtsfest und ein gutes Neues Jahr

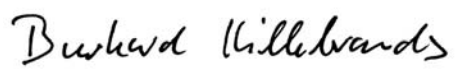

Kaiserslautern, im November 2009

Chapter 2: Personnel

2.1 Members of the group

Group leader:

Prof. Dr. Burkard Hillebrands

Senior scientists:

Dr. Britta Leven, Akad. Oberrätin
Dr. Jaroslav Hamrle
Dr. Alexander Serga

Postdocs and long-term guest scientists:

Dr. Andreas Beck	
Dr. Andrii Chumak	
Dr. Andrés Conca Parra	
Dr. Abdelghani Laraoui	until 04/09
Dr. Thomas Schneider	since 07/09
Dr. Simon Trudel (Humboldt Research Fellowship)	until 10/09
Dr. Vitaliy Vasyuchka	

PhD students:

Dipl.-Phys. Florin Ciubotaru	
Dipl.-Phys. Frederik Fohr	
Dipl.-Phys. Oksana Gaier	until 08/09
Dipl.-Phys. Sebastian Hermsdörfer	
Dipl.-Phys. Lisa Kleinen (Rheinbreitbach)	
Dipl.-Phys. Roland Neb	
Dipl.-Math. Timo Neumann	
Dipl.-Phys. Björn Obry	since 03/09
Dipl.-Phys. Ana Ruiz Calaforra	since 07/09
Dipl.-Phys. Christian Sandweg	
Dipl.-Phys. Sebastian Schäfer	
Dipl.-Phys. Thomas Schneider	until 06/09
Dipl.-Phys. Helmut Schultheiss	
Dipl.-Phys. Georg Wolf	

Diploma Students:

Peter Clausen	since 03/09
Benjamin Jungfleisch	since 12/08
Volker Kegel	since 12/08
Björn Obry	until 02/09
Philipp Pirro	since 01/09
Christopher Rausch	until 08/09
Thomas Sebastian	since 12/08
Katrin Vogt	since 01/09

Engineers and Technicians

Jörg Elmer (Rheinbreitbach)	
Klaus-Peter Frohnhöfer	since 09/09
Oliver Hahn	since 09/09
Dipl.-Ing. (FH) Dieter Weller	

Adminstration:

Sibylle Müller	
Dr. Isabel Sattler	since 07/09

2.2 Visiting scientists, postdoctoral fellows and exchange students

Timo Kuschel, Hauke Bardenhagen, Universität Osnabrück, Germany — 25.02.09 - 27.02.09

Timo and Hauke are graduate students of the group Prof. Joachim Wollschläger. During their visit they were investigating Fe and FeO films using MOKE and QMOKE magnetometry.

Prof. Andrei Slavin, Oakland University, U.S.A. — 11.05.09 - 07.06.09

Andrei's stay was supported by our DFG Graduate School (GRK 792 *"Nichtlineare Optik und Ultrakurzzeitphysik"*). He delivered several lectures on nonlinear cooperative dynamics of an array of nonlinear spin-torque nano-oscillators and on nonlinear microwave signal processing based on spin waves in dielectric and metallic magnetic films. During his visit he also was working on theoretical studies of anisotropic propagation of spin-waves in thin magnetic films.

Dr. Vasil Tiberkevich, Oakland University, U.S.A. — 11.05.09 - 07.06.09

Vasil's visit was supported by the Deutsche Forschungsgemeinschaft in the frame of the SFB/Transregio 49 *"Condensed Matter Systems with Variable Many-Body Interactions"*. During his visit he was working on theoretical description of evolution of pumping-free magnon gases and condensates.

Dr. Yasuhiro Fukuma, Institute of Physical and Chemical Research (RIKEN), Wakoshi, Tokyo (Japan) — 29.06.09 - 11.07.09

Yasuhiro visited our group in the framework of our German-Japanese collaboration *"Mapping of spin accumulation using Brillouin light scattering spectroscopy"*. During his visit Yasuhiro was participating in investigations on devices, he had built in his home laboratory.

Prof. Gennadiy A. Melkov, National Taras Shevchenko University of Kiev, Ukraine — 01.07.09 - 22.08.09

Gennadiy's visit was supported by the Deutsche Forschungsgemeinschaft in the frame of project *"Linear and nonlinear magnonic crystals"*. During his stay he was participating in experimental and theoretical studies of linear and nonlinear spin-wave dynamics in magnonic crystals.

Oleksandr Talalaevskyy, National Taras Shevchenko University of Kiev, Ukraine — 02.07.09 - 02.09.09

Oleksandr is a student, coming from the group of Prof. Gennadiy A. Melkov. During his visit that was funded by a scholarship of TU Kaiserslautern Oleksandr familiarized himself with modern microwave equipment and with basics of BLS spectroscopy technique. He succeeded in developing control software to automate ferromagnetic resonance measurements.

Alexy Karenowska, Department of Condensed Matter Physics, Clarendon Laboratory, University of Oxford, U.K. — 07.09.09 - 18.09.09

Alexy is a graduate student from the group of Prof. John Gregg. Her visit was supported by our DFG Graduate School (GRK 792 *"Nichtlineare Optik und Ultrakurzzeitphysik"*). Alexy's stay in Kaiserslautern gave her the opportunity to perform some experiments, and to discuss, plan, and prepare future work. Her particular interest is in the investigation of active spinwave loops, and the realization of spin-mechatronic structures.

2.3 Guest seminars

Dr. Alexandra Trzaskowska 27.10.2008	Adam Mickiewicz University Poznan, Poland *Surface phonons investigation in different materials by surface Brillouin spectroscopy* Group seminar
Prof. Yoshichika Otani 12.12.2008	University of Tokyo, Japan *Spin current induced phenomena in metallic nano-structures* Seminar Graduiertenkolleg 792
Dr. Gleb Kakazei 15.12.2008	Universidade do Porto, Portugal *Probing magnetic microdots and their arrays by ferromagnetic resonance* Group seminar
Prof. Jürgen Kübler 03.02.2009	TU Darmstadt, Germany *Spin-wave dispersion ab initio* Internal Workshop *"Exchange interaction in Co_2-based Heusler compounds"*
Dr. Josef Kudrnovský 03.02.2009	Academy of Science of the Czech Republic *First-principles approach to electronic, magnetic and transport properties of disordered Heusler alloys* Internal Workshop *"Exchange interaction in Co_2-based Heusler compounds"*
Dr. Stanislav Chadov 03.02.2009	Universität Mainz, Germany *Theoretical description of the spectral properties of Heusler compounds* Internal workshop *"Exchange interaction in Co_2-based Heusler compounds"*
Dr. Sabine Wurmehl 09.02.2009	Leibniz-Institut für Festkörper- und Werkstoffforschung (IFW) Dresden, Germany *Nuclear magnetic resonance - application to spin polarized Heusler compounds* Group seminar
Dr. Matthieu Bailleul 19.02.2009	Université Strasbourg, France *Current-induced spin-wave Doppler shift* Special group seminar
Dr. Gleb Kakazei 18.05.2009	Universidade do Porto, Portugal *Probing arrays of magnetic microdots by ferromagnetic resonance* Special group seminar

Prof. Andrei Slavin 25.05.2009	Oakland University, Rochester, U.S.A. *Non-autonomous dynamics of spin-torque oscillators* Special group seminar
Prof. Andrei Slavin 27.05.2009	Oakland University, Rochester, U.S.A. *Nonlinear microwave signal processing based on spin waves in dielectric and metallic magnetic films* Seminar Graduiertenkolleg 792
Dr. Martin Jourdan 27.05.2009	Universität Mainz, Germany *Materials with large spin polarization: significance of the interface* Special group seminar
Prof. Can-Ming Hu 09.06.2009	University of Manitoba, Canada *Spin dynamics in ferromagnetic and spintronic materials* Special group seminar
Prof. Joachim Wosnitza 15.06.2009	Forschungszentrum Dresden-Rossendorf, Germany *Die Jagd nach dem Feldrekord - Forschung in hohen Magnetfeldern* Physics colloquium
Dr. Yasuhiro Fukuma 08.07.2009	Institute of Physical and Chemical Research (RIKEN), Tokyo, Japan *Quest for efficient spin accumulation in lateral structures* Special group seminar
Prof. Herwig Ott 15.06.2009	TU Kaiserslautern, Germany *Electron microscopy of ultracold quantum gases* Group seminar

2.4 Visits of group members at other laboratories

Jaroslav Hamrle	Technical University of Ostrava, Czech Republic 12.11. - 14.11.2008 Host: Prof. J. Pištora
Florin Ciubotaru	Universite Paris Sud, France 24.11. - 27.11.2008 Host: Prof. C. Chappert
Timo Neumann	University of Western Australia, Crawley, Australia 14.01. - 28.03.2009 Host: Prof. R.L. Stamps
Helmut Schultheiß	University of Perugia, Italy 26.01. - 02.02.2009, 16.04. - 25.04.2009 Host: Prof. G. Carlotti
Katrin Vogt	University of Perugia, Italy 26.01. - 02.02.2009, 16.04. - 25.04.2009 Host: Prof. G. Carlotti
Jaroslav Hamrle	Universität Osnabrück, Germany 17.06. - 19.06.2009 Host: Prof. J. Wollschläger
Florin Ciubotaru	IMEC, Leuven Belgium 24.08. - 28.08.2009 Host: Dr. L. Lagae
Frederik Fohr	Institute of Physical and Chemical Research (RIKEN), Tokyo, Japan 29.09. - 12.10.2009 Host: Prof. Y. Otani
Jaroslav Hamrle	Institute of Physical and Chemical Research (RIKEN), Tokyo, Japan 29.09. - 03.10.2009 Host: Prof. Y. Otani
Jaroslav Hamrle	Tohoku University, Sendai, Japan 05.10. - 08.10.2009 Host: Prof. Y. Ando

2.5 Group member photo gallery

Dr. Andreas Beck
Postdoc

Dr. Andrii Chumak
Postdoc

Florin Ciubotaru
Ph.D. student

Peter Clausen
Diploma student

Dr. Andrés Conca Parra
Postdoc

Jörg Elmer
Technician

Frederik Fohr
Ph.D. student

Klaus-Peter Frohnhöfer
Technician

Oksana Gaier
Ph.D. student

Oliver Hahn
Technician

Dr. Jaroslav Hamrle
Senior scientist

Sebastian Hermsdörfer
Ph.D. student

Prof. Dr. Burkard Hillebrands
Group leader

Benjamin Jungfleisch
Diploma student

Volker Kegel
Diploma student

Lisa Kleinen
Ph.D. student

Dr. Abdelghani Laraoui
Postdoc

Dr. Britta Leven
Senior scientist

Sibylle Müller
Secretary

Roland Neb
Ph.D. student

Timo Neumann
Ph.D. student

Björn Obry
Ph.D. student

Philipp Pirro
Diploma student

Christopher Rausch
Diploma student

Ana Ruiz Calaforra
Ph.D. student

Christian Sandweg
Ph.D. student

Dr. Isabel Sattler
Administration

Sebastian Schäfer
Ph.D. student

Thomas Schneider
Postdoc

Helmut Schultheiss
Ph.D. student

Thomas Sebastian
Diploma student

Dr. Alexander Serga
Senior scientist

Dr. Simon Trudel
Postdoc

Dr. Vitaliy Vasyuchka
Postdoc

Katrin Vogt
Diploma student

Dieter Weller
Mechanical engineer

Georg Wolf
Ph.D. student

Chapter 3: Equipment

A) Preparation and characterization of thin films and multilayers

1. multi–chamber molecular beam epitaxy system (Pink GmbH) comprising
   a. deposition chamber
      (electron beam and Knudsen sources, RHEED, LEED, Auger)
   b. scanning tunneling microscopy chamber
      (*in-situ* STM, Omicron)
   c. Brillouin light scattering and Kerr magnetometry chamber
      (magnetic field 1.2 T, temperature range 80 – 400 K)
   d. load lock chamber
   e. preparation chamber
      (optical coating, heating station 2300°C)
   f. transfer chamber
   g. atom beam reactor chamber with *in-situ* four point probe resistance measurement stage
2. two-chamber UHV multideposition system
   a. deposition chamber
      (electron beam and Knudsen sources, LEED, Auger)
   b. ion beam chamber with fine focus noble gas keV ion source (Omicron), ion beam oxidation module and mask system
3. two-magnetron sputtering system for hard coatings
4. atomic force microscope (Solver, NT-MDT)
5. clean room facility with flow box, spin coater, etc.

B) Magnetic characterization

1. vector Kerr magnetometer
   (longitudinal and transverse Kerr effect, magnetic field 1.2 T, temperature range 2 – 350 K, automated sample positioning)
2. time-resolved vector Kerr magnetometer (10 ps time resolution and microwave setup for generation of short field pulses)
3. scanning Kerr microscope with time resolution
4. picosecond all-optical pump-probe setup (adjustable delay up to 6 ns; ps-laser Lumera Lasers GmbH)
5. magnetic force microscope with magnet (NT-MDT)
6. three Brillouin light scattering spectrometers, computer controlled and fully automated (magnetic field 2.2 T) with stages for
   a. low temperature measurements (2 – 350 K)
   b. space-time resolved measurements for spin wave intensity mapping (resolution 50 µm, 0.83 ns)

c. time-resolved BLS microscope (resolution 250 nm, 250 ps)
d. time-resolved BLS microscope with variable out of plane magnetic field (0.8 T)
e. *in-situ* measurements
f. elastic measurements

7. microwave setup (up to 32 GHz) comprising a network analyzer, microwave amplifiers, modulators, pulse generators, etc.
8. magnetotransport setups (magnetic field 1.5 T, temperature range $20 - 400$ K)

C) Equipment at the Institute for Thin Film Technologies (IDST), Rheinbreitach

1. Preparation of thin films:
   a. chemical vapor deposition (CVD) facility
   b. physical vapor deposition (PVD) facility
   c. plasma enhanced CVD (PECVD) facilities with an inductively coupled rf-plasma beam source and several magnetrons of different sizes
2. Surface and thin film analysis:
   a. profilometer: measurement of coating thickness and roughness determination of intrinsic stress and Young modulus
   b. Ball on Disk: measurement of friction coefficient analysis of surface friction
   c. Revetest: determination of adhesive strength analysis of microcracks
   d. microindention: determination of plastic and elastic microhardness (Vickers)
   e. optical contact angle measurement: determination of solid surface free energy and surface tension evaluation of hydrophobicity and hydrophilicity
   f. reflection- and transmission-spectroscopy (UV-VIS): optical measurements with wavelength range from 185 nm to 915 nm (resolution 1 nm), determination of absorption coefficient and optical gap (Tauc)
   g. (environmental) scanning electron microscopy (ESEM)[1]: comprehensive structural microanalysis of conducting, isolating, anorganic, organic and wet samples
   h. energy dispersive X-ray microanalysis (EDX)[1]: non-destructive fast analysis of elements
   i. neutron activation analysis (NAA)[2]: qualitative und quantitative analysis of main and trace components
   j. elastic recoil detection analysis (ERDA)[2]: analysis of trace elements with depth resolution analysis of hydrogen content
   k. Rutherford Backscattering (RBS)[2]: analysis of trace elements with depth resolution
   l. synchrotron-X-ray-fluorescence (SYXRF)[2]: non-destructive analysis of elements

[1] in cooperation with NTTF GmbH, Rheinbreitbach

[2] accelarator enhanced analysis in cooperation with the accelarator laboratories of the Universities of Munich, Bonn and Cologne

Chapter 4: Transfer of Technology

1. Magnetism

With our facilities within the Department of Physics at the University of Kaiserslautern we offer consultance and transfer of technology in the areas of thin film magnetism, magnetic film structures and devices, magnetic sensors, and in corresponding problems of metrology.

We are equipped to perform magnetic, transport, elastic and structural measurements of films and multilayer systems.

This is in detail:

- magnetometry using vibrating sample magnetometry, Kerr magnetometry, Brillouin light scattering spectroscopy
- magnetic anisotropies, optionally with high spatial resolution
- magneto-transport properties
- test of homogeneity of magnetic parameters
- exchange stiffness constants in magnetic films
- elastic constants
- surface topography

2. Institut für Dünnschichttechnologie (IDST) - Transferstelle der Technischen Universität Kaiserslautern, Rheinbreitbach

(Institute for Thin Film Technology - Center for Technology Transfer of the University of Kaiserslautern, Rheinbreitbach)

As part of technology transfer the Institute of Thin Film Technology (IDST) offers among other activities

- consultance in tribological problems
- development of product specific coatings
- optimization of coatings especially for medical applications
- coating of polymers and temperature sensitive materials
- coating of samples and small scale production series
- management for R&D-projects

The institute is located in Rheinbreitbach about 20 km south of Bonn in the Center for Surface Technologies (TZO) to support the economy in the northern part of the Rheinland-Pfalz State.

Address:

Institut für Dünnschichttechnologie
Maarweg 30-32
53619 Rheinbreitbach, Germany

Scientific director:

Prof. Dr. B. Hillebrands phone: +49 631 205 4228
e-mail: hilleb@physik.uni-kl.de

Contact:

Lisa Kleinen phone: +49 2224 900 693
fax: +49 2224 900 694
e-mail: kleinen@physik.uni-kl.de

Please contact us for more information.

Chapter 5: Reports on Experimental Results

A. Magnon Gases

In ferromagnetic materials atoms having unpaired electrons act as individual magnets. Their magnetism is mostly caused by the magnetic moments of the uncompensated electron spins. Since these atomic magnets tend to be oriented in the same direction due to specific quantum-mechanical exchange interaction, a macroscopic magnetic moment appears. As the atoms strongly interact a reversal of a single atomic magnetic moment is not spatially localized but spreads through the solid as a wave of discrete magnetic momentum transfer. This wave is known as a spin wave, and in frame of the second quantization it is associated with a quasi-particle called magnon. Weakly interacting magnons can be considered as a gas of magnetic bosonic quasi-particles, and therefore is called a magnon gas. This gas may serve as a model system for the investigation of interacting bosonic particles and for correlated systems in general. Its potential is based on the wide controllability of the magnon density as well as on the spectral properties influencing the magnon-magnon interaction. The recent observation of Bose-Einstein condensation of magnons at room-temperature in the minimum of the spin-wave spectrum demonstrates this clearly (see Nature 443, 430 (2006)).

The spectrum of a magnon gas can be easily controlled by change of orientation and strength of an external bias magnetic field. The most effective mechanism to inject magnons into the gas is microwave parametric pumping (see Gurevich and Melkov, *Magnetization Oscillation and Waves*, CRC, Cleveland, 1996). In the simplest case one photon of the pumping electromagnetic field excites two magnons with half the energy that propagate in the opposite directions. Such mechanism creates a huge quantity of phase correlated magnons, called condensate of photon-coupled magnon pairs. Among other, such magnon pairs serve as an energy source and as a strong disturbing factor for the entire spin-wave system. Formation, thermalization and disintegration of this condensate as well as its interaction with the other magnonic states and especially with the Bose-Einstein condensate (BEC) of magnons constitute a hot topic of research. To investigate these processes we use time- and wavevector-sensitive Brillouin light scattering spectroscopy in combination with conventional microwave techniques.

In this Annual Report our recent results on the behavior of parametrically driven magnon gases and condensates are presented. Studies on the peculiarities of different types of parametric pumping in thin magnetic film are presented in Report 5.1, followed by the Report 5.2 on the pump-free evolution of a non-equilibrium magnon system after switching-off the pump source. These experiments establish the first observation of the interaction between two physically different condensates of Bose particles. In Report 5.3 the storage and recovery of a microwave signal in a ferrite film is discussed. This phenomenon is interpreted by competing interactions between different magnon states populated by parametric pumping. We analyse how the process of decoherence of these states influences macroscopic microwave signals emitted by the parametrically driven magnetic medium. Finally, in Report 5.4, we demonstrate the ability of microwave signal processing using parametrically non-resonant wave front reversal of spin waves.

A. Magnonische Gase

In ferromagnetischen Materialien treten Atome, die ungepaarte Elektronen haben, als einzelne Magnete auf. Ihr Magnetismus wird in der Regel durch die magnetischen Momente des nicht kompensierten Elektronenspins verursacht. Diese atomaren Magneten richten sich aufgrund der quantenmechanischen Austauschwechselwirkung im Allgemeinen parallel zueinander aus. Daher beobachtet man ein makroskopisches magnetisches Moment. Da die Atome stark miteinander wechselwirken, wird das Umklappen eines einzelnen atomaren Moments nicht räumlich lokalisiert sein, sondern sich als Welle mit einem diskretisierten magnetischen Moment über den gesamten Festkörper ausbreiten. Diese Welle wird als Spinwelle bezeichnet und ist im Rahmen der zweiten Quantisierung mit einem Quasiteilchen, dem so genannten Magnon, verbunden. Schwach miteinander wechselwirkende Magnonen können als Gas von magnetischen bosonischen Quasiteilchen angesehen werden. Daher werden sie auch als Magnonengas bezeichnet. Dieses Gas kann als Modellsystem für die Untersuchung von wechselwirkenden bosonischen Teilchen und von korrelierten Systemen im Allgemeinen dienen. Sein Potenzial liegt dabei in der guten Kontrollierbarkeit der Magnonen-Dichte und den Eigenschaften des Spektrums, die die Magnon-Magnon-Wechselwirkung beeinflussen. Die kürzlich erfolgte Beobachtung der Bose-Einstein-Kondensation von Magnonen bei Raumtemperatur im Minimum des Spinwellen-Spektrums zeigt dies deutlich (s. Nature 443, 430 (2006)).

Das Spektrum des Magnonengases kann leicht durch eine Änderung der Richtung oder der Stärke eines externen Magnetfelds kontrolliert werden. Der wirkungsvollste Mechanismus, Magnonen in ein Magnonengas einzufüllen, ist parametrisches Pumpen mittels Mikrowellen (s. Gurevich and Melkov, *Magnetization Oscillation and Waves*, CRC, Cleveland, 1996). Im einfachsten Fall erzeugt ein Photon des elektromagnetischen Pumpfeldes zwei Magnonen mit der Hälfte der Energie, die sich in entgegengesetzte Richtungen ausbreiten. Dieser Mechanismus erzeugt eine große Anzahl von phasenkorrelierten Magnonen, ein Kondensat von photonengekoppelten Magnonen-Paaren. Unter anderem dienen solche Magnonen-Paare als Energiequelle und als starke Störung des gesamten Spinwellensystems. Erzeugung, Thermalisierung und Zerfall dieses Kondensats sowie seine Wechselwirkung mit anderen Magnonen-Zuständen und besonders mit dem Bose-Einstein Kondensat von Magnonen sind ein aktuelles Thema der Forschung. Zur Untersuchung dieser Prozesse verwenden wir zeit- und wellenvektroaufgelöste Brillouin Lichtstreuspektroskopie in Verbindung mit konventioneller Mikrowellentechnik.

In diesem Jahresbericht werden einige wichtige Ergebnisse der Untersuchung des Verhaltens von parametrisch gepumpten Magnonengasen und Kondensaten vorgestellt. Zuerst werden Untersuchungen über die Eigenschaften der verschiedenen Arten des parametrischen Pumpens in dünnen magnetischen Filmen in Kapitel 5.1 präsentiert. Anschließend wird in Kapitel 5.2 auf die pump-freie Entwicklung Magnonen Systems außerhalb des Gleichgewichts nach dem Abschalten der Pumpquelle eingegangen. Diese Experimente sind die erste Beobachtung der Wechselwirkung zwischen zwei physikalisch verschiedenen Kondensaten von Bose-Teilchen. Im Kapitel 5.3 wird die Speicherung und Wiederabstrahlung eines Mikrowellensignals in einem Ferritfilm besprochen. Dieses Phänomen wird mit Hilfe der konkurrierenden Wechselwirkung von verschiedenen Magnonen Zuständen, die durch parametrisches Pumpen besetzt werden, gedeutet. Wir untersuchen, wie der Prozess der Dekohärenz dieser Zustände die makroskopischen Mikrowellensignale beeinflusst, die durch den parametrischen Prozess abgestrahlt werden. Schließlich wird in Kapitel 5.4, die Möglichkeit der Mikrowellen-Signalverarbeitung unter Verwendung von nicht-resonanter parametrischer Wellenfront-Umkehr von Spinwellen demonstriert.

5.1 Field-induced transition from parallel to perpendicular parametric pumping for a microstrip transducer

T.M. Neumann, A.A. Serga, V.I. Vasyuchka, and B. Hillebrands

Microstrip and coplanar transducers have become a standard instrument in magnetism at microwave frequencies. For the forced excitation of spin waves they posses several advantages. They can be applied to thin films and nano-scaled magnetic structures. When used to realize parametric pumping, the pump region is accessible with optical techniques and the applied microwave power is concentrated into a very high pump field.

Parametric pumping by itself plays an important role in experiments on fundamental properties of magnetic excitations as well as in applications since it allows the amplification, shaping and processing of microwave signals [1–3]. One of the most exciting applications of this technique was the recent observation of Bose-Einstein condensation of magnons at room temperature [4].

The original theory on parametric pumping was developed by Suhl [5] and Schlömann [6] who considered microwave pump fields oriented perpendicular and parallel to the bias magnetic field, respectively. In the first case, known as subsidiary absorption, the pump field excites a uniform precession which couples to spin-wave modes. For parallel pumping, the pump field directly amplifies spin-wave modes. As for subsidiary absorption this is a threshold process which only sets in above a certain threshold pump field. The theoretical predictions for the threshold value were successfully tested using cavity resonators which create a spatially uniform pump field [7–9].

The pump field created by microstrip and coplanar transducers, however, is strongly localized and non-uniform. This affects the pump process not only in the beneficial ways mentioned above. It is, for instance, well known, that the localization plays an important role in the amplification of traveling spin waves [10–12]. But, so far the general question how the use of a microstrip

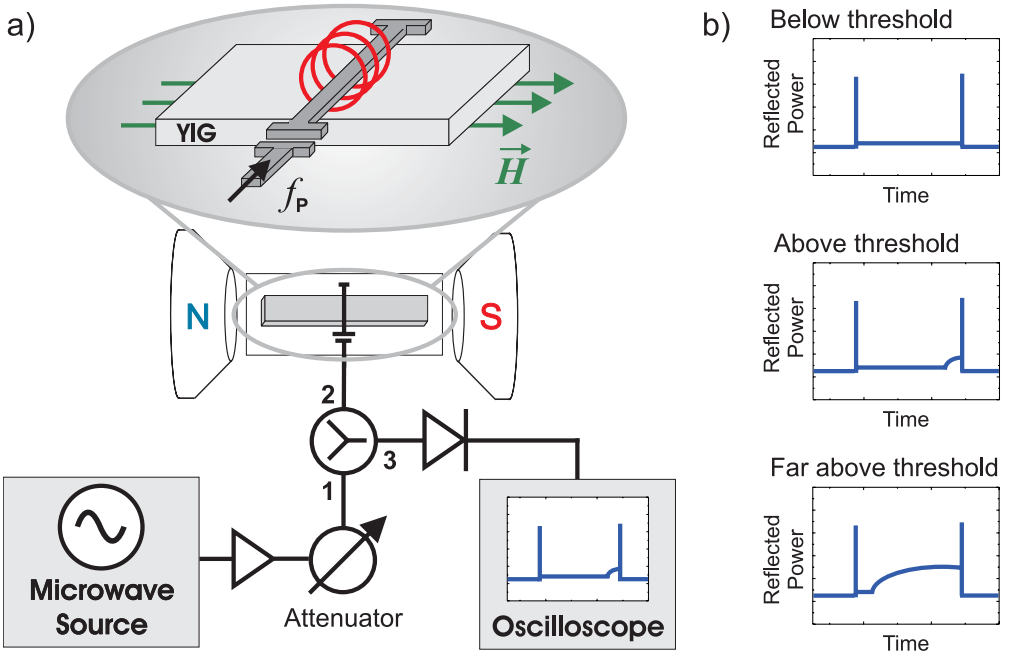

Fig. 1: a) Sketch of the experimental setup. b) Schematic oscilloscope pictures for different pump powers.

transducer affects the pump process, remains unanswered. In particular, the magnetic pump field around the transducer has a component oriented perpendicular to the bias magnetic field which is usually neglected in experiments.

To answer the question if this assumption is feasible, the threshold of parametric instability for a microstrip transducer is investigated. It is shown that below the critical field H_c which corresponds to the minimal threshold power and is given by $H_c = -2\pi M_S + \sqrt{(2\pi M_S)^2 + (\omega_p/(2\gamma))^2}$, where M_S is the saturation magnetization, ω_p is the pump frequency and γ is the gyromagnetic ratio, pure parallel pumping is achieved. In this case, the amplified spin waves propagate along the microstrip transducer and are not affected by the spatial localization of the pump field. Above the critical field, the spatial confinement of the pump region leads to an abrupt increase of the threshold because the amplified spin waves leave the pump region. This increased threshold is accompanied by a transition from parallel to perpendicular pumping. At bias magnetic fields $H \geq 1.2\, H_c$, the parametric process at the threshold is completely determined by the perpendicular component of the magnetic pump field.

The efficiency of the amplification by the perpendicular field component is noteworthy. For pump powers slightly above 10 mW amplification was observed, although the difference between the applied microwave frequency and the frequency of ferromagnetic resonance was 1500 times the resonance linewidth. This has to be kept in mind for numerous experiments with microstrip transducers, where perpendicular pumping could unintentionally occur.

Figure 1a shows the experimental setup. A 20 µs long microwave pulse with a carrier frequency $\omega_p/(2\pi) = 14.14\,\mathrm{GHz}$ was generated every 1 ms. Its power was adjusted by a power amplifier and an attenuator. The signal was sent to a half-wavelength microstrip resonator placed on a tangentially magnetized yttrium iron garnet film of 7.8 µm thickness grown in (111)-direction. A Y-circulator passed the reflected signal to a detector.

The reflected signal depends significantly on the applied pump power (Fig. 1b). Below the threshold, almost no signal is reflected due to the good adjustment of the pump resonator. As soon as the applied pump power exceeds the threshold power a kink at the end of the reflected signal appears (middle panel of Fig. 1b). This is a consequence of the change in the quality factor and the dynamic detuning of the resonator caused by the excitation of spin waves [13]. In the experiment, the threshold pump power was determined when the kink appeared after 20 µs at the end of the pump pulse.

The measured data on the threshold pump power is shown in Fig. 2a. In general, the data matches previously reported results with cavities: (i) When the pump frequency coincides with twice the frequency of ferromagnetic resonance the threshold power is minimal. The corresponding bias field is defined as H_c. (ii) For fields below H_c the threshold power decreases with increasing applied bias field. (iii) For fields above H_c the threshold power increases with increasing applied bias field. It grows towards infinity as the bias field approaches $H_0 = \omega_p/(2\gamma)$ and half the pumping frequency leaves the spin-wave band (see inset in Fig. 2a).

The specialty of the data presented here is a sharp jump which occurs just above H_c. Within a change of the bias field of $1/(4\pi)15\,\mathrm{kA\cdot m^{-1}}$ the threshold increases more than 4 times (7 dB) before it quickly levels off.

To interpret the observed data consider

$$h_{\mathrm{thr}} = \min_k \frac{\Gamma_k}{V_k} \tag{1}$$

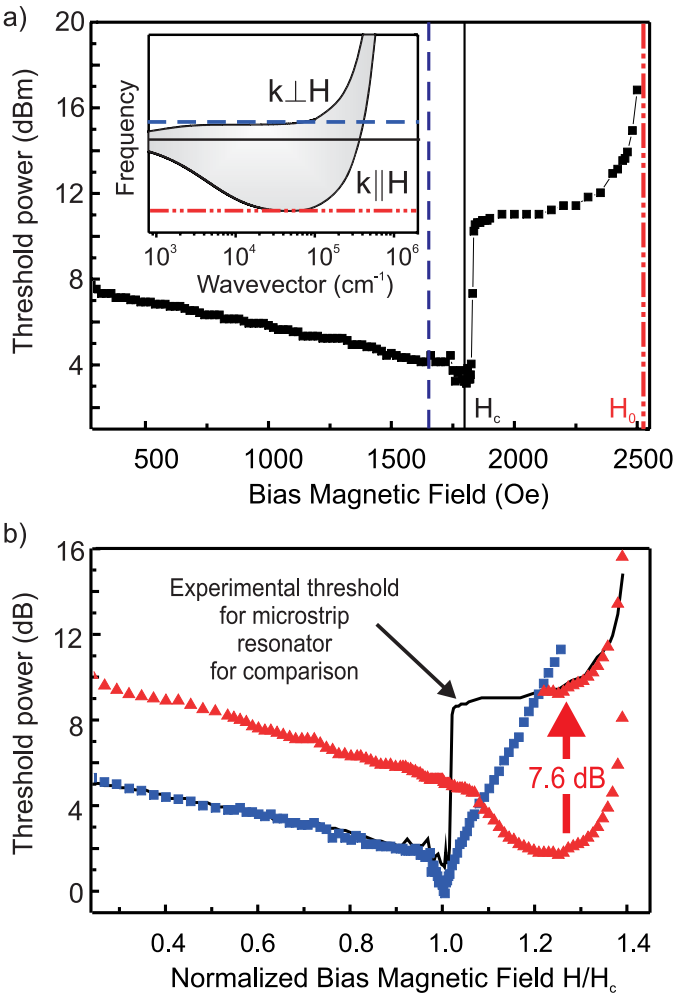

Fig. 2: Threshold pump power for a) a microstrip resonator and b) a dielectric resonator in parallel (■) and perpendicular (▲) alignment. The inset in a) shows a sketched spin-wave spectrum. The horizontal lines in the inset correspond to the respective vertical lines in the main panel and indicate the relative spectral position of the pumped spin waves.

describing the threshold field h_{thr} which depends on the ratio of the spin-wave relaxation frequency Γ_k and the coupling constant V_k of the pump field to the spin wave with wave vector k [14].

At the threshold, only one group of spin waves, which satisfies $\omega_k = \omega_\mathrm{p}/2$ and simultaneously has the minimal ratio Γ_k/V_k, is amplified. The decrease of the threshold for low fields is caused by a decrease in the respective spin-wave relaxation frequency Γ_k [6]. Small jumps in the threshold are due to the finite film thickness which results in a discrete character of the spectrum [15, 16].

Below H_c the spin waves with the lowest threshold propagate at an angle $\varphi_k = 90°$ with respect to the bias field because their coupling $V_k^{\parallel} \sim \sin^2\varphi_k$ to the parallel pump field is at a maximum. Such spin waves with frequency $\omega_k = \omega_\mathrm{p}/2$ do not exist for bias fields above H_c. Hence, above H_c the angle φ_k of the amplified spin waves is smaller than 90°, the coupling $V_k^{\parallel}$ is weaker and the threshold, consequently, higher. In particular, these spin waves possess a non-zero group velocity component parallel to the bias field. Therefore, they leave the area of amplification after a finite time which leads to an increased damping Γ_k. The smaller the pump region, the more striking this effect becomes as has been shown in [17] with dielectric resonators of different sizes. In the investigated case of a microstrip resonator, this effect is expected to be especially pronounced.

The observed leveling of the threshold is directly related to the influence of the perpendicular pump field component. For the perpendicular component the coupling $V_k^{\perp} \sim \sin(2\varphi_k)$ to spin waves of angle $\varphi_k \approx 45°$ is much more efficient than for the parallel field component. For this reason, the perpendicular pump field component starts to govern the processes at the threshold above H_c.

As the applied bias magnetic field approaches H_0 both coupling constants $V_k^{\parallel}$ and $V_k^{\perp}$ decrease leading to a steady increase in the threshold power.

The interpretation was tested by comparing the threshold observed for the microstrip resonator with the threshold of parametric instability for a dielectric resonator.

For this purpose the YIG-sample was placed inside a $4.2 \times 3.1 \times 1.5\,\mathrm{mm}^3$ dielectric resonator. Resonator and sample were then fixed inside a waveguide which was on one end shortened with an adjustable piston and on the other end connected to the setup shown in Fig. 1. Measurements were performed with the same duration of the pump pulse once with the resonator field pointing parallel and once perpendicular to the bias magnetic field which realizes in good approximation pure parallel and pure perpendicular pumping.

The measurement results are shown in Fig. 2b. The obtained curves agree well with previously reported experiments and the established theory (see references above). Two observations are essential:

(i) The threshold for perpendicular pumping falls below the one for parallel pumping at a field $H \leq 1.1\,H_c$. This illustrates, that the perpendicular coupling coefficient $V_k^{\perp}$ surpasses the parallel one $V_k^{\parallel}$ in this field range.

(ii) The slope of the threshold curve for parallel alignment of the dielectric resonator agrees with the one measured with the microstrip resonator for fields below H_c. At the same time, the threshold for the perpendicularly aligned dielectric resonator can be brought to coincidence with the microstrip resonator threshold for fields above $1.2\,H_c$.

We attribute the relative displacement by 7.6 dB of the threshold curves for parallel and perpendicular pumping, which is necessary to match the microstrip resonator threshold curve for low and high bias fields, to the aforementioned spin-wave mediated energy flux from the pump region.

Qualitatively, the influence of the energy outflow from the pump region on the threshold power can be estimated as follows: Let k be the wave vector of the excited spin wave group with the lowest threshold. For a localized, homogeneous pump region of length l in the direction of the externally applied field, the outflow of the spin waves from this region and the relaxation both lead to a dissipation of the spin-wave energy E_k. Hence,

$$\frac{d}{dt}E_k = -2\Gamma_k \cdot E_k - v_k^{\perp} \cdot \frac{dE_k}{dl} = -2\left(\Gamma_k + \frac{v_k^{\perp}}{2l}\right) \cdot E_k = -2\Gamma_k' \cdot E_k \tag{2}$$

where, $v_k^{\perp}$ denotes the component of the spin-wave group velocity perpendicular to the microstrip resonator. According to Eq. (2) the limited size of the pump region leads to an increase in damping by $v_k^{\perp}/2l$ which should be included in the effective damping Γ_k'. This effective damping should then enter Eq. (1) for the calculation of the threshold field. A more rigorous deduction [18] modifies the result slightly by including a geometric factor $\pi < b < 2\pi$ which depends on the ratio $\Gamma_k l / v_k^{\perp}$. According to L'vov we have

$$\Gamma_k' = \sqrt{\Gamma_k^2 + (b\, v_k^{\perp}/2l)^2} \quad . \tag{3}$$

The theory therefore confirms, that a decrease in the size l of the pump region leads to an increase in the threshold field, if the group velocity component $v_k^{\perp}$ does not vanish.

Though the outflow of energy is necessary to explain the jump in the threshold curve for the microstrip resonator, it is not sufficient. Note, that in Fig. 2b, at fields above $1.2\,H_c$, the threshold curve for the parallel aligned dielectric resonator surpasses the one for the microstrip resonator. If

only the parallel component of the pump field around the resonaotr is considered, this feature is impossible to explain – even when taking into account Eq. (3). In order to correctly describe the threshold behavior it is necessary to assume a transition from parallel pumping for bias fields $H < H_{\mathrm{crit}}$ to oblique pumping under some angle with respect to the bias field for $H > H_{\mathrm{crit}}$. The angle, under which the pump process takes place, is most certainly dependent on geometric properties of the resonator.

In any case, the shift of the pump angle corresponds to a spatial shift of the region where the pumping is most effective. While it takes place directly beneath the resonator for the case of parallel pumping, the pump region is split and shifted to the resonators edges for oblique and perpendicular pumping. Indeed, the existence of two spatially separated pump regions has been observed recently [20].

In conclusion, we have investigated the threshold of parametric spin-wave instability for a microstrip resonator. The experiment shows a characteristic jump in the threshold curve just above the critical bias field. The results are consistently understood as an increase in damping due to the outflow of energy from the strongly localized pump region around the microstrip resonator and the influence of the perpendicular pump field component. It is possible to change the character of the pumping by a change of the bias field H from below H_{c}, where the microstrip resonator acts as a source of parallel pumping, to H above H_{c}, where oblique pumping takes place. The comparatively high efficiency of the spin-wave excitation by the perpendicular pump field component even when the pump frequency is far above the frequency of ferromagnetic resonance should be considered in any experiment using microstrip transducers.

The authors would like to thank Prof. G.A. Melkov and Dr. M.P. Kostylev for their helpful remarks. This work has been financially supported by the Matcor Graduate School of Excellence and the DFG within the SFB/TRR 49.

References

[1] A.A. Serga, T. Schneider, B. Hillebrands, M.P. Kostylev, A.N. Slavin, Appl. Phys. Lett. **90**, 022502 (2007).
[2] A.A. Serga, B. Hillebrands, S.O. Demokritov, A.N. Slavin, P. Wierzbicki, V.I. Vasyuchka, O. Dzyapko, A.V. Chumak, Phys. Rev. Lett. **94**, 167202 (2005).
[3] G.A. Melkov, V.I. Vasyuchka, Yu.V. Kobljanskyj, A.N. Slavin, Phys. Rev. B. **70**, 224407 (2004).
[4] S.O. Demokritov, V.E. Demidov, O. Dzyapko, G.A. Melkov, A.A. Serga, B. Hillebrands, A.N. Slavin, Nature **443**, 430 (2006).
[5] H. Suhl, Jour. Phys. Chem. Solids **1**, 209 (1957).
[6] E. Schlömann, J.J. Green, U. Milano, J. Appl. Phys. **31**, 386S (1960).
[7] G. Wiese, P. Kabos, C.E. Patton, Phys. Rev. B **51**, 15085 (1995).
[8] W. Wettling, W.D. Wilber, P. Kabos, C.E. Patton, Phys. Rev. Lett. **51**, 1680 (1983).
[9] Y.H. Liu, C.E. Patton, J. Appl. Phys. **53**, 5116 (1982).
[10] S.O. Demokritov, A.A. Serga, V.E. Demidov, B. Hillebrands, M.P. Kostylev, B.A. Kalinikos, Nature **426**, 159 (2003).
[11] G.A. Melkov, A.A. Serga, A.N. Slavin, V.S. Tiberkevich, A.N. Oleinik, A.V. Bagada, JETP **89**, 1189 (1999).
[12] L.M. Gorbunov, JETP **40**, 689 (1974).
[13] V.E. Zakharov, V.S. L'vov, S.S. Starobinets, Sov. Phys. Usp. **17**, 6 (1974).
[14] A.G. Gurevich, G.A. Melkov, *Magnetization Oscillation and Waves* (CRC Press, Inc., 1996).
[15] B.A. Kalinikos, N.G. Kovshikov, N.V. Kozhus, Sov. Phys. Solid State **26**, 1735 (1984).
[16] M.P. Kostylev, B.A. Kalinkos, H. Dötsch, J. Mag. Mag. Mater. **145**, 93 (1995).
[17] G.A. Melkov, S.V. Scholom, Fiz. Tver. Tela **29**, 3257 (1987).
[18] V.S. L'vov, *Wave Turbulence under Parametric Excitations* (Springer-Verlag Telos, 1994).
[19] B.A. Kalinikos, A.N. Slavin, J. Phys. C: Solid State Phys **19**, 7013 (1986).
[20] O. Dzyapko, V.E. Demidov, M. Buchmeier, T. Stockhoff, G. Schmitz, G.A. Melkov, S.O. Demokritov, Phys. Rev. B **80**, 060401 (2009).

5.2 Pumping-free dynamics of Bose-Einstein condensate of magnons

C.W. Sandweg, A.A. Serga, V.I. Vasyuchka, T. Neumann, A.V. Chumak, B. Obry, H. Schultheiss, and B. Hillebrands[1]

Since the first observation of the formation of a magnon Bose-Einstein condensate (BEC) at room temperature [1] the study of this condensate has become of great importance for the deeper understanding of BECs in general. Magnons, the quanta of magnetic excitations, are bosons and hence they can be described by Bose-Einstein statistics with a temperature-dependent density and zero chemical potential in thermal equilibrium. If additional magnons are injected into the system a gas of quasi-equilibrium magnons is created with a non-zero chemical potential. The injection can be realized by using the technique of parametric microwave pumping [2, 3]. When increasing the external pumping, the chemical potential reaches the energy of the lowest magnon state and therefore a BEC of magnons can be formed [1]. At the same time the external pumping can be considered as a strong disturbing factor for the entire magnon system in general and for the BEC in particular. However, previous investigations of this condensate were performed either when the external source of energy was switched on [1] or the system of magnons was not in an equilibrium state [4].

Here we report on the characterization of the pumping-free dynamics of a completely formed BEC of magnons. In the presented experiments two different situations were investigated. Firstly the behavior of the BEC of magnons was analyzed after the external pumping had been switched off.

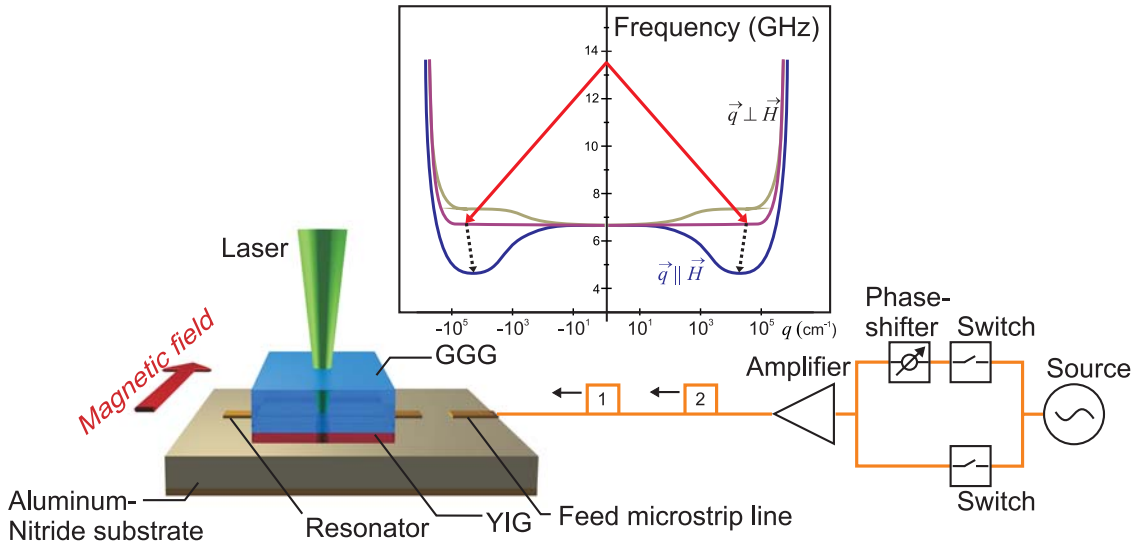

Fig. 1: Experimental setup. The microwave signal generated by a cw-mode source is split into two branches. The first one consists of a switch triggered by a pulse generator. The second one contains an identical switch and a phase shifter that is needed for additional investigations of the phase relation of the two pulses. After the combining the signal is amplified and sent to a resonator which is attached to the YIG film. A laser is focused on the YIG layer and the back-reflected light is directed to the interferometer. The inset shows the creation of two magnons by a single microwave photon (solid line arrow) by means of parametric amplification. Then the pumped magnons thermalize and flow to the minimum of the spectrum (dashed line arrow).

[1] In collaboration with G.A. Melkov, Department of Radiophysics, National Taras Shevchenko University of Kiev, Ukraine; V.S. Tiberkevich, A.N. Slavin, Department of Physics, Oakland University, Rochester, MI, USA.

Secondly, an additional pump pulse was switched with a certain delay with respect to the first one. In this way the characteristic response of the freely evolving BEC to a new disruption was studied. The experimental detection of the magnons was performed by means of Brillouin light scattering (BLS) spectroscopy [6]. This technique enables wide-range wave-vector sensitivity in comparison with conventional microwave measurements. The enhanced sensitivity is necessary for the direct observation of the BEC of magnons which is located at the lowest magnon state with wave numbers of about $5 \cdot 10^4\,\mathrm{cm}^{-1}$. Additionally, BLS has been improved to perform time-resolved measurements in order to study the evolution of a BEC on a time scale of a few nanoseconds.

Yttrium-Iron-Garnet (YIG) is an excellent model system to investigate the pumping-free evolution of a BEC due to the very low damping and consequently the relatively long lifetime of the condensate. The decay constant is in the range of 250 ns for dipolar dominated spin waves near the ferromagnetic resonance [5]. A YIG film of 7.8 µm thickness has been used, grown on a 500 µm thick Gadolinium-Gallium-Garnet (GGG) layer by liquid phase epitaxy in the (111) plane. The sample is placed on top of a 50 µm wide copper microstrip resonator with the length of half of the wavelength of the excitation frequency of 13.5 GHz (see Fig. 1). A microstrip resonator was used in order to accumulate the microwave power and concentrate the pump field spatially. The resonator again is fabricated on top of a grounded aluminum nitride substrate. Aluminum nitride has a very high thermal conductivity so that heating effects caused by the microwave current in the resonator can be minimized.

Figure 1 shows the experimental setup for the excitation of magnons and their detection using BLS spectroscopy. Next to the microwave source a power splitter is installed to separate the signal into two different branches. One branch consists of a switch triggered by a pulse generator that can vary the pulse duration, repetition time and delay if needed. The switch allows a switching time faster than 3.5 ns. The transition time is therefore significantly shorter than any characteristic time scale in the magnon gas and will not influence the measurement. The second branch contains an identical switch and a phase shifter in order to investigate the influence of the relative phase of two consecutive pump pulses on the condensate formation and decay. After combining the two branches the microwave signal is amplified to a power of 47.5 dBm in total. Afterwards, the signal is directed to the resonator.

The sample itself is placed between the two poles of an electromagnet so that the resonator lies perpendicular to the pumping field. BLS spectroscopy is realized in backward scattering geometry wherein the focused laser beam is reflected back from the copper microstrip resonator. The laser beam is focused on the YIG layer right next to the resonator.

To understand the pumping-free evolution of a BEC of magnons, firstly, one single pump pulse is applied. The pumping frequency hereby is 13.5 GHz, the duration of the pulse 2 µs and the repetition rate 20 µs. The proper choice of the on/off ratio and the pulse width ensures that no heating effects due to the high microwave power are distorting the measurements. A sufficiently long duration of the pulse plays also an important role for the BEC to reach a quasi-equilibrium state.

When the pump source is activated microwave photons split into pairs of phase-correlated magnons at half of the pumping frequency with opposite wave vectors, as shown in Fig. 1 (solid line arrows). Competing interactions of different groups of magnon pairs at half of the pumping frequency lead to the establishing of only one dominant group [2]. This dominant group can be considered as a condensate of magnons having the lowest damping and thus is absorbing predominantly the provided pumping energy. Afterwards the energy thermalizes very fast and flows with increasing pumping power to the minimum of the spectrum where the formation of the BEC takes place.

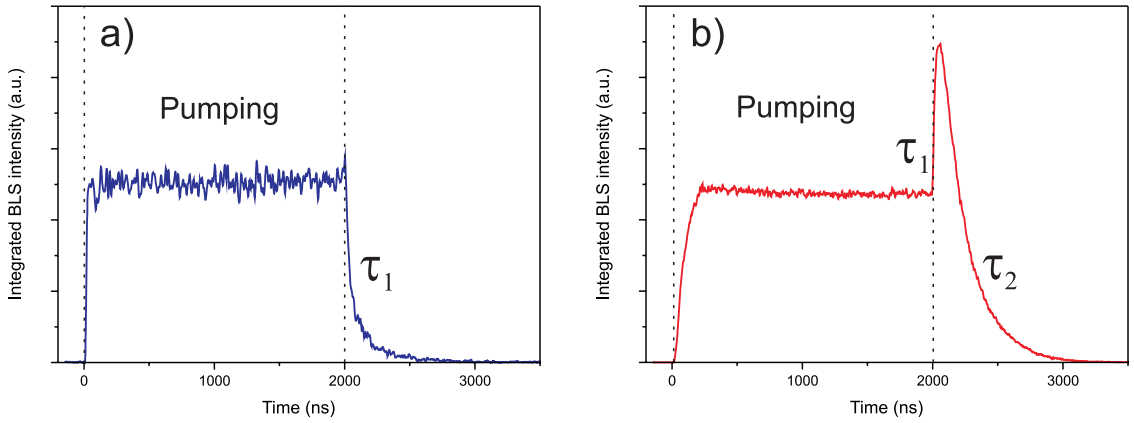

Fig. 2: Time-dependency of the dominant group and the BEC of magnons. a) Time profile of the signal from the dominant group at half of the pump frequency. A sharp increase of the signal can be observed when the pumping is switched on. After the pumping is switched of the signal decays with a time constant τ_1 of 45 ns. b) Time profile of the BEC of magnons. The transition into the equilibrium state is more gentle because of the slow thermalization that sets in after the formation of the dominant group. After the pump pulse is switched off a sharp peak arises with the same time constant τ_1 as in a). The final decay of the BEC occurs with a time constant $\tau_2 \ll \tau_1$.

Figure 2a shows the time profile of the dominant group at half of the pump frequency. After triggering the pump pulse a very sharp increase of the signal can be observed. Afterwards a saturated level is reached which remains constant until the end of the pump pulse. Then the signal decays as soon as the pump source is switched off. This decay is mostly caused by four-magnon-scattering processes which are proportional to the magnon density. Just after the end of the pump pulse the density of the dominant group is very high and the fast decay can be estimated to be exponentially with a time constant $\tau_1 = 45\,\text{ns}$.

The behavior of the signal from the bottom of the spectrum is completely different, see Fig. 2b. Firstly, the increasing of the signal to the equilibrium state is more gentle due to the fact that the thermalization to the bottom of the spectrum is much slower than the parametric process which is responsible for the formation of the dominant group. Secondly, after the pump pulse ends a sharp peak arises. We emphasize that this peak occurs when the pump process is switched off and hence the external flow of energy to the magnon system is stopped. The exponential rise of the peak has the same time constant (τ_1) as the decay of the dominant group. This unique behavior of the signal from the BEC of magnons can be understood as follows. The externally generated condensate of magnon pairs, the dominant group, acts as a constant source of energy for the BEC of magnons at the bottom of the spectrum. Therefore an equilibrium state of the BEC exists as long as the external source is pumping energy to the system. At the same time the t'spectrally localized dominant group is an immense source of disruption for the magnon system due to its high density of $10^{18}\,\text{cm}^{-3}$ to $10^{19}\,\text{cm}^{-3}$ [2,3]. The distortions can therefore cause a non-negligible suppression of the BEC of magnons. With the end of pump process this suppression ends and the BEC increases in intensity in the same manner as the dominant group decays. After reaching the maximum the BEC begins to decay on a much longer time scale of $\tau_2 \approx 400\,\text{ns}$ than the spin waves near the ferromagnetic resonance due to the reduced number of possible dissipation channels, e.g. two magnon scattering is suppressed in this case.

In order to check the hypothesis of the disruptive influence of the dominant group on the BEC of magnons a second pump pulse was applied to the system with a width of 100 ns and a delay of 200 ns with respect to the first one. As soon as the second pumping starts the intensity of the BEC

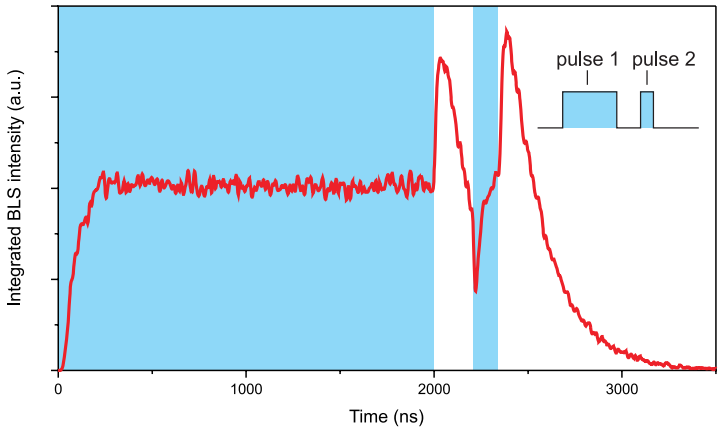

Fig. 3: Time-dependency of the BEC of magnons when two pump pulses are applied. 200 ns after the first pulse a second one with a width of 100 ns is generated in order to check the disruptive influence of the dominant group to the BEC. The intensity of the BEC created by the first pump pulse declines sharply as soon as the second pumping starts. Hence, the dominant group pumped by the second pulse exerts a distorting influence to the BEC of magnons. After additional magnons thermalize to the lowest energy state an increase of a second peak is observed.

created by the first pump pulse declines sharply even below the level of saturation (see Fig. 3). This behavior can be explained by the fact that the second pulse injects additional magnons to the dominant group. The additional magnons remain in the condensate of magnon pairs for a few hundred nanoseconds due to the relatively slow thermalization to the bottom. Shortly after the application of the second pulse the density of the dominant group is increased while the density of other areas of the magnon spectrum including the lowest energy state with the BEC of magnons should remain practically constant. However, the BLS measurements reveal a sharp drop in the intensity of the light scattered from the BEC, which is repopulated by the second pump pulse, exerts a disruptive force to the BEC of magnons. After additional magnons thermalize to the lowest energy state an increase in the BEC intensity and a second peak after switching off the second pump pulse is observed. Due to the fact that it is formed by the same mechanism the rise time and even more important the decay constant is the same as in the first case. In further measurements the influence of the relative phase between the two pump pulses has been investigated but no effect on the BEC evolution was observed.

In conclusion we demonstrate here the first observation of the direct interaction between the BEC of magnons and the condensate of magnon pairs at half of the pumping frequency. A decrease of the density of the condensate of magnon pairs results in a sharp rising of the BLS signal from the BEC of magnons at the bottom of the spectrum while an increase of the density of magnon pairs leads to a strong decay of the BEC.

References

[1] S.O. Demokritov, V.E. Demidov, G.A. Melkov, A.A. Serga, B. Hillebrands, A.N. Slavin, Nature **443**, 430 (2006).
[2] V.S. L'vov, *Wave Turbulence under Parametric Excitations. Applications to Magnetics.* Springer (1994).
[3] A.G. Gurevich, G.A. Melkov *Magnetization Oscillations and Waves.* CRC Press (1996).
[4] 0. Dzyapko, V.E. Demidov, S.O. Demokritov, G.A. Melkov, A.N. Slavin, New Journal of Physics **9**, 64 (2007).
[5] G.A. Melkov, A.A. Serga, A.N. Slavin, V.S. Tiberkevich, A.N. Oleinik, A.V. Bagada Sov. Phys. JETP **89**, 1189 (1999).
[6] S.O. Demokritov, B. Hillebrands, A.N. Slavin, Phys. Rep. **348**, 442 (2001).
[7] G.A. Melkov, S.V. Sholom, Sov. Phys. JETP **72**, 341 (1991).

5.3 Spin-wave pulse recovery with variable magnon damping and coherence

S. Schäfer, V. Kegel, A.A. Serga, and B. Hillebrands

In this article, we report on the investigation of magnon damping in yttrium iron garnet (YIG) thin films. We used the technique of spin-wave pulse recovery by parametric pumping [1–3] to probe a parametrically amplified [4] high-density magnon gas, thus gaining access to its relaxation behavior. We address the role of Gilbert damping [5, 6], variable four-magnon scattering and coherence in a parametrically driven magnon gas. The most salient experimental result is an increase in the response of the magnonic system on the external parametric pumping, when compared to a single pulse recovery as was reported in our earlier works [1–3]. This was unexpected, as the pulse-like recovered signal results from an already saturated system, thus not allowing higher signals without a change in significant system parameters. The results suggest a non-exponential damping behavior that is not explained by the Gilbert model of magnon damping.

In the experiments we report on here, a traveling spin-wave packet is excited by a microstrip input antenna as depicted in Fig. 1. An external magnetic field is applied within the plane of the YIG waveguide, perpendicular to the spin-wave propagation, i.e. in the Damon-Eshbach (DE) geometry [7]. The excited spin wave traverses the magnetic sample, a thin (5 µm) Yttrium iron garnet (YIG) waveguide magnetized in-plane along its short axis. Afterwards, the traveling spin-wave packet is detected by the output antenna, amplified, and observed with an oscilloscope. When this pulse has passed the central area of the YIG waveguide, a parallel parametric pumping field is applied [4] by a dielectric resonator, excited by a microwave field inside a waveguide. The magnetic microwave field is directed parallel to the magnetization. It oscillates with twice the frequency of the spin waves, and amplifies them by splitting of one microwave photon into two magnons. After applying this pumping pulse, an additional, recovered pulse is observed at the output antenna. Because the DE packet already left the area of parametric interaction, this is not the original, amplified signal pulse [8].

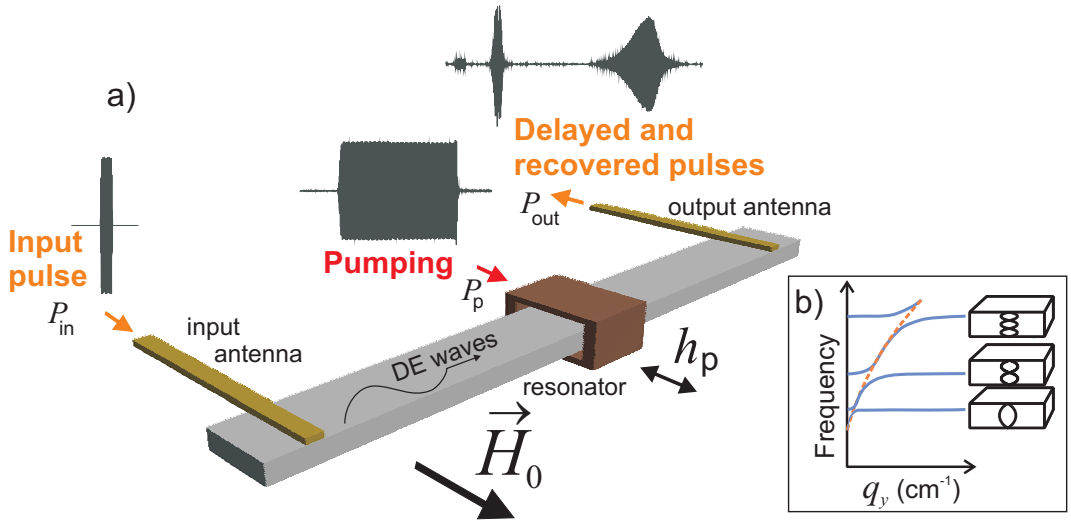

Fig. 1: a) Experimental setup, consisting of a single-crystal YIG waveguide, input and output antennas and a dielectric resonator for the application of the pumping microwave field. The waveforms schematically depict the form of the input, pumping and restored pulse as can be seen on the oscilloscope. b) Section of the spin-wave dispersion spectrum for a thin magnetic waveguide schematically showing the hybridization of Damon-Eshbach (dashed line) with perpendicular standing spin wave modes (solid lines).

Rather, the parametric interaction acts on the perpendicular standing spin-wave (PSSW) modes which are excited by the traveling DE packet by two-magnon scattering. Those PSSW modes exist due to the quantization along the finite thickness of the YIG sample and have quantized wave vectors q and thus eigenfrequencies. They are excited where the dispersions of DE and PSSW modes cross (see Fig. 1b). In our case, the parametric pumping process is only frequency selective, since we apply $\nu_{\mathrm{pump}}/2$ at frequency of the PSSW modes. Thus – given the large number of frequency-degenerate magnons within the PSSW branches of the dispersion – magnon groups over a large range of wave vectors are excited. This includes those close to the dispersion crossings, called the signal group, having wave vectors of $q \approx 10^2\,\mathrm{cm}^{-1}$ as well as magnons with q exceeding $10^5\,\mathrm{cm}^{-1}$. The latter ones are in fact amplified with a higher efficiency than the former [9], and therefore called the dominant, or dominantly excited, group. The standing modes are not directly accessible by the output antenna due to a very low excitation efficiency, and the negligible group velocity causing to remain constrained in the central area of the YIG film. Instead, the amplified PSSW modes can excite DE magnons at the dispersion crossings, and these DE magnons are finally detected at the output antenna. This process was already reported earlier [1] in detail, and will be referred to as the spin-wave signal recovery. Here, it is important to understand, that the recovered spin-wave signal has a pulse-like shape caused by the saturation of the magnon density. This pulse-like recovery is caused by the dominant group reaching a critical threshold amplitude A_{cr} large enough to influence the amplification of the signal group by the parametric pumping: Because the dominant group and the external excitation are out-of-phase, the resulting effective field acting on the signal group will be diminished when the density of the dominant group increases. This leads to the suppression of the signal group, while the dominant group reaches saturation. The signal retrieved by the signal group – via scattering into traveling DE spin waves – thus has a pulse-like form. After the restored pulse is formed, the system stays in a quasi-equilibrium state wherein the dominant group magnon density is saturated. The signal group is exposed to an effective pumping below the generation threshold [10] and thus decays with time to the thermal level.

In this work, we cut off this first recovered pulse by stopping the parametric pumping. Hence the signal group is not completely suppressed by the dominant group. After a certain delay time τ_{delay}, a second pumping pulse (see continuous line in Fig. 2b) is applied. We then observe the peak amplitude and arrival time of the second recovered pulse. Since those depend on the ratio of the magnon densities of the signal and dominant group A_{sig} and A_{dom} respectively, at the time at which the second parametric amplification sets in, we actually probe the relaxation behavior of these magnons. The most notable effect observed here was a gain of the maximum amplitude of the second recovered pulse compared to the experiment without interrupting the pumping pulse as shown in Fig. 2b. This is noteworthy, because the saturation effect – caused by the dominant group having a lower damping than the other relevant magnons – only allows for lower signals following the first recovery process. In the figure, the dashed line represents the case of one long pumping pulse and the continuous line the experiment with the interrupted pumping. The dependence of the amplitude on τ_{delay} is a parabolic one (Fig. 3a). The important process for the understanding of this dependency is the relaxation of the magnon gas, determining the relative magnon densities at the time the second pumping pulse sets in.

As can be seen in Fig. 3, the behavior of the second recovered pulse strongly depends on the duration of the first pumping pulse T_1 as well as on the delay time τ_{delay} during which pumping is interrupted. Figure 3a shows the peak amplitudes of this pulse, extracted from the original data like shown in Fig. 2b as a function of the delay time. The peak amplitudes are plotted for several durations of the first pumping pulse T_1 as a function of τ_{delay}. One can see that the second recovered pulse first increases, reaches a maximum, and then decreases in intensity. Besides the

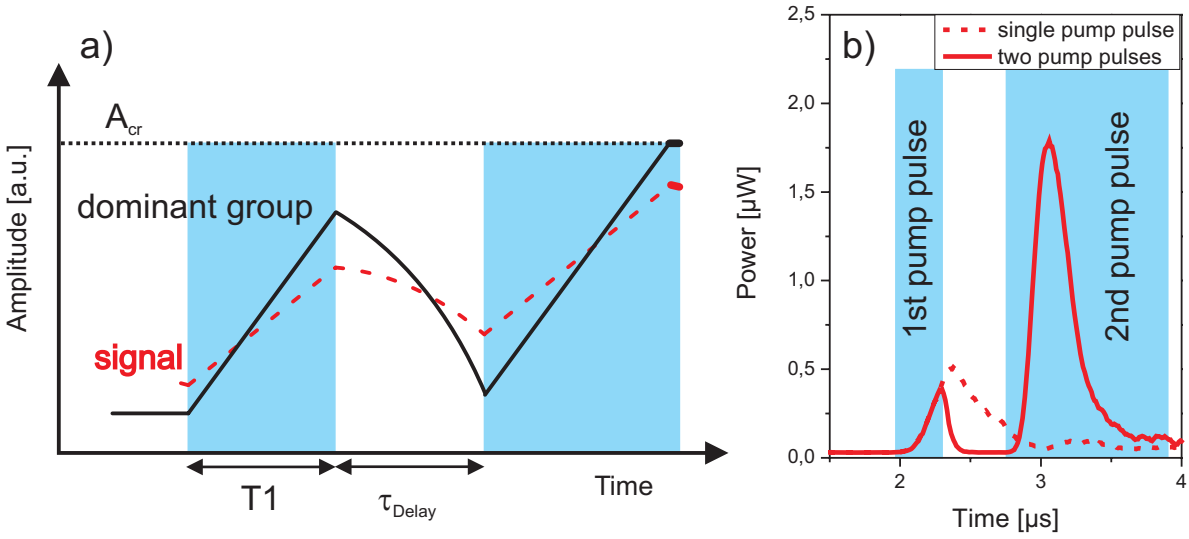

Fig. 2: a) Scheme of the temporal evolution of the integral PSSW mode density. The dashed line shows the signal group with wave vectors close to the dispersion gaps responsible for the interaction with the DE modes. The continuous line depicts the dominant group which is most efficiently amplified. The horizontal dotted line and the shaded areas show the critical magnon amplitude A_{cr} and the time, when the parametric pumping is active, respectively. The signal group starts initially with a higher amplitude due to its excitation by the traveling DE modes traversing the waveguide. Then both groups are amplified by the first pumping pulse, the dominant group having a higher effective gain. After the pumping is switched off, both groups decay and in addition dephase. The dephasing is seen as an additional quadratic decay term, because the second pumping only amplifies those magnons still in phase with the external field. After a delay time τ_{delay}, the pumping sets in again and this time is long enough for the recovery process to fully saturate like described in [1]. b) Spin-wave power as experimentally observed at the oscilloscope. The continuous line represents the results of the two-pump-pulse recoveries. The first pumping pulse is switched off before the recovered signal saturates. After a delay time τ_{delay} the pumping is switched on a second time and the (saturated) second signal retrieval is observed. The dashed line represents the experimental result for the pumping being not interrupted. The increase of signal intensity of the second pulse with respect to the first (saturated) pulse is clearly visible.

initial increase of amplitude, a non-exponential decay afterwards is observable (note the logarithmic scale). This non-exponential decay is not explained by the phenomenological Gilbert damping model.

In Figure 2a a scheme of the temporal magnon density evolution is shown for two different magnon groups. The dashed line represents the signal group, whereas the continuous line depicts the dominant group excited from the thermal background in the first place. Three distinct regions are visible in the scheme. It starts with the first applied pulse of pumping with both groups being amplified with their corresponding amplification efficiencies. The difference is caused by a different inherent damping, decreasing the effective pumping. Then, the pumping is switched off before the aforementioned saturation processes starts to dominate. During the pump-free time the magnonic system starts to relax. In the last part, the pumping resumes and the magnons are amplified with two distinctions to the first region: The amplification process starts at higher density levels for both groups, and with a different density ratio than for the first region of amplification. In addition, the pumping field now is not switched off, but rather applied long enough for a saturation process to set in and finally cause the pulse-like recovered signal [1] as described above.

The relevant situation for the second retrieval of the signal is now the situation at the point t_0 when the second pumping pulse sets in. This means that the magnonic damping behavior during the time the external pumping field is interrupted is responsible for the parabolic amplitude dependence visible in Fig. 3a. The maximum recovered amplitude A_{max} depends on the ratio of the different

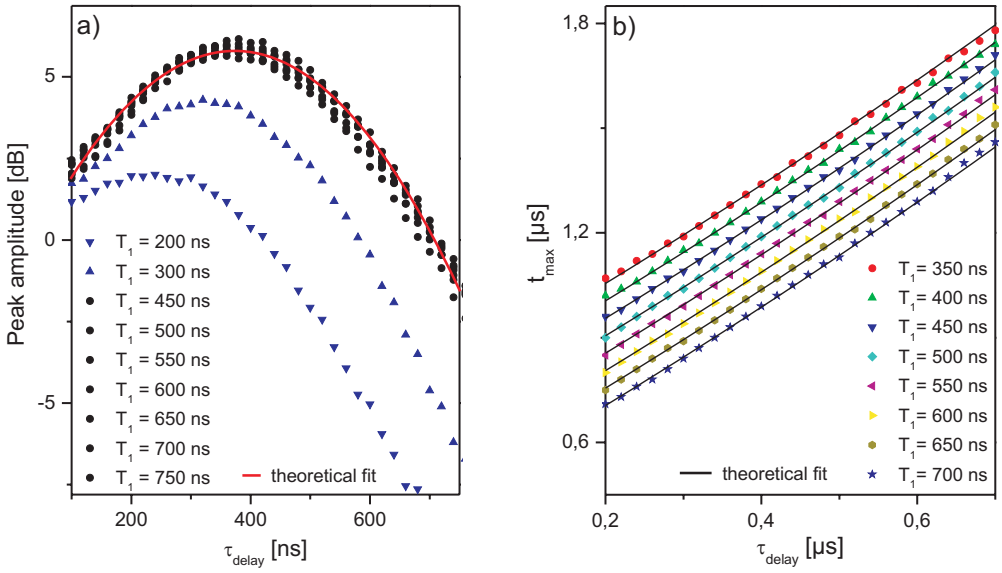

Fig. 3: a) Here, the peak amplitudes of the second pulse shown in Fig. 2b are extracted and plotted against τ_{delay} for different T_1. The amplitudes are normalized to the maximum observable amplitude using only one long pumping pulse. The continuous line represents the fit according to Eq. (3). As indicated in the text, the amplitudes for small T_1 are smaller because of the lower effective power distributed within the spectral width of the PSSW modes. b) The time t_{max} at which the peak amplitude shown in a) occurs as a function of τ_{delay}. Note the good agreement of the results with the fits (continuous lines) according to Eq. (2).

magnon densities A_{sig} and A_{dom} of the signal and the dominant group at the time t_0 as well as on the ratio $\delta = \frac{h_p V - \Gamma_{\mathrm{sig}}}{h_p V - \Gamma_{\mathrm{dom}}}$ between the amplification efficiencies of both signal and dominant group. Here h_p, V, Γ_{sig} and Γ_{dom} denote the amplitude of the parametric pumping (h_p), the coupling coefficient between the pump field and the magnons (V), and the inherent spin-wave damping of the signal (Γ_{sig}) and dominant (Γ_{dom}) group, respectively. V is considered equal for all parametrically amplified magnons [11]. The simplified expression for this peak amplitude is [1]:

$$\ln(A_{\mathrm{max}}) = \ln(A_{\mathrm{sig}}) + \delta\,[\ln(A_{\mathrm{cr}}) - \ln(A_{\mathrm{dom}})] \quad . \tag{1}$$

Here, A_{cr} is the aforementioned critical threshold, at which the dominant group's density is high enough to suppress the effective amplification of the signal group. The amplitudes A_{sig} and A_{dom} are determined by the duration of the first pumping pulse T_1 and τ_{delay}. The latter dependency now is responsible for the parabolic behavior of A_{dom} shown in Fig. 3a which was not expected nor can be described just by the competing amplifications responsible for the known recovery model.

The new feature in our experiments is the fast non-linear decay while the pumping is interrupted, caused by strong four-magnon scattering and dephasing of the dominant group. The dephasing is caused by the finite frequency width of the excited magnons, given by the finite pumping pulse duration and the frequency width of the PSSW dispersion of the order of 1 MHz. This dephasing of a system of magnons with slightly different eigenfrequencies has been observed and described for different system before [12]. Because the amplified magnons present an ensemble of oscillators with slightly different eigenfrequencies, they start to dephase after their coherence is not enforced by the phase of the external microwave field anymore. This dephasing process is not a loss of energy - and therefore not a damping process. Thus, for timescales smaller than the spin-wave decay time, the macroscopic signal may even vanish totally while remnants of the original excitation are still present in the system. One can utilize this for the creation of magnonic echoes [13], similar to the well-known nuclear echoes [14].

By the technique used here, no phase or time reversal is achieved, but the parametric amplification is a phase selective mechanism. This means that only those magnons with the proper phase – i.e. a phase shift of $\pi/2$ with respect to the pumping field – will be generated, while the parametric field cannot act on those with the wrong phase. The dependence introduced by the dephasing is quadratic, because the magnon density – or amplitude – is dephasing linearly and the parametric amplification efficiency depends quadratically on the phase mismatch to the pumping frequency [12]. Thus for the decay during the pump-free time and – via Eq. (1) – the recovered amplitude, a linear term for the damping as well as a quadratic term for the dephasing has to be accounted for.

The relevant frequency width of the excited magnons was described in [12] as $\Omega^2 = \frac{h_p V}{2\tau_p}$, i.e. it depends on the time τ_p when the pumping is applied as well as on the pumping field power h_p. It is determined by the spectral characteristics of the microwave pumping pulse and is not an inherent property of the magnonic system. In our case Ω cannot increase arbitrarily for shorter pulse durations, because of the given frequency width of the PSSW modes mentioned above. Outside that frequency band, the dispersion does not allow for the existence and amplification of magnons.

Only introducing the dephasing would account for a quadratic decay in Fig. 3a, but not for the initial increase in amplitude. This is clear considering the essential assumption of the model for the recovery process being a smaller damping for the dominant than for the signal group. If this was to be unchanged for the excitation-free relaxation, the maximum recoverable signal amplitude could only decrease with the delay time (see Eq. (1)). Thus, the increased response of the system indicates a damping behavior deviating from the simple Gilbert model. Namely, the damping of the dominant group has to depend not only on the magnon density – as would be expected for four-magnon scattering – but also on the existence of an external parametric field. This is understood by the suppression of four-magnon scattering while the parametric excitation acts on the magnonic system, leading to a relative change in the relaxation rate as soon as the external excitation ceases.

When the above mentioned assumptions are applied to the old model (see Eq. (1)) of spin-wave recovery, the time $t_{\max}$, at which the maximum recovered amplitude is observed after pumping is applied, can be written as

$$t_{\max} = t_{\text{offs}} - T_1 + \frac{\Gamma_{\text{dom}}^{\text{free}} \cdot \tau_{\text{delay}}}{h_p V - \Gamma_{\text{dom}}} + \frac{\Omega^2 \cdot \tau_{\text{delay}}^2}{h_p V - \Gamma_{\text{dom}}} \quad , \tag{2}$$

with the resulting peak amplitude

$$\ln A_{\max} = \ln A_{\text{offs}} + \delta \cdot \ln A_{\text{cr}} + a \cdot \tau_{\text{delay}} + b \cdot \Omega^2 \cdot \tau_{\text{delay}}^2 \quad , \tag{3}$$

with a constant offset t_{offs}, $a = \delta \cdot \Gamma_{\text{dom}}^{\text{free}} - \Gamma_{\text{sig}}^{\text{free}}$, $b = \delta - 1$, the damping Γ_{dom} and Γ_{sig} of the dominant and signal group and Γ^{free} being the respective damping with no external pumping applied with $\Gamma^{\text{free}} > \Gamma_{\text{dom}}$.

With the dephasing considered for both relevant magnon groups, a parabolic difference in the amplitudes A_{sig} and A_{dom} at t_0 is observed, responsible for the experimental results in Fig. 3a. The experimental data as well as the fit with Eq. (3) for values of T_1 between 450 and 750 ns are shown there and the excellent agreement is obvious. Different symbols here depict different durations of the first pumping pulse T_1. We also extracted the times $t_{\max}$ at which the peak occurs and plotted the results with the fits according to Eq. (2) in Fig. 3b. Here, too, the good reproduction of the dependence on T_1 and τ_{delay} is evident.

Although the maximum recovered amplitude shown in Fig. 3a as described by Eq. (3) does not directly depend on T_1, one can observe a deviation for small T_1. While the peak amplitudes for a rather wide range of 450 to 750 ns do not vary significantly, the behavior is obviously different for 200 and 300 ns. This can be explained by the dependence of $A_{\max}$ on A_{cr} as described in Eq. (3). A_{cr} is the magnon density of the dominant group, at which internal effects, i.e. magnon-magnon interactions, start to dominate the overall magnon excitation instead of the externally applied parametric field. That means, that A_{cr} is proportional to the applied pumping power. Considering now the finite frequency width of PSSW magnons taking part in the observed processes, the dependence on T_1 is revealed: for short pulse durations, the frequency width of the pumping field exceeds the available bandwidth of the PSSW modes, hence only the spectral part inside the PSSW modes is to be taken into account when considering the effective applied pumping power. For T_1 far larger than shown above, the quadratic contribution – and therefore also the maximum peak amplitude – will decrease again as described by Eq. (3) because Ω decreases. With the observed amplitudes being equivalent for $T_1 \geq 450$ ns, we can assume for T_1 bigger than this that Ω is only a function of the applied parametric pulse and thus the same for the signal and dominant group.

In conclusion we investigated the relaxation of a free gas of previously parametrically amplified magnons. The experimental results show a clear deviation from the phenomenological Gilbert model of spin-wave damping. They also exceed the observations on non-linear four-magnon scattering caused damping described so far. In addition, the magnons experience a dephasing during the free relaxation. This could provide insight into the spectral width of the dispersion of the investigated magnons with a high frequency resolution. We were able to understand and reproduce the experimentally observed characteristics with a phenomenological model, incorporating the changing damping parameter as well as the dephasing.

Financial support by the DFG within the TR49 is gratefully acknowledged.

References

[1] A.A. Serga, A.V. Chumak, A. Andre, G.A. Melkov, A.N. Slavin, S.O. Demokritov, B. Hillebrands, Phys. Rev. Lett. **99**, 2-5 (2007).
[2] S. Schäfer, A.V. Chumak, A.A. Serga, G.A. Melkov, B. Hillebrands, Appl. Phys. Lett. **92**, 162514 (2008).
[3] A.V. Chumak, A.A. Serga, B. Hillebrands, V. Tiberkevich, A.N. Slavin, Phys. Rev. B **79**, 1-10 (2009).
[4] R.M. White, M. Sparks, Phys. Rev. **130**, 632-638 (1963).
[5] H. Suhl, IEEE Trans. on Magnetics **34**, 1834-1838 (1998).
[6] M. Lakshmanan, Phys. Rev. Lett. **53** 2497-2499 (1984).
[7] R.W. Damon, J.R. Eshbach, J. Appl. Phys. **31**, 104-105 (1960).
[8] B.A. Kalinikos, N.G. Kovshikov, M.P. Kostylev, H. Benner, JETP **64**, 171-176, (1996).
[9] V.E. Zakharov, V.S. L'vov, S.S. Starobinets, Sov. Phys. Uspekhi **17**, 896-919 (1975).
[10] H. Suhl, J. of Phys. and Chem. of Solids **1**, 209-227 (1957).
[11] V.S. L'vov, *Wave Turbulence Under Parametric Excitation*, Berlin, Springer (1994).
[12] G.A. Melkov, Yu.V. Kobljanskyj, A.A. Serga, V.S. Tiberkevich, Phys. Rev. Lett. **86**, 4918-4921 (2001).
[13] G.F. Herrmann, R.M. Hill, D.E. Kaplan, Phys. Rev. B **2**, 2587-2596 (1970).
[14] A. Abragam, American J. Of Phys. **29**, 860 (1961).

5.4 Non-resonant wave front reversal of spin waves used for microwave signal processing

V.I. Vasyuchka, A.V. Chumak, and B. Hillebrands[1]

The phenomenon of wave front reversal (WFR), wherein a propagating wave packet of a carrier frequency ω_s can be reversed by external pumping of a carrier frequency $\omega_p \simeq \omega_s$, is well known in nonlinear optics and acoustics, where it is caused by a four-wave second-order parametric interaction [1]. For spin waves in magnetically ordered substances it is possible to realize WFR in a three-wave parametric process [2, 3] with conservation laws:

$$\omega_s + \omega_i = \omega_p \quad , \quad \mathbf{k}_s + \mathbf{k}_i = \mathbf{k}_p \quad , \tag{1}$$

where $\mathbf{k}_p$, $\mathbf{k}_s$, are the carrier wave vectors of the pumping and signal pulses, and ω_i and $\mathbf{k}_i$ are the carrier frequency and wave vector of the "idle" wave pulse formed as a result of the parametric interaction. When the pumping wave vector is much smaller than the carrier wave vector of the signal ($\mathbf{k}_p \ll \mathbf{k}_s$) the generated "idle" pulse is wave-front reversed, i.e. $\mathbf{k}_i \simeq -\mathbf{k}_s$.

WFR of microwave spin-wave packets propagating in a thin ferromagnetic film is performed by applying a pulse of electromagnetic parametric pumping to the film [2, 4]. Previously, WFR of spin waves was realized when the the pumping frequency was exactly twice as large as the carrier frequency of the incident spin-wave packet, i.e. $\omega_p = 2\omega_s$.

Here, we demonstrate that the phenomenon of *non-resonant* WFR, where the input signal frequency is not exactly equal to half of the pumping frequency ($\omega_s \neq \omega_p/2$), opens interesting new possibilities for signal processing in the microwave frequency range. Spectrum analysis of microwave pulses using the non-resonant WFR process can be realized when the frequency band Ω_p of the signal amplification by the applied parametric pumping is narrower than the spectral width $\Omega_s = 2\pi/\tau_s$ of the input signal pulse ($\Omega_p \ll \Omega_s$), where τ_s is the duration of the input signal pulse. In the opposite limiting case, when $\Omega_p \gg \Omega_s$, the non-resonant WFR can be used for active (with amplification) filtering of input microwave signals.

We would like to mention, that an attempt to use non-resonant three-wave parametric interaction of spin waves for microwave spectrum analysis was undertaken in a recent paper [5]. However, the interaction process used in [5, 6] involves several different spin-wave groups and, as a result, the information about the duration, and shape of the input signal pulse was lost, and the amplitude of the obtained spectrum of the input pulse was considerably modified. This is not the case in the results reported here.

A scheme of the setup used in our experiments is shown in Fig. 1. The input microwave signal pulse was converted by a microstrip antenna into a packet of dipolar spin waves propagating in a long (20 mm) and narrow (1.8 mm) 5 µm thick waveguide made of a ferrimagnetic yttrium iron garnet (YIG) film epitaxially grown on a gallium gadolinium garnet (GGG) substrate. A bias magnetic field was applied in the plane of the YIG film along the spin-wave propagation direction. Thus, similar to the earlier experiment [2], backward volume magnetostatic waves (BVMSW) were excited in the waveguide. The input BVMSW wave packets were excited by microwave pulses of the carrier frequency ω_s, power $P_s = 0.25$ mW, and duration varying from $\tau_s = 50$ ns to 100 µs.

[1] In collaboration with Prof. G.A. Melkov and V.A. Moiseienko, Department of Radiophysics, National Taras Shevchenko University of Kiev, Ukraine, and Prof. A.N. Slavin, Department of Physics, Oakland University, Rochester, MI, USA.

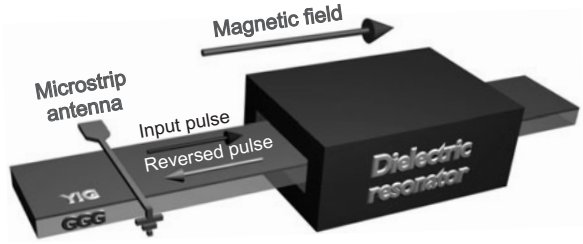

Fig. 1: Schematic experimental setup used for the non-resonant wave front reversal investigation.

The central part of the YIG waveguide was placed inside an open dielectric resonator (ODR), as is shown in Fig. 1. The ODR was used for supplying the pumping pulses at a fixed carrier frequency ω_p. The pumping magnetic field was oriented parallel to the bias magnetic field, leading to parallel pumping conditions. Pumping pulses lasting from $\tau_p = 50\,\text{ns}$ to $500\,\text{ns}$ and power of up to $5\,\text{W}$ were supplied at time t_d. The parametric interaction of the signal wave packet with the pumping pulse, which has a carrier frequency close (but not exactly equal) to ω_s, created a wave-front reversed wave packet, propagating in the opposite direction. This wave packet was detected at the input antenna at the time $2t_d + \tau_p$ after the input signal was launched.

The simplified formalism previously developed in Ref. [4] was used for the theoretical analysis of the observed non-resonant WFR process. In the framework of this formalism, performed in wave vector space for the case of strong pumping, the "k-th" Fourier component of the front-reversed spin-wave pulse at the time $t = 2t_d + \tau_p$, when this component has a maximum value, can be approximately evaluated as:

$$C_{-k} \approx C_{k0} \cdot \exp\left[(V_k h_p - \Gamma)\tau_p - \Gamma(2t_d + \tau_p) - \left(\frac{\Delta\omega_k}{\Omega_p}\right)^2\right] \quad , \tag{2}$$

where C_{k0} is the "k-th" Fourier component of the input (signal) spin-wave pulse, h_p is the amplitude of the pumping magnetic field, V_k is the coefficient of parametric coupling between pumping and spin waves defined in [4], Γ is the spin-wave relaxation parameter, $\Delta\omega_k = \omega_k - \omega_p/2$ is the detuning between half of the pumping frequency and the frequency ω_k of the "k-th" Fourier component of the signal, and

$$\Omega_p = \sqrt{2V_k h_p/\tau_p} \quad , \tag{3}$$

is the bandwidth of parametric amplification of the signal by pumping.

It is clear from Eq. (2) that the amplitude C_{-k} of the front-reversed spin wave increases with an increasing pumping magnetic field h_p and is at maximum for $\Delta\omega_k = 0$, which is the case of exact parametric resonance. One can see in Eq. (3) that the parametric amplification bandwidth Ω_p is determined by the pumping pulse amplitude h_p and duration τ_p.

As is pointed out above, the analytic expression of Eq. (2) is approximate, and it is applicable only to a qualitative analysis. For a more accurate calculation of the power P_r of the front-reversed output pulse we performed a numerical summation of the Fourier components of Eq. (2) ($P_r(t) = |\sum C_{-k}(t)|^2$), taking into account fast phase oscillation and the accurate dispersion relation for BVMSW. The results of this more accurate approach are shown as theoretical curves in the figures of this paper.

Below, we shall consider two limiting cases of the non-resonant WFR: the broadband input signal case, when $\Omega_s \gg \Omega_p$, and the narrow-band input signal case, when $\Omega_s \ll \Omega_p$.

The spectral picture of the non-resonant WFR in the case of broadband input signal is shown in the inset of Fig. 2. The parametric amplification bandwidth is narrow (it is equal to the delta function

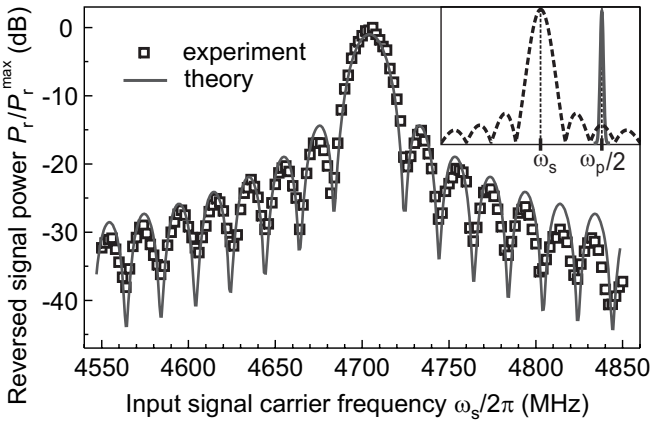

Fig. 2: Experimental (symbols) and calculated (line) dependences of the reversed signal power on the input signal frequency in the regime of broadband input signal ($\Omega_s/\Omega_p \approx 3.5$). Inset: the spectrum of the input signal (dashed line) and the band of parametric amplification (solid line).

$\delta(\omega - \omega_p/2)$ in the limiting case), thus only one input signal spectral component C_{k0} with the frequency equal to half of the pumping frequency $\omega_p/2$) can be amplified by the pumping. The amplitude of the C_{-k} component in the reversed pulse is proportional to the amplitude of the corresponding component $C_{k0}\,|_{\omega_k=\omega_p/2}$ of the input signal. The process looks like "sampling" of the input signal spectrum C_{k0} by the spectrally narrow pumping, as it is illustrated in the inset of Fig. 2. As a result, the spectrum of the input signal can be directly extracted by the non-resonant WFR process. The carrier frequency of the output reversed signal in this case is equal to $\omega_p/2$.

The results of comparison between the experimentally measured (squares) and theoretically calculated (solid line) power of the reversed pulse as a function of the carrier frequency of the input (signal) wave packet are shown in Fig. 2 for the case when the signal duration τ_s was 50 ns, pumping duration τ_p was 50 ns, and the pumping field multiplied with the coupling coefficient was $h_p V_k/2\pi = 5$ MHz. The ratio of the characteristic bandwidths was $\Omega_s/\Omega_p \approx 3.5$, and, therefore a broadband input signal regime of WFR was realized. The bias magnetic field was equal to 1020 Oe, the pumping frequency was $\omega_p/2\pi = 9420$ MHz, the spin-wave relaxation parameter was $\Gamma/2\pi = 0.42$ MHz, and the delay time between the signal and pumping was $t_d = 65$ ns. It is clear from Fig. 2 that theory is in excellent agreement with experiment.

The opposite limiting case of a narrow-band input signal regime of WFR is realized when the input signal pulse is sufficiently long (or/and when the pumping pulse is sufficiently short and strong), i.e when the condition $\Omega_s \ll \Omega_p$ is fulfilled. It is clear that in this case the spectral width of the signal is much smaller than the band of frequencies amplified by pumping (see inset in Fig. 3). The amplitude of the reversed pulse is determined by the amplitude of the main harmonic of the input signal, by the detuning ($\omega_s - \omega_p/2$), and by the parametric amplification bandwidth Ω_p.

The measured (symbols) and theoretically calculated (lines) power of the reversed pulse as a function of the carrier frequency of the input signal obtained for two different pumping pulses are compared in Fig. 3. In both cases the theoretical and experimental curves were normalized by the corresponding maxima of experimentally measured power of the reversed pulse. The duration of the input signal pulse was $\tau_s = 100\,\mu$s. The bias magnetic field was 950 Oe and the pumping carrier frequency was $\omega_p/2\pi = 9408$ MHz.

We performed experiments for two pumping amplitudes and durations. In the first case (circles and solid line in Fig. 3) the duration of the pumping pulse τ_p was 500 ns and the pumping field multiplied with the coupling coefficient was $h_p V_k/2\pi = 1$ MHz (corresponding to the pumping power of $P_p \approx 8$ mW). The characteristic ratio Ω_s/Ω_p was equal to 0.01 for these conditions. In the second case (squares and dashed lines in Fig. 3) the parameters were: $\tau_p = 100$ ns and $h_p V_k/2\pi = 5$ MHz (corresponding to $P_p \approx 200$ mW), and the characteristic ratio Ω_s/Ω_p was equal

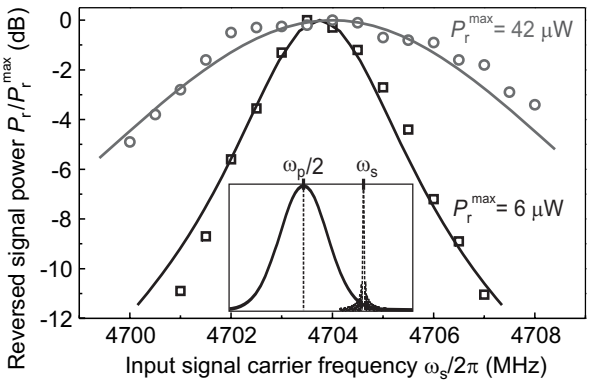

Fig. 3: Experimental (symbols) and calculated (lines) dependences of the reversed signal power on the input signal frequency in the regime of narrow-band input signal. Circles and solid line correspond to the pumping power $P_p \approx 8\,\mathrm{mW}$ and pumping duration $\tau_p = 500\,\mathrm{ns}$ ($\Omega_s/\Omega_p \approx 0.01$). Squares and dashed line correspond to the pumping power $P_p \approx 200\,\mathrm{mW}$ and pumping duration $\tau_p = 100\,\mathrm{ns}$ ($\Omega_s/\Omega_p \approx 0.0025$). Both curves were normalized by corresponding maximum powers. Inset: the band of parametric amplification (solid line) and the spectrum of input signal (dashed line).

to 0.0025. Thus, a narrow-band input signal regime of the WFR process was realized for both pumping pulses.

The curves presented in Fig. 3 can be interpreted as the amplitude-frequency characteristics of an active parametric pass-band microwave filter i.e. tunable by a pumping filter with amplification of the filtered signal. The bandwidth and the gain factor of the filter can be tuned by varying the duration and the power of the applied pumping pulse. Indeed, for the first pumping pulse (circles in Fig. 3) the pass-band of the active filter at the $-3\,\mathrm{dB}$ level is equal to $6.4\,\mathrm{MHz}$ and for the second pumping pulse (squares in the figure) this pass-band is $2.4\,\mathrm{MHz}$. Note that the gain coefficient of the active filter is substantially higher for the first pumping pulse than for the second one, but the curves shown in Fig. 3 were normalized. It should also be mentioned that in order to achieve good quantitative agreement between the theory and experiment shown in Fig. 3 it was necessary to perform the full summation of all the Fourier components of the interacting pulses and release the condition of strong pumping. The approximate analytic formula Eq. (3) describes the active filtering process only qualitatively. Nevertheless, it correctly predicts the decrease of the filter pass-band with the increase of the power and decrease of duration of the pumping pulse.

In conclusion, we explicitly demonstrated that non-resonant wave front reversal for dipolar spin waves can be effectively used for spectral analysis and active filtering of pulsed microwave signals. We believe that signal processing devices based on parametric interaction of spin waves in magnetic films will find important applications in microwave technology.

Support by the Deutsche Forschungsgeminschaft within the SFB/TRR 49 is gratefully acknowledged.

References

[1] B.Ya. Zel'dovich, N.F. Pilipetsky, V.V. Shkunov, *Principles of Phase Conjugation* (Springer, Berlin, 1985).
[2] G.A. Melkov, A.A. Serga, V.S. Tiberkevich, A.N. Oliynyk, A.N. Slavin, Phys. Rev. Lett. **84**, 3438 (2000).
[3] A.A. Serga, B. Hillebrands, S.O. Demokritov, A.N. Slavin, P. Wierzbicki, V. Vasyuchka, O. Dzyapko, A. Chumak, Phys. Rev. Lett. **94**, 167202 (2005).
[4] G.A. Melkov, A.A. Serga, A.N. Slavin, V.S. Tiberkevich, A.N. Oleinik, A.V. Bagada, J. Exp. Theor. Phys. **89**, 1189 (1999).
[5] S. Schäfer, A.V. Chumak, A.A. Serga, G.A. Melkov, B. Hillebrands, Appl. Phys. Lett. **92**, 162514 (2008).
[6] A.A. Serga, A.V. Chumak, A. André, G.A. Melkov, A.N. Slavin, S.O. Demokritov, B. Hillebrands, Phys. Rev. Lett. **99**, 227202 (2007).

B. Magnonic crystals and Spin Waves in Anisotropic Media

Magnonic crystals are defined as magnetic structures in which the magnetic properties vary periodically in one, two or three dimensions. With spin waves as their dynamic excitation, they are the magnetic analogue to photonic and sonic crystals, suitable to work in the microwave frequency range. Magnonic crystals can exhibit full band gaps, where spin waves are not allowed to propagate. They are interesting for microwave and signal processing applications due to their potential ability to efficiently localize and guide spin waves along a waveguide constructed in the crystal as well as due to a wide tuneability of their characteristic parameters.

The simplest type of a magnonic crystal is a one-dimensional diffraction grating created in a spin-wave waveguide by modulating periodically the internal magnetic field along the propagation direction. The waveguide typically has the form of a thin and narrow stripe of a magnetically ordered material. When the spin wave is channeled along the main axis of such a waveguide, this grating behaves like a one-dimensional magnonic crystal. Such structures can be created using single crystal ferrimagnetic films of yttrium-iron-garnet (YIG). This material is the most suitable one for the investigation of spin-wave propagation because it has very low propagation losses for dipole-dominated spin waves (also called magnetostatic waves).

Results on scattering of surface and volume magnetostatic spin waves in a one-dimensional magnonic crystal prepared in the form of an array of shallow grooves chemically etched across the YIG stripe are presented in Report 5.5. This magnonic crystal was further used for the wavenumber selection of active rings in the geometry of magnetostatic backward-volume modes, as presented in Report 5.6. The propagation of the backward wave through the dynamically controlled periodic magnetic potential created by the Oersted field of the electric current flowing near the YIG film surface is studied both theoretically and experimentally in Report 5.7. Finally, scattering of the backward volume magnetostatic modes on the moving reflection grate formed by the surface acoustic wave propagating along the YIG stripe was used for observation of the reverse Doppler effect, see Report 5.8.

Two-dimensional magnonic crystals can also be obtained by creating two-dimensional magnetic periodic structures in large (quasi-unbounded) magnetic films. Thus, the understanding of peculiarities of two-dimensional spin waves propagation becomes crucial. Generally, in an in-plane magnetized film the group and phase spin-wave velocities are not collinear due to the uniaxial anisotropy imposed by the magnetization orientation. As magnetisation is controlled by the bias magnetic field this enables an externally addressable, in-plane anisotropic magnetic potential through which the spin waves propagate. In the Report 5.9 we experimentally demonstrate the concentration of energy of quasi-uniformly excited spin waves along the preferable propagation directions and formation of very narrow difractionless spin-wave beams.

B. Magnonische Kristalle und Spinwellen in anisotropen Medien

Magnonische Kristalle sind magnetische Strukturen, deren magnetische Eigenschaften sich periodisch in ein, zwei oder drei Dimensionen ändern. Mit ihren dynamischen Anregungen, den Spinwellen, sind sie die im Mikrowellenbereich arbeitenden, magnetischen Entsprechungen zu photonischen und phononischen Kristallen. Magnonische Kristalle können Bandlücken aufweisen, in denen Spinwellen nicht propagieren können. Aufgrund ihrer Eigenschaft Spinwellen in einem Wellenleiter innerhalb des Kristalls zu führen und zu lokalisieren und der weiten Einstellbarkeit ihrer Parameter sind sie für Mikrowellen- und Signalverarbeitungsanwendungen interessant.

Der einfachste Typ eines magnonischen Kristalls ist ein eindimensionales Beugungsgitter, das in einem Spinwellen-Wellenleiter durch periodische Modulation des internen Magnetfelds entlang der Propagationsrichtung erzeugt wird. Der Wellenleiter hat üblicherweise die Form eines dünnen, schmalen Streifens aus einem magnetisch geordneten Material. Wenn eine Spinwelle entlang der Achse dieses Wellenleiters propagiert, wirkt das Gitter als eindimensionaler magnonischer Kristall. Solche Strukturen können aus einkristallinen ferrimagnetischen Yttrium-Eisen-Granat (YIG) Filmen erzeugt werden. Dieses Material ist aufgrund seiner sehr niedrigen Dämpfung für dipolare Spinwellen am geeignetsten für die Untersuchung dieser Wellen.

Die Ergebnisse der Untersuchung der Streuung von dipolaren (oder magnetostatischen) Volumen- und Oberflächenwellen in einem eindimensionalen magnonischen Kristall, der aus einer Reihe von chemisch geätzten, flachen Gräben im YIG-Streifen besteht, werden in Kapitel 5.5 vorgestellt. Dieser magnonische Kristall wurde weiter zur Wellenvektor-Selektion in einem aktiven Ringe für magnetostatischen Rückwärtsvolumen-Moden verwendet, wie in Kapitel 5.6 gezeigt wird. Die Ausbreitung von sog. magnetostatischen Backward-Volumenwellen durch ein dynamisch kontrolliertes, periodisches magnetisches Potenzial, das durch das Oerstedtfeld eines elektrischen Stroms nahe der YIG Filmoberfläche verursacht wird, wird theoretisch und experimentell in Kapitel 5.7 untersucht. Schließlich wurde die Streuung dieser Wellen an einem propagierenden Reflexionsgitter untersucht. Dieses wurde durch akustische Oberflächenwellen, die entlang des YIG-Streifens propagieren, gebildet. Wie Kapitel 5.8 zeigt, lässt sich unter diesen Voraussetzungen der inverse Doppler-Effekt beobachten.

Zweidimensionale magnonische Kristalle können durch das Erzeugen von zweidimensionalen magnetischen periodischen Strukturen in quasi-unbegrenzten magnetischen Filmen aufgebaut werden. Dabei ist das Verständnis der Eigenschaften von zweidimensionalen Spinwellen entscheidend. In einem in-plane magnetisierten Film sind im Allgemeinen Phasen- und Gruppengeschwindigkeit einer Spinwelle aufgrund der uniaxialen Anisotropie, die durch die Richtung der Magnetisierung vorgegeben wird, nicht parallel. Da die Magnetisierung durch das anliegende Magnetfeld kontrolliert wird, ergibt sich eine von außen kontrollierbare in-plane Anisotropie, durch die die Spinwellen propagieren. In Kapitel 5.9 zeigen wir experimentell, dass die Energie einer quasi homogen angeregten Spinwelle entlang von ausgezeichneten Propagationsrichtungen konzentriert wird und sich schmale, Spinwellenstrahlen mit Breiten im Subwellenlängenbereich ausbilden können.

5.5 Scattering of surface and volume magnetostatic spin waves in a magnonic crystal

A.V. Chumak, A.A. Serga, and B. Hillebrands[1]

Magnonic crystals, which are periodically structured magnetic materials, attract special attention in view of their applicability for both fundamental research on linear and nonlinear wave dynamics in artificial media, and for signal processing in the microwave frequency range [1–4]. An array of parallel grooves formed on the surface of a magnetic film seems to be one of the most effective methods to create a magnonic crystal [1, 2].

Thin magnetic films support propagation of different types of spin-waves depending on the angle between the wave propagation direction and the external magnetic field orientation. Backward volume magnetostatic spin wave (BVMSW) and magnetostatic surface spin wave (MSSW) configurations are characterized by parallel and perpendicular wave propagation relative to the magnetizing field applied in the film plane [5]. Both types of spin waves can be used in the magnonic crystal. As a whole, MSSW devices offer more benefits for microwave applications in comparison to BVMSW devices, in particular, because of more efficient excitation and reception by means of microwave antennas. Furthermore, MSSW devices possess a noteworthy specificity: they are nonreciprocal, which means that waves propagating in opposite directions in the film plane are localized at different film surfaces. They also couple differently to surface scatterers (for example to microstrip antennas) which results in nonreciprocal excitation of these waves [6]. Thus, the investigation of propagation of magnetostatic surface spin waves in an artificial magnonic crystal establishes the general problem of propagation and scattering of nonreciprocal waves in structured media.

In our recent paper [2] we presented results on scattering of BVMSW from a quasi-one-dimensional periodic structure of grooves in a film surface. The main advantage of BVMSW-based magnonic crystals was the excellent spin-wave signal rejection ratio of more than 30 dB. In contrast to MSSW, BVMSW are reciprocal waves. In this work we compare the operational characteristics of MSSW-based magnonic crystals with characteristics of BVMSW-based magnonic crystals [7].

To fabricate magnonic crystals, a 5.5 µm thick yttrium iron garnet (YIG) film was used. Photolithographic patterning followed by hot orthophosphoric acid etching was used to form the grooves. The etch mask had 20 parallel lines of width $w = 30\,\mu\text{m}$ spaced 270 µm away from each other, so that

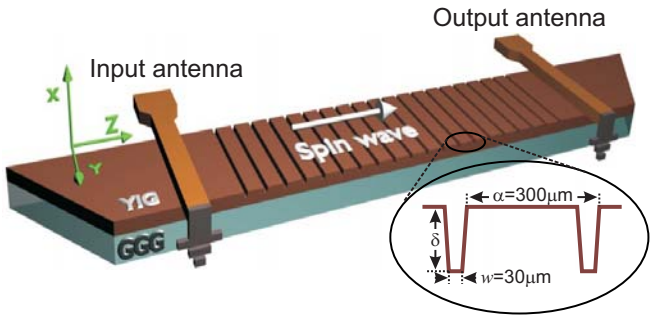

Fig. 1: Sketch of magnonic crystal structure used in the experiments.

[1] In collaboration with M.P. Kostylev, School of Physics, University of Western Australia, Crawley, Western Australia 6009, Australia.

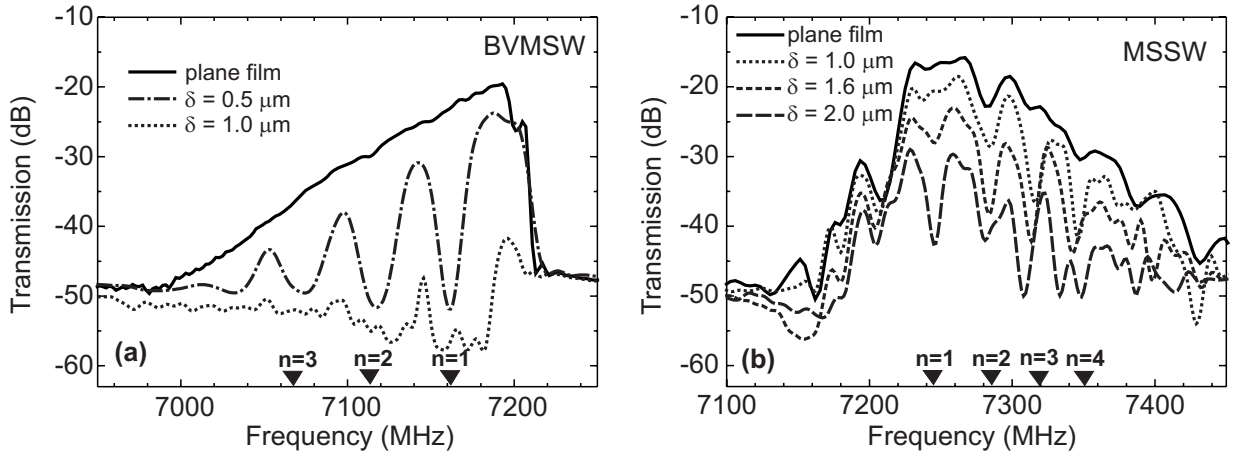

Fig. 2: Microwave transmission characteristics for an unstructured film (bold lines) and for magnonic crystals measured for different groove depth δ in BVMSW (a) and MSSW (b) configurations. Triangles show theoretically calculated positions of Bragg rejection bands of order n.

the lattice constant is $\alpha = 300\,\mu$m [2] (see Fig. 1). The grooves depth δ was varied from 100 nm to 2.3 µm by controlling the etching time and was measured using a surface profilometer. Two microstrip antennas placed 8 mm apart on each side of the grooved area were used to excite and receive spin waves as shown in Fig. 1. A bias magnetic field of $1/4\pi \cdot 1845\,\mathrm{kA/m}$ was applied in the plane of the YIG film, either along or perpendicular to the z-axis depending on the type of spin waves under investigation. Under these conditions the ferromagnetic resonance frequency is 7.21 GHz. A microwave network analyzer was used to measure transmission characteristics of these magnonic crystals.

The experimental BVMSW transmission characteristics for the unstructured film as well as for the gratings with $\delta = 500$ and 1000 nm are shown in Fig. 2a. In this case the bias magnetic field was applied along the z-axis (see Fig. 1). The BVMSW transmission characteristics for the unstructured film is limited from above by the ferromagnetic resonance frequency and from below by a drop in the microwave antenna excitation efficiency for shorter wavelengths. The insertion loss is determined by the energy transformation efficiency by the input and the output antennas and by the spatial decay of spin waves. As can be seen in Fig. 2a grooves as shallow as $\delta = 500\,$nm result in the appearance of a set of pronounced rejection bands (or transmission gaps), where spin-wave transmission is highly reduced. The onset of the rejection bands corresponds to a groove depth δ of 100 nm [2,7]. For $\delta = 1\,\mu$m the insertion loss in the whole spin-wave band is so pronounced that almost no spin-wave propagation is observed (see Fig. 2a). Triangles in the figure show theoretically calculated positions of rejection bands, with n denoting the number of the respective Bragg reflection band.

The measured MSSW transmission characteristics for the unstructured film as well as for the gratings with $\delta = 1, 1.6,$ and $2\,\mu$m are shown in Fig. 2b. In this case bias magnetic field was applied perpendicular to the spin-wave propagation direction (i.e. along the y-axis in Fig. 1). The MSSW transmission characteristics for the unstructured film is limited by the ferromagnetic resonance frequency from below and by the microwave antenna excitation efficiency from above, thus it looks like a mirror reflection to the BVMSW transmission characteristics. Several rejection bands in the transmission characteristics for the unstructured YIG film can be seen in Fig. 2b. These bands are formed due to exchange gaps in the MSSW spectrum. Their origin is hybridization of MSSW with higher-order standing-wave resonances across the film thickness [8,9]. Positions and depths

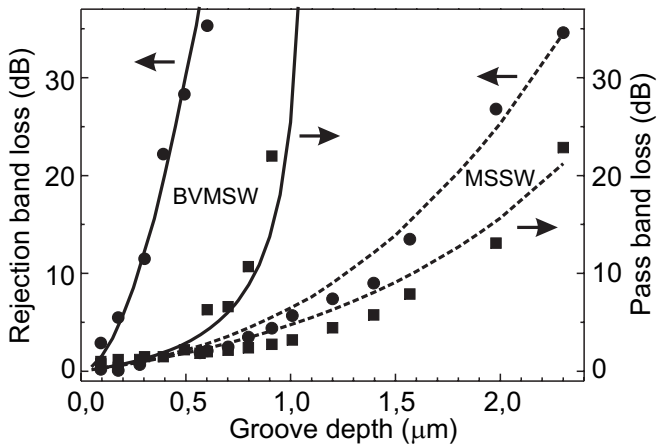

Fig. 3: Insertion loss in the first-order rejection band (circles) and in the first pass band (squares) measured for the BVMSW- and MSSW-based magnonic crystals (open and filled symbols, respectively) as a function of the groove depth δ. The solid and dashed lines present the insertion loss calculated for BVMSW and MSSW cases, respectively.

of these rejection bands are determined by the film thickness and conditions for magnetization pinning at the film surface.

Upon formation of the groove arrays on the surface of the YIG film additional rejection bands appear (see Fig. 2b). Some of them overlap the exchange gaps. A groove depth $\delta = 0.5\,\mu\text{m}$ (not shown in Fig. 2b) results only in a slight modification of the MSSW transmission, while for BVMSW the same structure shows rejection bands of approximately 30 dB in depth (see Fig. 2a). An increase in δ to 1 μm results in the appearance of pronounced rejection bands (while for BVMSWs one sees complete rejection for this groove depth). Further increase in δ results in an increase in the rejection efficiency and in insertion loss in the pass bands. Thus, the operational characteristics of magnonic crystals with $\delta = 2.0\,\mu\text{m}$ is completely unsatisfactory.

Triangles in Fig. 2b show positions of the rejection bands calculated based on Bragg's law. Apart from the formation of rejection bands two more effects occur. These effects are weak, but noticeable. First, with increase in δ the rejection bands are slightly shifted towards lower frequencies for the MSSW-based crystal. A similar shift but towards higher frequencies was previously shown experimentally and theoretically for the BVMSW geometry [2]. In both cases this shift corresponds to a slight decrease in wave vectors of the waves, for which the Bragg condition is fulfilled. Another effect, which seems to take place, is the increase in the depth of exchange gaps. We suppose that it is caused by chemical processing of the film surface at the place of the grooves. Chemical etching increases magnetization pinning at the film surface which leads to an increase in rejection band depth.

As seen in Fig. 2, the groove depth determines the transmission characteristics of the fabricated magnonic crystals for both types of spin waves. In order to investigate this effect, the insertion loss for the first-order rejection band and the parasitic loss in the first pass band for the BVMSW and MSSW-based magnonic crystals are plotted in Fig. 3 as functions of the groove depth δ. The central frequency for the first-order gap for BVMSW is 7160 MHz, and it is 7245 MHz for MSSW.

It can be seen from Fig. 3 that the behavior of the operational characteristics for MSSW and BVMSW-based crystals is qualitatively similar: with increase in the groove depth the loss in the rejection bands increases as well as the loss in the pass bands, but the latter effect is smaller. However, one sees that for MSSW-based magnonic crystals the increase in loss is weaker, or, in other words, MSSW is not as sensible to inhomogeneities at the film surface as BVMSW. For example, for a 5.5 μm-thick YIG film and for the BVMSW configuration the rejection efficiency reaches 30 dB for $\delta \approx 0.5\,\mu\text{m}$, while for the MSSW configuration this groove depth results in a rejection about six hundred times smaller (2 dB).

The dependencies shown in Fig. 3 can be approximated by the simple model we previously presented in Ref. [2]. This model is based on the analogy of a spin-wave waveguide with a microwave transmission line. In the framework of this theory it was assumed that spin-wave reflection is caused by periodical variation of the effective characteristic impedance of the spin-wave waveguide due to the periodic variation of the YIG-film thickness in the grooved area. As it is seen from Fig. 3 the theory agrees well with the experimental data for the BVMSW-based magnonic crystal. However, in order to achieve the qualitative agreement with the experimental data we had to multiply the theoretical reflection coefficient with an empirical coefficient $\eta = \eta_{\mathrm{BVMSW}} = 6$ [2]. For MSSW one also obtains good qualitative agreement with the experiment, however to obtain quantitative agreement a much smaller value for the empirical coefficient $\eta = \eta_{\mathrm{MSSW}} = 0.5$ is necessary. This phenomenological theory does not reveal physical mechanisms underlying the drastic difference in the spin-wave scattering efficiencies for these two types of waves. However, it suggests that the behavior of both types of waves is qualitatively the same. In order to explain the difference in rejection one has to explain the factor 12 in the strength of scattering from a single groove.

The problem of scattering of spin waves from inhomogeneities can be posed as a conventional integral-equation formulation of the scattering problems [10]. In the case of BVMSW [2] the integral equation is scalar, but for MSSW it is a vector one and makes use of the whole tensorial Green's function of excitation of spin waves by an external source [6]. Both types of spin waves possess an in-plane and an out-of-plane component of the dipole field. However, only the out-of-plane component of the dipole field exerts a torque on the magnetization vector in the BVMSW case, while for MSSWs both field components contribute to the torque. The vector character of the integral equation for MSSW reflects the latter fact. MSSW are non-reciprocal waves, which is also reflected in the Green's function of excitation [6]. However, solving the scattering problem for the periodical potential of grooves in the first Born approximation [10] gives a result which is of the same form as was previously found for BVMSWs in Ref. [2]. No effect of nonreciprocity is seen in the expressions derived for MSSW. Furthermore, in the first Born approximation the amplitude of the wave transmitted through the groove structure is of the same order of magnitude for both BVMSW and MSSW. This result is in clear contradiction with the experimental data.

Thus, accurate numerical modeling of both BVMSW and MSSW cases (which is out of the scope of this paper) is necessary to explain the observed large difference in the depths of rejection bands for these two cases. In contrast to Ref. [6, 10], this model should be two-dimensional, i.e. it should include dynamic-field variations across the film thickness, since one of the possible contributions to this difference is coupling of the incident BVMSW to higher-order BVMSW thickness modes in the grooved area. The latter is seen in the thickness-resolved integral equation formulation of the problem of BVMSW scattering. More efficient transfer of energy of the incident lowest-order mode of BVMSW into the higher-order modes when the condition for the standing-wave resonances (Bragg's law) in the grooved area is met, can be responsible for the increased depths of the rejection bands in the BVMSW case.

In conclusion, we have experimentally demonstrated the strong difference of operational characteristics of chemically etched one-dimensional magnonic crystals for cases when reciprocal backward volume magnetostatic spin waves or nonreciprocal magnetostatic surface spin waves were used as signal carriers. It has been shown that even small regular distortions of the surface of a magnetic film result in the appearance of pronounced rejection bands in the BVMSW frequency spectrum. At the same time such distortions only slightly affect the propagation of the surface spin wave.

The scattering of the lowest BVMSW mode to the higher-order thickness modes is assumed as a possible mechanism of the observed effective rejection of this wave.

Financial support by the DFG SE 1771/1-1, Australian Research Council, and the University of Western Australia is acknowledged.

References

[1] C.G. Skyes, J.D. Adam, J.H. Collins, Appl. Phys. Lett. **29**, 388 (1976).
[2] A.V. Chumak, A.A. Serga, B. Hillebrands, M.P. Kostylev, Appl. Phys. Lett. **93**, 022508 (2008).
[3] K.S. Lee, D.S. Han, S.K. Kim, Phys. Rev. Lett. **102** 127202 (2009).
[4] Z.K. Wang, V.L. Zhang, H.S. Lim, S.C. Ng, M.H. Kuok, S. Jain, A.O. Adeyeye, Appl. Phys. Lett. **94**, 083112 (2009).
[5] R.W. Damon J.R. Eshbach, Phys. Chem. of Solids, **19**, 308 (1961).
[6] T. Schneider, M.P. Kostylev, A.A. Serga, T. Neumann, B. Hillebrands, Phys. Rev. B **77**, 214411 (2008).
[7] A.V. Chumak, A.A. Serga, S. Wollf, B. Hillebrands, M.P. Kostylev, Appl. Phys. Lett. **94**, 172511 (2009).
[8] B.A. Kalinikos A.N. Slavin, J. Phys. C **19**, 7013 (1986).
[9] A.A. Serga, A.V. Chumak, A. Andre, G.A. Melkov, A.N. Slavin, S.O. Demokritov, B. Hillebrands, Phys. Rev. Lett. **99**, 227202 (2007).
[10] M.P. Kostylev, A.A. Serga, T. Schneider, T. Neumann, B. Leven, B. Hillebrands, R.L. Stamps, Phys. Rev. B **76**, 184419 (2007).

5.6 Forced dominant wavenumber selection in spin-wave active rings

A.V. Chumak, A.A. Serga, and B. Hillebrands[1]

Self-exciting positive-feedback spin-wave systems − often referred to as spin-wave active rings — have long been a focus of attention within the field of magnetic dynamics. The basis of the active ring is a dispersive spin-wave waveguide with exciting and receiving antennae connected together through a variable-gain external feedback loop (see Fig. 1). If certain conditions are met, noise-initiated signals propagate in the ring, the character of which has a strong nonlinear dependence on the properties and magnetic environment of the waveguide. Such systems not only offer fundamental insight into nonlinear magnetic dynamics, but provide the possibility of performing practical investigations into general nonlinear behaviors − for example, solitonic phenomena, fractal formation and parametric amplification processes − not readily observable in other physical domains [1–6].

Spontaneous excitation of active ring systems occurs at a certain threshold value of external gain commonly referred to as the self-generation threshold. At the onset of excitation, the ring signal is monochromatic, and the spin-wave wavenumber k_d corresponds to the lowest-loss feasible mode: the dominant mode or k_d-mode. If the external gain is increased beyond the self-generation threshold, the propagation of the dominant mode suppresses the excitation of all others until a second, higher threshold, beyond which nonlinear splitting processes permit excitations with multiple k-values, and the system becomes multi-moded. The value of k_d is highly sensitive to the internal and external magnetic and thermal environment of the spin-wave transmission medium, and − in any real system − almost impossible to predict.

Here, we describe an experimental spin-wave active ring geometry in which, by exploiting resonant spin-wave reflections from a magnonic crystal structure, we are able to determinably select the wavenumber k_d of the dominant mode. In this report we outline the construction and behaviour of our experimental ring system, and show that its characteristics are highly consistent with theoretical predictions.

In the presence of an external magnetic field, thin ferri- and ferromagnetic films support several distinct types of spin-waves, classified according to the relative angle between their propagation direction and the applied field [7]. Owing to their unusual dispersion characteristics and nonlinear properties, the behaviour of backward volume magnetostatic spin-waves (BVMSW) in active loop systems attracts particular contemporary interest (see for example [4]).

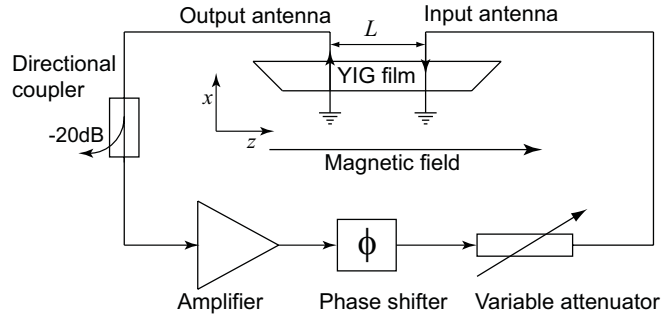

Fig. 1: A simple BVMSW active ring structure. Two microstrip antennae are affixed a distance L apart on a narrow yttrium iron garnet (YIG) film. An external magnetic field is applied parallel to the z-axis. The output and input antennae are connected via an amplifier, a phase shifter, and a variable attenuator. When the ring is active, spin-wave signals propagate in the film parallel to the direction of the applied field.

[1] In collaboration with A.D. Karenowska and J.F. Gregg, Department of Condensed Matter Physics, Clarendon Laboratory, University of Oxford, UK.

A simple BVMSW active ring structure – the conceptual start-point for our study – is shown in Fig. 1. Two microstrip antennae, separated by a distance L, are affixed to a narrow yttrium iron garnet (YIG) film. YIG is the material of choice on account of its favourable spin-wave transmission characteristics, in particular, its intrinsically low spin-wave damping. An external magnetic field is applied parallel to the long (z-) axis of the film. The antennae are connected via an amplifier, a phase shifter (delivering an input-output phase shift ϕ), and a variable attenuator. The combination of the amplifier and the attenuator control the closed-loop gain. The signal in the loop is sampled via a $-20\,\mathrm{dB}$ directional coupler. Allowed monochromatic modes k_i correspond to feasible, unique, unity values of the Laplace domain transfer function $G(k)$ of the ring:

$$G(k_\mathrm{i}) = 1 \quad , \tag{1}$$

at which the loss in the YIG between input and output antennae is exactly compensated by the gain in the external loop (gain feasibility), and the net phase shift around the ring is zero, or an integer multiple of 2π (phase feasibility). As alluded to above, in a given ring, the dominant mode is – in general – the lowest-loss mode capable of satisfying phase feasibility, but its wavenumber k_d is not readily predicted.

The experimental active ring system at the focus of the work reported here is similar to the arrangement of Fig. 1, but with the addition of a magnonic crystal structure located at a variable distance Δ from the input antenna (Fig. 2a). The term magnonic crystal describes a structure with spin-wave transmission characteristics determined by artificially engineered periodic variations in its geometry [8–12]. Perhaps the simplest magnonic crystal structure – and the one chosen for the purposes of our study – is a thin-film spin-wave waveguide with a regular pattern of etched grooves (i.e. a periodic variation in thickness) perpendicular to the direction of spin-wave propagation. The transmission characteristics of this type of magnonic crystal operating in conjunction with BVMSW are well approximated by a simple model, based on an analogy of a spin-wave waveguide with a conventional microwave transmission line [9]. The theory assumes that resonant spin-wave reflections, brought about by periodic variations in the waveguide's effective characteristic impedance, give rise to Bragg type rejection bands.

In an experimental implementation of the active ring system of Fig. 2a, we employed a YIG film, of substantially uniform thickness ($5.5\,\mu\mathrm{m}$) with a short magnonic crystal region offset from its centre. The magnonic crystal comprised 10 acid-etched grooves of width $30\,\mu\mathrm{m}$, depth $300\,\mathrm{nm}$ and spacing $270\,\mu\mathrm{m}$, giving an effective lattice constant of $a = 300\,\mu\mathrm{m}$ ($0.03\,\mathrm{cm}$) and reciprocal lattice constant $\frac{2\pi}{a} = b = 209.44\,\mathrm{cm}^{-1}$ [9].

The BVMSW transmission characteristics of both the uniform region of the film and the magnonic crystal are illustrated in Fig. 3. In the case of the magnonic crystal, rejection bands corresponding to the first three Bragg reflection orders are clearly defined.

In the system of Fig. 2a, spin-wave excitations originating from the input antenna have two components parallel to the applied magnetic field (Fig. 2b). One component propagates directly toward the output antenna (T_1) whilst the other (T_2) travels toward the magnonic crystal. If the wavenumber k of the spin-wave signal arriving at the magnonic crystal satisfies:

$$2nk = b \quad , \qquad \text{where} \quad n = 1,2,3,4,\ldots \tag{2}$$

(i.e. the Bragg condition for the n^{th} rejection band of the magnonic crystal is met) then the wave is strongly reflected, resulting in the production of an in-phase return signal R, which arrives back at the input antenna. The total phase accumulation of the reflected signal $T_2 - R$ between transmission from, and return to, the input antenna is

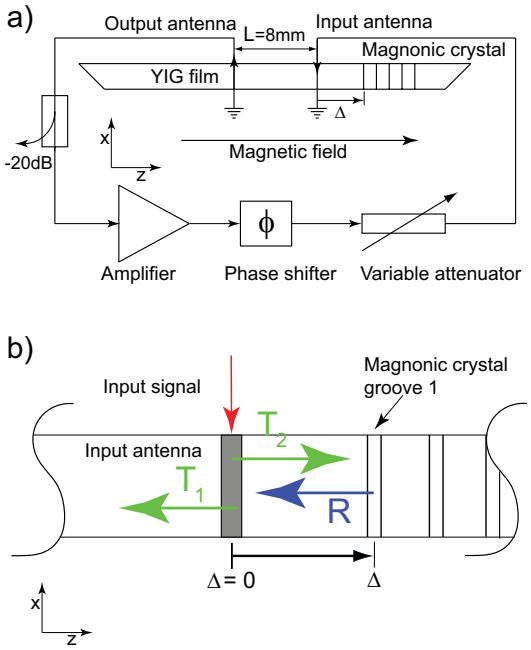

Fig. 2: a) Schematic of experimental active ring system. The external feedback loop is identical to that of Fig. 1. Two fixed microstrip antennae excite and receive spin-waves through a 8 mm long region of YIG film of uniform thickness. A magnonic crystal (part of the same film) comprising ten equally spaced etched grooves, is located proximal to the input antenna. The film is moveable relative the antennae, a micro-positioning stage allowing the distance Δ between the centre of the input antenna and the centre of the first groove of the magnonic crystal to be varied over a range of 5.00 mm to within $\pm 5\,\mu$m. A bias magnetic field of $1/4\pi \cdot 2000\,$kA/m is applied parallel to the z-axis of the film. b) Expanded plan (xz) view (not to scale) of the region of the YIG film proximal to the input antenna. Counter-propagating spin-wave signal components originating from the input antenna travel toward the output antenna (T_1) and toward the magnonic crystal (T_2). If the spin-wave wavenumber meets the Bragg condition for the n^{th} rejection band of the magnonic crystal, the signal T_2 is reflected, resulting in an in-phase return signal R.

$$\phi_\Delta = 2\Delta k \quad . \tag{3}$$

Accordingly, if it is possible to simultaneously satisfy Eq. (2) and

$$\phi_\Delta = 2\pi p \qquad \text{where} \quad p = 0, 1, 2, 3, \ldots . \tag{4}$$

the signal propagating toward the output antenna is enhanced by a factor

$$\frac{T_1 + R}{T_1} = 1 + \rho e^{-2\beta\Delta} \quad . \tag{5}$$

In the context of the system of Fig. 2a, this simple argument suggests that if the magnitude of the enhancement effect (Eq. (5)) is sufficient to increase the effective ring gain in the vicinity of a phase-feasible mode lying in a rejection band of the magnonic crystal (i.e. where the condition of Eq. (2) is met) above that of all other phase-feasible modes, this mode may be artificially promoted to dominance by arranging that the conditions of Eq. (3) and Eq. (4) are met.

The maximum theoretical enhancement in loop gain attainable through the magnonic crystal reflection mechanism is 3 dB (Eq. (5)). For the spin-wave transmission structure used in our investigations, this implies that only modes associated with the first Bragg order ($n = 1$) of the magnonic crystal can be activated through this process, since the transmission loss in the unstructured film at k-values corresponding to the second and higher orders is at least 10 dB in excess of that associated with the low-loss region between the first rejection band and the FMR frequency (see Fig. 3a).

For the case of the first Bragg rejection band ($n = 1$), Eq. (2) simplifies to $k = \frac{b}{2}$. For clarity in the discussion which follows, we will use the symbol k^* to denote the particular value of spin-wave wavenumber associated with the $n = 1$ Bragg reflection specific to our experimental system: $k = k^* = \frac{b}{2} = 104.72\,$rad/cm. A theoretical model of the BVMSW dispersion relationship appropriate to

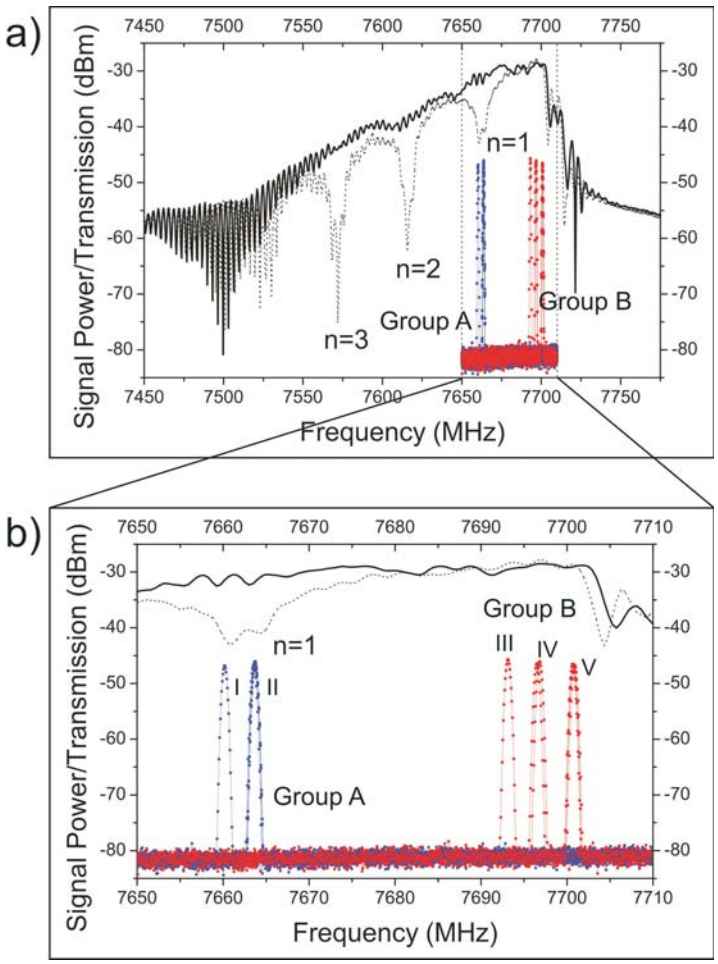

Fig. 3: a) BVMSW transmission characteristics for the uniform (bold, solid) and magnonic crystal (dotted) regions of the YIG film used in the study. Data correspond to a bias magnetic field of $1/4\pi \cdot 2000\,\mathrm{kA/m}$ parallel to the spin-wave propagation direction, the FMR frequency is around 7710 MHz. The n^{th} order Bragg rejection bands of the magnonic crystal are indicated. Inset diagram is a composite of overlaid power spectra obtained via a $-20\,\mathrm{dB}$ directional coupler within the active ring (Fig. 2a) for eleven distinct values of Δ at an external gain 5 dB above the self-generation threshold. Each separate spectrum features a single peak at the frequency corresponding to k_{d}. Modes positioned within the first rejection band of the magnonic crystal (Group A) correspond to near-integer ($\pm$ 1.5 %) values of $\frac{\Delta}{a}$, whilst those in the lowest-loss region of the uniform part of the film (Group B) correspond to values outside this range. b) Magnified view of the section of the upper plot between the dotted lines. Roman numerals relate spectral peaks to modes identified in Fig. 4.

the film used in the study predicts an enhancement band associated with k^* centred on 4663 MHz, accessible (combining Eq. (3) and Eq. (4)) for

$$\Delta = \frac{2\pi}{b} p = ap \qquad \text{where} \quad p = 0, 1, 2, 3, \ldots \tag{6}$$

i.e. integer values of $\Delta\frac{b}{2\pi} = \frac{\Delta}{a}$.

The diagram inset to Fig. 3a and expanded in Fig. 3b is a composite of overlaid power spectra obtained via the $-20\,\mathrm{dB}$ directional coupler within the active ring (Fig. 2a) for eleven distinct Δ values. Each separate spectrum features a single peak at the frequency of the corresponding k_{d}-mode. The sharpness of the spectral peaks is limited by the scanning window of the spectrum analyzer, their true width is less than 25 kHz. For near-integer values of Δ ($\pm$ 1.5 %) the observed k_{d}-modes are positioned within the first rejection band of the magnonic crystal in the vicinity of k^* (Group A), whilst outside of this range they sit within the lowest-loss region of the pass-band of uniform part of the film (Group B) at indeterminate k. Excellent agreement between theory and experiment is clearly indicated. The roman numerals adjacent to the peaks in Fig. 3b relate individual spectral peaks to modes identified on Fig. 4. (Note that the slight discrepancy between the frequencies at which the modes are recorded on Fig. 3 and Fig. 4 is due to the fact that the two data sets were gathered non-simultaneously, at slightly different ambient temperatures).

The data of Fig. 4 show the Δ dependence of the ring mode activated at the self-generation threshold, for a fixed input ϕ at the phase shifter in the external loop (tuned for phase-feasibility in the

vicinity of k^*). The vertical dashed lines indicate integer values of $\frac{\Delta}{a}$. Note that the solid line joining the points is a spline intended to highlight the pattern of the data and is not a fitted curve. The data points are indicated by solid triangles. The horizontal dotted lines identify discrete quantized modes I to V, falling into lower (Group A) and upper (Group B) frequency bands. Group A modes (I and II) correspond to integer $\frac{\Delta}{a}$ ($\pm$ 1.5 %) and k_d-values co-incident with the first Bragg rejection band of the magnonic crystal (proximal to k^*), whilst Group B modes (III to V) are located within the lowest-loss region of the passband of the unstructured part of the film (k constrained by Eq. (1) only), and are associated with non-integer values of $\frac{\Delta}{a}$.

For the magnetic film used in the study, the maximum positive integer value of $\frac{\Delta}{a}$ at which dominant wavenumber selection using the magnonic crystal reflection mechanism is achievable is 2. At $\frac{\Delta}{a} = 3$, loss in the 6Δ effective enhancement signal path reduces the loop gain proximal to k^* below that for the lowest-loss modes associated with the uniform region of the film.

Each distinct accessible mode corresponds to a separate solution of Eq. (1). Since the phase shift across the spin-wave waveguide is wavenumber dependent, it follows that each observed k corresponds to a unique value of phase shift in the external loop. In an ideal system, for fixed ϕ, we would expect to observe just two modes: one associated with k^* and integer (or near-integer) $\frac{\Delta}{a}$ (the A mode), and one with general k (the B mode, constrained only by Eq. (1)) and non-integer $\frac{\Delta}{a}$ values. The presence of multiple Group B modes (as indicated on Fig. 4 and in the spectra of Fig. 3) is due to the fact that, in real experimental system, there is slight non-uniformity in the thickness of the YIG film. This provides a secondary mechanism for the phase accumulation across the waveguide to vary with Δ, independently of ϕ.

A single mode, lying within the $n = 1$ Bragg rejection band of the magnonic crystal is associated with $\frac{\Delta}{a} = +1, +2$. This mode (mode II, Group A) is considered the strict k^*-mode.

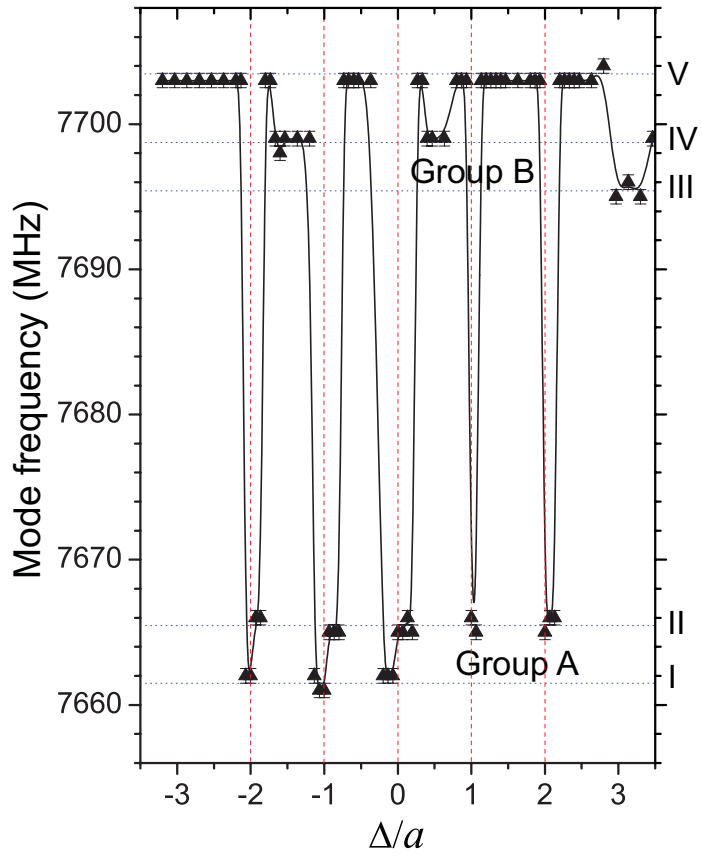

Fig. 4: Δ dependence of the k_d-mode frequency observed at the self-generation threshold in the experimental ring system at fixed external phase shifter input ϕ. Vertical dashed lines indicate integer values of $\frac{\Delta}{a}$. The line joining the points is a spline intended to highlight the pattern of the data and is not a fitted curve. Data points are indicated by solid triangles. The horizontal dotted lines indicate discrete quantized modes I to V falling into lower (Group A) and upper (Group B) frequency bands. In the proximity of integer $\frac{\Delta}{a}$ ($\pm$ 1.5 %), the activated modes appear within the lower band, corresponding to k_d-values co-incident with the first Bragg rejection band of the magnonic crystal (Fig. 3, Group A modes). Remote from integer values of $\frac{\Delta}{a}$, frequencies of k_d-modes correspond to the lowest-loss region of the passband of the unstructured film (Fig. 3, Group B modes) and the upper band of frequencies.

Forced k_d-mode selection capability is observed at $\frac{\Delta}{a} = 0$, and extends symmetrically to negative integer values of $\frac{\Delta}{a}$ (i.e. values of Δ corresponding to the magnonic crystal entering the region between the input and output antennae). However, in the vicinity of $\frac{\Delta}{a} = 0, -1, -2$, as well as the strict k^*-mode (mode II), a second Group A mode (mode I), is also observed. The presence of mode I is attributed to a combination of: a) a high effective signal enhancement efficiency associated with $\frac{\Delta}{a} = 0, -1, -2$ loop configurations, b) the Δ-dependent phase accumulation effect brought about by variations in the film's thickness (discussed above in the context of Group B modes), and c) (specific to the case of $\frac{\Delta}{a} = -1, -2$) bi-directional reflection of spin-waves to the input antenna. Detailed discussion of the interplay between these factors is beyond the scope of this short report, however − in brief − it is postulated that for $\frac{\Delta}{a} = 0, -1, -2$, there is a non-negligible signal enhancement effect over a range of spin-wave wavenumbers within the $n = 1$ Bragg rejection band of the magnonic crystal, including the k-value corresponding to mode I, which − by virtue of the non-uniform thickness effect − satisfies phase feasibility at $\frac{\Delta}{a} = 0^+, -1^+, -2^+$.

In summary, a new BVMSW active ring geometry incorporating a one-dimensional magnonic crystal structure has been explored theoretically and experimentally. It has been shown that a wavenumber dependent signal enhancement mechanism reliant on the transmission properties of the magnonic crystal and the geometrical arrangement of the ring, is capable of artificially selecting dominant feasible ring modes co-incident with, or within a very narrow range of, a single wavenumber. This wavenumber (denoted by k^* in our experimental study) is associated with the centre of the first rejection band of the magnonic crystal, and − as such − is readily determinable from the crystal's periodicity.

Our work serves as a demonstration that combining magnonic crystal and active ring concepts may offer valuable fundamental physical insight into spin-wave transmission in structured magnetic films. The active ring geometry detailed in this study potentially provides a new means to investigate the scattering mechanisms responsible for BVMSW rejection band formation in magnonic crystals, both in linear and nonlinear signal regimes. Additionally, the k-value selective mechanism we have established and observed is envisaged to have applications in spin-wave logic structures, mode-locked microwave oscillators, sensors, and other practical devices.

Financial support by the DFG SE 1771/1-1 and DFG Graduate School ("Graduiertenkolleg" 792: "Nichtlineare Optik und Ultrakurzzeitphysik") is gratefully acknowledged.

References

[1] M. Wu, A.M. Hagerstrom, R. Eykholt, A. Kondrashov, B.A. Kalinikos, Phys. Rev. Lett. **102**, 237203 (2009).
[2] A.M. Hagerstrom, W. Tong, M. Wu, B.A. Kalinikos, R. Eykholt, Phys. Rev. Lett. **102**, 207202 (2009).
[3] M. Wu, B.A. Kalinikos, L.D. Carr, C.E. Patton, Phys. Rev. Lett. **96**, 187202 (2006).
[4] A.B. Ustinov, B.A. Kalinikos, V.E. Demidov, S.O. Demokritov, Phys. Rev. B **80**, 052405 (2009).
[5] A.A. Serga, S.O. Demokritov, B. Hillebrands, Phys. Rev. Lett. **92**, 117203 (2004).
[6] B.A. Kalinikos, N.G. Kovshikov, C.E. Patton, Phys. Rev. Lett. **80**, 19, 4301, (1998).
[7] R.W. Damon, J.R. Eshbach, Phys. Chem. of Solids, **19**, 308 (1961).
[8] C.G. Skyes, J.D. Adam, J.H. Collins, Appl. Phys. Lett. **29**, 388 (1976).
[9] A.V. Chumak, A.A. Serga, B. Hillebrands, M.P. Kostylev, Appl. Phys. Lett. **93**, 022508 (2008).
[10] A.V. Chumak, A.A. Serga, S. Wollf, B. Hillebrands, M.P. Kostylev, Appl. Phys. Lett. **94**, 172511 (2009).
[11] K.S. Lee, D.S. Han, S.K. Kim, Phys. Rev. Lett. **102** 127202 (2009).
[12] Z.K. Wang, V.L. Zhang, H.S. Lim, S.C. Ng, M.H. Kuok, S. Jain, A.O. Adeyeye, Appl. Phys. Lett. **94**, 083112 (2009).

5.7 Current controlled dynamic magnonic crystal

A.V. Chumak, T.M. Neumann, A.A. Serga, and B. Hillebrands[1]

Spin waves in magnetic materials attract special attention because of their potential application as information units in signal processing devices. Digital spin wave logic devices [1, 2] as well as devices for analogous signal processing [3–5] can be fabricated based on spin waves. It has been shown that the spin-wave relaxation, one of the main obstacles for spin-wave application, can be overcome by means of parametric amplification [5, 6].

The study of spin waves in magnetic materials is also interesting from a fundamental point of view. The interaction of the numerous spin-wave modes in ferromagnetic samples [7] as well as nonlinear effects such as soliton formation [8, 9] are just some examples.

Magnonic crystals are defined as artificial media with a spatially periodic variation of some of their magnetic parameters [10–14]. The spectra of spin-wave excitations in such structures are considerably modified compared to uniform media and exhibit features such as full band gaps where spin waves are not allowed to propagate. Therefore, they constitute a research field which connects fundamental physics with application.

Promising functionalities arise by taking advantage of the dynamic controllability and by potentially changing the characteristics of the magnonic crystal faster than the spin-wave relaxation time: even the simple possibility to "switch" a periodic inhomogeneity on and off immediately offers a method to trap and release a spin wave packet. This can be exploited for instance in information storage.

Here, we present a first realization of such a dynamic magnonic crystal. It is based on spin-wave propagation in an yttrium-iron-garnet (YIG) film placed in a periodically varying, dynamically controllable magnetic field. The magnetic field is created by a spatially homogeneous bias magnetic field which is superposed with the localized Oersted fields of current carrying wires placed in an array layout close to the YIG film surface [15]. By controlling the direct current in the wires the field modulation is adjusted and the spin-wave transmission can be changed. The dynamic controllability constitutes a major difference to previous realizations of magnonic crystals with a periodically varying magnetic field [16].

Previous studies focused on the interaction of propagating spin-wave packets with the Oersted field of a single current carrying wire or a set of two wires at most [17–21]. It was shown that the spin-wave transmission can be effectively changed by varying the value of the direct current. However, as will be discussed in the following, the appearance of a pronounced frequency stop-band, for which spin-wave transmission is prohibited (while it remains almost unaffected outside the band), is only observed for larger wire numbers.

A sketch of the experimental section is shown in Figure 1. It consisted of a 5 µm-thick YIG film which was epitaxially grown on a gallium gadolinium substrate. A bias magnetic field of $1/(4\pi) \cdot 1600\,\mathrm{kAm}^{-1}$ was applied along the YIG waveguide so that the conditions for the propagation of backward volume magnetostatic waves (BVMSWs) are given.

To achieve a periodic modulation of the magnetic field an array of connected, parallel wires was designed. The wire structure was patterned by means of photolithography on an aluminium nitride

[1] In collaboration with M. Kostylev and R.L. Stamps at the School of Physics, University of Western Australia, Crawley, Australia.

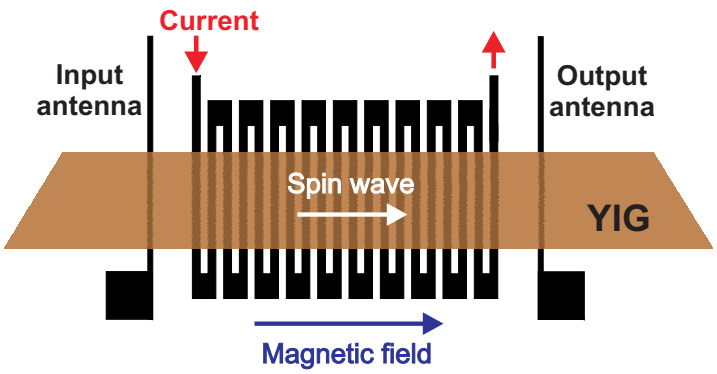

Fig. 1: Sketch of the magnonic crystal structure used in the experiments.

substrate with high thermal conductivity in order to avoid heating. The structure consists of 40 wires of 75 µm width with a 75 µm spacing.

The wire array was placed above the YIG film in such a way that the wires ran perpendicularly to the spin-wave waveguide. Thus, the magnetic Oersted field produced by each of the current carrying wire segments is oriented in first approximation parallel to the bias magnetic field.

In the experiment the individual wires were connected to form a meander structure [15] where the current in neighboring wires flows in opposite directions (see Fig. 1). Thus, a magnonic crystal with a lattice constant $a = 300\,\mu\text{m}$ and 20 repetitions was fabricated.

Another possible configuration would have all currents flowing in the same directions ("multi-strip structure") so that for all wires the Oersted fields have identical orientation. This situation is "purer" compared to the meander layout in the sense that it only realizes one of two physically different regimes that our previous studies have shown to exist for the different field orientations: When the Oersted field decreases the internal field one implements the spin-wave tunneling regime [18]. When the internal field is locally increased the conditions for resonant spin-wave scattering [19] can be fulfilled for which the spin-wave transmission depends non-monotonically on the applied current and exhibits a strong frequency dependence [20].

However, the meander structure has important advantages: (i) It produces a much stronger field modulation because the in-plane components of the Oersted fields for neighbouring wires are oriented in opposite directions. (ii) It ensures that the magnetic field averaged over the structure remains constant for any current magnitude.

Two microstrip antennas were placed, one in front and another one behind the wire structure (see Fig. 1) in order to excite and detect BVMSWs. A network analyzer connected to the input and output antennas was used to measure the spin-wave transmission characteristics.

In order to minimize the electromagnetic coupling between the current carrying wire segments and the spin waves, a 100 µm thick SiO_2 spacer was placed between the YIG film and the wire structure. Note, that the spin-wave dipole field decays exponentially with the distance form the film surface while the Oersted field around the wires scales with the inverse distance between the wire and the film surface. The distance of 100 microns between the wire array and the film surface proved to be large enough to avoid any disturbance of the spin-wave propagation by the meander conductor, but it is still small enough to ensure an efficient modulation of the magnetic field in the film by the current field.

Experimental results are shown in Fig. 2. The dotted curves in the panels show the transmission characteristics without direct current applied to the wires. They are typical for BVMSWs, limited by the ferromagnetic resonance frequency towards high frequencies and by the antenna excitation

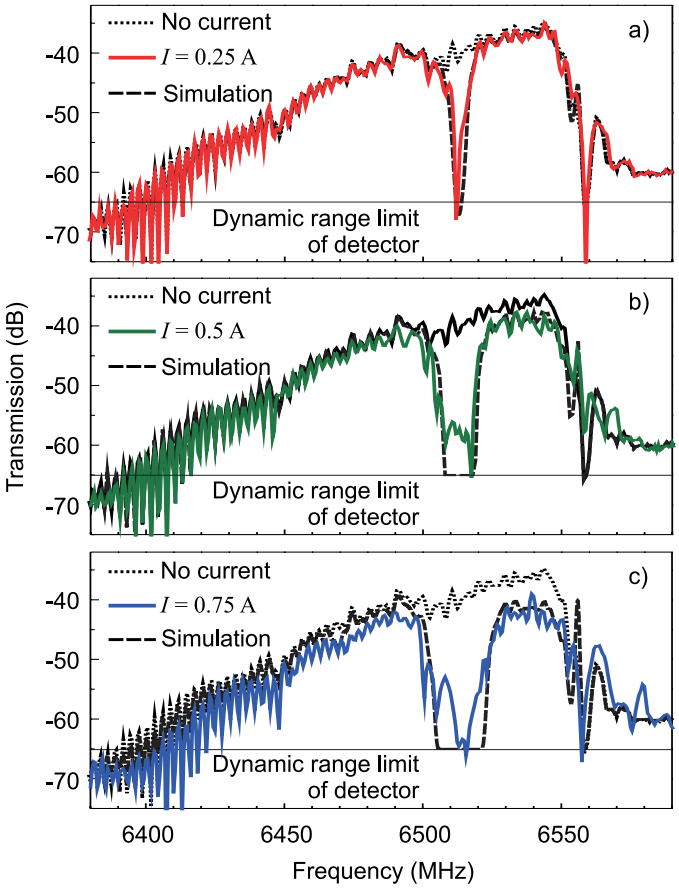

Fig. 2: Spin-wave transmission characteristics in a uniform magnetic field (dotted curves) and in a magnetic field which is periodically modulated by the current I applied to the wires (solid curves). The dashed curves are calculated as the product of the experimentally observed transmission in a uniform field with the transmission coefficient obtained from the numerical simulations (where the limited dynamic range of the experimental setup is additionally taken into account).

efficiency from the opposite side. The minimal transmission loss of about 35 dB is determined by the spin-wave excitation/reception efficiency of the microwave antennas and by the spin-wave relaxation parameter of the ferrite film.

Figure 2a shows that the application of a current $I = 0.25$ A to the structure results in the appearance of a pronounced rejection band at a frequency $f_1 \approx 6510$ MHz where the transmission of spin waves is prohibited. The rejection band already appears for a current as small as 80 mA. With an increase in the current the rejection band depth increases rapidly and for 0.25 A it reaches the dynamic range of the experimental setup which is limited mainly by the direct electromagnetic leakage between the microstrip antennas. A further increase in the current applied to the wires results in a pronounced broadening of the rejection band (see Fig. 2b and Fig. 2c).

We emphasize one particularly interesting feature of the presented magnonic crystal: Only one rejection band is formed. This is not the case for magnonic crystals consisting of an array of grooves on the YIG film surface [13] where multiple rejection bands are formed. As shown by our calculations, for the magnonic crystal studied here the spatially periodic modulation of the magnetic field is close to sinusoidal. For an ideal harmonic variation only one rejection band should exist since the reflection amplitude is proportional to the Fourier component of the inhomogeneity profile corresponding to twice the spin-wave wave vector as seen from Eq. (6) in [19].

The presence of only one rejection band is an advantage for applications in a microwave filter device. Another positive aspect of the presented dynamic crystal is that practically no losses occur for frequencies outside the induced stop band with increasing current (see Fig. 2c). In the groove-structure-based magnonic crystal [13] such undesired parasitic increase of losses in the transmission bands was observed for larger groove depths.

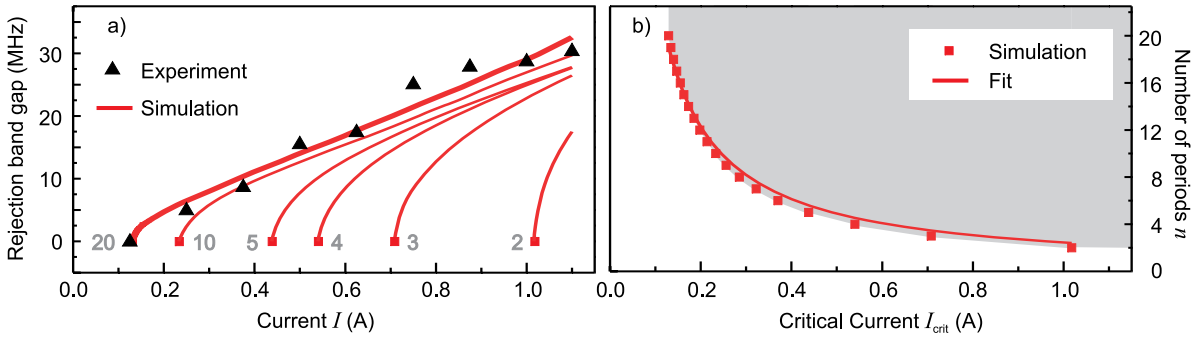

Fig. 3: a) Experimentally obtained width of the first rejection band as a function of the current applied to the wires. The lines and filled circles represent the results of numerical simulations. The calculations were performed for different numbers n of periods as indicated in the figure. b) Calculated critical current I_{crit} for which a band gap with a suppression $\geq 90\%$ is obtained for different numbers of parallel wire segments. The line indicates a fit according to $n \sim 1/I_{\mathrm{crit}}$.

In order to investigate the dynamic properties of the magnonic crystal additional experiments with a pulsed direct current supplied to the meander structure were performed. The microwave frequency which was applied to the input antenna to excite the spin-wave signal was chosen inside the rejection band ($f = 6510\,\mathrm{MHz}$). The direct current supplied to the meander structure was pulsed with a duration of 50 ns and a strength of 0.5 A. The obtained results show that the spin-wave transmission can be dynamically turned on and off with a transition time for the magnonic crystal of approximately 50 ns.

The measured rejection band width as a function of the applied current is shown in Fig. 3a. It was measured for the rejection band at the power level where the spin-wave intensity decreases to one tenth, i.e. $-10\,\mathrm{dB}$, of its value without applied current. One can see that the band width can be tuned from 5 MHz for a current $I = 0.125\,\mathrm{A}$ to 31 MHz for $I = 1.25\,\mathrm{A}$ and exhibits a linear behavior with respect to the current value. The possibility to dynamically control the rejection band width seems to be promising for the design of a dynamic stop-band microwave filter. The center frequency of the rejection band can be controlled by means of the applied bias magnetic field.

The experimental results were confirmed by numerical simulations. We used a 1-dimensional approach, in which the dipole field was expressed via a Green's function and the magnetic field was averaged over the film thickness. The details of the model can be found in [19]. The calculated frequency-dependent transmission curves show a single, well pronounced stop-band for low currents which coincides well with the experiment (see Fig. 2). The calculated rejection efficiency, given by the depth of the stop band, reached up to $-150\,\mathrm{dB}$ which exceeds the dynamic range in the experiment greatly.

Two effects are observed if the number of parallel wire segments in the simulation is decreased: Firstly, the achieved stop-band width for a given current decreases slightly. Secondly, the rejection efficiency decreases dramatically. As a consequence, the desired signal suppression (e.g. one tenth of the transmission for no applied current) is only reached for higher currents which results in the behavior of the rejection band gap width shown in Fig. 3a. Figure 3b summarizes the calculated dependence of the critical current I_{crit} necessary to obtain a $-10\,\mathrm{dB}$ signal suppression for the center frequency of the stop band on the number of parallel wire segments. As can be seen a larger number of wires reduces the critical current. An analytic analysis reveals taht in the low current limit the critical current I_{crit} is related to the number n of periods by $n \sim 1/I_{\mathrm{crit}}$.

In conclusion, we presented a current-controlled magnonic crystal whose operational characteristics can be tuned dynamically within a transition time of 50 ns. The spatially periodic Oersted field of a meander conductor located in the vicinity of YIG film surface results in a pronounced modification of spin wave dispersion which leads to the appearance of a pronounced spin-wave rejection band. The width of this rejection band varies linearly with the magnitude of the applied direct current and can be tuned in the range from 5 MHz to 30 MHz. Numerical simulations are in good qualitative agreement with the experiment. Overall, the presented dynamic magnonic crystal is promising for the investigation of linear and nonlinear spin-wave dynamics and can be used as a dynamically controlled microwave stop-band filter.

Financial support by the DFG project SE 1771/1-1, the Matcor Graduate School of Excellence, the Australian Research Council, and the University of Western Australia is acknowledged. Special acknowledgments go to the Nano+Bio Center, TU Kaiserslautern. T.M. Neumann would like to thank especially R.L. Stamps and the University of Western Australia for their assistance during his research stay.

References

[1] T. Schneider, A.A. Serga, B. Leven, B. Hillebrands, R.L. Stamps, M.P. Kostylev, Appl. Phys. Lett. **92**, 022505 (2008).
[2] K. Lee, S. Kim, J. Appl. Phys. **104**, 053909 (2008).
[3] J.D. Adam, Proc. IEEE **76**, 159 (1988).
[4] Yu.V. Kobljanskyj, G.A. Melkov, A.A. Serga, V.S. Tiberkevich, A.N. Slavin, Appl. Phys. Lett. **81**, 1645 (2002).
[5] A.A. Serga, A.V. Chumak, A. Andre, G.A. Melkov, A.N. Slavin, S.O. Demokritov, B. Hillebrands, Phys. Rev. Lett. **99**, 227202 (2007).
[6] E. Schlömann, J.J. Green, U. Milano, J. Appl. Phys. **31**, 386S (1960).
[7] B.A. Kalinikos, A.N. Slavin, J. Phys. C **19**, 7013 (1986).
[8] B.A. Kalinikos, N.G. Kovshikov, A.N. Slavin, JETP Lett. **38**, 413 (1983).
[9] S.O. Demokritov, A.A. Serga, V.E. Demidov, B. Hillebrands, M.P. Kostylev, B.A. Kalinikos, Nature **426**, 159 (2003).
[10] K.W. Reed, J.M. Owens, R.L. Carter, Circ. Syst. Signal Process. **4**, 157 (1985).
[11] Yu.V. Gulyaev, S.A. Nikitov, L.V. Zhivotovskii, A.A. Klimov, Ph. Tailhades, L. Presmanes, C. Bonningue, C.S. Tsai, S.L. Vysotskii, Yu.A. Filimonov, JETP Letters **77**, 567 (2003).
[12] M.P. Kostylev, P. Schrader, R.L. Stamps, G. Gubbiotti, G. Carlotti, A.O. Adeyeye, S. Goolaup, N. Singh, Appl. Phys. Lett. **92**, 132504 (2008).
[13] A.V. Chumak, A.A. Serga, B. Hillebrands, M.P. Kostylev, Appl. Phys. Lett. **93**, 022508 (2008).
[14] Z.K. Wang, V.L. Zhang, H.S. Lim, S.C. Ng, M.H. Kuok, S. Jain, A.O. Adeyeye, Appl. Phys. Lett. **94**, 083112 (2009).
[15] A.N. Myasoedov, Y.K. Fetisov, Sov. Phys. Tech. Phys. **34**, 666 (1989).
[16] A.V. Voronenko, S.V. Gerus, V.D. Haritonov, Sov. Phys. J. **31**, 76 (1988).
[17] A.A. Serga, T. Neumann, A.V. Chumak, B. Hillebrands, Appl. Phys. Lett. **94**, 112501 (2009).
[18] S.O. Demokritov, A.A. Serga, A. André, V.E. Demidov, M.P. Kostylev, B. Hillebrands, Phys. Rev. Lett. **93**, 047201 (2004).
[19] M.P. Kostylev, A.A. Serga, T. Schneider, T. Neumann, B. Leven, B. Hillebrands, R.L. Stamps, Phys. Rev. B **76**, 184419 (2007).
[20] T. Neumann, A.A. Serga, B. Hillebrands, M.P. Kostylev, Appl. Phys. Lett. **94**, 042503 (2009).
[21] U.-H. Hansen, M. Gatzen, V.E. Demidov, S.O. Demokritov, Phys. Rev. Lett. **99**, 127204 (2007).

5.8 Reverse Doppler effect in backward spin waves scattered on surface acoustic wave

A.V. Chumak, A.A. Serga, and B. Hillebrands[1]

The Doppler effect (or Doppler shift) is a well known phenomenon in which a wave emitted from a moving source or reflected off of a moving boundary is shifted in frequency [1,2]. When the source or reflector is approaching the receiver, the frequency of received wave is shifted up in frequency. Similarly, the frequency shifts down if the source or reflector is moving away from the observer. The effect is widely used in radar systems, laser vibrometry and astronomical observations.

In left-handed media the reverse (or anomalous) Doppler effect occurs [3–5]. This effect is characterized by the opposite frequency shift: waves reflect from an approaching boundary with lowered frequency. Conversely, waves reflect from a receding boundary with higher frequency. The explanation for the reversal Doppler shift is that in left-handed media, the group and phase velocities of the waves are in opposite directions [6]. The frequency at which the reflector produces waves is determined by the rate at which it encounters the wave crests from the source. For a wave group approaching the reflector in a left-handed medium, the wave crests are actually moving away from the reflector. Thus, the reflector encounters fewer (more) crests per second if it is moving towards (away from) the source than if it were stationary, resulting in a lower (higher) frequency of the reflected wave.

Magnetostatic spin waves travelling in a thin film magnetic material, saturated by a magnetic field along the direction of propagation, are known to have negative dispersion. That is, the phase velocity and group velocity are in opposite directions. Such waves are termed backward volume magnetostatic waves (BVMSW) [7]. Stancil *et al.* previously observed the reverse Doppler effect in BVMSW for the case where the receiver is moving relative to the source [5]. We report here the observation of a reverse Doppler effect for BVMSW reflecting off of a moving target, namely a travelling surface acoustic wave. These results are interesting for both fundamental research on linear and nonlinear wave dynamics, magnon-phonon interactions and for signal processing in the microwave frequency range. Microwave devices such as frequency shifters, adaptive matched filters and phonon detectors may be conceived using inelastic scattering of spin waves on acoustic waves.

The experiments were performed using 6 µm-thick yttrium iron garnet (YIG) films, which were epitaxially grown on 500 µm-thick, (111) oriented gadolinium gallium garnet (GGG) substrates. The substrates were cut into strips approximately 3 mm wide and 2 cm long. To produce the conditions for backward volume magnetostatic wave propagation, an external bias magnetic field of

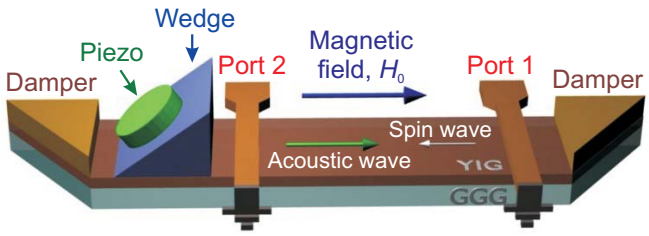

Fig. 1: Experimental setup. Spin waves are excited and received in the YIG film by stripline antennae (Port 1 and Port 2). The SAW is excited on the YIG/GGG substrate by a piezoelectric quartz crystal and an acrylic wedge transducer.

[1] In collaboration with P. Dhagat and A. Jander, School of Electrical Engineering and Computer Science, Oregon State University, Corvallis, OR, USA.

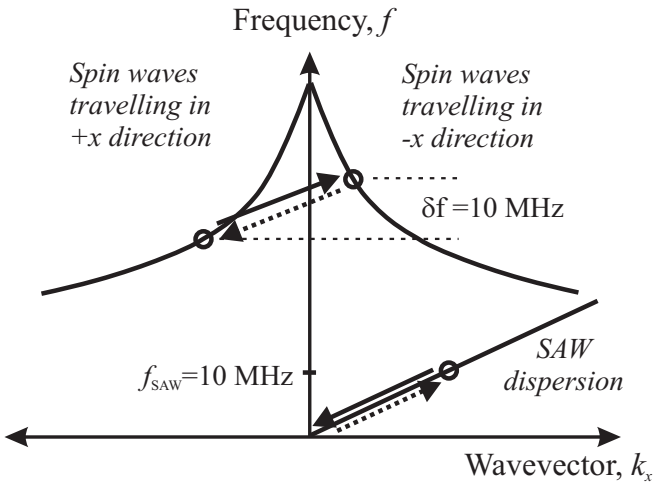

Fig. 2: Schematic of dispersion curves for BVMSW and SAW. Circles indicate the waves that participate in Bragg scattering. Solid arrows show the process of scattering of BVMSW on *co-propagating* SAW resulting in spin-waves shifted up in frequency while a phonon is annihilated. Dashed arrows show the process of scattering of BVMSW on *counter-propagating* SAW with the resulting spin-wave frequency shifted down while a phonon is generated.

$H_0 = 1640\,\mathrm{Oe}$ was applied in the plane of the YIG film strip along its length and parallel to the direction of spin-wave and SAW propagation (see Fig. 1). BVMSWs were excited and detected in the YIG film using microwave stripline antennae spaced 8 mm apart (shown as Port 1 and Port 2 in Fig. 1). The spin waves were generated by driving the antennae with the microwave source of a network analyzer (model Agilent N5230C). The microwave signal power, at 1 mW, was low enough to avoid non-linear processes. The microwave frequency was swept through the range $6.4 - 6.6\,\mathrm{GHz}$. Simultaneously, surface acoustic waves were launched to propagate along the same path on the YIG/GGG sample. Longitudinal compressional waves at frequency $f_{\mathrm{SAW}} = 10\,\mathrm{MHz}$ were generated using a piezoelectric quartz crystal and coupled to surface modes in the YIG/GGG with an acrylic wedge transducer [8]. The wedge was machined to 51° for most efficiently transforming bulk acoustic waves into surface acoustic waves. A transformer and resonant circuit were used for impedance matching between the $50\,\Omega$ source and the piezoelectric crystal. The ends of the YIG/GGG sample were cut at a 45° angle and coated with a silicone acoustic absorber to avoid reflections (see Fig. 1).

The acoustic waves interact with the spin waves through the magnetostrictive effect in the magnetic material [9, 10]. The strain of the acoustic wave thereby periodically modulates the magnetic properties of the film, effectively producing a travelling Bragg grating off of which the spin waves are reflected. Figure 2 shows schematically the dispersion curves for both the BVMSW and SAW. One can see that the group velocity of BVMSW, as determined from the slope of the dispersion curve, is negative for positive wave vectors and vice versa. Thus, points on the BVMSW curve to the left of the axis represent waves propagating or carrying energy to the right from Port 2 to Port 1. Conversely, spin waves propagating to the left from Port 1 to Port 2 appear on the right side of the plot. The surface acoustic waves have a normal, linear dispersion relation: SAW travelling to the right from the prism are indicated by points on the right side of the plot.

The scattering process of spin waves on the acoustic waves must conserve energy and momentum. Figure 2 shows schematically the transitions allowed by the conservation laws. The annihilation of a phonon (solid arrows in Fig. 2) corresponds to the annihilation and the generation of a magnon of higher frequency and travelling in the opposite direction of the original spin wave. It is clear that for the experimental setup shown in Fig. 1, this interaction can be realized only for the spin wave which propagates in the $+x$ direction, *i.e.*, in the same direction as the SAW. One can see that the Doppler effect is reversed since the reflected spin wave has higher frequency. Another process is realized with the generation of the phonon (dashed arrows in Fig. 2), which corresponds to the annihilation and the generation of a magnon of lower frequency travelling in the opposite direction

of the original spin wave. This process takes place between counter-propagating spin and acoustic waves. The Doppler shift, δf, is equal to the SAW frequency in both cases.

Figure 3a shows the experimentally measured BVMSW transmission characteristics for the YIG film as determined from the S_{21} parameter (power received at Port 2 relative to the power delivered to Port 1). The spin-wave transmission band is bounded above by the ferromagnetic resonance frequency and below by the antenna excitation efficiency. It has a maximum just below the point of ferromagnetic resonance ($f_{\mathrm{FMR}} = 6577\,\mathrm{MHz}$).

Figure 3b shows the reflection characteristics for Port 1 (S_{11} parameter) due to spin waves generated at Port 1 being reflected back to the same antenna. The Doppler shifted frequencies were measured by tuning the network analyzer to detect signals at frequencies offset by plus and minus 10 MHz (*i.e.*, $\pm f_{\mathrm{SAW}}$) from the swept source frequency. Similarly, the reflection characteristics for Port 2 are shown in Fig. 3c. In each case, the frequency axis is the swept source frequency.

One can see from Fig. 3b that both up and down-shifted frequencies exist for the reflected spin waves (P_+ and P_- signals in figure). The reason is as follows: with the microwave signal applied to Port 1, the antenna excites spin waves propagating outwards in both directions from the antenna. The spin waves propagating to the left, towards the acoustic source, encounter approaching surface acoustic waves and are partially scattered back towards the source antenna with a reverse Doppler shift down in frequency. The spin waves propagating to the right, away from the acoustic source, encounter receding acoustic waves and are scattered back with an up-shift in frequency due to the reverse Doppler effect.

The allowed transitions shown in Fig. 2 are equivalent to the Bragg reflection conditions. For frequencies meeting these conditions, the reflected spin wave power is maximized. Thus, the peaks in the P_+ and P_- curves correspond to the phonon annihilating up-shift and phonon generating down-shift processes respectively. The down-shift process must start at a higher spin wave source frequency and, in the reverse transition, the up-shift process must start from a lower original spin wave frequency. Thus, the difference in source frequency for the up-shift and down-shift process, δf, should be equal to the SAW frequency, f_{SAW}. This is seen in the experimental results shown in Fig. 3b: the source frequency at which the P_+ signal reaches a maximum is 10 MHz lower as compared to the P_- signal. The peak of the down-shifted reflection is larger and narrower because the path length over which the acoustic and spin waves can interact is approximately two times longer on the left side of the antenna. Although both up-shifted and down-shifted signals are present in the experimental results, it is clear from the relative amplitudes that the up-shifted signal is due to the co-propagating waves, verifying the reverse Doppler effect.

To construct a simple and representative theoretical model, we consider the BVMSW dispersion relation to be nearly linear for small wavenumbers ($kd \ll 1$, where d is the thickness of the YIG film). Thus, we can write

$$f_{\mathrm{SW}}(k) = f_{\mathrm{FMR}} + v_{\mathrm{SW}} \cdot k \quad , \tag{1}$$

where

$$v_{\mathrm{SW}} = -\frac{f_{\mathrm{H}} f_{\mathrm{M}}}{4 f_{\mathrm{FMR}}} \quad , \tag{2}$$

is the group velocity of BVMSW. Here $f_{\mathrm{H}} = \gamma H_0$, $f_{\mathrm{M}} = 4\pi\gamma M_0$, where $\gamma = 2.8\,\mathrm{MHz/Oe}$ is the gyromagnetic ratio.

The dispersion relation for the SAW is linear in good approximation with $f_{\mathrm{SAW}}(k) = v_{\mathrm{SAW}} \cdot k$, where v_{SAW} is the phase and group velocity of the acoustic wave. Fulfilling laws of energy and

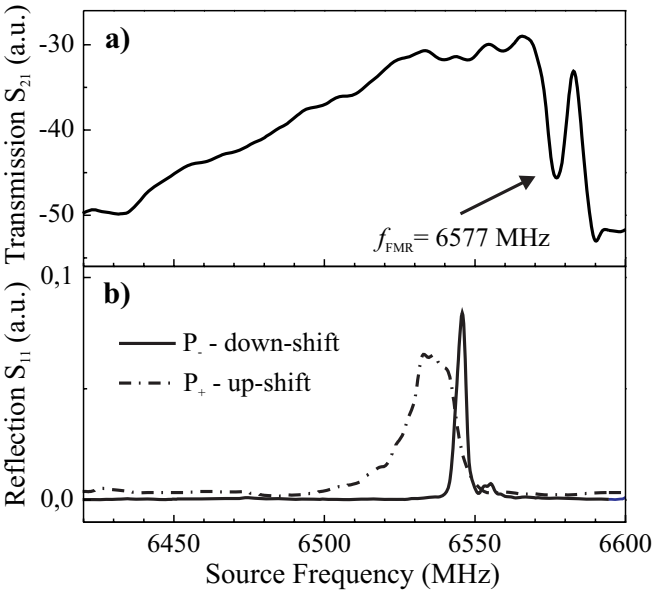

Fig. 3: a) BVMSW transmission characteristics for the YIG film. b) The reflection characteristics for Port 1. The solid curve, P_+, is for the detector frequency set 10 MHz below the source frequency. The dashed curve, P_-, is for the detector frequency set 10 MHz above the source frequency. In each case, the frequency axis is the swept source frequency.

momentum conversation by the transitions indicated in Fig. 2, a simple equation can be derived for the initial spin-wave frequencies f_+ and f_- which correspond to the maxima of P_+ and P_-:

$$f_\pm = f_{\mathrm{FMR}} - \frac{f_{\mathrm{SAW}}}{2}\left(\frac{\upsilon_{\mathrm{SW}}}{\upsilon_{\mathrm{SAW}}} \pm 1\right) \quad . \tag{3}$$

Using saturation magnetization $4\pi M_0 = 1750\,\mathrm{G}$ for the YIG film, BVMSW group velocity $\upsilon_{\mathrm{SW}} = 3.2\,\mathrm{cm/\mu s}$, and SAW velocity $\upsilon_{\mathrm{SAW}} = 0.5\,\mathrm{cm/\mu s}$ this equation gives the values for $f_+ = 6537\,\mathrm{MHz}$ and $f_- = 6547\,\mathrm{MHz}$ which is in good agreement with the experimental data (see Fig. 3).

In conclusion, we have observed the reverse Doppler effect in backward spin waves reflected off of surface acoustic waves. Both possible situations were analyzed: the scattering of BVMSW from co-propagating and counter-propagating SAW. It was shown that the frequencies of scattered spin waves in both cases were shifted by the frequency of SAW according to the reverse Doppler effect. The results are in good agreement with the theoretical analysis based on the dispersion curves of spin waves and acoustic waves. Similar reverse Doppler effects are to be expected in other left-handed media.

This work was partially supported by the DFG SE 1771/1-1, and NSF ECCS 0645236. Special acknowledgments to Prof. G. A. Melkov for valuable discussions.

References

[1] C. Doppler, Abh. Koniglichen Bohmischen Ges. Wiss. **2**, 465 (1843).
[2] C.H. Papas, Theory of Electromagnetic Wave Propagation (McGraw-Hill, New York, 1965).
[3] V.G. Veselago, FTT, **8**, 3571 (1966).
[4] N. Seddon, T. Bearpark, Science **302**, 1537 (2003).
[5] D.D. Stancil, B.E. Henty, A.G. Cepni, J.P. Van't Hof, Phys. Rev. B , **74**, 060404(R) (2006).
[6] V.G. Veselago, Usp. Fiz. Nauk **92**, 517 (1967).
[7] R.W. Damon, J.R. Eshbach, Phys. Chem. of Solids **19** 308 (1961).
[8] S. Hanna, G. Murphy, K. Sabetfakhri, K. Stratakis, Proc. Ultrason. Sym. 209 (1990).
[9] S.M. Hanna, G.P. Murphy, IEEE Trans. Magnetics, **24**, 2814 (1988).
[10] Yu.V. Gulyaev, S.A. Nikitov, Sov. Phys. Solid State, **26**, 1589 (1984).

5.9 Non-diffractive narrow wave beams in a medium with controlled anisotropy

T. Schneider, A.A. Serga, A.V. Chumak, C.W. Sandweg, S. Trudel, and B. Hillebrands[1]

A feature common to all types of wave beams is the tendency to increase their transverse aperture, as they propagate, due to unavoidable diffraction within the propagation medium. This effect is especially pronounced when the initial width of the wave beam is comparable with or even smaller than the wavelength of the waves forming the beam. Here we demonstrate that wave beam diffraction can be drastically reduced when waves propagate in a planar medium with a strong induced in-plane anisotropy in which the frequency of propagating waves $f(\mathbf{k}) = f(k_y, k_z)$ strongly depends on the direction of the in-plane wavevector $\mathbf{k} = k_y\mathbf{y}_0 + k_z\mathbf{z}_0$. The creation and propagation of quasi-diffractionless wave beams of sub-wavelength width was observed.

In an anisotropic medium, the direction of the wave group velocity $\mathbf{v}_g = 2\pi \cdot \partial f(\mathbf{k})/\partial \mathbf{k}$ indicating the direction of energy propagation does not, in general, coincide with the direction of the wavevector $\mathbf{k}$. When the medium's anisotropy is sufficiently strong, the direction of the group velocity of the wave beam may become independent of the wavevectors of the waves forming the beam in the vicinity of a certain carrier wavevector $\mathbf{k}_c$. In such a case, wave packets excited with a broad angular spectrum of wavevectors may be concentrated along this direction. The described effect was first observed for phonons propagating in an anisotropic crystal potential [1]. As is shown in this article, this leads to the formation of a practically non-diffractive wave beam which maintains its transverse aperture over large propagating distances, which we call caustic wave beams, in analogy with conventional optics.

In this work, dipolar spin waves propagating in yttrium iron garnet (YIG) films are used as an experimental model system for controlled caustic wave beam propagation, as was previously suggested [2,3]. These waves are weakly damped, easily excited by microstrip antennas, and observed at the film's surface using Brillouin light scattering (BLS) spectroscopy [2,5,6]. In this system the uniaxial symmetry axis is imposed by the magnetization and can thus be controlled by the in-plane bias magnetic field $\mathbf{H}_0$. This enables an externally addressable, in-plane anisotropic magnetic potential through which the spin waves propagate.

The clear observation of caustic beams in an anisotropic medium requires the excitation of wave packets consisting of many wave components having different in-plane wavevectors, i.e. wave packets with a wide angular spectrum. While the ideal source for such a wave packet is a point-source, a source whose size is comparable to (or smaller than) the carrier wavelength of the excited wave packet is also suitable.

In early studies of spin-wave propagation in YIG, spin wave packets were excited by microstrip antennas having large (several mm) apertures [2,4]. The angular spectra of the excited wave packets were not sufficiently wide to form caustics. Thus, only indirect evidence of caustic formation was found in these experiments, as seen from beam scattering from a natural defect of the magnetic film (Fig. 6 in [2]).

[1] In collaboration with S. Wolff, Nano+Bio Center, TU Kaiserslautern, Germany; M.P. Kostylev, School of Physics, M013, University of Western Australia, Crawley, Australia; V.S. Tiberkevich, A.N. Slavin, Department of Physics, Oakland University, Rochester, Michigan, USA.

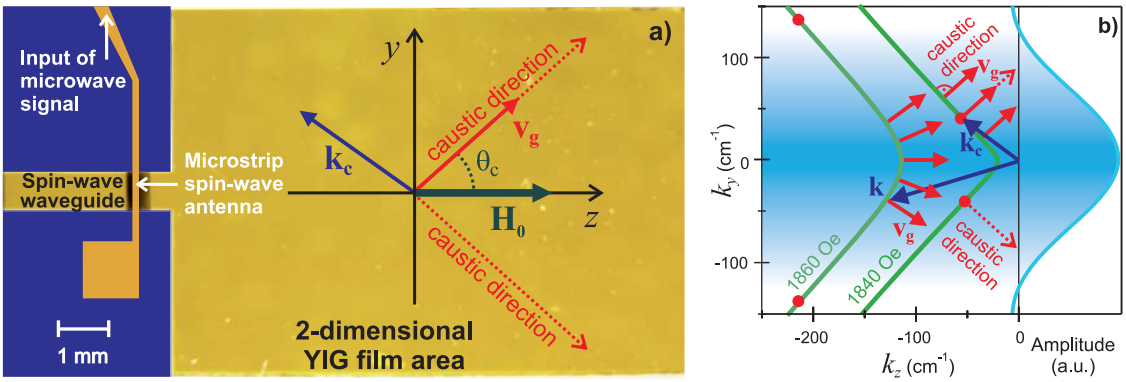

Fig. 1: a) Experimental setup. The YIG film is shown together with the strip-line antenna. b) Left part: iso-frequency curves for different magnetic fields. Dots mark caustic points. b) right part: Excitation amplitude of the waveguide antenna ($W = 750\,\mu$m). The shading marks the area were the spin-wave excitation is efficient. Only for the lowest field does the caustic point lie inside the excitation spectrum and, thus, a pronounced caustic beam is expected only for that field.

To overcome these limitations, a novel excitation structure delivering wave packets with wide angular spectra was designed, as shown in Fig. 1a [7]. The transition between the waveguide and the continuous area of the film acts as an approximate point source. A microstrip antenna (see Fig. 1a) was used to excite dipolar, backward volume magnetostatic spin waves [8] into the waveguide. The spin waves propagating in both the waveguide and the continuous area are accessible to probing by space-, time-, and phase-resolved BLS spectroscopy [2,5,6], allowing the direct investigation of the excited spin-wave beams in the two-dimensional YIG film area. Demidov et al. [9] recently demonstrated that the developed structure can also be used to excite spin-wave beams on the µm-scale in permalloy.

A formalism for caustic beam formation in a medium with anisotropic dispersion law $f(\mathbf{k})$ can be developed using the approximate dispersion relation given in [2]. The angle θ which $\mathbf{v}_g$ makes with $\mathbf{H}_0$ is, in general, different at different points of the spectrum, and can be calculated as

$$\theta = \arctan(v_y/v_z) = -\arctan(dk_z/dk_y) \quad . \tag{1}$$

The caustic beams are formed when the direction of the wave energy transmission, coinciding with the direction of group velocity and determined by the angle θ, is the same for waves having different wavevectors $\mathbf{k}$. This condition can be formulated as $d\theta/dk_y = 0$, or, using Eq. (1)

$$\frac{d^2k_z}{dk_y^2} = 0 \quad . \tag{2}$$

For a given excitation frequency f_s the dispersion relation can be rewritten as $k_z = k_z(k_y, f_s, H_0)$. The resulting iso-frequency curves corresponding to bias magnetic field magnitudes of $\mu_0 H_0 = 184\,$mT and $186\,$mT (μ_0 is the vacuum permeability) are presented in the left part of Fig. 1b. A vector connecting the origin of the coordinate system with any point lying on an iso-frequency curve is the wavevector $\mathbf{k}$. The normal to the iso-frequency curve shows the local direction of the wave group velocity. The dots on the iso-frequency curves show the points where the curvature (d^2k_z/dk_y^2) is zero. Such points are referred to as caustic points. The vectors $\mathbf{k}_c$ connecting the origin to caustic points are the carrier wavevectors of the caustic wave beams [3].

The right part of Fig. 1b presents the k_y spectrum of spin waves excited by a waveguide antenna of finite width $W = 750\,\mu\text{m}$. The shading between the first two points of zero amplitude of the spectrum indicates where wave excitation is effective. For a low bias magnetic field (184 mT), the region of effective wave excitation by the waveguide antenna includes the caustic point as well as the approximately linear segment of the iso-frequency curve around this point (Fig. 1b). On this segment, the direction of the group velocity is the same for all wavevectors $\mathbf{k}$. Thus, a caustic wave beam can form, and the energy of this beam will propagate along the caustic directions perpendicular to the linear segments of the iso-frequency curve making the angle θ_c with the bias magnetic field $\mathbf{H}_0$. The condition (2) defines the carrier wavevector $\mathbf{k}_c$ of the caustic beam, the caustic group velocity $\mathbf{v}_c$, and the propagation direction θ_c of the caustic beam.

An analytical calculation of the beam profile shows that compared to the case of a usual "diffractive" wave beam of finite initial width W, the "non-diffractive" propagation distance of the caustic beam is drastically increased. In particular, for the experimental parameters (YIG film thickness $L = 7.7\,\mu\text{m}$, magnetic field $\mu_0 H_0 = 184\,\text{mT}$, operation frequency $f_s = 7.132\,\text{GHz}$, and $W = 750\,\mu\text{m}$) used here the non-diffractive propagation length is $\xi_c = 1.5\,\text{m}$.

Also note that the carrier wavelength of the caustic beam is around 0.96 mm ($k_c = 65.36\,\text{cm}^{-1}$, see Fig. 1a) while the width (defined by the width of the waveguide) is 750 µm and thus significantly smaller than λ.

For a bias magnetic field of 184 mT (with the caustic point within the excitation region, Fig. 1b), two clear wave beams are seen in the BLS intensity map (Fig. 2a). As expected for a caustic beam, the observed beams are laterally stable, and no diffractive spreading is observed. Fig. 2d presents the numerically calculated caustic spin wave beam profiles expected under these experimental conditions. The calculation was based on Huygens principle using the anisotropic dispersion relation and the excitation amplitude shown in Fig. 1. Comparing frames a and d of Fig. 2 demonstrates the very good agreement between the experiment and our model, and unambiguously confirms the observed beams are indeed caustics. Only the reflection of the caustic at the sample's edge were not be reproduced numerically, given the calculations were performed for an unbound space.

Efficient caustic beam formation cannot happen if the curvature of the iso-frequency curve is non-zero through the range of efficient spin wave excitation. This is the case for the higher magnetic fields studied here. For $\mu_0 H_0 = 186\,\text{mT}$, the caustic point lies beyond the range of efficient excitation (see Fig. 1b). While still possible, caustic beam formation is strongly hindered. Thus for higher bias fields, both experiment (frames b and c) and numerical calculations (frames e and f) indicate that the caustic beams become less pronounced.

Figure 2g, h, and i show the measured phase structure of the propagating spin waves. The measurements have been performed by phase-resolved BLS [5, 6]. One sees the spin-wave wavefronts visualized through constructive and destructive interference between the spin-wave signal and a reference signal having constant phase. The results of the numerical calculation of the spin wave phase fronts are shown in Fig. 2j, k, and l. Within the caustic beams the wavefronts are not perpendicular to the beam direction, since the wavevector $\mathbf{k}$ and the group velocity $\mathbf{v}_g$ are not collinear (see Fig. 2k).

It should be pointed out once again, that for $\mu_0 H_0 = 184\,\text{mT}$, where caustic formation was clearly observed in the intensity image, the distance between phase fronts (i.e., the wavelength), is clearly larger than the transverse aperture (only one wave front is observed in Fig. 2g). As the wavelength becomes smaller than the waveguide's aperture (frames h and i), caustic formation is less pronounced (frames b and c). As for the intensity profiles, a very good qualitative agreement between the calculations and experiments is observed.

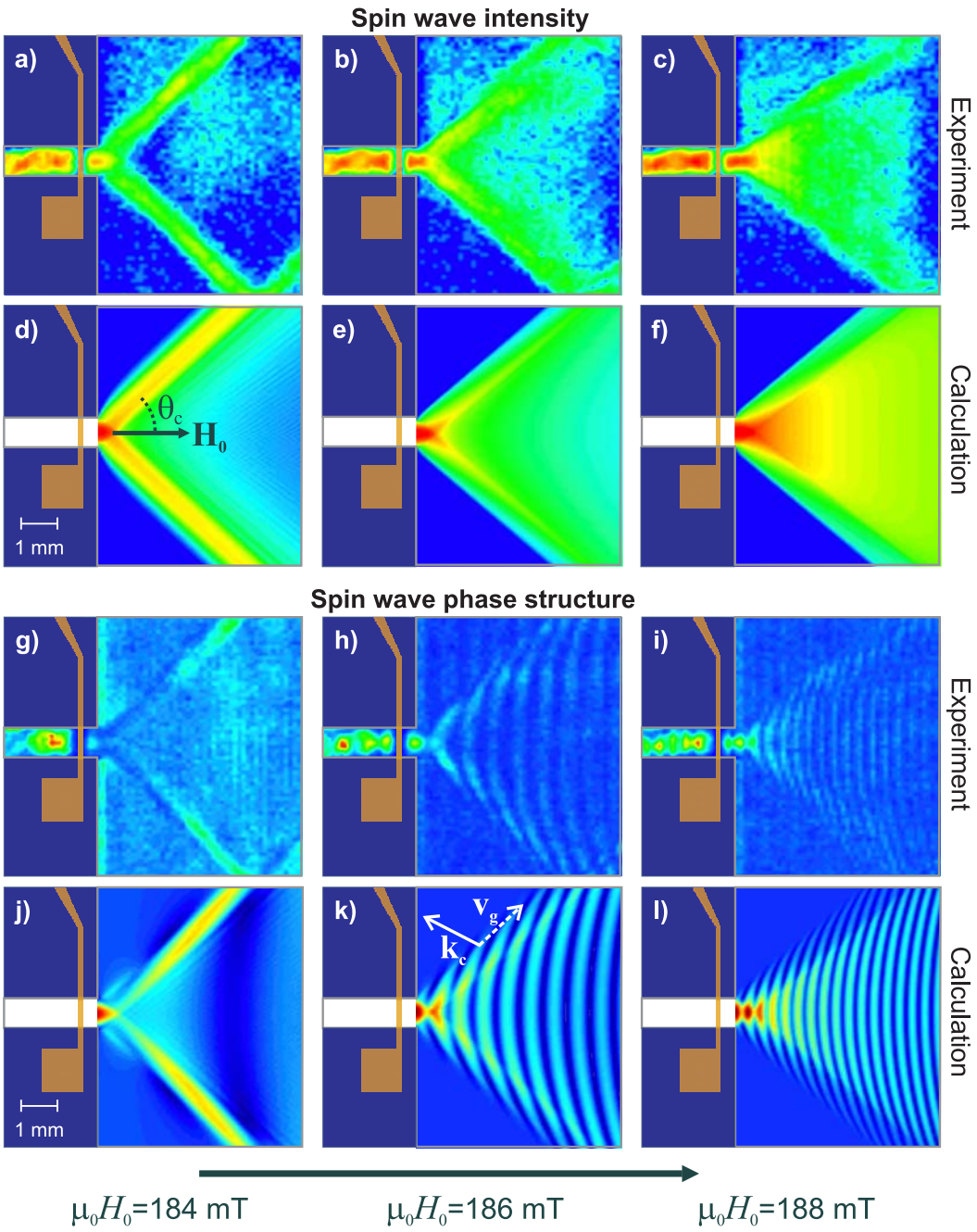

Fig. 2: Measured and calculated intensity and phase profiles of the propagating spin wave beams for bias magnetic fields $\mu_0 H_0 = 184\,\mathrm{mT}$, 186 mT, 188 mT (left to right columns). a), b), and c): measured spin wave intensity profiles. d), e), and f): Numerically calculated profiles. g), h), and i): Measured spin wave phase profiles. j), k), and l): Numerically calculated phase profiles. The relative direction of the caustic beam carrier wavevector $\mathbf{k}_c$ and group velocity $\mathbf{v}_g$ are explicitly shown in frame k. For all frames, waveguide is $W = 750\,\mu\mathrm{m}$ wide and $f_s = 7.132\,\mathrm{GHz}$.

The unique relation between caustic wave beam propagation and the axis of anisotropy was further explored. Figure 3a demonstrates the scattering of caustic spin wave beams from the YIG film boundaries when $\mathbf{H}_0$ is directed along these boundaries. The boundary region from which the propagating caustic wave beam scatters acts as a secondary wave source, whose finite size is of the order of the beam's width. This secondary source also radiates a wave packet with a wide angular spectrum, that again forms caustic wave beams propagating at the same angle θ_c to the anisotropy axis defined by $\mathbf{H}_0$ as the initial caustic wave beam.

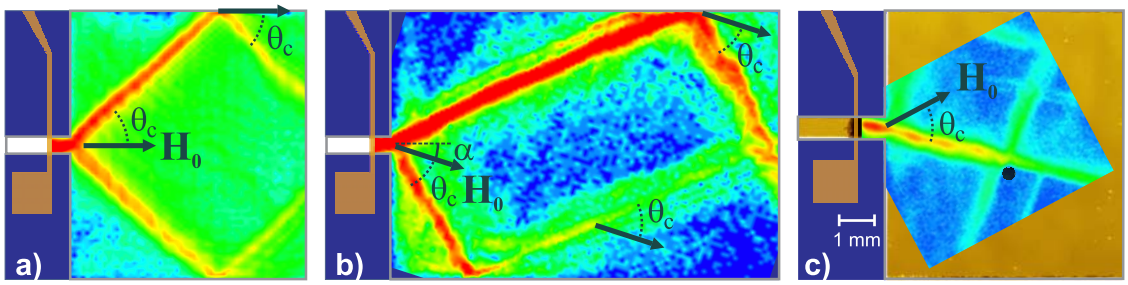

Fig. 3: Scattering of caustic beams from the medium boundaries (frames a) and b)) and a defect (black dot) (frame c)). Conditions: $\mu_0 H_0 = 186\,\mathrm{mT}$, $f_s = 7.132\,\mathrm{GHz}$, and $W = 400\,\mu\mathrm{m}$ (frames a) and b)) and $500\,\mu\mathrm{m}$ (frames c)).

At a first glance it might seem that the reflection of the caustic at the medium boundary follows the laws of geometric optics, as the incident and reflection angles are equal. However, as we rotate the bias magnetic field clockwise through the angle $\alpha = 20°$ to be inclined with respect to the medium boundary, the pattern of the beam reflection at the boundary drastically changes (see Fig. 3b). First, since the angular spectrum of the initial wave packet is tilted the amplitudes of the upper and lower caustic beams are now substantially different. Second, and more importantly, the incidence and reflection angles of the propagating caustic are no longer equal. Indeed, the direction of the secondary, re-radiated wave beam is determined by the direction of the inclined anisotropy axis in the medium, $\mathbf{H}_0$.

A similar effect is seen in Fig. 3c, where the bias magnetic field was rotated counter-clockwise by 30°, to directly aim the caustic beam at the intentionally made defect in the film (shown as a black dot). It is clear from Fig. 3c, that as in Fig. 3a/b, scattering of the caustic beam from the defect creates a secondary finite-sized source that excites caustic beams propagating at the same angle with respect to the anisotropy axis $\mathbf{H}_0$, preserving their transverse aperture through propagation. It should be pointed out that the defect re-radiates caustic beams in all four possible directions.

In conclusion, it is demonstrated that a narrow wave source excites caustic spin wave beams with a stable transverse aperture which can be sub-wavelength. These caustic beams propagate and scatter along well-defined directions, that can be controlled by rotating the medium's anisotropy axis by orienting an externally applied field. These results are useful not only for the fundamental understanding of spin-waves propagating, but can also easily transferred to any wave in a strongly anisotropic medium.

This work was supported by the DFG (Graduiertenkolleg 792 and grant No. SE 1771/1-1) and the AvH foundation (ST).

References

[1] B. Taylor, H.J. Maris, C. Elbaum, Phys. Rev. Lett. **23**, 416 (1969).
[2] O. Büttner, M. Bauer, S.O. Demokritov, B. Hillebrands, Y.S. Kivshar, V. Grimalsky, Yu. Rapoport, T. Shevchenko, A.N. Slavin, Phys. Rev. B **61**, 11576 (2000).
[3] V. Veerakumar, R.E. Camley, Phys. Rev. B **74**, 214401 (2006).
[4] A.B. Valyavsky, A.V. Vashkovsky, A.V. Stal'makov, V.A. Tyulyukin, Sov. Tech. Phys. Lett. **34**, 616 (1989).
[5] A.A. Serga, T. Schneider, B. Hillebrands, S.O. Demokritov, M.P. Kostylev, Appl. Phys. Lett. **89**, 063506 (2006).
[6] T. Schneider, A.A. Serga, B. Hillebrands, M.P. Kostylev, Europhys. Lett. **77**, 57002 (2007).
[7] T. Schneider, A.A.Serga, C. Sandweg, B. Hillebrands, Abstracts of the 52nd Annual Conference on Magnetism and Magnetic Materials, Tampa, Florida, 2007, No. ER-05.
[8] R.W. Damon, J.R. Eshbach, J. Phys. Chem. Solids **19**, 308 (1961).
[9] V.E. Demidov, S.O. Demokritov, D. Birt, B. O'Gorman, M. Tsoi,X. Li, Phys. Rev. B **80**, 014429 (2009).

C. Dynamics in Nanostructures and Domain Walls

Magnetization dynamics in magnetic nanostructures exhibits specific features caused by the strong influence of the surface and demagnetization effects. The manipulation of spin currents in nanostructures has potential applications in effective computing devices and magnetic memory. It is determined by the possibility to use not only the charge of the electron as done in conventional electronics but also its spin orientation for information processing. For the successful utilization of spin information, e.g. for spin electronics (spintronics), difficulties like the short distance over which an electron retains memory of its spin direction have to be overcome. This propagation distance through a material is referred to as spin diffusion length. The problem of the short spin diffusion length can be solved by combining standard spintronic approaches with spin-wave dynamics. It is known that spin waves in ferromagnetic materials can propagate over distances many orders of magnitude larger than the spin-diffusion length. Spin waves, in this case, can serve as an information carrier for spintronic devices. Thus, detailed investigations of spin-wave propagation in magnetic stripes of submicron size are required. The phase-resolved Brillouin light scattering (BLS) microscopy technique, which was developed in our group, opens new possibilities for the research on linear and nonlinear spin-wave dynamics in nanostructures.

The investigation of the spin-wave interaction with locally pinned domain walls in nanostructures is also a focus of our interest. The ability to move domain walls by spin-waves can be used to fabricate memory devices, where domain walls serve as a carrier of information (see Annual Report 2008 and APL 94, 112502 (2009), APL 94, 223510 (2009)).

Another direction of memory-oriented research is the utilization of separate nano-scaled magnetic elements (e.g. nano-dots). Here the magnetization orientation in the stationary state of a single nano-element (up or down, in the simplest case) serves as one bit of information. The switching properties are determined by the shape and the crystalline anisotropy in the element. These memory devices provide long-time information storage capability and a high storage density, but only a low write/read speed. One way to increase the operating speed is the utilization of the magnetization precession. The highest information writing speed is in this case limited by the eigen mode frequencies of the element, which normally is in the GHz frequency range. Thus, detailed investigations of the magnetization dynamics in microstructures are required. Time and space resolved BLS microscopy and magneto-optical Kerr Effect (MOKE) magnetometry are used in our group for these studies. An alternative to an array of memory nano-elements is the utilization of a magnetic film with spatially varying magnetic properties. In the simplest case the variation of the saturation magnetization by means of ion implantation or temperature variation can be used.

In this Annual Report results on the study of static and dynamic phenomena in nanostructures are presented. Report 5.10 presents results on the optical detection of a spin current induced in a nonmagnetic copper film placed on a nickel iron magnetic alloy (permalloy) via spin pumping. In Report 5.11 the spin-wave propagation in permalloy waveguides is studied by means of phase resolved BLS microscopy. Report 5.12 is devoted to the theoretical study of magnetization dynamics in thermally induced magnetization wells in permalloy films. Finally, Report 5.13 is focused on the investigation of magnetization switching in elliptical elements.

C. Dynamik in Nanostrukturen und Domänenwänden

Die Magnetisierungsdynamik in magnetischen Nanostrukturen zeigt durch den Einfluss der Oberfläche und des Entmagnetisierungsfelds ein spezifisches Verhalten. Die Manipulation von Spinströmen in Nanostrukturen hat Anwendungspotential in effizienteren Computerchips und magnetischen Speichern, da in diesem Fall nicht nur die Ladung des Elektrons wie in der konventionellen Elektronik, sondern auch die Ausrichtung seines Spins zur Informationsverarbeitung verwendet werden kann. Um die Spininformation zu nutzen und sogenannte Spinelektronik- (oder Spintronik-) Bauteile konstruieren zu können, müssen verschiedene Probleme gelöst werden. Beispielhaft sei hier die kurze Ausbreitungsdistanz genannt, über die Elektronen ihren Spinzustand behalten (Spin-Diffusionslänge).

Dieses Problem kann gelöst werden, indem man den klassischen Spintronikansatz mit Spinwellen kombiniert. Es ist bekannt, dass sich Spinwellen in ferromagentischen Materialien über Entfernungen ausbreiten können, die mehrere Größenordnungen über der Spin-Diffusionslänge liegen. Spinwellen können damit als Informationsträger für spintronische Bauteile dienen. Daher ist die detaillierte Untersuchung der Spinwellenausbreitung im Mikrometer-Maßstab in magnetischen Streifen nötig. Die phasenaufgelöste Brillouin-Lichtstreumikroskopie (BLS-Mikroskopie) die in unserer Arbeitsgruppe entwickelt wurde, eröffnet neue Möglichkeiten zur Untersuchung der linearen und nichtlinearen Spinwellendynamik in Nanostrukturen.

Ein weiterer Schwerpunkt unseres Interesses ist die Untersuchung der Wechselwirkung von Spinwellen mit lokal verankerten Domänenwänden in Nanostrukturen. Die Möglichkeit, Domänenwände mit Spinwellen zu bewegen, kann zum Aufbau von Speicherbauteilen verwendet werden, bei denen die Information von Domänenwänden getragen wird (siehe auch Jahresbericht 2008, APL 945, 112502 (2009) und APL 94, 223510 (2009)).

Eine weitere Möglichkeit zur Realisierung von Speicherbausteinen ist die Verwendung von nanometergroßen magnetischen Elementen (z.B. Nanodots). Hier beschreibt die Richtung der Magnetisierung eines einzelnen Nanoelements im stationären Zustand ein Bit an Information. Die Schalteigenschaften werden durch die Form und die kristallographische Anisotropie des Elements bestimmt. Diese Speicherbausteine ermöglichen die Langzeitspeicherung von Information und eine hohe Speicherdichte, allerdings mit einer geringen Schreib/Lese-Geschwindigkeit. Eine Möglichkeit diese Geschwindigkeit zu erhöhen, ist das Ausnutzen der magnetischen Präzession. Die Schreibgeschwindigkeit ist in diesem Fall durch die Frequenz der Eigenmoden des Elements limitiert, die üblicherweise im GHz Bereich liegen. Es werden daher genaue Untersuchungen der Magnetisierungsdynamik in Mikrostrukturen benötigt. In unserer Gruppe werden zu diesem Zweck zeit- und ortsaufgelöste BLS Mikroskopie und magnetooptischer Kerr-Effekt- (MOKE-) Magnetometrie eingesetzt. Eine Alternative zu einem Speicher-Array aus Nanoelementen ist die Verwendung eines magnetischen Films mit räumlich variierenden magnetischen Eigenschaften. Im einfachsten Fall kann dazu die Variation der Sättigungsmagnetisierung durch Ionenbeschuss oder Temperaturänderungen verwendet werden.

In diesem Jahresbericht werden Ergebnisse der Untersuchung der statischen und dynamischen Eigenschaften in Nanostrukturen vorgestellt. Kapitel 5.10 präsentiert die Ergebnisse der optischen Detektion von Spinströmen, die durch Spin-Pumpen in einem nichtmagnetischen Kupferfilm auf einer magnetischen Nickel-Eisen-Legierung (Permalloy) induziert wurden. In Kapitel 5.11 wird die Ausbreitung von Spinwellen in Permalloy-Wellenleitern mit Hilfe der phasenaufgelösten BLS Mikroskopie untersucht. Kapitel 5.12 beschäftigt sich mit der theoretischen Magnetisierungsdynamik in thermisch induzierten Magnetisierungsbarrieren in Permalloy-Filmen. Abschließend behandelt Kapitel 5.13 magnetisches Schalten in elliptischen Elementen.

5.10 Optical detection of spin-pumped magnetization in a $Ni_{81}Fe_{19}$/Cu multilayer

F. Fohr, J. Hamrle, H. Schultheiß, A.A. Serga, and B. Hillebrands[1]

The investigation of lateral electron angular momentum transfer has attracted much attention in the past years due to its huge importance to next generation spintronic devices [1, 2]. One of the related questions is the investigation of spin currents and induced magnetization from a ferromagnetic to a non-ferromagnetic material. However, up to now there is no technique allowing to observe induced magnetization in metallic systems by optical means. Here we report on preliminary Brillouin light scattering (BLS) investigations showing that BLS can detect the induced magnetization. The experiment was realized using the spin transfer from a ferromagnetic material to an adjacent paramagnetic material via the spin pumping effect [3, 4].

The sample design is shown in Fig. 1. The entire structure has been fabricated at the RIKEN institute, Wakoshi, Japan. A coplanar waveguide (CPW) is prepared by means of maskless laser photolithography on top of a SiO_2 substrate. The CPW consists of a 200 nm thick Au layer with a 100 µm wide signal line (S). On top of the waveguide a 7 µm wide multilayer structure is placed. It consists of a 30 nm thick $Ni_{81}Fe_{19}$-layer deposited by electron beam evaporation and two insulating interlayers. The CPW generates an oscillating magnetic field in the sample plane and perpendicular to the magnetization of the $Ni_{81}Fe_{19}$-layer.
The multilayer structure is finalized by a copper wedge on top of the $Ni_{81}Fe_{19}$. The copper wedge is deposited by electron beam evaporation with a moving shutter and raises to a thickness of 300 nm. The slope of the wedge can be controlled by the velocity of the moving shutter and is in our case about 1 nm copper thickness per 100 µm distance in x-direction.

To guarantee a most efficient spin pumping, a homogeneous excitation of the magnetization in the pumping $Ni_{81}Fe_{19}$-layer is required. In order to cope with this requirement, a 5 nm thick Al_2O_3 insulating interlayer is deposited between $Ni_{81}Fe_{19}$ and CPW to make sure that (*i*) the magnetization in our sample is excited externally by the magnetic field created by the CPW and not directly by a microwave current flowing through the $Ni_{81}Fe_{19}$-layer, and (*ii*) it prevents microwave

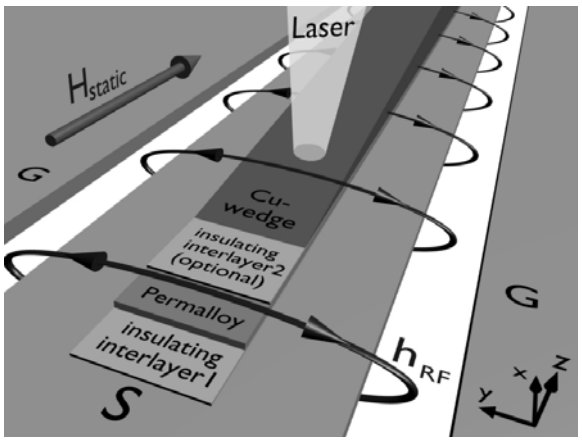

Fig. 1: Scheme of the sample layout. A copper wedge is prepared on top of the signal line of a coplanar waveguide. The wedge is separated from the CPW by a $Ni_{81}Fe_{19}$-stripe and one or two insulating interlayers, the first between CPW and $Ni_{81}Fe_{19}$ and an optional second between $Ni_{81}Fe_{19}$ and copper. The first interlayer is deposited to prevent microwave current flowing from the CPW into the $Ni_{81}Fe_{19}$ and the optional second interlayer is used to block spin pumping from $Ni_{81}Fe_{19}$ to copper. The static magnetic field $\mu_0 H_{static}$ of 20 mT is applied parallel to the signal line and perpendicular to the dynamic magnetic field $\mathbf{h}_{RF}$, which is caused by an alternating microwave current flowing through the CPW.

[1] In collaboration with Y. Fukuma, L. Wang, and Y. Otani, ASI, RIKEN, 2-1 Hirosawa, Wako 351-0198, and ISSP, University of Tokyo, 5-15-5 Kashiwanoha, Kashiwa 277-8581, Japan.

current flowing from the CPW through the copper wedge and creating a spurious magnetic field which would change with raising copper thickness of the wedge. In a second reference sample we used an additional insulating Al_2O_3 layer between the copper wedge and the $Ni_{81}Fe_{19}$-layer to prevent spin pumping from $Ni_{81}Fe_{19}$ to copper.

To determine the absolute value of the copper thickness and to compare the measurements performed on the main sample and the reference sample at any point of the BLS scan, it is necessary to know the start point and the slope of the wedge on each sample. The positioning of the samples in the evaporation chamber is not completely reproducible, so we expect the copper wedge to start at different points of the CPW. As the copper has a higher reflectivity than $Ni_{81}Fe_{19}$, we define the wedge start at that point where the intensity of the backscattered light starts to increase.

The expected BLS intensity $I(d)$ depends on the thickness d of the copper wedge and consists of two contributions: One part of the signal is due to the precessing magnetization in the $Ni_{81}Fe_{19}$, the second part originates from the spin-pumped magnetization in copper. Since BLS is sensitive to the intensity of the inelastic backscattered light, the total BLS intensity is proportional to:

$$I(d) \propto |E_{Py} + E_{Cu}|^2 = |E_{Py}|^2 + 2\,\mathrm{Re}\left(E_{Py}E_{Cu}^*\right) + |E_{Cu}|^2 \tag{1}$$

where E_{Py} and E_{Cu} are the electric field strengths of the probing laser light scattered inelastically in $Ni_{81}Fe_{19}$ and copper respectively. For small copper thicknesses it can be assumed that the phase shift of the light in copper is negligible. Hence the interference term in Eq. (1) provides an effective amplification of the BLS detection sensitivity in the copper due to constructive interference.

The amplitude of the backscattered light from $Ni_{81}Fe_{19}$ is decaying exponentially with increasing copper thickness. The optical penetration depth λ_{opt} is 32 nm in case of copper at the laser wavelength of 532 nm [5]:

$$E_{Py} = E_{Py,0} \cdot \exp\left(-\frac{2d}{\lambda_{opt}}\right) \tag{2}$$

The amplitude of the backscattered light from copper is a sum of contributions from different depths of the copper wedge, weighted by the decaying intensity of the probing laser light as well as by the decaying spin-pumped magnetization (inset of Fig. 2a). The spin-pumped magnetization in copper is also decaying exponentially from the $Ni_{81}Fe_{19}$/Cu interface, but with a much lower decay given by the spin diffusion length λ_{sd}, which is about 300 nm at room temperature [6].

$$E_{Cu} = E_{Cu,0} \cdot \int_0^d \exp\left(-\frac{z}{\lambda_{sd}}\right) \cdot \exp\left(-\frac{2\,(d-z)}{\lambda_{opt}}\right) dz \tag{3}$$

Substituting Eq. (2) and Eq. (3) into Eq. (1) and assuming, that $|E_{Py}| \gg |E_{Cu}|$ as well as that the copper thicknesses d and optical penetration depth λ_{opt} are small compared to the spin diffusion length λ_{sd}, the total BLS intensity can be written in the following way:

$$I(d) = I_{Py} \cdot \exp\left(-\frac{4d}{\lambda_{opt}}\right) + I_{Cu} \cdot \exp\left(-\frac{2d}{\lambda_{opt}}\right) \cdot \left[\exp\left(-\frac{d}{\lambda_{sd}}\right) - \exp\left(-\frac{2d}{\lambda_{opt}}\right)\right] \tag{4}$$

Figure 2a shows the calculated normalized BLS intensities according to Eq. (4). The intensities $I_{Py} = E_{Py,0}^2$ and $I_{Cu} = E_{Py,0} \cdot E_{Cu,0} \cdot \lambda_{opt}$ are free parameters and can be extracted from the fitting of the measurement data (Fig. 2b). The ratio of the intensities $I_{Py}/I_{Cu} = 7.9$ is a measure of the BLS detection efficiency of the spin pumped magnetization in copper. In Fig. 2b the BLS scans

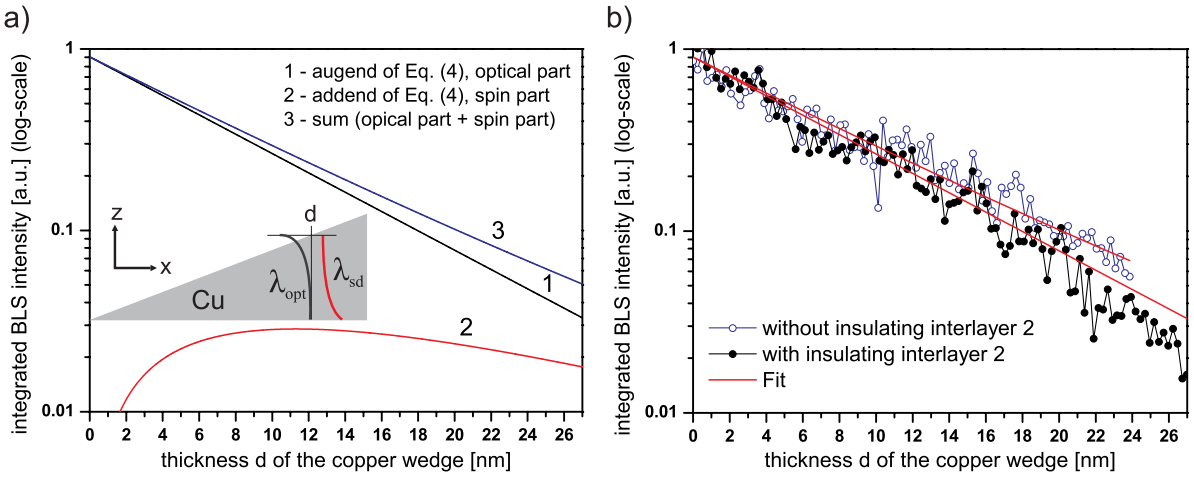

Fig. 2: a) Calculated BLS intensities according to Eq. (4). b) BLS scans over the copper wedge of the sample without the insulating interlayer 2 and the reference sample with the insulating interlayer 2 to block spin pumping from $Ni_{81}Fe_{19}$ to copper. For small copper thicknesses, the signal detected from the precessing magnetization is dominating and covers the spin part of the signal, which becomes more pronounced with increasing copper thickness. Both experimental curves are normalized.

performed on the main sample and the reference sample are shown. The signal from the sample without the interlayer 2 contains both, the optical decay from the signal of $Ni_{81}Fe_{19}$ and of the decaying induced magnetization in copper, while the signal from the reference sample with the interlayer 2, which prevents spin pumping, contains only the decaying signal from $Ni_{81}Fe_{19}$.

In spite of the fact that the BLS signals in Fig. 2b are still very noisy and the effect of spin pumping is very small, we have found a reproducible difference in BLS intensity for the main sample and the reference sample, which corresponds well with the theoretical model. To the knowledge of the authors this would be the first successful attempt to detect induced spin polarization in a metallic material by optical means. However, note that in this preliminary data the noise is rather strong and has to be improved by sample optimization.

Support by the Deutsche Forschungsgemeinschaft within the project JST-DFG Hi380/21-1 is gratefully acknowledged.

References

[1] G.A. Prinz, Science **282**, 1660 (1998).
[2] S.A. Wolf, D.D. Awschalom, R.A. Buhrmann, J.M. Daughton, S. von Molnár, M.L. Roukes, A.Y. Chtchelkanova, D.M. Treger, Science **294**, 1488 (2001).
[3] R.H. Silsbee, A. Janossy, P. Monod, Phys. Rev. B **19**, 4382 (1979).
[4] Y. Tserkovnyak, A. Brataas, G.E.W. Bauer, Phys. Rev. Lett. **88**, 11 (2002).
[5] E. Palik, *Handbook of optical constants of solids*, Academic Press Handbook Series, London (1985).
[6] J. Bass, W.P. Pratt Jr, J. Phys.: Condens. Matter **19**, 183201 (2007).

5.11 All-optical detection of phase fronts of propagating spin waves in a $Ni_{81}Fe_{19}$ microstripe

K. Vogt, H. Schultheiss, S.J. Hermsdoerfer, P. Pirro, A.A. Serga, P.A. Beck, and B. Hillebrands

Magnetization dynamics in small magnetic structures has been widely investigated in the past years. One main aspect of these studies was the spin wave excitation and propagation in magnetic microstructures [1–4]. The detailed knowledge of the spin-wave characteristics, including the phase profile, opens the gate to a new class of experiments like magnetic logic in microstructures based on the phase manipulation of a propagating spin wave, as has been earlier demonstrated on a larger scale [5]. Numerical studies devoted to this topic [6, 7] show promising approaches towards a deeper understanding of spin waves and their interaction with topological objects such as domain walls. Although several experiments investigating the propagation as well as interference of spin waves have been performed [2, 8], a simple tool for determining the phase of spin waves with spatial resolution on the sub-micrometer scale has not been available so far.

In this Report we discuss our results on the direct all-optical detection of the phase fronts of spin waves propagating in a $Ni_{81}Fe_{19}$ spin-wave waveguide. Recently, many research groups investigated spin-wave transport on the micrometer scale for the development of new devices or for the discovery of spin-wave nano-optics [9]. Experiments on spin-wave propagation in magnetic wires by means of Brillouin light scattering (BLS) microscopy [2, 9, 10] are very promising for the investigations of spin-wave characteristics on the micrometer-scale because of the high sensitivity and the spatial resolution only limited by the numerical aperture of the objective lens used to collect the light [11]. However, they only show the intensity distribution of an excited spin wave. We developed the phase-resolved BLS-microscopy technique to determine the wavelength and phase

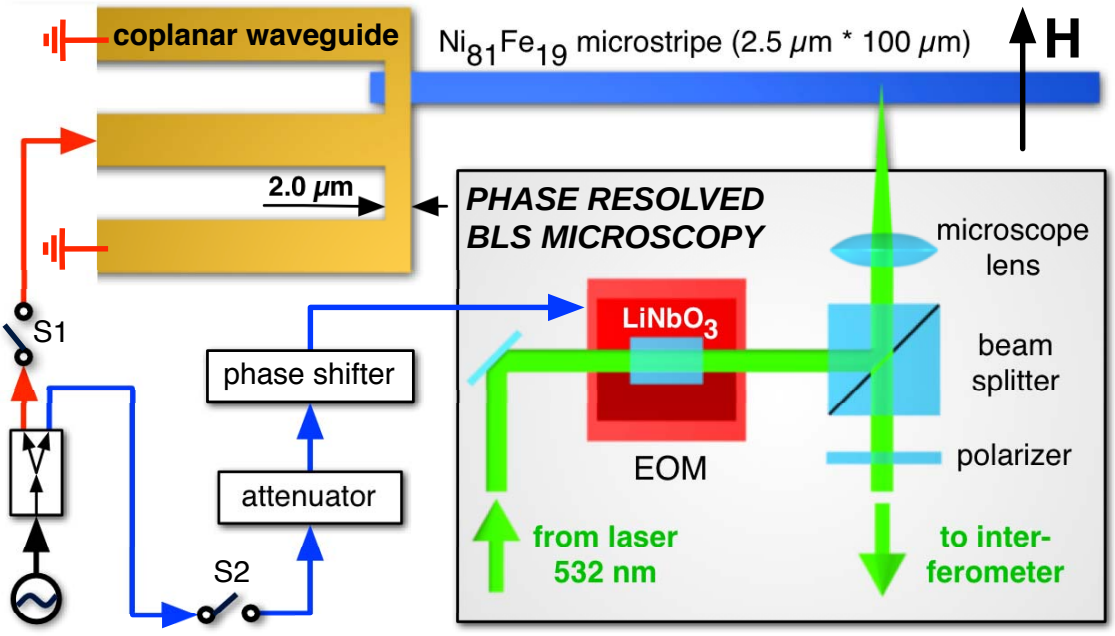

Fig. 1: Scheme of the sample layout and the experimental setup. A shorted coplanar waveguide is used to excite spin waves in a $Ni_{81}Fe_{19}$ stripe with dimensions of $2.5 \times 100\,\mu m^2$. The microwaves generated by a synthesizer are split and guided through two switches to the coplanar waveguide (S1) and to the electro-optic modulator (EOM) (S2), respectively.

profile of propagating spin waves. In addition, this technique provides a method to verify that spin waves are propagating and not driven by, e.g., far-field effects of the exciting antenna. The proof of propagating spin waves can be obtained in phase resolved experiments, where not only the envelope function of the spin waves is measured but also a snapshot of the spin-wave amplitude for a fixed time and phase. In principle, time-resolved MOKE microscopy [8] could also give access to the phase information, but due to the high intrinsic damping of $Ni_{81}Fe_{19}$ the sensitivity of MOKE microscopy is usually not sufficiently high to study spin-wave propagation over a large distance.

A schematic description for the realization of phase resolved BLS-microscopy and the sample geometry is given in Fig. 1. Using a microwave current flowing through the shorted end of a coplanar waveguide (CPW) made of copper, spin waves are excited in a $Ni_{81}Fe_{19}$ stripe with dimensions of $2.5 \times 100\,\mu m^2$ and a thickness of 40 nm. The structure has been produced on a thermally oxidized silicon substrate. The $Ni_{81}Fe_{19}$ stripe is magnetized by an externally applied magnetic field H along its short axis, i.e. in the Damon-Eshbach geometry [12]. The shorted end of the CPW has a thickness of 500 nm and a width of $w = 2\,\mu m$ and is processed on top of the $Ni_{81}Fe_{19}$ stripe. This shorted end acts as an antenna which enables efficient local spin-wave excitation with wave numbers up to $k_{max} = 2\pi/w = 3.14 \cdot 10^4\,cm^{-1}$.

The phase information of the spin waves is acquired by interfering the light scattered from spin waves with a reference light of constant phase. This method relies on the transfer of the phase of the spin waves to the light during the scattering process [13]. To make interference possible, the reference light needs to have the same frequency as the spin-wave excitation. This is achieved

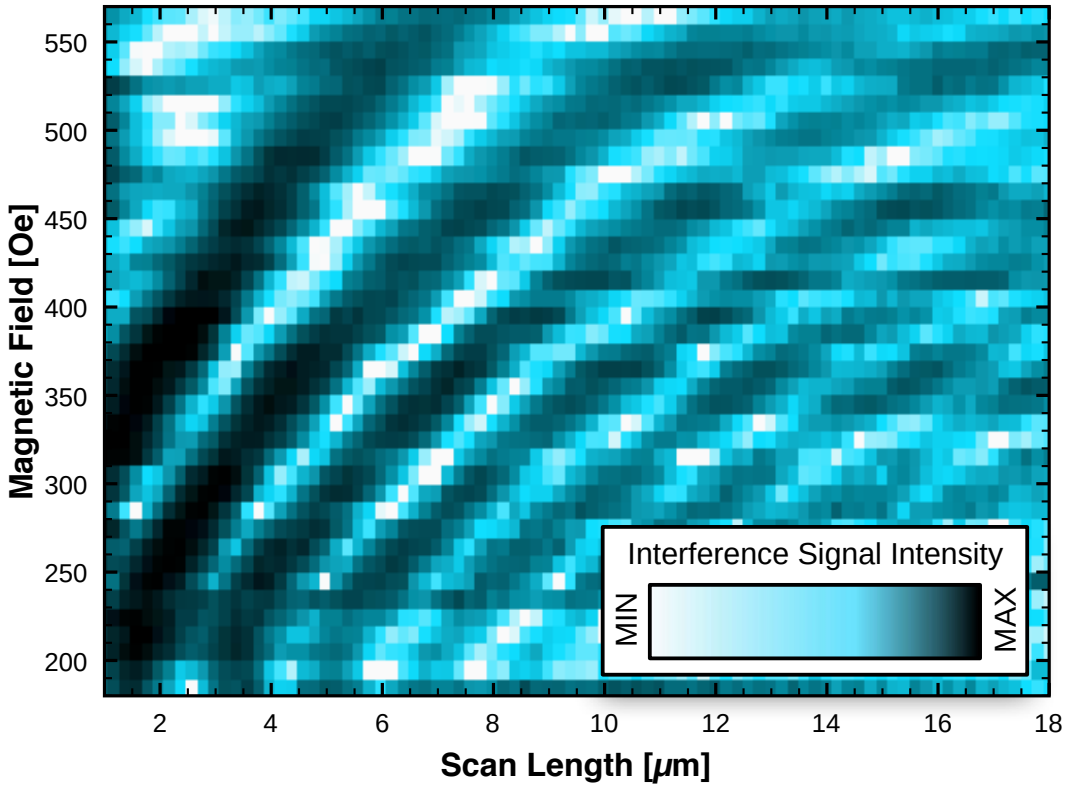

Fig. 2: The intensity plot shows the interference of the light inelastically scattered at spin waves and the light of constant phase. For different applied magnetic fields (y-axis) the interference signal was measured as a function of the distance from the antenna (x-axis). The wavelength of the spin waves is determined by the spatial modulation of the interference signal, where black (white) represents constructive (destructive) interference, respectively.

by sending the probing laser beam through an electro-optic modulator (EOM) driven by the same microwave source as the CPW generating the spin waves. A phase-stable, tunable attenuator placed in the microwave branch feeding the EOM allows to match the intensity of the reference light with the light scattered from spin waves. The phase of the reference light can be adjusted by a tunable phase shifter (see Fig. 1).

Typical results of an interference measurement for characterizing the propagation of spin waves are shown in Fig. 2 for different magnetic fields ranging from 180 Oe to 570 Oe and for an excitation frequency of 7.13 GHz. The spatial intensity distribution of the interfering lights is color coded in an intensity plot. Black (white) corresponds to high (low) signals and shows the position of constructive (destructive) interference. Each row of the intensity plot represents a phase resolved BLS-microscopy scan along the long axis of the $Ni_{81}Fe_{19}$ stripe for a fixed value of the externally applied magnetic field. Instead of the envelope function of an exponentially decaying spin wave, clear oscillations of the light intensity are observed as a function of position. The periodicity of the interference signal is equal to the wavelength of the spin waves, and changes if the externally applied magnetic field is varied.

To validate the wavelength data obtained from the phase resolved measurements, a theoretical analysis of the spin-wave dispersion relations for the investigated magnetic field values was carried out. The dispersion relations shown in Fig. 3a are calculated as in [14] using standard material parameters for $Ni_{81}Fe_{19}$ [15] and taking into account a first order quantization of the spin waves along the short axis of the stripe (spin-wave waveguide modes) [16]. As can be seen in Fig. 3a, the dispersion relation is shifted to higher frequencies as the magnetic field is increased. Since the resonance frequency of the EOM used in the experiment is fixed at 7.13 GHz, the excitation frequency of the spin waves is fixed as well. For each value of the magnetic field, there exists only one point of intersection of the dispersion relation with the excitation frequency, resulting in a

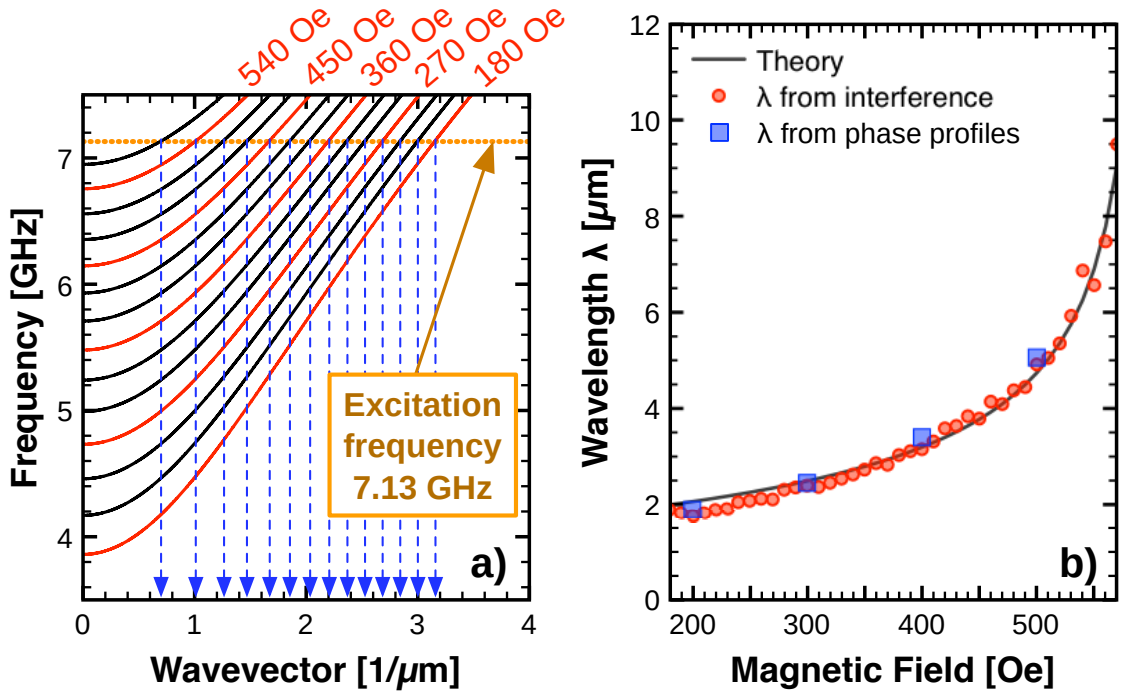

Fig. 3: a) Theoretical spin-wave dispersions for different applied magnetic fields. b) Wavelength of the excited spin waves as a function of the applied magnetic field. The solid line represents the calculated values extracted from the dispersions in a). Dots display the results extracted from the interference pattern in Fig. 2. Boxes show the results obtained from the phase profiles in Fig. 4b.

well defined wavevector of the spin wave. Extracting the wavevector for each field and calculating the corresponding wavelength via $\lambda = 2\pi/k$ yields the black solid line in Fig. 3b. The dots correspond to the measured wavelengths extracted from the data presented in Fig. 2. The very good agreement of the theory with the experimental data corroborates the application of phase resolved BLS-microscopy for the investigation of spin-wave transport phenomena.

Besides the interference signal, the phase profile of the excited spin waves was reconstructed by taking four separate measurements for each position: (i) interference signal, (ii) interference signal with additional $\pi/2$ phase shift of the reference light, (iii) the light only generated by the EOM and (iv) the light only scattered inelastically from spin waves. The measurements can be performed by opening or closing the switches S1 and S2 indicated in Fig. 1. Applying an algorithm described in detail in [13] the phase accumulation can be calculated as a function of position. For example, Fig. 4a shows these four measurements for a magnetic field of 200 Oe. The dots show a standard BLS-microscopy scan of the exponential decay of the spin-wave amplitude due to the intrinsic damping of $Ni_{81}Fe_{19}$. The triangles correspond to the intensity of the light generated by the EOM which is a measure of the local reflectivity of the sample. The solid line and the dotted line are both interference measurements. Note that a relative phase shift of $\pi/2$ of the microwaves applied to the EOM results in a relative shift of $\lambda/4$ of the interference patterns with respect to each other. The resulting phase profile of the excited spin waves as a function of position is shown in Fig. 4b for different values of the externally applied magnetic field. As already demonstrated in Fig. 2 and 3 the wavevector of the spin waves is increasing if the external field is decreased. According to

$$\Phi(x) = \int_0^x k(H, v)\, dx' \tag{1}$$

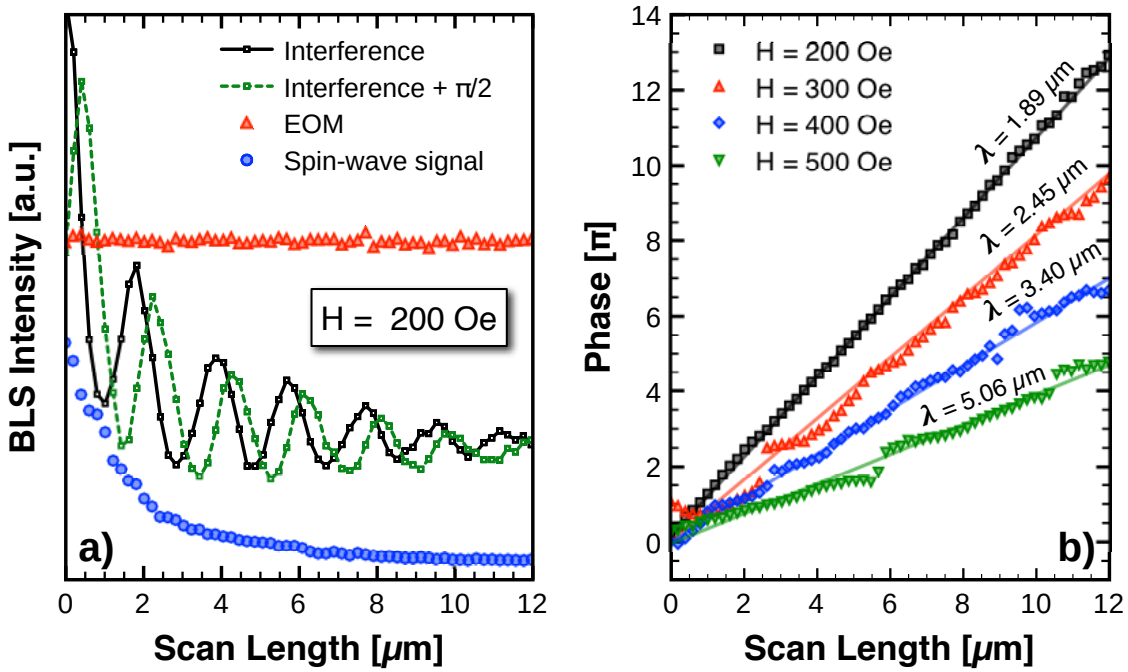

Fig. 4: a) The four measurements required for the reconstruction of the spatial spin-wave phase profile. Dots are the conventional BLS signal, triangles are a measure of the signal solely generated by the EOM. Solid and dashed lines show the interfering spin-wave and EOM signals, in the dashed plot with an additional phase shift of $\pi/2$ of the EOM reference light. The plots are shifted vertically for clarity. b) Phase profiles of the spin waves for various applied magnetic fields. Solid lines represent linear fits.

an increasing wavevector $k(H, \nu)$, which is a function of the magnetic field and the excitation frequency, leads to a faster accumulation of the phase Φ [13]. This can be seen in Fig. 4 where the slope of the phase accumulation is increasing with decreasing magnetic field, resulting in the excitation of smaller wavelengths. For an applied magnetic field of 200 Oe the measured wavelength is $\lambda = 1.89\,\mu$m, which is in the same range as the width of the antenna used for the excitation. This demonstrates that the smallest wavelength which can be excited by a stripe antenna is not simply given by the antenna width w. A rectangular excitation profile from a stripe antenna yields a wavevector spectrum described by $\sin^2(k)/k^2$. This function has minima at integer wavevectors $k_n = n \cdot 2\pi/w$ with $n = 1,\ 2,\ 3\ldots$ where the excitation efficiency is zero, but there exists no fundamental upper limit for the wavevectors possibly excited.

In conclusion, we observed the phase fronts of spin waves propagating in a micrometer-sized $Ni_{81}Fe_{19}$ stripe. Comparison with theory shows an excellent agreement of the measurements with the expected values. Thus, phase resolved Brillouin light scattering microscopy allows for an all-optical access to the phase information of these waves and fills the experimental gap in characterization techniques for sub-micrometer spin-wave propagation phenomena.

Support by the Priority Program SPP 1133 is gratefully acknowledged. The authors would like to thank the Nano+Bio Center of the Technische Universität Kaiserslautern for their assistance in sample preparation.

References

[1] V. Vlaminck, M. Bailleul, Science **322**, 410 (2008).
[2] V.E. Demidov, S.O. Demokritov, K. Rott, P. Krzysteczko, G. Reiss, Appl. Phys. Lett. **91**, 252504 (2007).
[3] H. Schultheiss, S. Schäfer, P. Candeloro, B. Leven, B. Hillebrands, A.N. Slavin, Phys. Rev. Lett. **100**, 047204 (2008).
[4] S.M. Seo, K.J. Lee, H. Yang, T. Ono, Phys. Rev. Lett. **102**, 147202 (2009).
[5] T. Schneider, A.A. Serga, B. Leven, B. Hillebrands, R.L. Stamps, M.P. Kostylev, Appl. Phys. Lett. **92**, 022505 (2008).
[6] R. Hertel, W. Wulfhekel, J. Kirschner, Phys. Rev. Lett. **93**, 257202 (2004).
[7] D.S. Han, S.K. Kim, J.Y. Lee, S.J. Hermsdoerfer, H. Schultheiss, B. Leven, B. Hillebrands, Appl. Phys. Lett. **94**, 112502 (2009).
[8] K. Perzlmaier, G. Woltersdorf, C.H. Back, Phys. Rev. B **77**, 054425 (2008).
[9] V.E. Demidov, S.O. Demokritov, K. Rott, P. Krzysteczko, G. Reiss, Appl. Phys. Lett. **92**, 232503 (2008).
[10] V.E. Demidov, S.O. Demokritov, B. Hillebrands, M. Laufenberg, P.P. Freitas Appl. Phys. Lett. **85**, 2866 (2004).
[11] J.R. Sandercock, Optics Communications **2**, 73 (1970).
[12] S.O. Demokritov, B. Hillebrands, A.N. Slavin, Phys. Reports **348**, 441 (2001).
[13] A.A. Serga, T. Schneider, B. Hillebrands, S.O. Demokritov, M.P. Kostylev, Appl. Phys. Lett. **89**, 063506 (2006).
[14] B.A. Kalinikos, A.N. Slavin, J. Phys. C: Solid State Phys. **19**, 7013 (1986).
[15] The material parameters used for the calculation of the spin-wave dispersion are:
Saturation magnetization $M_s = 860\,$G
Gyromagnetic ratio: $\gamma = 0.0176\,$GHz/Oe
Exchange stiffness constant: $A = 1.6 \cdot 10^{-6}\,$erg/cm
[16] The effective quantization length was defined by measuring the transverse intensity profile and was found to be 1 µm for the maximum applied magnetic field (570 Oe) and decreased by approximately 200 nm when reducing the magnetic field to 180 Oe. This effect is well understood and is described in detail in [17]. However, these changes in the quantization length cause only minor variations in the dispersion relation and are therefore neglected in the following calculations.
[17] C. Bayer, J.P. Park, H. Wang, M. Yan, C.E. Campbell, P.A. Crowell, Phys. Rev. B. **69**, 134401 (2004).

5.12 Spin-wave quantization in a thermal well

S. Schäfer, H. Schultheiss, and B. Hillebrands

In this report, we address on micromagnetic simulations of two-dimensional spin-wave quantization due to a spatially localized reduction of the saturation magnetization M_s in a $Ni_{81}Fe_{19}$ film. This reduction aims to model the influence of a locally increased temperature on the spin dynamics, and, in analogy to a spin-wave well, we call this a *thermal well*. The quantization of spin-waves due to geometrical or magnetic confinement has been studied extensively in the last decade [1–6]. With the emerging field of *spin-caloritronics* the coupling of heat currents to both, charge and spin currents [7], is addressed. Therefore, the interaction of localized temperature variations with the magnetization dynamics will become of interest, too. Heating of the magnetic system will not only influence the static properties of the material but may also alter the spin dynamics.

In a first numerical approach, we model the effect of a locally increased temperature in a $Ni_{81}Fe_{19}$ film by decreasing the value of M_s locally. Such a decrease of M_s could for example be caused by an intense, focused laser beam. Previous studies of spin-wave eigenmodes in small magnetic ring structures show a clear dependence of the eigenmode frequencies as a function of the applied laser power [1], to which the local temperature is directly proportional. However, in these measurements we only observed the modification of an already existing eigenmode system due to heating. The observed frequency shifts could be calculated taking into account a reduction of M_s. Here we investigate to what extent a local reduction of M_s causes a new type of quantization mechanism for spin waves. We used the freely available OOMMF code [8] for time-resolved micromagnetic simulations of the magnetization dynamics in a square-shaped sample of $2\times2\,\mu m^2$ with a thickness of 10 nm. The cell size of the simulation grid was chosen to be $7.5\times7.5\times10\,nm^3$. In order to exclude numerical artifacts simulations with a cell size of $5\times5\times10\,nm^3$ have been conducted, too, and showed only a small shift in the resulting spin-wave frequencies but nearly identical spatial profiles of the eigenmodes. The *thermal well* as schematically shown in Fig. 1a was modeled by a two-dimensional distribution given by

$$M_S(x,y) = M_{S,0} - M_{well} \cdot e^{-\frac{x^2+y^2}{2\sigma^2}} \quad . \tag{1}$$

with a maximum reduction M_{well} of the initial saturation magnetization $M_{S,0} = 800\,kA/m$ and a lateral width of σ. An external static magnetic field of 50 mT was applied in x-direction. A schematic description of the simulation geometry is given in Fig. 1a. The lowest layer shows the distribution of M_s as modeled by Eq. (1) in an intensity plot exemplarily for a well depth of $250\,kA/m$ and $\sigma = 250\,nm$. Despite the strong spatial variation of the absolute value of M_s its orientation is nearly unaffected in the region of the well. The upper layer of Fig. 1a shows the magnetization distribution as a vector plot and the angle of the magnetization vector with respect to the x-direction. Only a negligible deflection of less than 1.1° from the x-direction, not taking into account the area of the edge domains in the square structure, can be seen, even for a strong reduction of M_s within the *thermal well* by $250\,kA/m$. The continuous variation of M_s across the *thermal well* results in a non-zero divergence $\nabla \cdot M_S$. This creates magnetic volume charges which increase locally the magnitude of the total internal magnetic field similar to a field enhancement in the pole gap of a magnet yoke. The distribution of the total magnetic field along the x- and

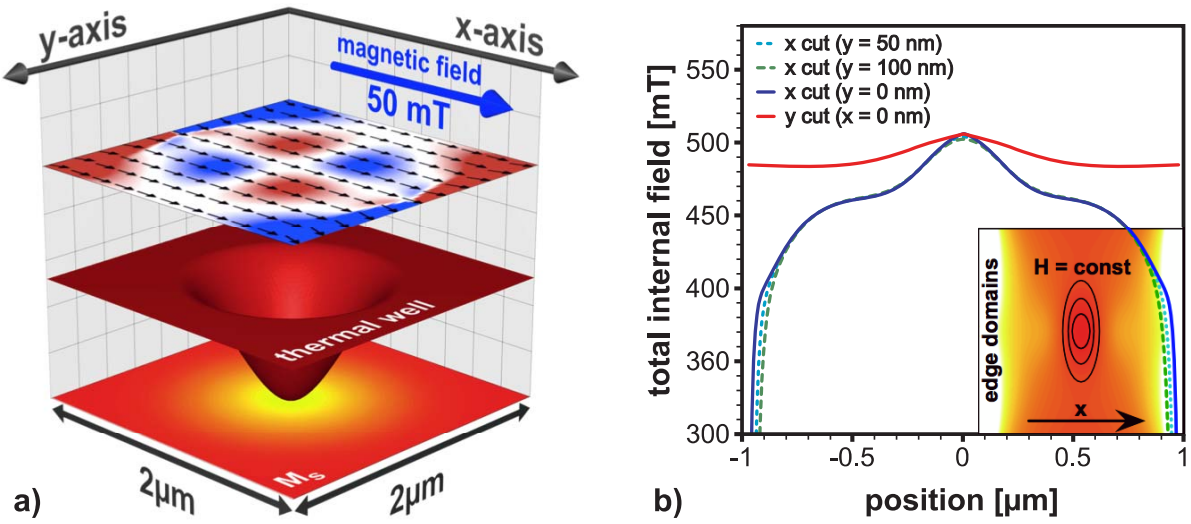

Fig. 1: a) Schematic illustration of a *thermal well* created by a reduction of M_s. The lowest layer displays the distribution of M_s in an intensity plot exemplarily for a well depth of 250 kA/m and a FWHM of 250 nm. The upper layer shows the corresponding ground state of the magnetization under an externally applied field of 50 mT. The orientation of the magnetization is nearly unaffected by the local change of the value for M_s. The color code defines the deflection of the magnetization vector from the *x*-direction with a maximum deflection of 1.1° in the area of the *thermal well* not considering the edge domains of the square. b) Distribution of the total internal magnetic field. Cuts in *x*-direction show the well-known reduction of the internal field at the structure borders due to the edge domains. In the middle of the square the total magnetic field is strengthened due to dipolar fields caused by the gradient of the magnetization in the area of the *thermal well*. Note that the extension of the area where the magnetic field is increased is different for cuts in *y*-direction, resulting in ellipsoidal distribution of the magnetic field magnitude.

y-direction is shown in Fig. 1b. The contour lines in the inset of Fig. 1b for the total magnetic field show an anisotropic ellipsoidal shape with the extension in *y*-direction being larger than that in *x*-direction.

After the calculation of the ground state of the magnetic system, we used an out-of-plane magnetic field pulse with a gaussian time profile. For an efficient excitation of a broad frequency range the length of the field pulse was set to 25 ps at FWHM. To ensure the linear regime of spin waves a low amplitude of 0.1 mT was chosen. The spectra were obtained by a fast Fourier transform of the first 10 ns of the temporal evolution of the magnetic system. Figures 2a and 2b show the spectral intensities along the *y*-direction for a well depth of $M_{well} = 50$ kA/m and $\sigma = 50$ nm and 400 nm. Besides the typical spin-wave eigenmodes of a small magnetic square element in the frequency range from 6 GHz to 9 GHz a strongly localized spin-wave eigenmode can be seen inside the *thermal well* at $x = y = 0$ nm with distinctly higher frequencies and intensities. The spatial confinement of the most intense spin-wave mode inside the *thermal well* is evident from the intensity plots in Fig. 2c-g, which display the spatial distribution of the FFT-intensity at the eigenmode frequency. The confinement area scales with σ^2 and is reduced with increasing the well depth from $M_{well} = 50$ kA/m to 150 kA/m.

The influence of the mode confinement due to a varying value of σ on the frequencies of the well eigenmodes is presented in Fig. 3. A general trend to increasing eigenmode frequencies is observed for *thermal wells* with larger lateral extensions. Besides a variation of the localization region of the spin-waves in the well area a spectral broadening of the dominant excitation is observed for the decreasing σ.

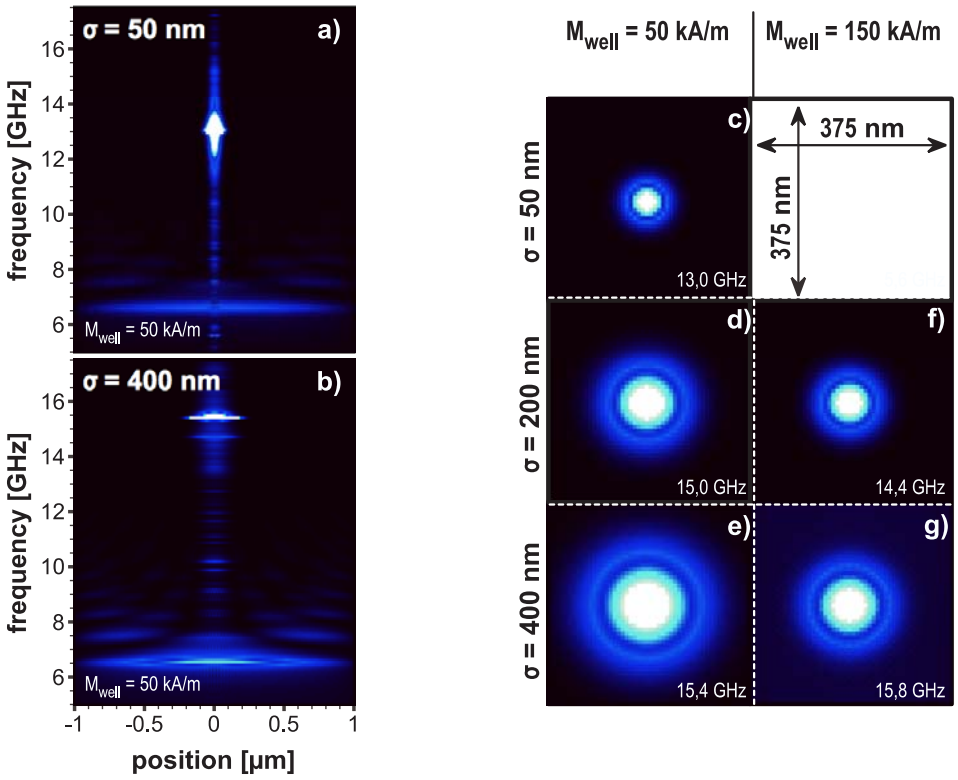

Fig. 2: Spatial profile of the FFT-intensity of the temporal evolution of the magnetization. The spectral intensities for a line scan in y-direction – perpendicular to the external field – are shown for a well width σ of 50 nm a) and 400 nm b), respectively. The depth of the well M_{well} was $50 \cdot 10^3\,\text{A/m}$ in both cases. Next to the spin-wave resonances of the square-shaped element strongly localized spin-wave resonances with high frequencies are present in the middle of the structure. c) - g) Two-dimensional intensity distribution of the spin-wave excitations inside the thermal wells for different values of M_{well} and σ.

In conclusion, we found an intriguing behavior of spin dynamics in a two-dimensional gaussian well of reduced M_S, well worth to devote further, more rigorous numerical as well as experimental studies. The spatial confinement and the eigenmode frequencies are tunable with σ and M_{well} as expected. Despite the fact, that the internal field distribution is anisotropic, the observed modes show a rotational symmetry. Apparently the mode structure is governed by the gaussian distribution of the saturation magnetization and not by the internal magnetic field distribution, as seen in previous studies of spin-wave quantization.

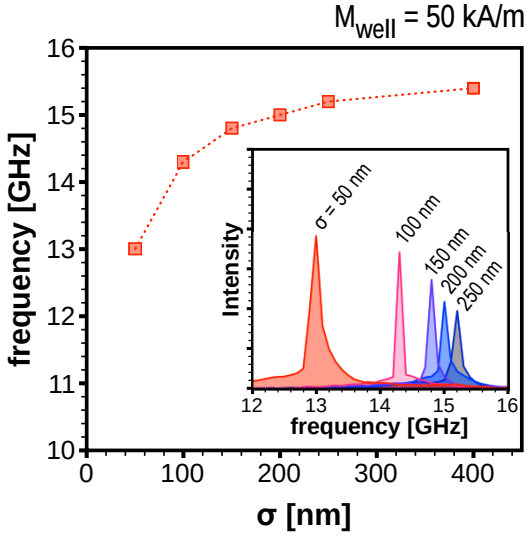

Fig. 3: Extracted mode frequencies for a well depth of $M_{\text{well}} = 50\,\text{kA/m}$ and varying well widths σ. The eigen-frequencies decrease with decreasing σ. The inset displays a part of the corresponding FFT spectra. Besides the change in frequency, an increase in intensity is observed for decreasing well width.

References

[1] H. Schultheiss, S. Schäfer, P. Candeloro , B. Leven, B. Hillebrands, A.N. Slavin, Phys. Rev. Lett. **100**, 047204 (2008).

[2] I. Neudecker, M. Kläui, K. Perzlmaier, D. Backes, L.J. Heyderman, C.A.F. Vaz, J.A.C. Bland, U. Rüdiger, C.H. Back, Phys. Rev. Lett. **96**, 057207 (2006).

[3] G. Gubbiotti, M. Madami, S. Tacchi, G. Carlotti, H. Tanigawa, T. Ono, L. Giovannini, F. Montoncello, F. Nizzoli, Phys. Rev. Lett. **97**, 247203 (2006).

[4] X. Zhu, M. Malac, Z. Liu, H. Qian, V. Metlushko, M. R. Freeman, Appl. Phys. Lett. **86**, 262502 (2005).

[5] J. Jorzick, S.O. Demokritov, B. Hillebrands, M. Bailleul, C. Fermon, K.Y. Guslienko, A.N. Slavin, D.V. Berkov, N.L. Gorn, Phys. Rev. Lett. **88**, 047204 (2002).

[6] F. Giesen, J. Podbielski, T. Korn, M. Steiner, A. van Staa, D. Grundler, Appl. Phys. Lett. **86**, 112510 (2005).

[7] M. Johnson, R.H. Silsbee, Phys. Rev. B **35** 4959 (1987).

[8] M.J. Donahue, D.G. Porter, Report NISTIR 6376, National Institute of Standards and Technology, Gaithersburg, MD (1999).

5.13 Anisotropy of single magnetic elements

T. Sebastian, G. Wolf, A. Conca Parra, and B. Hillebrands

The exploitation of the properties of micro-structured magnetic elements has undergone a steady increase in the last years, not only for basic research but also for industrial applications. These elements consist mainly in magnetic tunneling junctions (MTJs) or giant magnetoresistance (GMR) devices. As potential applications, it is worth to mention the use in magnetic random access memories (MRAM), in magnetic field sensors for positioning in robotics, in field strength or direction sensors or in logic devices. New materials and new geometric concepts are continuously being tested in order to achieve a better performance or to explore new application possibilities. The magnetic properties of these micro-structured elements is one of the crucial aspects in that field. For this reason it is necessary to carefully investigate the mechanisms that are determining these properties.
In a continuous thin film or in relatively large structures (sizes $> 10\,\mu m$), the crystal anisotropy plays a dominant role. This anisotropy is mainly defined by the crystalline structure of the film but it can be manipulated during the film growth, for instance, by growing the film in an applied magnetic field. In this case, the anisotropy is often referred to as "induced anisotropy". With reduced structure size, the shape anisotropy becomes more and more important and it can even dominate the magnetic behavior of the element. The interplay of competing anisotropies plays an important role for the magnetization reversal process. This interplay can result in very complex behavior.

The Magneto-optical Kerr Effect (MOKE) is a well established technique for investigating anisotropies of ferromagnetic materials. Measuring the magnetization reversal as a function of the sample orientation to the applied magnetic field is a common way to determine anisotropies of continuous magnetic thin films or multilayer systems [1, 2]. In the same way the anisotropy of arrays of micro-structured elements has been also determined [3], in this case the signal is averaged

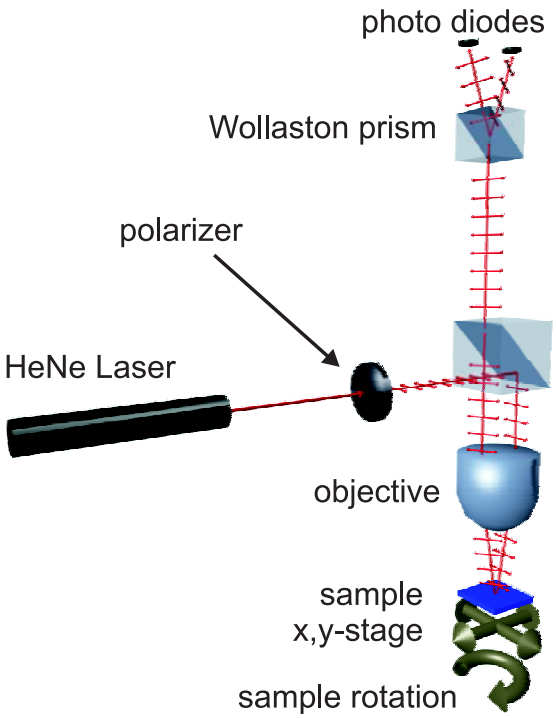

Fig. 1: Scheme of the Kerr microscope. The HeNe Laser operates at 632 nm. The light source illuminates the sample for direct observation with the CCD camera.

over a large number of elements. This approach has the drawback that some effects which are related to small defects in the elements or have an intrinsic distribution in the different elements of the array, are averaged out.

With a micro-focused MOKE system, it is possible to investigate single elements. In the following lines we describe a recently developed micro-focused MOKE system for the study of the magnetic anisotropy of single micro-structured elements. The big advantage here is that we can study single elements, no averaging is needed. Later on, we present and discuss the results of the first measurements.

Figure 1 shows a schematic drawing of the setup. The system combines MOKE microscopy with a rotational system. The laser light of a HeNe laser with a wavelength of 632 nm is s-polarized through a thin film polarizer and guided through a microscope objective. The beam enters the objective perpendicular in an out-of-center position, thus the beam is focused under an angle of incidence of about 30° on the sample. This enables to measure the longitudinal Kerr effect, which is sensitive to the in-plane magnetization component in the plane of incidence. The reflected light is again collected by the objective and then the polarization is analyzed by a Wollaston prism and two photodiodes. The optical spot size has been determined to approximately 1 µm (full width half maximum). The micro structures on the sample are illuminated by a LED light source and observed with a CCD-camera in order to verify the position of the micro-structured element (not shown in Fig. 1). The observation can be done either in a common bright field illumination or dark field illumination. Depending on the sample reflectivity one or the other method can be more convenient. The sample holder is equipped with a high resolution x,y,z stage with an accuracy of around 20 nm, to position the investigated element precisely under the laser spot. The sample stage is placed on top of a rotator to change the sample orientation with respect to the direction of incidence and the applied magnetic field. In general the rotation axis of the stage and the laser focus position do not coincide. For this reason it is necessary to regulate the sample position after each rotation step. The position is corrected via an automated routine using the CCD-camera image to move the sample back in the laser focus. Additionally, this routine enables an active stabilization of the position during the measurement. A pair of magnet-coils provides the magnetic field. It can be set up to a value of 3 kOe and is monitored during the measurement with a calibrated Hall probe. The measurement software, written in National Instruments LabView, controls the data acquisition, magnetic field and sample positioning. With this system we are able to measure

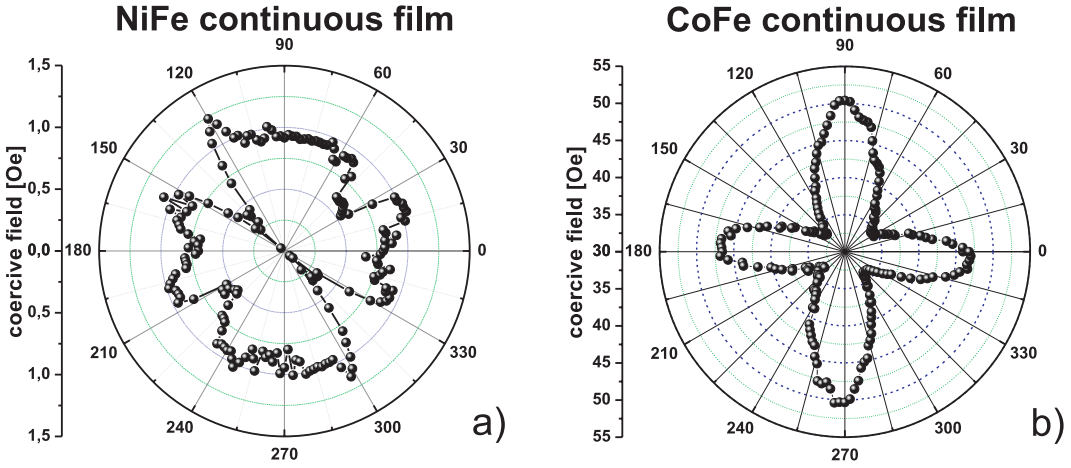

Fig. 2: Coercive field as a function of the sample orientation to the applied magnetic field a) of a continuous NiFe film and b) for a continuous CoFe film. The thickness of the film is in both cases 5 nm.

magnetization reversal as a function of the sample orientation and thus gain information about the anisotropies of a single element.

In the following we present first results on structured NiFe and CoFe elements. First we applied the rotation method to the continuous films of a thickness of 5 nm. From the individual magnetization reversal loops we extract the coercive field and plot it as a function of the sample orientation. The films were deposited in Sensitec, Mainz, using a dc sputtering technique. The materials were grown on glass substrate, thus we assume a polycrystaline structure.

As shown in Fig. 2a, the NiFe film shows a combination of a very weak four-fold anisotropy and a stronger two-fold anisotropy. The coercive field reaches maximum values of about 1 Oe. In contrast to the prior case, the CoFe film (Fig. 2b) shows a strong four-fold anisotropy, although a small uniaxial contribution is present. The coercive field is an order of magnitude larger ($\sim$ 50 Oe). This behavior is expected, since NiFe is known to be a very soft magnetic material whereas CoFe is know to be a rather hard magnetic material. The anisotropies were induced with an external magnetic field during the sputter process.

Afterwards the thin films were structured by means of electron beam lithography and ion etching in the Nano+Bio Center at the TU Kaiserslautern. The first investigated elements are elliptically shaped, with the long axis of the ellipses aligned along the magnetic easy axis of the material.

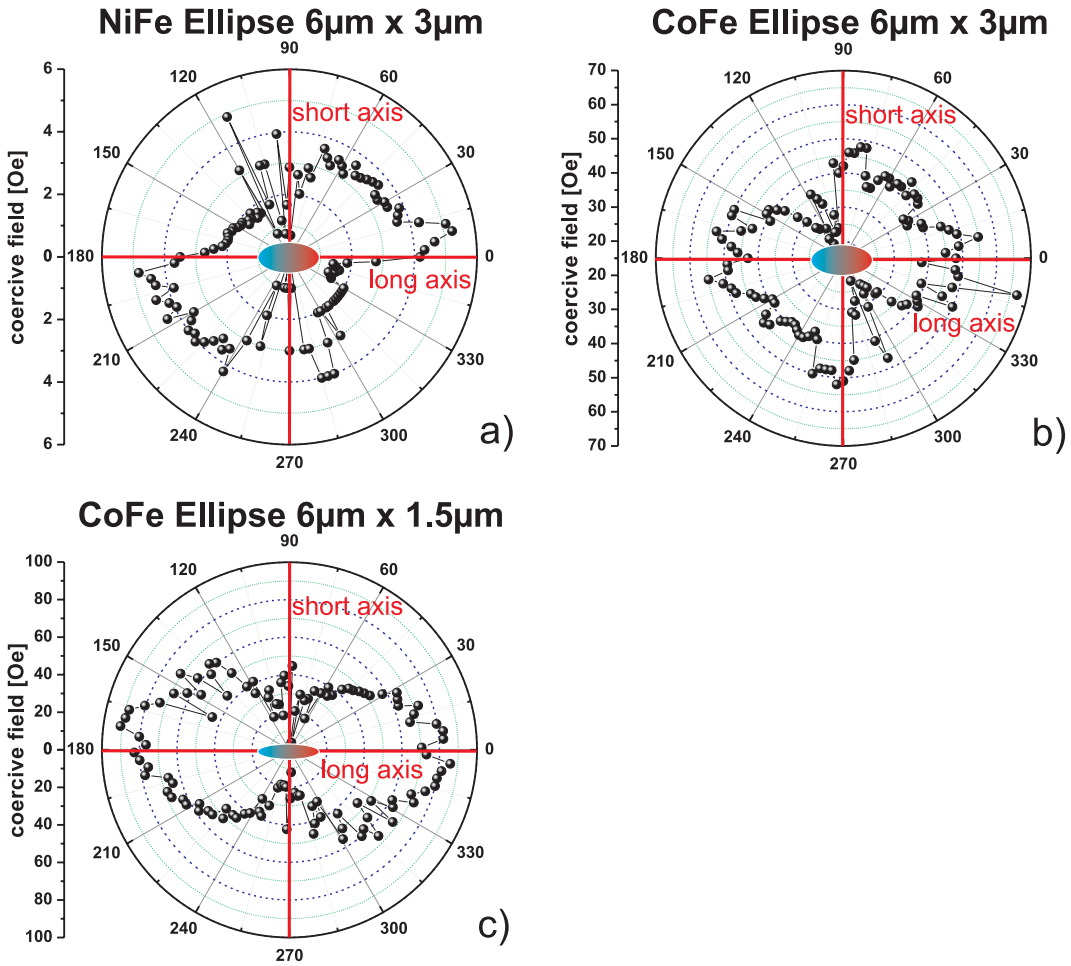

Fig. 3: Coercive field as a function of the sample orientation to the applied field of a) a NiFe ellipse with a size of 6 µm × 3 µm b) a CoFe ellipse of with a size of 6 µm × 3 µm and c) of a structured CoFe ellipse with a size of 6 µm × 1.5 µm. The thickness of the elements is 5 nm.

For NiFe the only investigated element was an ellipse with a size of 6 µm in the long axis and 3 µm in the short axis (aspect ratio 2). In Figure 3a the coercive field as a function of the sample orientation is displayed. One can observe an increase of the coercive field up to 4 Oe compared to the continuous film (Fig. 2a). This can be explained with the acting demagnetizing fields. The shape of the polar plot changes as well compared to the continuous film. A dominant easy axis can be identified, but its direction does not coincide with the long axis of the ellipse. This may be due to a misalignment during the electron beam writing process.

In the case of CoFe the polar plot of an element with the same size (Fig. 3b) shows a more complex angular dependency of the coercive field. The four-fold symmetry of the continuous film is competing with shape anisotropy, which leads to a reduction of the coercive field in the short axis of the ellipse. As well as for NiFe the symmetry axis does not coincide with the axis of the element. The maximum values of the coercive field increased by 4 Oe with respect to the continuous film values, similar to the NiFe element.

The situation changes drastically when the aspect ratio of the element is increased. Figure 3c shows the results for a CoFe element with the size 6 µm$\times$1.5 µm (aspect ratio 4). The strong demagnetizing fields of the geometrical shape lead to a clear two-fould anisotropy. The shape anisotropy is dominating over the anisotropy of the film. The coercive field in the magnetic easy direction increased to 80 Oe, while in the hard axis it decreased to 20 Oe.

It is worth noting, that the point to point variation in the polar plots of the structured elements (for example Fig. 3b in the range between 20° to 340°) is reproducible and not due to measurement accuracy or noise. The origin of these variations is a current topic of investigation and likely connected to the domain structure.

These first results show the effects of competing anisotropies on the total anisotropy of an structured element. The resulting anisotropy determines strongly the behavior of the magnetization during a dynamic reversal process. Further investigations with different sizes and aspect ratios or even different shapes will be carried out.

The authors thank Sensitec in Mainz for film deposition and the Nano+Bio Center at the TU Kaiserslautern for electron beam structuring and the BMBF project Multimag for financial support in this work.

References

[1] J. Hamrle, S. Blomeier, O. Gaier, B. Hillebrands, R. Schäfer, M. Jourdan, J. Appl. Phys. **100**, 103904 (2006).
[2] T. Mewes, H. Nembach, M. Rickart, S.O. Demokritov, J. Fassbender, B. Hillebrands, Phys. Rev. B **65**, 224423 (2002).
[3] I.V. Roshchin, J. Yu, A.D. Kent, G.W. Stupian, M.S. Leung, IEEE Trans. Magn. **37**, 2101 (2001).

D. Heusler Compounds and other Magnetic Films

Heusler compounds are promising as a new class of materials due to their possible use in the novel field of spin-dependent devices, such as non-volatile memory with low energy consumption and new types of magnetic sensors. The interest in Heusler compounds comes from the half-metallic character of their spin-split band structure, as predicted by ab-initio calculations for many compounds of this material class. Half-metallic character means that the material provides metallic behavior for electrons with one spin component (e.g. for electrons with spins oriented 'up'), and insulating behavior for the other spin orientation (e.g. for electrons with spins oriented 'down'). As such, these materials may exhibit a 100 % spin polarization at the Fermi level, which would make them ideal candidates for e.g. spin polarizers or spin detectors. Heusler compounds are materials with the very general composition X_2YZ (with X, Y being a transition metal and Z an element from the III-V groups), where each element X,Y,Z can be chosen from about 10 different elements. Hence, the desired properties of the Heusler compounds can be tuned by adjusting their composition. The most well-known example are Co_2YZ compounds showing a large Curie temperature, a large magnetic moment, and are predicted to provide half-metallic behavior. Furthermore, for a fine tuning, quaternary Heusler compounds can be used, such as $X_2YZ1_{1-x}Z2_x$, where Z1 and Z2 are different chemical elements.

Our group is a part of a larger initiative, the Research Unit 559 funded by the Deutsche Forschungsgemeinschaft, allying several research groups at the Universities of Kaiserslautern, Mainz and Sendai. Within this initiative, our object is to investigate magnetic properties of Heusler compounds, namely the exchange stiffness, the magnetic anisotropy and the magneto-optical properties. In Report 5.14 we provide a comparison of the experimentally found exchange stiffnesses for a variety of Co_2-based Heusler compounds. We have found that for the investigated compounds, the exchange stiffness is a function of the valence electron concentration and the crystallographic order. Report 5.15 discusses the impact the exchange stiffness has on the temperature dependence of the spin dependent transport properties of Co_2-based tunneling magnetic junctions in a thermal magnon limited scenario. We demonstrate that in order to reduce the temperature dependence of the tunnel junctions, a large exchange stiffness of the the FM electrodes is a prerequisite. In Report 5.16, we consider the exchange stiffness, coercivity and magneto-optical Kerr properties of a non-stoichiometric Mn- and Ge-deficient $Co_2Mn_{0.77}Ge_{0.42}$ thin film. Report 5.17 addresses a different issue, tailoring of magnetic properties of an Fe/Cr/Fe multilayer by gentle ion irradiation. This model system is well-known for its strong interlayer exchange coupling between both Fe layers through the Cr spacer layer, being antiferromagnetic for a Cr thickness of 0.7 nm. As a patterning technique, a Ga^+ focused ion beam irradiation is employed, locally destroying the Cr interlayer coupling, thereby creating ferromagnetically coupled patterns in an antiferromagnetic environment. Here, we report on the creation of small lateral structures using Ga^+ ion irradiation, and we study the magnetization state of such elements.

D. Heusler-Legierungen und andere magnetische Schichten

Heusler-Verbindungen sind eine vielversprechende Materialklasse aufgrund ihrer möglichen Verwendung für neuartige, den magnetischen Spin nutzende Bauteile, z.B. für nichtflüchtige Computerspeicher mit geringem Energiebedarf oder für neue magnetischen Sensoren. Aufgrund ihres spin-aufgespaltenen Valenzbands zeigen diese synthetischen anorganischen Verbindungen ein halbmetallisches Verhalten: Für eine der beiden Spinorientierungen (z.B. Spin "up") verhält sich das Material wie ein Metall, für die entgegen gesetzte Orientierung (z.B. Spin "down") wie ein Isolator. Diese Verbindungen können daher eine vollständige Spin Polarisation an der Fermi Kante aufweisen. Damit sind Heusler-Verbindungen ideale Kandidaten für Spinpolarisatoren oder Spindetektoren. Heusler-Verbindungen haben die chemische Struktur X_2YZ, wobei X, Y, Z aus etwa zehn verschiedenen Elementen des Periodensystems gewählt werden können. Die gewünschten Eigenschaften der Heusler-Verbindungen können daher durch die geeignete chemische Zusammensetzung eingestellt werden. Außerdem sind viele Heusler-Verbindungen mit den Anforderungen der modernen Halbleitertechnik kompatibel (z.B. können sie epitaktisch auf Gallium-Arsenid (GaAs) aufgewachsen werden). Weitere Vorteile sind, das sie stabil und relativ einfach zu wachsen sind und oft aus preisgünstigen Materialien bestehen. Die am besten untersuchten Beispiele sind Kobalt basierende Verbindungen (Co_2YZ). Diese zeigen eine hohe Curie-Temperatur, ein großes magnetisches Moment und, wie von ab-initio Rechnungen vorhergesagt, ein halbmetallisches Verhalten.

Als Teil einer Kooperation mit Arbeitsgruppen an den Universitäten Kaiserslautern, Mainz und Sendai haben wir die magnetischen Eigenschaften von Heusler-Verbindungen hinsichtlich der Stärke der Austauschwechselwirkung (Austausch-Steifigkeitskonstante), der magnetischen Anisotropien und der magneto-optischen Eigenschaften untersucht. In Kapitel 5.14 liefern wir einen Vergleich der experimentell gefundenen Austausch-Steifigkeitskonstanten von verschiedenen Co_2 basierenden Heusler-Verbindungen. Wir konnten zeigen, dass für die untersuchten Verbindungen die Austausch-Steifigkeitskonstanten von der Valenzelektronenkonzentration und der kristallographischen Ordnung abhängen. Kapitel 5.15 beschreibt, dass eine große Austausch-Steifigkeitskonstante in der ferromagnetischen Elektrode eine Voraussetzung zur Reduzierung der Temperaturabhängigkeit von magnetischen Tunnelkontakten in Co_2 basierenden Heusler-Verbindungen ist. In Kapitel 5.16 wird die Austausch-Steifigkeitskonstante, das Koerzitivfeld und die magneto-optischen Kerr Eigenschaften von dünnen Filmen aus nicht-stöchiometrischer, Mangan (Mn) und Germanium (Ge) defizienten Zusammensetzung ($Co_2Mn_0.77Ge_{0.42}$) untersucht.

Kapitel 5.17 untersucht keine Heusler-Verbindungen, sondern die Anpassung der magnetischen Eigenschaften von Eisen-Chrom-Schichtsystemen (Fe/Cr/Fe). Dieses Modellsystem ist bekannt für seine starke Austauschkopplung zwischen den beiden Fe Schichten durch die Cr Abstandsschicht hindurch. Es wird antiferromagnetisch bei einer Dicke der Cr-Schicht von 0.7 nm. Als Strukturierungstechnik wurde fokussierter Ga^+ Ionen Beschuss eingesetzt. Durch den Beschuss wird lokal die Cr Zwischenschicht zerstört und so ferromagnetisch gekoppelte Muster in einer antiferromagnetischen Umgebung erzeugt. Wir berichten über die Erzeugung von kleinen lateralen Strukturen und den magnetischen Zustand dieser Elemente.

5.14 Exchange in Heusler compounds

J. Hamrle, S. Trudel, O. Gaier, and B. Hillebrands[1]

Heusler compounds, which for certain compositions are predicted to be half-metallic materials with a 100% spin polarization at the Fermi level, are attracting considerable attention for their use in spintronic devices [1–3]. One of the pressing issues for these materials is the experimentally often observed reduction of the idealized 100% spin polarization at finite temperature [1, 4, 5]. Some of the proposed mechanisms of this phenomenon include inelastic electron-magnon interactions which create states near the Fermi level in the minority spin channel band gap [4, 6], and the decrease in spin polarization due to thermally excited magnons [5]. As such, the investigation of magnons, and hence the exchange interaction, is an important issue in order to understand the strong temperature dependence of the spin polarization in Heusler compounds. The knowledge of the exchange strength is also crucial for micromagnetic simulations and the study of dynamic phenomena.

While there have been several theoretical investigations of exchange in Heusler compounds (see *e.g.* [7–9]), a systematic experimental investigation and comparison of the exchange stiffness in Heusler compounds is still lacking. Our recent efforts towards this goal have concentrated on the use of BLS spectroscopy to determine the exchange stiffnesses of a variety of Co_2-based Heusler compounds with composition Co_2MZ [10–12], where M and Z are a transition metal and a main group element, respectively. In this Report, we present a comparison of experimentally determined exchange stiffness D for Co_2MZ Heusler compounds, in particular revealing the dependence on the number of valence electrons N_v. A tentative qualitative explanation for this trend is provided.

The Heusler compounds are well known to be systematized by the number of valence electrons N_v. Striking examples are the magnetic moment described by the Slater-Pauling rule [13–15] or the Curie temperature T_C [16], which are both generally proportional to N_v. Here we show that the exchange stiffness D in Heusler compounds scales with N_v as well.

We have collected D values of various Co_2-based Heusler compounds. Most of these were determined by us, namely: $Co_2FeSi(L2_1)$ [17], $Co_2MnSi(L2_1)$ [11], $Co_2FeAl(B2)$ and $Co_2Cr_{0.6}Fe_{0.4}Al$ (CCFA)(B2) [12], $Co_2MnAl(B2)$ [18]. Belmeguenai et al. recently reported on the exchange stiffness of Co_2MnGe [19]. However, the crystallographic order of the investigated Co_2MnGe films was not specified. All values of D were determined on Heusler films of typical thickness 30-80 nm using Brillouin light scattering (BLS) spectroscopy at room temperature (RT). The collected values of the exchange (expressed as both exchange stiffness D and exchange constant A), saturation magnetization M_s, bulk lattice constant a and bulk Curie temperature T_C are presented in Table 1.

The dependence of D on N_v is presented in Fig. 1a. The salient features are: (i) A very large change in D is observed between Co_2FeSi (D=7.15 meV nm^2) and CCFA or Co_2MnAl (both $\sim$ 2.0 meV nm^2). Such a large change is associated with the introduction of only 0.5 valence electrons per atom. (ii) The experimental points are segregated into two branches related to B2- and $L2_1$-ordered compounds. In both branches, D is monotonously increasing with increasing N_v. Although the trends appear to be linear, the investigation of further compounds would clarify the

[1] In collaboration with , H. Schneider, E. Vilanova Vidal, G. Jakob, Ch. Herbort, E. Arbelo, M. Jourdan, C. Felser, University of Mainz, Germany and T. Kubota, Y. Sakuraba, M. Oogane, Y. Ando, Tohoku University, Sendai, Japan.

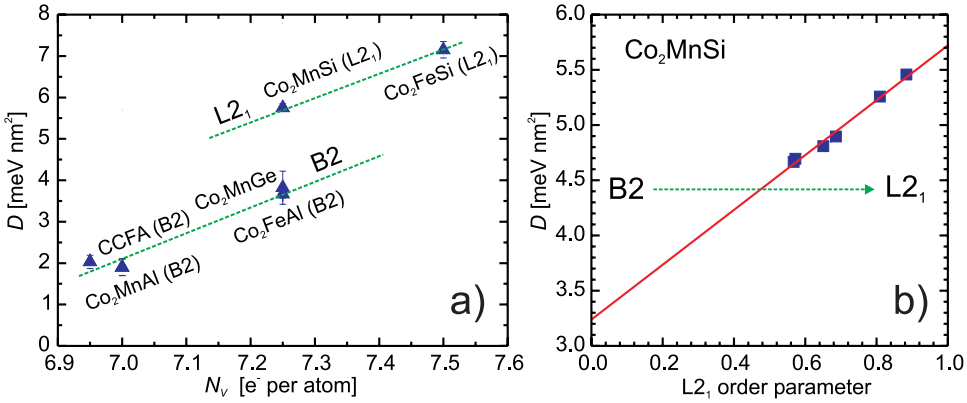

Fig. 1: (full triangles) a) Experimental exchange stiffness D of various Co_2MZ compounds. The straight dashed lines are guide for eye for $L2_1$ and B2 ordered compounds. b) Dependence of D on $L2_1$ order for Co_2MnSi. The straight line shows a linear fit. Data determined from our previous work [10, 11].

exact functional form of this dependence. Even though the ordering of the Co_2MnGe sample was not provided [19], it appears to fall on the B2 branch of the data. (iii) The B2-ordered Co_2MnAl and CCFA have similar N_v's (7 and 6.95 valence electrons per atom) and very similar D values.

The observations (i) – (iii) suggest that D is a function of both N_v and the crystallographic ordering. The latter observation is consistent with our previous study of a series of Co_2MnSi samples with a varying degree of $L2_1$ order [10]. The determined D values are shown in Fig. 1b and linearly increase with increasing degree of $L2_1$ ordering. Extrapolating these data, it can be inferred that the D value for a perfectly B2-ordered Co_2MnSi sample would be reduced to ∼56% (*i.e.* to 3.24 meV nm^2) compared to an $L2_1$ ordered sample of the same composition (5.75 meV nm^2). The extrapolated B2 value of D for Co_2MnSi compares favorably with the experimental D of B2-ordered Co_2FeAl (3.70 meV nm^2) (both Co_2MnSi and Co_2FeAl have $N_v = 7.25\,e^-$/atom). It again suggests D to be a function of N_v and the crystallographic ordering.

One of the most attractive features of Heusler compounds is the possibility to tune their magnetic properties, such as M_S [20, 21], T_C [16], and Fermi level position [22, 23], using the chemical handle provided by N_v. As was discussed above, the exchange stiffness D scales with N_v, for a given atomic ordering. While a quantitative description of this trend is still elusive, here we point out a few features that help to understand the dependence of D on N_v.

In the following, we discuss three possible contributions which may give rise to the observed dependence between the composition (and N_v) and the Heisenberg exchange integral J, which is related to the exchange stiffness D. (1) The increase of N_v adds electrons to the electronic structure. The additional electrons will be primarily found in the t_{2g} orbitals of the transition metal M in the Co_2MZ Heusler compound [24]. Thus, increasing N_v increases the electron density that will participate in exchange. Additionally, *ab-initio* atom-resolved calculations of the density of states in Co_2MZ (M=Mn,Fe; Z=Al,Si) [16, 25, 26] show that for a given non-magnetic element Z, substituting Mn by the more electronegative Fe results in a lowering of the energy of the M-based bands. This results in an improved alignment of the band energy between M and Co atoms, providing a stronger overlap of the electronic functions, and hence a stronger exchange interaction. (2) The difference in electronegativity between Co and Si (−0.02 on the Pauling electronegativity scale) is much less than between Co and Al (0.27). As such, Co-Si bonding is of more covalent character than Co-Al bonding [24]. While this will impact the electronic properties, it is not clear how this affects the exchange interactions. However, this appears to be correlated to an enhanced exchange stiffness. (3) Finally, increasing N_v is related with smaller atomic diameter

Compound	N_v	a^{bulk}	M_S^{bulk}		T_C^{bulk}	thin film	M_S^{bulk}		D^{BLS}	A^{BLS}
		[Å]	[kA/m]	[μ_B/fu]	[K]	order	[kA/m]	[μ_B/fu]	[meV nm^2]	[pJ/m]
Co_2FeSi[1]	7.5	5.640	1230	5.95	1100	$L2_1$	1019(10)	4.93	7.2(2)	31.5(5)
Co_2MnSi[2]	7.25	5.654	1020	4.97	985	$L2_1$	970(8)	4.73	5.8(2)	23.5(1)
Co_2MnGe[3]	7.25	5.743	1040	5.31	905	–	743	3.79	3.8(4)	12.0(1.6)
Co_2FeAl[4]	7.25	5.730	978	4.96	≈1000	B2	1027±10	5.21	3.7(1)	15.5(5)
Co_2MnAl[5]	7	5.756	786	4.04	693	B2	560	2.88	1.9	4.8
CCFA[6]	6.95	5.737	668	3.40	750	B2	520(20)	2.65	2.03(16)	4.8(4)

[1] [17,20]; [2] [11,23,29]; [3] [19,29]; [4] [12,37,38]; [5] [18,29,37]; [6] [12,34]

Table 1: Magnetic and crystallographic properties of the Co_2-based Heusler compounds.

of the constituent elements, leading to a contraction of the unit cell of the Heusler compounds. Hence, a stronger exchange interaction is expected due to the better overlap of orbitals, a result of the closer proximity between the magnetic elements [8,9]. Indeed, larger exchange stiffnesses are generally observed for smaller (bulk) lattice constants a, as is shown in Fig. 2.

It is important to note that the trend between D and N_v is not solely due to N_v, as is the case for the magnetic moment determined by the Slater-Pauling rule [21]. In particular, the same exchange stiffness would not be expected *a priori* for systems having the same N_v, due to generally different electronic structures, and thus exchange integrals. However, we have observed the same exchange for Co_2MnAl and CCFA (having nearly the same $N_v = 7$ and $6.95\,e^-$/atom, respectively). Furthermore, the exchange value of Co_2MnSi extrapolated to the B2-ordered state is comparable to the D values for Co_2FeAl and Co_2MnGe, all having $N_v = 7.25\,e^-$/atom.

Figure 3 compares the exchange stiffness D associated to a variety of Co_2-based Heusler compounds, the ferromagnetic 3d-metals, and Fe-rich bcc-Fe_xCo_{100-x} intermetallic compounds, as a function of N_v. Note that these are experimental data collected from our own work on Co_2-based Heuslers [10–12,18] and various third-party publications [19,20,27–34].

As discussed above, Co_2-based Heusler compounds appear to follow a roughly linear dependence of D on N_v, reaching a maximum value with Co_2FeSi ($D = 7.15 \pm 0.20$ meV nm^2) [17]. The Fe_xCo_{100-x} compounds also provide a roughly linear dependence between D and N_v in the x range of 50–100, reaching a maximum value of $D = 8.0 \pm 0.5$ meV nm^2 with $Fe_{53}Co_{47}$ [27] which is

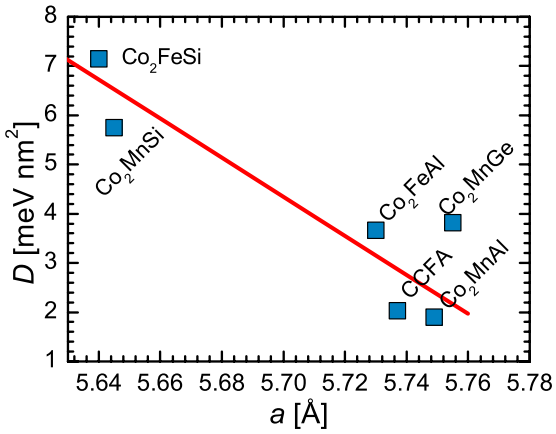

Fig. 2: Exchange stiffness D as a function of the bulk lattice constant a. The solid line is a guide to the eye.

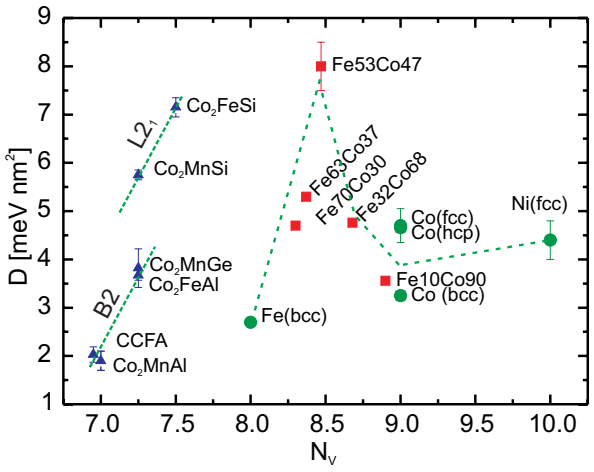

Fig. 3: Exchange stiffness D as a function of number of valence electrons N_v for Co_2MZ Heusler compounds, the ferromagnetic 3d-metals, and bcc-Fe_xCo_{100-x} compounds. Lines are guides to the eye.

(to the best of our knowledge), the largest exchange stiffness ever reported. This shows that the exchange values of the $L2_1$-ordered Co_2MnSi and Co_2FeSi are extraordinarily large. They are larger than D of the pure ferromagnetic 3d metals, and nearly as large as the maximum value of D obtained for the Fe_xCo_{100-x} series. It is also worth noting that higher exchange constants also correlate with higher Curie temperatures, as is shown in Table 1. This is the expected trend for Heusler compounds [16], and is in line with previously reported trends, for example in the bcc-Fe_xCr_{1-x} series [35, 36].

In conclusion, the careful comparison between exchange stiffnesses in various Co_2-based Heusler compounds shows that the exchange stiffness D is a function of the number of valence electrons N_v and the crystallographic order. Hence, the dependence of D on N_v is provided by two different branches for $L2_1$ and B2 order, the latter one being about 60% of the former. In both branches, D increases with increasing N_v, which corresponds to the larger overlap of the wave functions due to (i) an increase of the electron density, (ii) better match of the band energies and (iii) shrinking of the lattice constant.

This project was financially supported by the DFG Research Unit 559 and the Stiftung Rheinland-Pfalz für Innovation (project 961 – 386261/842). S.T. gratefully acknowledges the Alexander von Humboldt foundation for a post-doctoral fellowship. We thank J. Kübler, H.J. Elmers, J. Kudrnovský, and G. Fecher for stimulating discussions.

Appendix: Different expressions of exchange strengths

There are different expressions of exchange strength through the literature, most common of which are the exchange stiffness D, the exchange constant A and the Heisenberg exchange integral J. The exchange stiffness D describes the energy of a magnon (neglecting dipolar interaction) through $E = Dk^2$, where k is wavevector of the magnon. In another words, D expresses the parabolic curvature in the magnon dispersion at the dispersion minima for $k = 0$ (*i.e.* at Γ-point) – see *e.g.* Fig. 7 in [7]. Since D is the experimentally accessible quantity (*e.g.* by means of BLS or neutron diffraction), it is a natural exchange expression bridging theory and experiment. Therefore, this expression will be particularly employed in the following discussion of exchange in Heusler compounds. On the other hand, the exchange constant A describes the exchange energy density $\mathscr{E}$ in case of continuous magnetization model, $\mathscr{E} = A|\nabla \mathbf{m}|^2$. Hence, such an expression is usually used for micromagnetic calculations or the description of domain walls, where a continuous magnetization model is employed. Finally, the Heisenberg Hamiltonian uses the exchange integral J

to describe the energy between pairs of spins, $\mathscr{H}_{\text{Heisenberg}} = \sum J_{ij} \mathbf{S_i} \cdot \mathbf{S_j}$. This exchange expression is particularly used in case of theoretical description of the exchange, as its value is difficult to directly determine experimentally. For relations between various exchange expressions, see *e.g.* [11, 16, 39].

References

[1] Y. Sakuraba, M. Hattori, M. Oogane, Y. Ando, H. Kato, A. Sakuma, T. Miyazaki, H. Kubota, Appl. Phys. Lett. **88**, 192508 (2006).
[2] C. Felser, G. Fecher, B. Balke, Angew. Chem. Int. Ed. **46**, 668 (2007).
[3] K. Inomata, N. Ikeda, N. Tezuka, R. Goto, S. Sugimoto, M. Wojcik, E. Jedryka, Sci. Technol. Adv. Mater. **9**, 014101 (2008).
[4] A. Rajanikanth, Y.K. Takahashi, K. Hono, J. Appl. Phys. **105**, 063916 (2009), and references therein.
[5] R. Shan, H. Sukegawa, W.H. Wang, M. Kodzuka, T. Furubayashi, T. Ohkubo, S. Mitani, K. Inomata, K. Hono, Phys. Rev. Lett. **102**, 246601 (2009).
[6] P.A. Dowben, R. Skomski, J. Appl. Phys. **95**, 7453 (2004).
[7] J. Thoene, S. Chadov, G. Fecher, C. Felser, J. Kübler, J. Phys. D: Appl. Phys. **42**, 084013 (2009).
[8] E. Şaşıoğlu, L.M. Sandratskii, P. Bruno, I. Galanakis, Phys. Rev. B **72**, 184415 (2005).
[9] Y. Kurtulus, R. Dronskowski, G.D. Samolyuk, V.P. Antropov, Phys. Rev. B **71**, 014425 (2005).
[10] O. Gaier, J. Hamrle, S.J. Hermsdoerfer, H. Schultheiß B. Hillebrands, Y. Sakuraba, M. Oogane, Y. Ando, J. Appl. Phys. **103**, 103910 (2008).
[11] J. Hamrle, O. Gaier, S.-G. Min, B. Hillebrands, Y. Sakuraba, Y. Ando, J. Phys. D: Appl. Phys. **42**, 084005 (2009).
[12] O. Gaier, J. Hamrle, S. Trudel, A.C. Parra, B. Hillebrands, C.H.E. Arbelo, M. Jourdan, J. Phys. D: Appl. Phys. **42**, 084004 (2009).
[13] I. Galanakis, P. Mavropoulos, P.H. Dederichs, J. Phys. D: Appl. Phys. **39**, 765 (2006).
[14] G.H. Fecher, H.C. Kandpal, S. Wurmehl, C. Felser, G. Schönhense, J. Appl. Phys. **99**, 08J106 (2006).
[15] J. Kübler, Physica B and C **127**, 257 (1984).
[16] J. Kübler, G.H. Fecher, C. Felser, Phys. Rev. B **76**, 024414 (2007).
[17] O. Gaier, J. Hamrle, S. Trudel, B. Hillebrands, H. Schneider, and G. Jakob, J. Phys. D: Appl. Phys., in press (2009).
[18] T. Kubota, J. Hamrle, Y. Sakuraba, O. Gaier, M. Oogane, A. Sakuma, B. Hillebrands, K. Takanashi, Y. Ando, 2009, submitted.
[19] M. Belmeguenai, F. Zighem, Y. Roussigné, S.-M. Chérif, P. Moch, K. Westerholt, G. Woltersdorf, G. Bayreuther, Phys. Rev. B **79**, 024419 (2009).
[20] S. Wurmehl, G.H. Fecher, H.C. Kandpal, V. Ksenofontov, C. Felser, H.-J. Lin, J. Morais, Phys. Rev. B **72**, 184434 (2005).
[21] I. Galanakis, P.H. Dederichs, N. Papanikolaou, Phys. Rev. B **66**, 174429 (2002).
[22] G. H. Fecher, C. Felser, J. Phys. D: Appl. Phys. **40**, 1582 (2007).
[23] B. Balke, G.H. Fecher, H.C. Kandpal, C. Felser, K. Kobayashi, E. Ikenaga, J.-J. Kim, S. Ueda, Phys. Rev. B **74**, 104405 (2006).
[24] H.C. Kandpal, G.H. Fecher, C. Felser, J. Phys. D: Appl. Phys. **40**, 1507 (2007).
[25] K. Özdoğan, B. Aktaş, I. Galanakis, E. Şaşioğlu, J. Appl. Phys. **101**, 073910 (2007).
[26] K. Özdoğan, E. Şaşioğlu, B. Aktaş, I. Galanakis, Phys. Rev. B **74**, 172412 (2006).
[27] X. Liu, R. Sooryakumar, C.J. Gutierrez, G.A. Prinz, J. Appl. Phys. **75**, 7021 (1994).
[28] X. Liu, M.M. Steiner, R. Sooryakumar, G.A. Prinz, R.F.C. Farrow, G. Harp, Phys. Rev. B **53**, 12166 (1996).
[29] P.J. Webster, J. Phys. Chem. Solids **32**, 1221 (1971).
[30] T. Fukuda, M. Yuge, T. Terai, T. Kakeshita, Journal of Physics: Conference Series **51**, 307 (2006).
[31] S.M. Rezende, M.A. Lucena, A. Azevedo, F.M. de Aguiar, J.R. Fermin, S.S.P. Parkin, J. Appl. Phys. **93**, 7717 (2003).
[32] G. Shirane, V.J. Minkiewicz, R. Nathans, J. Appl. Phys. **39**, 383 (1968).
[33] S. Shallcross, A.E. Kissavos, V. Meded, A.V. Ruban, Phys. Rev. B **72**, 104437 (2005).
[34] T. Block, C. Felser, G. Jakob, J. Ensling, B. Mühling, P. Gütlich, R. Cava, J. Sol. Stat. Chem. **176**, 646 (2003).
[35] A. Katsuki, Brit. J. Appl. Phys. **18**, 199 (1967).
[36] E. Wohlfarth, *Quantum Theory of the Solid State* (Academic Press, New York, 1966), p. 485.
[37] K.H.J. Buschow, P.G. van Engen, R. Jongebreur, J. Magn. Magn. Mater. **38**, 1 (1983).
[38] G. Fecher, 2008, private communication.
[39] M. Pajda, J. Kudrnovský, I. Turek, V. Drchal, P. Bruno, Phys. Rev. B **64**, 174402 (2001).

5.15 Relation between the exchange stiffness and the temperature dependence of tunnelling magnetoresistance

S. Trudel, J. Hamrle, O. Gaier, and B. Hillebrands

In this Report, we briefly discuss the impact the exchange stiffness values have on the temperature dependence of the performance of spintronic devices based on Heusler compounds. We use a simple thermal magnon model as recently discussed for $Co_2FeAl_{0.5}Si_{0.5}/MgAl_2O_x/Co_{50}Fe_{50}$ tunnelling junctions [1].

Despite the high tunnelling magnetoresistance (TMR) ratios observed at low temperature, the strong temperature dependence of the TMR in Co_2MZ/insulator/ferromagnet tunnelling magnetic junctions (TMJs) is one of the greatest challenge towards their wide-spread implementation in devices operating at or above room temperature [2]. This temperature dependence is due to a decay of the spin polarization P, which reduces the tunnelling magnetoresistance (TMR) ratio according to the Jullière model [3] (under the conditions of incoherent tunnelling, such as with an amorphous aluminum oxide barrier),

$$TMR = \frac{2P_1P_2}{1-P_1P_2} \quad , \tag{1}$$

where the subscripts denote the two ferromagnetic electrodes forming the junctions. While several models have been established to explain this temperature dependence, such as the introduction of nonquasiparticles states near the edges of the minority conduction and valence bands [4, 5], and inelastic electron-magnon interactions [6, 7], we will here focus our attention on a simpler and more intuitive model in which the spin polarization's temperature dependence is dominated by thermally populated magnons, wherein the key parameter is the exchange stiffness D.

The saturation magnetization of ferromagnetic materials is well known to decay with increasing temperature, due to the thermal excitation of spin waves, as

$$M_s(T) = M_s(0\,\mathrm{K})(1-\mathscr{B}T^{3/2}) \quad , \tag{2}$$

a behavior known as Bloch's law [8, 9], with

$$\mathscr{B} = 2.612\frac{V_o}{\langle S\rangle}\left(\frac{k_B}{4\pi D}\right)^{3/2} \tag{3}$$

where V_o is the atomic volume ($a^3/16$ for a Heusler compound, a being the lattice parameter), $\langle S\rangle = M_s/(8\mu_B)$ is the average spin per atom (using M_s in μ_B/fu), and k_B is Boltzmann's constant [10]. There is a known proportionality between the saturation magnetization and the spin polarization [11–14], and as such it has been suggested that the spin polarization should also follow a similar behavior to Eq. (2) [1, 15–17], *i.e.*

$$P(T) = P(0\,\mathrm{K})(1-\alpha T^{3/2}) \tag{4}$$

where α is a parameter analogous to $\mathscr{B}$ in Eq. (2). Upon inserting Eq. (4) into Eq. (1), one can model the temperature dependence of the TMR for a given junction. This Bloch-law-like temperature dependence has successfully been applied to the TMR temperature dependence of

Compound	$\mathscr{B}$ $[\times 10^{-6}\mathrm{K}^{-3/2}]$
Co_2FeSi	1.40
Co_2MnSi	2.03
$Co_{50}Fe_{50}$ [1]	3.5
Co_2MnGe	5.00
Co_2FeAl	3.76
Co_2MnAl	18.75
CCFA	18.27

Table 1: Calculated Bloch parameters $\mathscr{B}$ for Co_2-based Heusler compounds.

wide variety of TMJs [15–18], including $Co_2FeAl_{0.5}Si_{0.5}/MgAl_2O_x/Co_{50}Fe_{50}$ TMJs [1]. Here we use this simple model to provide insight into how the exchange constants of various Heusler compound will impact their spin-dependent transport properties.

It is interesting to note that for Heusler compounds, both M_s [19] and D (*c.f.* Fig. 1a) increase with an increasing number of valence electrons. Hence, assuming other sources of spin depolarization are negligible, the temperature dependence should diminish (*i.e.* $\mathscr{B}$ is smaller) for Heusler compounds with high N_v.

Here we have calculated the $\mathscr{B}$ values for the Heusler compounds discussed above (see Table 1), assuming the bulk lattice constants a and saturation magnetizations M_s^{BLS} presented in Table 1 in the previous Section 5.14. By changing the valence electron concentration by less than 10%, $\mathscr{B}$ changes by more than an order of magnitude. Using these $\mathscr{B}$ values, $M_s(T)/M_s(0\,\mathrm{K})$ was calculated, as is shown in Fig. 1a. Only a very weak dependence is observed for Co_2FeSi and Co_2MnSi, where a decrease of $\sim$1% in M_s is observed. For Co_2MnAl and CCFA, this decrease is of around 12% at 350 K.

Before calculating the temperature dependent spin polarizations $P(T)$, it must be realized that the terms $\mathscr{B}$ and α of Eq. (2) and (4) are generally not equal. For example, Shan et al.. report $\mathscr{B} = 4.3\times10^{-6}\,\mathrm{K}^{-3/2}$ and $\alpha = 3.2\times10^{-5}\,\mathrm{K}^{-3/2}$ for $Co_2FeAl_{0.5}Si_{0.5}$ and $\mathscr{B} = 3.5\times10^{-6}\,\mathrm{K}^{-3/2}$ and $\alpha = 2.0\times10^{-5}\,\mathrm{K}^{-3/2}$ for $Co_{50}Fe_{50}$ [1], while Shang and coworkers report $\mathscr{B} = 1.23\times10^{-6}\,\mathrm{K}^{-3/2}$ and $\alpha \approx 3-5\times10^{-5}\,\mathrm{K}^{-3/2}$ for $Ni_{80}Fe_{20}$ [17]. This is mainly due to the fact that the spin polar-

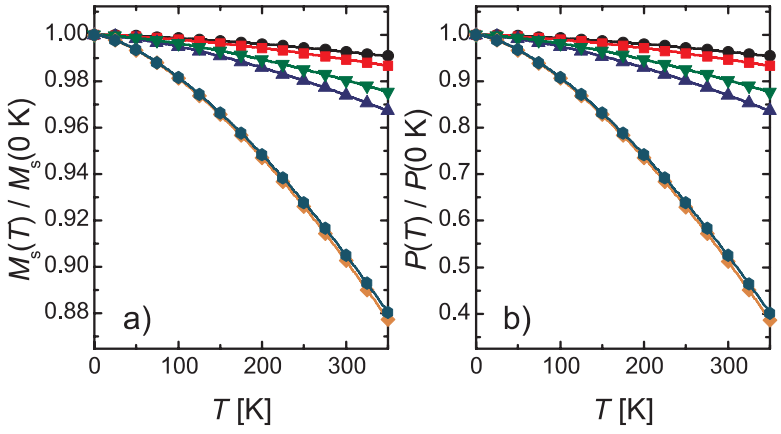

Fig. 1: Temperature dependent magnetization a) and spin polarization b) calculated for Co_2FeSi (●), Co_2MnSi (■), Co_2MnGe (▼), Co_2FeAl (▲), Co_2MnAl (◆), and CCFA (⬢) using Bloch $T^{3/2}$ power laws (see text).

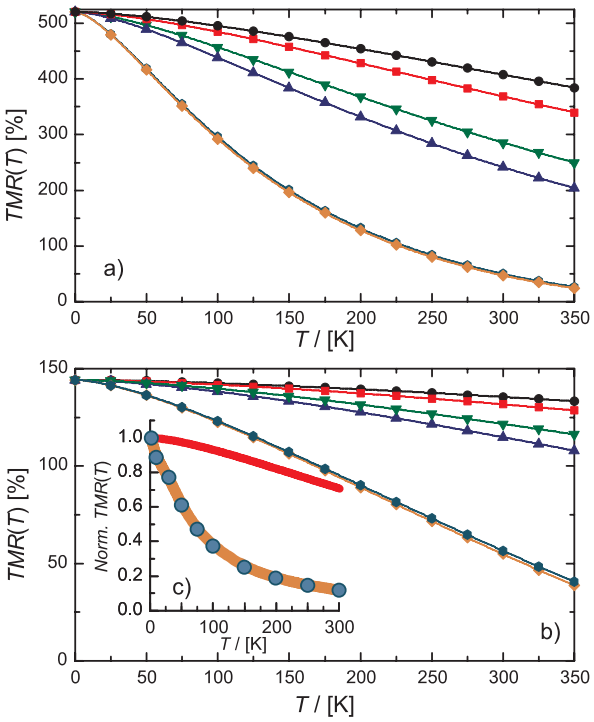

Fig. 2: Calculated TMR as a function of temperature for a) $Co_2MZ/AlO_x/Co_2MZ$ TMJ a), and b) $Co_2MZ/AlO_x/Co_{50}Fe_{50}$ TMJ. For both, $P(0\,K)$ is assumed to be 0.85 for all Co_2MZ, for purpose of comparison. c) Predicted TMR ratio for $Co_2MnSi/AlO_x/Co_2MnSi$ junction (solid line), and experimental results from Sakuraba et al. [2] for a real junction. Both data sets are normalized for comparison. The symbols are assigned as in Fig. 1.

ization is a very surface dependent property, and the surface magnetization decays faster than the bulk magnetization due to surface exchange softening [12, 20]. The spin polarization and surface exchange also strongly depend on the surface cleanliness [21].

For the purpose of comparison without losing generality, in the following we assume $\alpha \approx 5\mathscr{B}$. This allows to calculate $P(T)/P(0\,K)$, shown in Fig. 1b. The dependence naturally looks the same as for the saturation magnetization, with the major difference that the range of changes is now much larger for the Heusler compounds of interest here. As above, Co_2MnSi and Co_2FeSi show only a small decay of the spin polarization, whereas it is reduced by almost 60% for CCFA and Co_2MnAl. Again, it is worth mentioning this drastic change is obtained by a very slight modification of the valence electron concentration.

Using the above calculated temperature-dependent spin polarizations, the TMR ratio for $Co_2MZ/AlO_x/Co_2MZ$ TMJs using the compounds studied here was estimated. These are shown in Fig. 2a. Here an initial spin polarization at 0 K of 0.85 is assumed for all compounds. Note that a spin polarization of 0.85 would be in good agreement with reported device performance based on $Co_2FeAl_{0.5}Si_{0.5}$ [1] and Co_2MnSi [2] electrodes. For devices based on Co_2FeSi and Co_2MnSi, high (>350%) TMR ratios are seen at room temperature. Of relevance to this discussion is not the absolute TMR ratio value, but rather their decay with temperature, and the difference between various compounds.

The same trend is observed for $Co_2MZ/AlO_x/Co_{50}Fe_{50}$ junctions (see Fig.2b), albeit with lower TMR ratios due to the smaller spin polarization of $Co_{50}Fe_{50}$ (0.493 [1]) and less pronounced temperature dependence, as α for $Co_{50}Fe_{50}$ is in general lower than any of the α estimated for Heusler compounds considered here apart from Co_2FeSi and Co_2MnSi. It was observed experimentally by Oogane and coworkers [22] that the TMR ratio of Co_2FeSi-based junctions decreases slower than Co_2MnSi-based TMJs, which is the behavior we qualitatively reproduce here in our simple model.

We have compared our calculated magnetoresistance for a $Co_2MnSi/AlO_x/Co_2MnSi$ junction to the experimental data by Sakuraba and coworkers [2] in the inset of Fig. 2b. As is clear, our simple

model does not take into account all spin depolarization channels relevant to that particular TMJ device, as the TMR ratio is seen to decrease much faster than what we would anticipate if thermal magnons were the only relevant pathway to depolarization. For Co_2MnSi, the Fermi level lies close to the bottom of the minority spin conduction band, and the smearing of the conduction due to nonquasiparticle states could in this case dominate the spin transport properties [4]. However, we believe our estimates do provide an upper limit to what an ideal device can achieve, where tuning of the Fermi level reduces or even nullifies the effect of temperature smearing of the electronic bands, such as was demonstrated recently for $Co_2FeAl_{0.5}Si_{0.5}$ [1].

Using our previously published results on the effect of annealing and increased $L2_1$ ordering in Co_2MnSi thin films [23, 24], we also evaluated the spin polarization for Co_2MnSi with various degrees of $L2_1$ ordering. The reduced spin polarizations $P(300\,\mathrm{K})/P(0\,\mathrm{K})$ changed by approximately 1.2% when comparing the range of data we had ($T_{\mathrm{annealing}}$ changing from 350°C to 500°C). While the spin polarization itself, and thus the absolute TMR ratio, may increase substantially, our analysis points out that the improvement towards reducing the decay of the TMR ratio with increasing annealing temperature is most probably not due to the increase of the *bulk* exchange constants. On the other hand annealing, in particular when done *in-situ*, likely improves the interfaces (structure, cleanliness, etc.), which may improve the *surface* exchange and polarization [21], which is not an effect that would be detected in our BLS experiments, but is of the utmost importance when it comes to spin dependent transport.

While here we have focussed on a model where the spin polarization decays according to a Bloch behavior, the population of thermal magnons is also an important parameter if considering spin-dependent transport when interface states near the Fermi level of the minority (m) spin band are present. In this case, when electrons emitted by the electrode come from the m-spin band, the current is likely due to interface states [25]. Electrons excited to these interface states can tunnel through the barrier to the m-spin band interface states (when the moments of the electrodes are aligned in a parallel fashion) or the majority (M) spin band (when in an antiparallel alignment) of the collector electrode. One channel leading to the population of the interface states is inelastic electron-magnon scattering.

Yamamoto et al. [26] have shown that when interface states are relevant, the TMR ratio (defined as $[R_{\mathrm{AP}} - R_{\mathrm{P}}]/R_{\mathrm{P}}$) decay with increasing T is largely determined by the temperature dependence of the resistance of the junction in the anti-parallel configuration R_{AP}, whereas the resistance in the parallel state R_{P} is comparatively constant. This was attributed to $m \rightarrow M$ spin-flipping electron-magnon scattering populating interface states in the emitter electrode, and $M \rightarrow m$ transitions freeing up the minority interface states in the collector electrode. A higher spin wave exchange stiffness results in fewer thermally excited magnons at a given temperature. As such, electron-magnon scattering is less likely, and the tunnelling current T dependence in the anti-parallel state, which should be absent in a true half-metal, is (at least partially) suppressed. This would then inhibit the decay of the TMR ratio with increasing temperature. At the same time, the magnitude of the TMR ratio would be expected to increase, as R_{AP} would increase with respect to R_{P}. In a qualitative sense, these considerations suggest, as was the case for the Bloch model presented above, that materials with a higher spin wave exchange stiffness should provide TMR ratios that are more stable with respect to temperature.

We finally discuss a major challenge our results clearly highlight towards fully understanding the temperature dependence of the magnetoresistance in Heusler based TMJs. The strong dependence of the spin wave exchange stiffness on composition (*c.f.* Fig. 1a) suggests the decay of the TMR ratio is also a strong function of the stoichiometry of the Heusler compounds used. As is shown in

Fig. 2a, a drastic change is seen upon changing the composition. As such, meaningful comparisons between various devices is only possible if the stoichiometry is well characterized. Currently, much more emphasis is put on atomic ordering, which, as we discussed above, might be arguably far less important *vis-à-vis* temperature dependence of the TMR ratios.

To close this Report, a few guidelines towards achieving better device performance are here outlined. The comparison of our calculated TMRs with experimental results suggest there is still quite a bit of improvement possible if electronic effects (*e.g.* band-smearing, electron-magnon scattering, etc.) can be minimized, for example through Fermi level tuning [1]. When thermal magnon limited, which could be a fundamental limit for the temperature dependence of the spin polarization, Fig. 2 clearly shows that it is important to maximize the value of spin-wave stiffness, to hinder magnon creation, thus preserving spin polarization over a larger temperature range.

In conclusion, we show how the temperature dependence of the spin polarization and TMR ratios of TMJs based on these various Heusler compounds are drastically affected by the exchange constant in a thermal magnon limited scenario. The establishment of such trends is crucial towards devising new materials, as well as providing guidelines towards a better first-principle understanding of the underlying electronic structures of Co_2-based Heusler compounds.

References

[1] R. Shan, H. Sukegawa, W.H. Wang, M. Kodzuka, T. Furubayashi, T. Ohkubo, S. Mitani, K. Inomata, K. Hono, Phys. Rev. Lett. **102**, 246601 (2009).
[2] Y. Sakuraba, M. Hattori, M. Oogane, Y. Ando, H. Kato, A. Sakuma, T. Miyazaki, H. Kubota, Appl. Phys. Lett. **88**, 192508 (2006).
[3] M. Jullière, Phys. Lett. A **54**, 225 (1975).
[4] L. Chioncel, Y. Sakuraba, E. Arrigoni, M.I. Katsnelson, M. Oogane, Y. Ando, T. Miyazaki, E. Burzo, A.I. Lichtenstein, Phys. Rev. Lett. **100**, 086402 (2008).
[5] M.I. Katsnelson, V.Y. Irkhin, L. Chioncel, A.I. Lichtenstein, R.A. de Groot, Rev. Mod. Phys. **80**, 315 (2008).
[6] P.A. Dowben, R. Skomski, J. Appl. Phys. **95**, 7453 (2004).
[7] A. Rajanikanth, Y.K. Takahashi, K. Hono, J. Appl. Phys. **105**, 063916 (2009), and references therein.
[8] C. Kittel, *Introduction to Solid State Physics*, 7th ed. (Wiley, New York, 1996).
[9] A. Aharoni, *Introduction to the Theory of Ferromagnetism*, 2nd ed. (Oxford University Press, Oxford, 2000).
[10] L. Ritchie, G. Xiao, Y. Ji, T.Y. Chen, C.L. Chien, M. Zhang, J. Chen, Z. Liu, G. Wu, X.X. Zhang, Phys. Rev. B **68**, 104430 (2003).
[11] M.B. Stearns, J. Magn. Magn. Mater. **5**, 167 (1977).
[12] D.T. Pierce, R.J. Celotta, J. Unguris, H.C. Siegmann, Phys. Rev. B **26**, 2566 (1982).
[13] D. Mauri, D. Scholl, H.C. Siegmann, E. Kay, Phys. Rev. Lett. **61**, 758 (1988).
[14] R. Meservey, P.M. Tedrow, Phys. Rep. **238**, 173 (1994).
[15] J.S. Moodera, J. Nowak, R.J.M. van de Veerdonk, Phys. Rev. Lett. **80**, 2941 (1998).
[16] S.G. Wang, R.C.C. Ward, G.X. Du, X.F. Han, C. Wang, A. Kohn, Phys. Rev. B **78**, 180411 (2008).
[17] C.H. Shang, J. Nowak, R. Jansen, J.S. Moodera, Phys. Rev. B **58**, R2917 (1998).
[18] T. Hagler, R. Kinder, G. Bayreuther, J. Appl. Phys. **89**, 7570 (2001).
[19] I. Galanakis, P. Mavropoulos, P.H. Dederichs, J. Phys. D: Appl. Phys. **39**, 765 (2006).
[20] J. Mathon, S.B. Ahmad, Phys. Rev. B **37**, 660 (1988).
[21] D. Mauri, D. Scholl, H.C. Siegmann, E. Kay, Phys. Rev. Lett. **61**, 758 (1988).
[22] M. Oogane, M. Shinano, Y. Sakuraba, Y. Ando, J. Appl. Phys. **105**, 07C903 (2009).
[23] O. Gaier, J. Hamrle, S.J. Hermsdoerfer, H. Schultheiß B. Hillebrands, Y. Sakuraba, M. Oogane, Y. Ando, J. Appl. Phys. **103**, 103910 (2008).
[24] J. Hamrle, O. Gaier, S.G. Min, B. Hillebrands, Y. Sakuraba, Y. Ando, J. Phys. D: Appl. Phys. **42**, 084005 (2009).
[25] P. Mavropoulos, M. Ležaić, S. Blügel, Phys. Rev. B **72**, 174428 (2005).
[26] T. Ishikawa, N. Itabashi, T. Taira, K. ichi Matsuda, T. Uemura, M. Yamamoto, Appl. Phys. Lett. **94**, 092503 (2009).

5.16 Magnetic properties of Co_2MnGe

S. Trudel, J. Hamrle, and B. Hillebrands[1]

Co_2MnGe, as many other Co_2-based Heusler compounds, is attracting considerable attention due to its predicted half-metallicity [1–4]. Materials endowed with this property support a particular band structure in which the majority spin channel is metallic, whereas the minority spin channel is semiconducting. In theory, this provides a 100% spin polarization at the Fermi level, which is attractive for spintronic applications. Furthermore, Co_2MnGe boasts a high Curie temperature of 905 K [5], which is a prerequisite for implementation in practical devices.

As a part of our ongoing investigation of the magneto-optical properties of Co_2-based Heusler compounds by means of magneto-optical Kerr effect (MOKE) magnetometry and Brillouin light scattering (BLS) spectroscopy, we here report on the investigation of Mn- and Ge-deficient epitaxial $Co_2Mn_{0.77}Ge_{0.42}$.

The nominal studied sample layer structure was as follows: MgO(001) substrate/MgO buffer (10 nm)/Co_2MnGe (50 nm)/MgO barrier (2 nm)/AlO_x capping layer (1 nm). The Mn- and Ge-deficient Co_2MnGe film was deposited at room temperature by radio frequency magnetron sputtering from a stoichiometric Co_2MnGe target, and subsequently annealed *in-situ* at 500 °C for 15 minutes. Further details of the sample preparation can be found in Refs. [6, 7].

X-ray diffraction measurements show the films grew as epitaxial single-crystal thin films, and the presence of $\{111\}$ reflections indicates the sample is at least partially $L2_1$ ordered [8]. Using inductively-coupled plasma optical emission spectroscopy, the composition of a thin film prepared under the same conditions was determined to be $Co_2Mn_{0.77}Ge_{0.42}$, with an accuracy of 2-3% for each element [6, 7].

Hysteresis loops were measured by MOKE magnetometry. The coercive fields determined for each in-plane sample orientation are compiled in Fig. 1. In this figure, the 0 ° orientation corresponds to the Co_2MnGe $[1\bar{1}0]$ orientation. The angular dependence clearly displays a uniaxial profile, where the easy axis of magnetization (highest coercive field) is oriented about 7 ° past the [110] direction (*i.e.* $\alpha \sim 97\,^\circ$), and the in-plane hard axis is oriented orthogonally to this direction.

The origin of such uniaxial symmetry may be hard to assess. The small step between our measurements also highlights the rather complex shape of the anisotropy, a feature that is often lost when fewer measurements are performed. To explain the experimental value of the saturated magnetization of $6.43\,\mu_B$/f.u., we tentatively estimated the formula unit composition to be $Co_{1.87}[Mn_{0.44}Co_{0.56}Ge_{0.51}][Ge_{0.45}Mn_{0.49}]$, as will be described below, where the first bracket relates to the site occupancy of the Mn site of the ideal $L2_1$ structure, and the second bracket relates to the Ge site occupancy [8]. We speculate that the observed uniaxial symmetry was probably related to the fact that (1) the Ge sites were only half-occupied by Ge atoms in the $Co_2Mn_{0.77}Ge_{0.42}$ film, and (2) a possible preferential distribution of the Ge atoms on the Ge sites is present.

As can be seen in Fig. 2 for measurements at an in-plane orientation of 173 °, the measured Kerr rotation exhibits an asymmetry with respect to an inversion of the magnetic field. The symmetric

[1] In collaboration with T. Taira and M. Yamamoto, Hokkaido University, Japan.

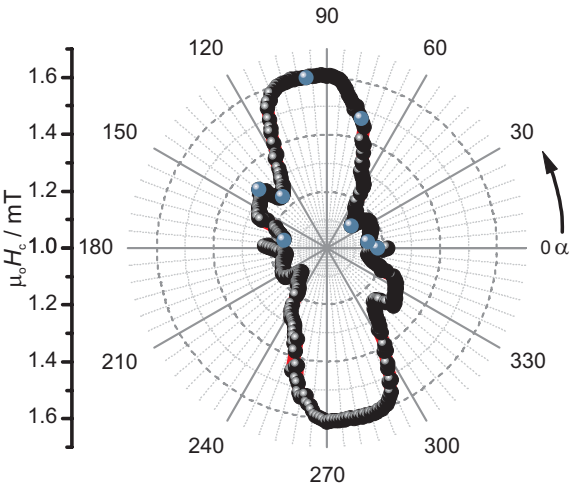

Fig. 1: Angular dependence of the coercive field determined by MOKE magnetometry. The angle α is defined by the applied in-plane magnetic field H and the $[1\bar{1}0]$ direction of the Co_2MnGe film.

and asymmetric components of the Kerr signal ϕ may be arithmetically extracted [9]. The two components are given as

$$LMOKE_{\uparrow\downarrow} \mapsto \phi_{\text{sym}} = \tfrac{1}{2}[\phi(H_{\uparrow\downarrow}) - \phi(-H_{\downarrow\uparrow})] \quad \text{(1-a)}$$

$$QMOKE_{\uparrow\downarrow} \mapsto \phi_{\text{asym}} = \tfrac{1}{2}[\phi(H_{\uparrow\downarrow}) + \phi(-H_{\downarrow\uparrow})] \quad \text{(1-b)}$$

where the arrows indicate the branches of the loop with increasing ($\uparrow$) and decreasing ($\downarrow$) field strengths. As is indicated, the component that is symmetric upon field inversion is attributed to the longitudinal component of the Kerr signal (LMOKE), and the asymmetric component is attributed to a quadratic component (QMOKE). The origin of QMOKE is not yet fully understood, but the contemporary view places its origin in second-order spin-orbit coupling [10]. The microscopic details leading to the observation of QMOKE in a given sample are not yet firmly established, but QMOKE has been observed in a range of cobalt-based Heusler compound thin films such as $Co_xMn_yGe_{1-x-y}$(111) [11, 12], Co_2FeSi(001) [9, 13], Co_2MnSi(001) [14], and (amongst other systems) thin Fe films [15–18].

QMOKE measurements in saturation were made using the instrument described in Section 5.18. Only results obtained at perpendicular incidence are shown. To quantify the amplitude of the QMOKE component, we have carried out the "8 field method" (see Refs. [9, 15, 16] for more details). The eight Kerr rotations ϕ_n measured with $\mathbf{H}$ along the indicated directions are combined according to

$$\phi^{\text{sat}}_{M_L} = \tfrac{1}{2}(\phi_{0^\circ} - \phi_{180^\circ}) \quad \text{(2-a)}$$

$$\phi^{\text{sat}}_{M_L M_T} = \tfrac{1}{4}(\phi_{45^\circ} + \phi_{225^\circ} - \phi_{135^\circ} - \phi_{315^\circ}) \quad \text{(2-b)}$$

$$\phi^{\text{sat}}_{M_L^2 - M_T^2} = \tfrac{1}{4}(\phi_{0^\circ} + \phi_{180^\circ} - \phi_{90^\circ} - \phi_{270^\circ}) \quad \text{(2-c)}$$

and yield the LMOKE signal in saturation $\phi^{\text{sat}}_{M_L}$, as well as two QMOKE signals $\phi^{\text{sat}}_{M_L M_T}$ and $\phi^{\text{sat}}_{M_L^2 - M_T^2}$, where M_L and M_T are the longitudinal and transverse components of the magnetization, respectively. The measured signals are presented in Fig. 2 as a function of in-plane sample orientation. As can be seen, the LMOKE does not depend on the sample direction. The two QMOKE signals exhibit a sinusoidal behavior. Both have the same amplitude of 0.4 mdeg, and the MOKE signal proportional to $M_L M_T$ is vertically offset from zero. The QMOKE amplitude, while clearly observed experimentally due to our sensitive experimental setup, is quite modest. For comparison, amplitudes of ∼2 mdeg and ∼18 mdeg were observed for Co_2MnSi [19] and Co_2FeSi [9] thin films, respectively.

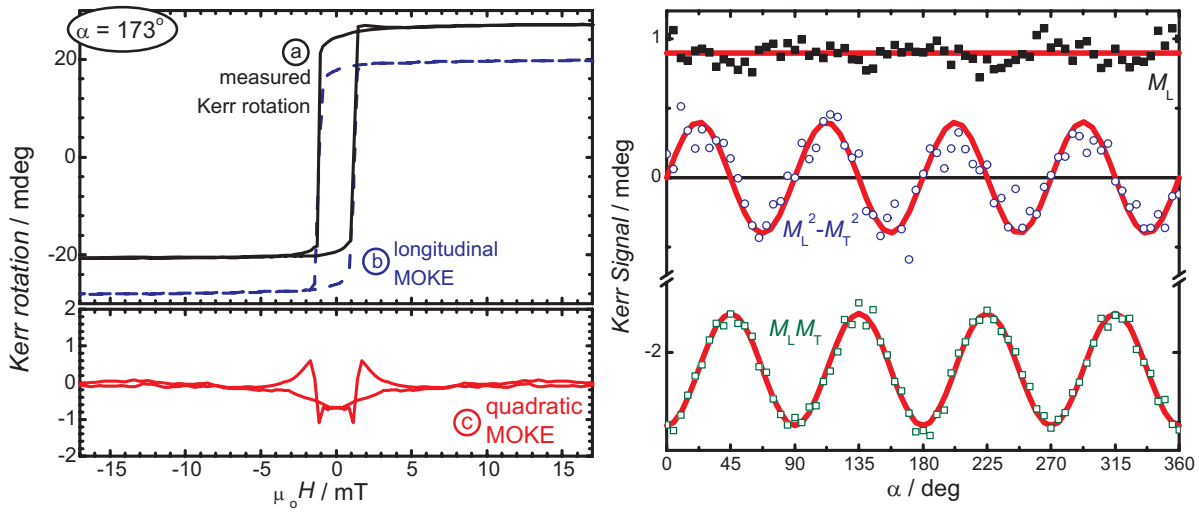

Fig. 2: Left: Loop measured at $\alpha = 173°$ (a), and extracted longitudinal (b) and quadratic (c) MOKE signals. Right: QMOKE measurements, showing longitudinal MOKE signal and the two quadratic terms $M_L^2 - M_T^2$ and $M_L M_T$. Lines are fit to Eq. (3).

The expected Kerr rotation for a cubic material, when taking into account effects up to the second order of the magnetization [16], is the real part of

$$\Phi_s = \mathscr{A} \cdot K M_L + \mathscr{B} \left[\left(-\frac{K^2}{\tilde{n}^2} + 2G_{44} + \frac{\Delta G}{2} \right) M_L M_T - \frac{\Delta G}{2} \cos 4\alpha \cdot M_L M_T - \frac{\Delta G}{4} \sin 4\alpha (M_L^2 - M_T^2) \right] \tag{3}$$

where $\mathscr{A}$ and $\mathscr{B}$ are (complex) optical weighting factors [20], K and G_{ij} are components of the linear and quadratic magneto-optical tensors, respectively, $\Delta G = G_{11} - G_{12} - 2G_{44}$ embodies the magneto-optical anisotropy, and $\tilde{n}$ is the complex refractive index of the material. The salient features of Eq. (3) are recognized in the data shown in Fig. 2. This suggests that the electronic properties of this sample are well described by a cubic environment, as expected for a Heusler compound [9, 13, 14, 19]. The solid lines in Fig. 2 are fits to the various components of Eq. (3).

It is worth to highlight the contrast between the results observed by both MOKE techniques presented above. The rotational scan clearly points to uniaxial symmetry (Fig. 1), and may be due to the atomic ordering of the non-stoichiometric system. On the other hand, the QMOKE measurements in saturation are in full agreement with the magneto-optical tensor for a material with cubic symmetry (Fig. 2). The perturbation leading to the observed complex uniaxial anisotropy of the magnetization reversal processes apparently has little influence on the electronic structure of the material, in particular with respect to the anisotropy of the spin-orbit coupling.

Using Brillouin light scattering spectroscopy, we determined the spin wave exchange stiffness ($413\,\mathrm{meV}^2$) and the saturation magnetization M_s ($6.4\,\mu_B$/f.u.). This was done by measuring the spin wave spectra under various conditions, and fitting the results to a phenomenological model [21].

The effect of point defects on the half-metallicity and saturation magnetization have been studied by means of *ab initio* calculations for $Co_{2\pm x}Mn_{1\mp x}Ge$ [22–25] and $Co_2Mn_{1+x}Ge_{1-x}$ [26]

compounds. While Co_{Mn} antisites, where a Mn site is replaced by a Co atom, destroy half-metallicity [22–24], this important feature is preserved for Mn_{Co} antisites [23–25].

Slater-Pauling behavior relates the magnetic moment m per formula unit (or strictly speaking, per formula unit for a non-stoichiometric material, including vacancies) to the number of valence electrons N_v in the formula unit by the simple relationship [27]

$$m = N_v - 24 \quad . \tag{4}$$

This behavior is expected for half-metallic ferromagnets [27], and predicted to remain valid for $Co_2Mn_{1+x}Ge_{1-x}$ for $-0.2 < x < 0.2$ [26]. It is worth mentioning this feature is also maintained for closely related Mn-rich Co_2MnSi compounds [28]. We will now discuss a possible formula unit composition of the $Co_2Mn_{0.77}Ge_{0.42}$ films by assuming this extended Slater-Pauling behavior is also valid for the Co-rich, Ge-deficient Co_2MnGe samples studied here.

According to the theoretically calculated energies of formation ΔE for various kinds of defects in Co_2MnSi [28], ΔE for a Co_{Mn} antisite (0.75 eV), where a Mn site is replaced by a Co atom, is much smaller than ΔE for a Co_{Si} antisite (2.25 eV), ΔE for a vacancy at a Mn site (1.43 eV), and ΔE for a vacancy at a Si site (3.74 eV). By assuming a similar tendency in ΔE for defects in Co_2MnGe [23], Co_{Mn} antisites are likely to be induced for Mn- and Ge-deficient $Co_2Mn_{0.77}Ge_{0.42}$. Taking into account the theoretical prediction that a vacancy at a Co site has a lower ΔE than a vacancy at a Mn site and a vacancy at a Si site in Co_2MnSi [28], vacancies are more likely to be introduced at Co sites in Co_2MnGe.

Given these considerations, we assume a possible formula unit composition of $Co_{1.87}\square_{0.13}[Mn_{0.44}Co_{0.56}][Ge_{0.51}Mn_{0.49}]$, where the formation of Co_{Mn} antisites, Mn_{Ge} antisites and vacancies at Co sites ($\square$) are assumed. This formula unit composition provides a number of valence electrons per formula unit (N_v) of 30.4. This N_v, assuming the generalized Slater-Pauling rule for the Mn- and Ge-deficient Co_2MnGe films, provides a M_s value of $6.4\,\mu_B$/f.u. (note that the composition of $Co_{1.87}\square_{0.13}[Mn_{0.44}Co_{0.56}][Ge_{0.51}Mn_{0.49}]$ is identical to the description of the film composition of $Co_2Mn_{0.77}Ge_{0.42}$). Again, the first and second brackets describe the site occupancy of the Mn and Ge sites of the ideal $L2_1$ structure, respectively [8]. The saturation magnetization of $6.4\,\mu_B$/f.u. thus calculated reproduces well the experimental M_s value of $6.43\,\mu_B$/f.u. measured by BLS spectroscopy. The good agreement suggests that Co_{Mn} antisites are induced and the Ge sites are partially occupied by Mn atoms.

In summary, we have examined an epitaxial, non-stoichiometric Mn- and Ge-deficient $Co_2Mn_{0.77}Ge_{0.42}$ thin film by means of MOKE magnetometery and Brillouin light scattering spectroscopy. We find the sample exhibits a unidirectional anisotropy. A modest quadratic MOKE with an amplitude of 0.4 mdeg is observed. Using BLS spectroscopy, we find the exchange constant $A = 22.5\,\mathrm{pJ/m}$ (exchange stiffness $D = 413\,\mathrm{meV^2}$), which is twice higher than previously reported for (110)-oriented Co_2MnGe films [29]. Event though the composition is highly off-stoichiometric, the magnetic moment appears to adhere to Slater-Pauling behavior. Furthermore, even though the magnetization reversal shows a clear uniaxial symmetry, the magneto-optical tensor describing this material is not significantly perturbed with respect to the ideal cubic symmetry.

We thank Dr. J. Lösch (IFOS, TU Kaiserslautern) for x-ray measurements. Support by the DFG Research Unit 559, “New Materials with High Spin Polarization” is gratefully acknowledged. S. T. acknowledges support by the Alexander von Humboldt foundation.

References

[1] S. Fujii, S. Sugimura, S. Ishida, S. Asano, J. Phys.: Cond. Matter **2**, 8583 (1990).
[2] S. Ishida, S. Fujii, S. Kashiwagi, S. Asano, J. Phys. Soc. Japan **64**, 2152 (1995).
[3] S. Picozzi, A. Continenza, A. Freeman, Phys. Rev. B **66**, 094421 (2002).
[4] I. Galanakis, P. Mavropoulos, P.H. Dederichs, J. Phys. D: Appl. Phys. **39**, 765 (2006).
[5] P.J. Webster, J. Phys. Chem. Solids **32**, 1221 (1971).
[6] T. Taira, T. Ishikawa, N. Itabashi, K.-i. Matsuda, T. Uemura, M. Yamamoto, Appl. Phys. Lett. **94**, 072510 (2009).
[7] T. Taira, T. Ishikawa, N. Itabashi, K.-i. Matsuda, T. Uemura, M. Yamamoto, J. Phys. D: Appl. Phys. **42**, 084015 (2009).
[8] The $L2_1$ structure for a $M_2M'Z$ full-Heusler compound is described by the $Fm\bar{3}m$ / 225 space group. The M atoms occupy the Wyckoff 8*c* positions $(\frac{1}{4},\frac{1}{4},\frac{1}{4})$, while the M' and Z atoms are located at the 4*a* (0,0,0) and 4*b* $(\frac{1}{2},\frac{1}{2},\frac{1}{2})$ positions, respectively.
[9] J. Hamrle, S. Blomeier, O. Gaier, B. Hillebrands, K. Postava, H. Schneider, G. Jakob, C. Felser, J. Phys. D: Appl. Phys. **40**, 1563 (2007).
[10] R.M. Osgood III, S.D. Bader, B. M. Clemens, R.L. White, H. Matsuyama, J. Magn. Magn. Mater. **182**, 297 (1998).
[11] P.K. Muduli, W.C. Rice, L. He, F. Tsui, J. Magn. Magn. Mater. **320**, L141 (2008).
[12] P.K. Muduli, W.C. Rice, L. He, B.A. Collins, Y.S. Chu, F. Tsui, J. Phys.: Condens. Matter **21**, 296005 (2009).
[13] J. Hamrle, S. Blomeier, O. Gaier, B. Reuscher, A. Brodyanski, M. Kopnarski, K. Postava, H. Schneider, G. Jakob, C. Felser, B. Hillebrands, J. Phys. D: Appl. Phys. **40**, 1558 (2007).
[14] O. Gaier, J. Hamrle, S.J. Hermsdoerfer, H. Schultheiß B. Hillebrands, Y. Sakuraba, M. Oogane, Y. Ando, J. Appl. Phys. **103**, 103910 (2008).
[15] K. Postava, H. Jaffres, A. Schuhl, F.N.V. Dau, M. Goiran, A. . Fert, J. Magn. Magn. Mater. **172**, 199 (1997).
[16] K. Postava, D. Hrabovský, J. Pištora, A.R. Fert, Š. Višovský, T. Yamaguchi, J. Appl. Phys. **91**, 7293 (2002).
[17] S. shen Yan, R. Schreiber, P. Grünberg, R. Schäfer, J. Magn. Magn. Mater. **210**, 309 (2000).
[18] M. Buchmeier, R. Schreiber, D.E. Bürgler, C.M. Schneider, Phys. Rev. B **79**, 064402 (2009).
[19] S. Trudel, G. Wolf, H. Schultheiß, J. Hamrle, B. Hillebrands, J. Phys.: Conf. Series, in print (2009).
[20] At normal incidence, $\mathscr{A} = (\tilde{n}_0^2\varphi)/[\tilde{n}^2(\tilde{n}_0^2-\tilde{n}^2)]$ and $\mathscr{B} = \tilde{n}_0/[\tilde{n}(\tilde{n}_0^2-\tilde{n}^2)]$, where φ is the angle of incidence and $\tilde{n}$ and $\tilde{n}_0$ are the complex refractive indices of the material and the incident medium, respectively.
[21] B. Hillebrands, Phys. Rev. B **41**, 530 (1990).
[22] S. Picozzi, A. Continenza, A.J. Freeman, J. Appl. Phys. **94**, 4723 (2003).
[23] S. Picozzi, A. Continenza, A.J. Freeman, Phys. Rev. B **69**, 094423 (2004).
[24] S. Picozzi A.J. Freeman, J. Phys.: Condens. Matter **19**, 315215 (2007).
[25] K. Özdoğan, I. Galanakis, E. Şaşioğlu, B. Aktaş, Solid State Commun. **142**, 492 (2007).
[26] I. Galanakis, K. Özdoğan, B. Aktaş, E. Şaşioğlu, Appl. Phys. Lett. **89**, 042502 (2006).
[27] I. Galanakis, P.H. Dederichs, N. Papanikolaou, Phys. Rev. B **66**, 174429 (2002).
[28] B. Hülsen, M. Scheffler, P. Kratzer, Phys. Rev. B **79**, 094407 (2009).
[29] M. Belmeguenai, F. Zighem, Y. Roussigné, S.-M. Chérif, P. Moch, K. Westerholt, G. Woltersdorf, G. Bayreuther, Phys. Rev. B **79**, 024419 (2009).

5.17 Antiferromagnetically coupled patterns in a ferromagnetic environment

R. Neb, P.A. Beck, P. Pirro, and B. Hillebrands[1]

Epitaxial Fe/Cr/Fe trilayer systems are well known to exhibit interesting properties depending on the thickness of the Cr interlayer [1]. At a thickness of 0.7 nm, both Fe layers couple antiferromagnetically. It was shown that a focused ion beam (FIB) can destroy the Cr interlayer and thereby locally change the coupling between the Fe layers from antiferromagnetic to ferromagnetic [2]. This can be used to create customized patterns with ferromagnetic behavior. Blomeier et al. have shown that by choosing an appropriate ion dose the topography remains largely unaltered, so that the patterns are embedded into the surrounding antiferromagnetically coupled environment [3].

Several studies about small quadratic embedded elements have revealed that they are influencing each other at distances smaller than 1 µm [4]. Domain wall widths were calculated to be of the order of 500 nm [5]. This is limiting the use of such embedded ferromagnetic elements for data storage, since a minimum distance of about 1 µm must be kept between two elements. Inverse structures, i.e. antiferromagnetically coupled patterns in a ferromagnetic environment, are also promising candidates, if they exhibit fixed states when magnetized or demagnetized (boolean 1 and 0). If made very small in comparison to the surrounding ferromagnetic square, they can be seen as "flaws" so that the behavior of such "flawed" structures can be investigated.

For this purpose, Fe/Cr/Fe (10 nm/0.7 nm/10 nm) trilayer systems were grown by molecular beam epitaxy (MBE) on MgO (100) substrates at 120 °C and covered with a 2.0 nm Cr capping layer to prevent them from corrosion. The patterning was made by FIB with 30 keV Ga^+-ions. A dose of $2.7 \cdot 10^{16}\,\mathrm{Ions/cm^2}$ was chosen to make sure that the topography remained mainly unchanged [3].

In order to create inverse elements, $50 \times 50\,\mu\mathrm{m}^2$ squares were patterned into the antiferromagnetic environment by focused ion beam, leaving an inner square of variable size untouched (see Fig. 1). The size of the outer square is limited by the fact that the writing time of the ion beam

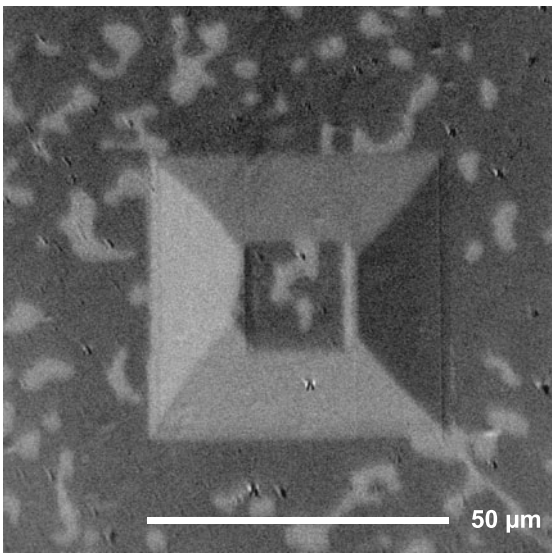

Fig. 1: A magneto-optical Kerr-effect (MOKE) image of a $20 \times 20\,\mu\mathrm{m}^2$ antiferromagnetically coupled square inside a $50 \times 50\,\mu\mathrm{m}^2$ ferromagnetically coupled square in remanence. The outer regions are also antiferromagnetically coupled. A flecked pattern can be seen in the outer region as well as in the inner square. This pattern corresponds to the magnetization of the upper layer, since the lower layer shows a considerably weaker signal when examined by MOKE. The domain diameter is roughly $5 - 10\,\mu\mathrm{m}$. If the inner square exceeds this size, it behaves like the outer region. The ferromagnetic-coupled outer square shows a slightly distorted Landau (or X-shaped) structure. Landau structures are typical for ferromagnetic squares of such a size.

[1] In collaboration with B. Reuscher, M. Kopnarski, Institut für Oberflächen- und Schichtanalytik, TU Kaiserslautern, and S. Pofahl, R. Schäfer, IFW Dresden.

is proportional to the irradiated area. This leads to a finite environment with an eigen-dynamics which is able to influence the inner antiferromagnetic square. It is thereby possible to study the behavior of a ferromagnetic embedded element with an antiferromagnetic "hole" in the middle, as well as studying the inner antiferromagnetic "hole" in comparison with the antiferromagnetic environment.

The sizes of the inner squares ("holes") were chosen to be $20 \times 20\,\mu m^2$, $10 \times 10\,\mu m^2$, $5 \times 5\,\mu m^2$ and $2 \times 2\,\mu m^2$. They were investigated using a magnetic force microscope (MFM) and a magneto-optical Kerr-effect (MOKE) microscope. MOKE pictures of the outer antiferromagnetically coupled regions show a flecked pattern with domain sizes of several µm (see Fig. 1). This pattern cannot be observed via MFM, for the stray field in the antiferromagnetic areas is largely compensated by the opposed direction of magnetization in the two layers. However, since MOKE is more sensitive to the upper layer than to the lower one, a mapping of the upper layer magnetization is possible.

In Figure 1 the pattern can also be observed in the "holes", where it looks identical to the outer region. Squares of $20 \times 20\,\mu m^2$ or larger in remanence therefore behave like "free" antiferromagnetically coupled areas. This result is in consistence with previous studies, since the border wall widths are only of the order of up to 1 µm [5]. No long range influence from the ferromagnetically coupled square can be observed. Also, there is no definite state in such a large square; the domains are distributed randomly throughout the area. If the (inner) square size is reduced down to the typical domain size of the antiferromagnetically coupled areas or lower, MOKE-pictures of the squares show a completely different behavior, as shown in Fig. 2.

In order to understand the domain structure in Fig. 2, we have to recall that a ferromagnetic element of the size of $50 \times 50\,\mu m^2$ exhibits a Landau structure in remanence. This is due to the fact that a flux closure like the Landau pattern minimizes the stray field. A slightly distorted Landau structure can also be seen in Fig. 2. Closing the flux, however, in the center is energetically unfavorable, because this would mean parallel alignment of the magnetization in the two Fe layers also in the center, where they are antiferromagnetically coupled. The system avoids this by creating two flux closure patterns on two opposite sides of the center (see Fig. 3). Please note that MOKE can detect the magnetization in both layers, but the upper layer will give a much stronger signal. Thus the picture we see is mainly the magnetization of the upper layer. The two vortices must therefore

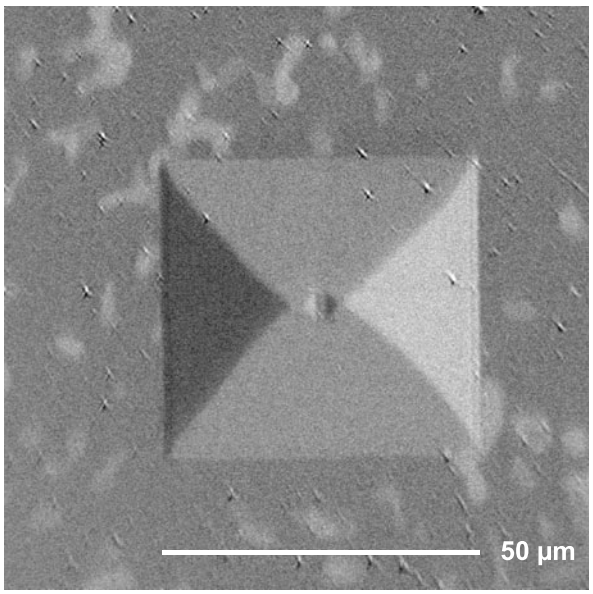

Fig. 2: A MOKE picture of a $5 \times 5\,\mu m^2$ antiferromagnetic-coupled square inside a $50 \times 50\,\mu m^2$ ferromagnetically coupled square in remanence. The ferromagnetically coupled outer square shows a slightly distorted Landau structure like in Fig. 1, but the inner square is dominated by small triangular structures, which can be interpreted as parts of a flux closure pattern.

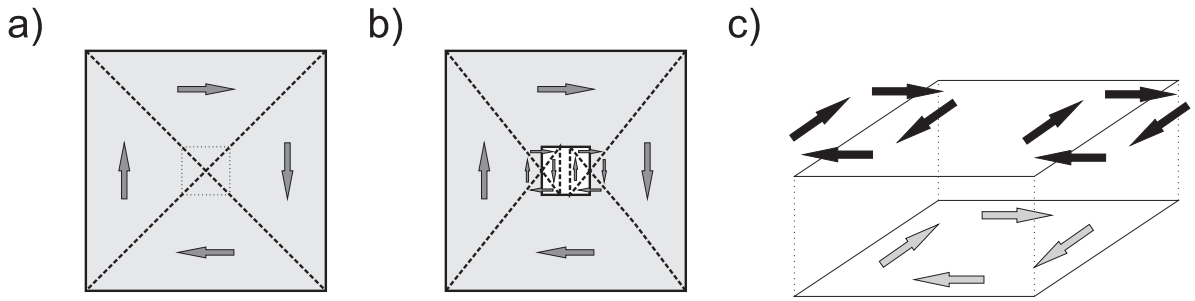

Fig. 3: a) Magnetization of a homogeneous ferromagnetically coupled square. The irradiated area is highlighted in grey, domain walls are represented by dashed lines. A common Landau structure is visible, and both layer magnetizations are parallel everywhere. This is the energetically lowest state with a nearly vanishing stray field. For a square with an antiferromagnetic "hole" (the dotted lines) the situation is different: Now the center is antiferromagnetically coupled, but both layer magnetizations are still aligned parallel, which is highly unfavorable. b) Magnetization of the upper Fe layer in a ferromagnetically coupled square with an antiferromagnetically coupled "hole" in the middle. Flux closure is generated by two vortices to the left and the right of the center. c) Deduced magnetic configuration of the two Fe layers in the region of the "hole", represented as a square. If the lower layer only has one vortex in the middle, this results in an antiferromagnetic coupling inside and a ferromagnetic coupling outside the center.

exist in the upper layer, but they cannot exist both in the lower layer, since this would result in an unfavorable parallel magnetization in the antiferromagnetic region. It is much more likely that there is a single vortex in the center of the lower layer which guarantees the antiferromagnetic alignment of the Fe layers in the middle square.

Earlier MFM measurements have shown striped domains in the inner squares (see Fig. 4). Although it still has to be investigated why the domain walls are parallel to the square edges, and why the distance between these walls and the edges is always about 2 µm (regardless of the dimen-

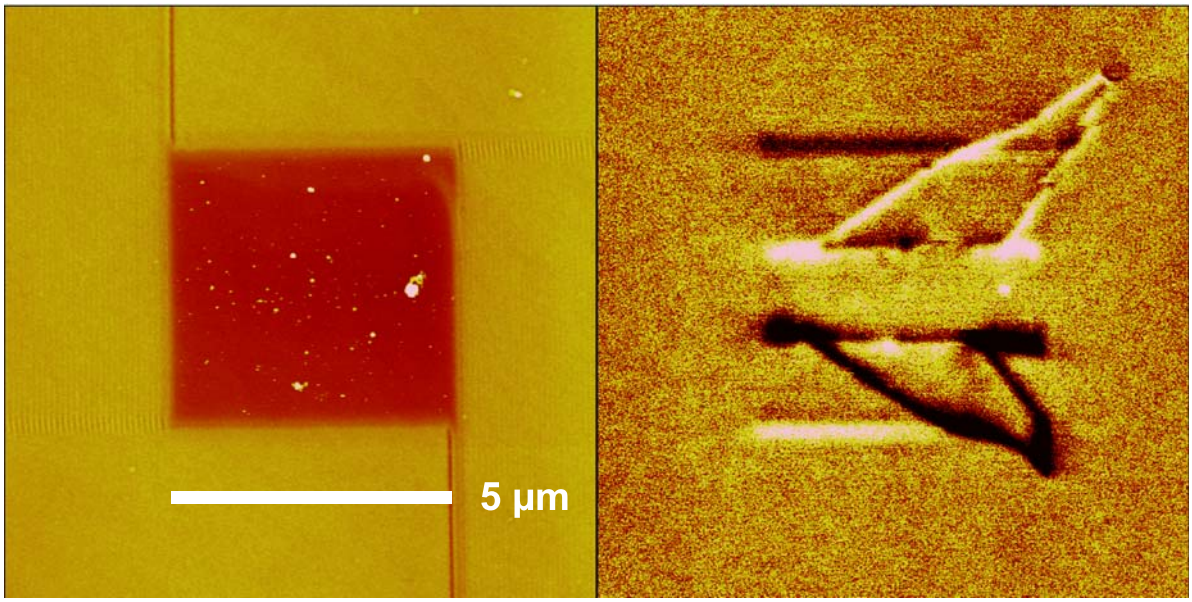

Fig. 4: Left: Atomic force microscopy (AFM) picture of a $5 \times 5\,\mu m^2$ antiferromagnetically coupled square. The lines emerging from the square edges are due to the writing process of the focused ion beam. Right: Related MFM picture. Triangular domains can be seen, which correspond to the vortex structures of Figs. 2 and 3. Their edges inside the antiferromagnetic square are parallel to the corresponding edges of the square, giving rise to a striped structure inside the inner square.

sions of the inner square), their origin seems to come from the ferromagnetically coupled square, as described above. These measurements coincide with our model and the observed MOKE measurements; the triangular structures are not symmetrical like in Fig. 3, but this can be due to a weak outer field or a small remaining magnetization in zero field.

Our results show that an antiferromagnetically coupled small square is primarily dominated by the behavior of the surrounding ferromagnetically coupled element. The observed domains are not "typical" for such antiferromagnetic areas, but a result of the flux closure pattern of the outer square. To prevent such patterns, the ferromagnetically coupled environment must be considerably larger than $50 \times 50\,\mu m^2$.

Support by the Deutsche Forschungsgemeinschaft and Graduiertenkolleg 792 is gratefully acknowledged.

References

[1] P. Grünberg, R. Schreiber, Y. Pang, M.B. Brodsky, H. Sowers, Phys. Rev. Lett. **57**, 2442 (1986).
[2] S.O. Demokritov, C. Bayer, S. Poppe, M. Rickart, J. Fassbender, B. Hillebrands, D.I. Kholin, N.M. Kreines, O.M. Liedke, Phys. Rev. Lett. **90**, 097201 (2003).
[3] S. Blomeier, B. Hillebrands, V.E. Demidov, S.O. Demokritov, B. Reuscher, A. Brodyanski, M. Kopnarski J. Appl. Phys. **98**, 093503 (2005).
[4] S. Blomeier, P. Candeloro, B. Hillebrands, B. Reuscher, A. Brodyanski, M. Kopnarski, Phys. Rev. B **74**, 184405 (2006).
[5] S. Blomeier, B. Hillebrands, B. Reuscher, A. Brodyanski, M. Kopnarski, R.L. Stamps, Phys. Rev. B **77**, 094405 (2008).

E. Applied Research and Technology

A general aim of our group is to span our research efforts between basic science and applied topics. Part of this is the development of new instrumentation and the advancement of the experimental techniques. In this Annual Report three new developments regarding instrumentation are reported.

In Report 5.18 we present our new setup for the simultaneous measurement of the linear and the quadratic Kerr effect. This instrument is now in operation and used to scan Heusler compound samples. In particular it allows for a rapid measurement of magnetic in-plane anisotropies. Report 5.19 addresses the problem of depth sensitivity of optical techniques sensitive to magnetization, such as MOKE magnetometry and Brillouin light scattering spectroscopy. Both techniques are based on the Faraday effect to rotate the polarization and to delay the phase of light. Interference by multiple reflection from the layers in a stack is used to make both techniques sensitive to particular layers. Here the relevant theory is described. In investigations of spin waves, not only their frequency but also their wavevector needs to be determined accurately. Report 5.20 describes a new wavevector-resolving Brillouin light scattering setup where the calibration of the zero wave-vector point is made using an electro-optic modulator.

E. Angewandte Forschung und Technologie

Ein generelles Ziel der Arbeitsgruppe ist es, Forschung in der Breite zwischen erkenntnisorientierter Grundlagenforschung und angewandter Forschung zu betreiben. Ein Teil der Arbeit ist dabei der apparativen Entwicklung und der Fortentwicklung der Experimentiertechniken gewidmet. In diesem Jahresbericht stellen wir drei entsprechende neue Entwicklungen vor.

Im Bericht 5.18 beschreiben wir den neuen apparativen Aufbau zur simultanen Messung des linearen und des quadratischen Kerr-Effektes. Das Instrument ist nun im Einsatz und wird insbesondere zur Untersuchung von Heusler-Verbindungen eingesetzt. Es erlaubt dabei die schnelle Messung von in-plane-Anisotropien. Bericht 5.19 adressiert das Problem der Tiefenselektivität von optischen Techniken zur Untersuchung der Magnetisierung, diese sind MOKE-Magnetometrie und Brillouin-Lichtstreuspektroskopie. Beide Techniken basieren auf dem Faraday-Effekt, welcher die Polarisation des Lichtes dreht und die Phase verzögert. Die Interferenz durch Vielfachreflexion im Schichtstapel kann dazu ausgenutzt werden, beide Techniken besonders sensitiv für bestimmte Schichtlagen zu machen. Hier wird die relevante Theorie vorgestellt. Für Spinwellen sind nicht nur die Messung der Frequenz sondern auch des Wellenvektors von großer Bedeutung. Bericht 5.20 beschreibt einen neuen Aufbau zur Wellenvektorbestimmung mit Hilfe der Brillouin-Lichtstreuung, in dem die Kalibrierung des Nullpunktes des Wellenvektors mit Hilfe eines elektrooptischen Modulators erfolgt.

5.18 QMOKE setup and first results on $Co_2FeAl_{0.5}Si_{0.5}$

G. Wolf, S. Trudel, H. Schultheiss, J. Hamrle, and B. Hillebrands[1]

Magneto-optical Kerr effect (MOKE) magnetometry is often used to characterize magnetic thin films and their properties, including their anisotropy, domain structure and magnetization reversal [1]. In most investigations only the expected linear response is observed, but some materials show a quadratic MOKE (QMOKE), such as NiFe bilayers [2] or epitaxial Fe films [3]. More recently QMOKE has been observed in Co-based Heusler compounds [4,5], which are under strong investigation as they are promising materials to show a high spin polarization at the Fermi level. A phenomenological explanation identifies second-order spin orbit coupling as the microscopic origin of QMOKE. In a more classical approach, the dielectric tensor can be expanded as a function of the magnetization including second order terms [7]. In order to achieve a better understanding of the QMOKE in Heusler materials, it is necessary to find correlations between the QMOKE strength and the electronic and structural properties of these materials.

For this reason, we have built a dual-beam MOKE magnetometer, which is sensitive to both the linear and quadratic MOKE. It enables a simple routine to determine the amplitude of the QMOKE in a sample, without changing the configuration of the instrument between measurements and without further data processing. We are now able to systematically investigate the QMOKE properties of different Heusler materials on a routinely basis.

Generally the linear MOKE consists of two parts. The longitudinal MOKE (LMOKE) is proportional to the magnetization along the direction of the incident light (M_L), and the polar MOKE (PMOKE) is proportional to the magnetization perpendicular to the sample plane (M_P). In magnetic thin films the M_P component is usually very small due to the strong demagnetizing field, which coerces the magnetization within the film plane and the PMOKE can be neglected. The sensitivity of the LMOKE is proportional to the sine of the angle of incidence. The quadratic MOKE arises from terms quadratic in the magnetization components such as $M_L M_T$ and $M_L^2 - M_T^2$, where M_T is the in-plane component perpendicular to the plane of the incident light.

$$\Theta_{\mathrm{Kerr}} = \Theta_L M_L + \Theta_P M_P + \Theta_{LM} M_L M_T + \Theta_{L2\text{-}M2}(M_L^2 - M_T^2) \tag{1}$$

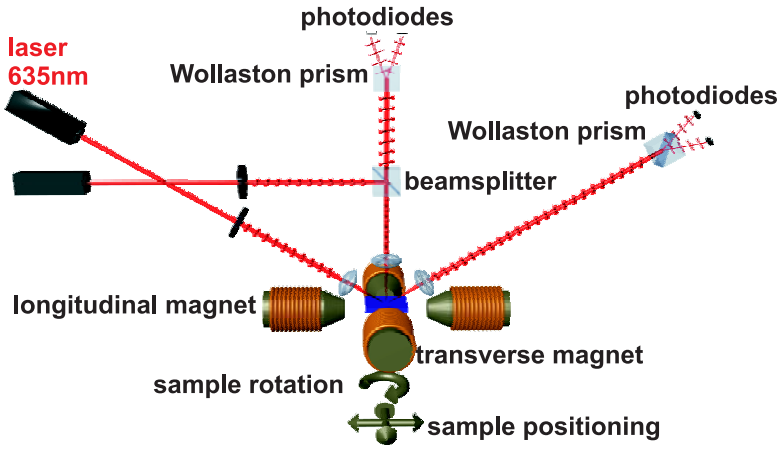

Fig. 1: Schematic drawing of the optical beam path of the dual-beam MOKE magnetometer. Both laser spots are probing the same area in parallel.

[1] In collaboration with the group of K. Inomata, Japan.

Here Θ_{Kerr} is the complex Kerr angle. The magneto-optical factors Θ_L, Θ_P, Θ_{LM} and $\Theta_{L2\text{-}M2}$ determine the proportion of the different contributions to the total signal. They include the dependency on the angle of incidence and on the elements of the dielectric tensor.

The instrument consists of two MOKE magnetometers working in parallel. A scheme is presented in Fig. 1. Both laser spots are focused at the same place, and probe the same area. The light in the first magnetometer impinges the sample at an angle of incidence $\theta = 45^\circ$ and the LMOKE and QMOKE contribution is measured. The second magnetometer works at normal incidence, where the LMOKE contribution vanishes, and only the QMOKE is detected. Probing the sample with both beams in parallel gives us access to the combined LMOKE and QMOKE and the pure QMOKE signal. Both systems are equipped with a low noise diode laser, operating at a wavelength of 635 nm. The light is s-polarized by a thin film polarizer and focused on the sample. The polarization of the reflected light is analyzed by a Wollaston prism. The Wollaston prism divides the beam into two orthogonally polarized beams, which are monitored by a pair of photodiodes. The detector works as an opto-electrical bridge circuit to achieve a better signal-to-noise ratio. The sample is placed in the center of the poles of two orthogonally arranged magnet pairs. With these two magnet pairs it is possible to set a magnetic field in any direction in the sample plane. The field strength is monitored by Hall probes and can be set up to value of 2500 Oe. Thus it is possible to use the "8 field method" to determine the different QMOKE contributions (see below). The sample holder is equipped with a x,y,z-stage and an in-plane rotator, so that the sample position as well as the sample orientation with respect to applied magnetic field and the plane of incidence can

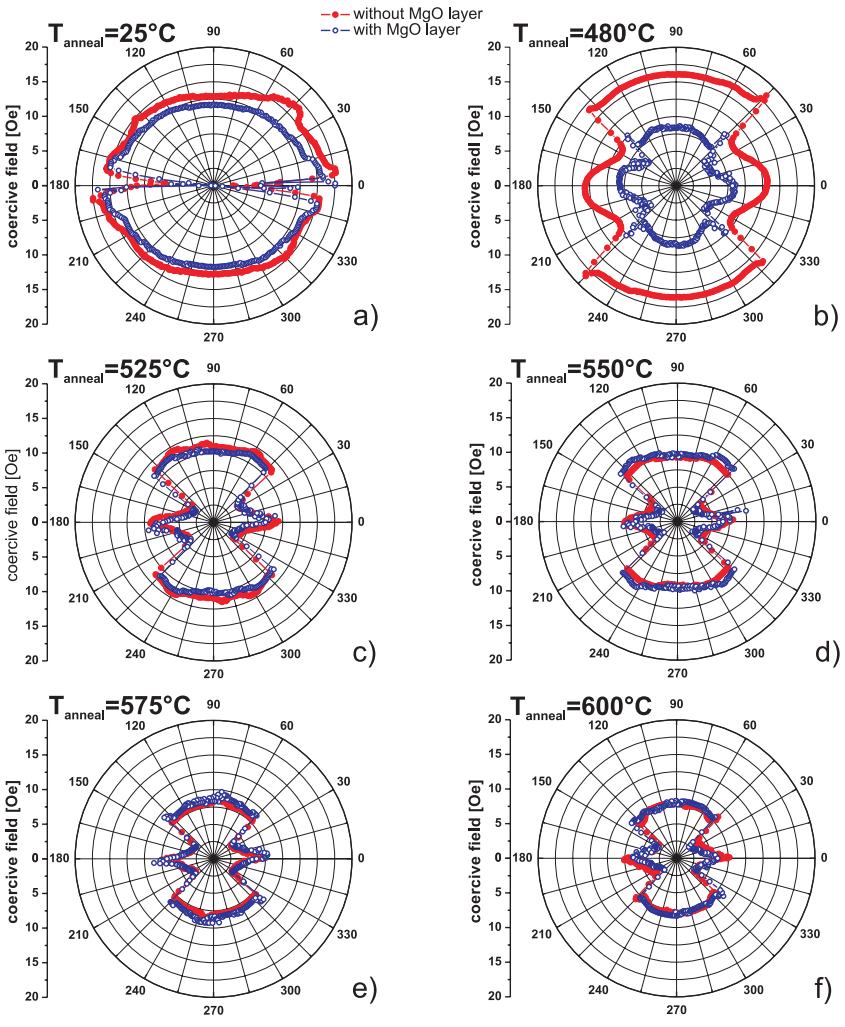

Fig. 2: Coercive field as a function of the sample orientation for both sample series for the different annealing temperatures. The filled circles are the samples without the additional MgO layer and the open circles are those with an additional MgO layer.

be changed. The software, written in National Instruments' LabView, controls the data acquisition of the two detectors, the magnetic fields and the sample positioning. It enables a fully automated measurement routine, for any desired combination of magnetic field, sample positioning and orientation. It is possible to measure longitudinal and transversal magnetization reversal as a function of the sample orientation to determine anisotropies as well as use the already mentioned "8 field method". A more detailed description of the setup can be found in [8].

In the following we present a study on the QMOKE of two series of $Co_2FeAl_{0.5}Si_{0.5}$ (CFAS) samples from the group of K. Inomata, Japan. The first series consists of a MgO (100) substrate with a 20 nm MgO buffer layer, a 30 nm thick $Co_2FeAl_{0.5}Si_{0.5}$ layer, and a 3 nm Al capping layer to prevent oxidation. The second series is also deposited on MgO (100) substrate, with a 20 nm MgO buffer layer, a 30 nm $Co_2FeAl_{0.5}Si_{0.5}$ layer, a 3 nm MgO layer and a 3 nm Al capping layer. The additional MgO layer on top of the Heusler material was deposited to simulate an insulating tunnel barrier, like in a magnetic tunnel junction (MTJ). Every sample of both series was annealed at a different temperature: as-prepared (no annealing), 485 °C, 525 °C, 550 °C, 575 °C and 600 °C.

Using only a conventional longitudinal MOKE geometry and rotating the sample with respect to the applied magnetic field we could determine the magnetic anisotropies of the samples. Figure 2 shows the coercive field as a function of the sample orientation for each sample of both series. For both series we see a transition with the annealing temperature. The as-prepared samples show a two-fold symmetry with one easy and one hard axis. The annealed samples still have a two-fold symmetry, but the shape changes drastically. An additional easy axis appears and consequently two hard axises. This can be understood by a superimposed cubic and uniaxial anisotropy [9]. The coercive field decreases with the annealing temperature. But there is no significant difference between the two series, except the sample annealed at 485 °C where the difference in the coercive field is significantly larger than in all other samples. Figure 3 shows an example of a longitudinal magnetization reversal loop measured for the sample annealed at 600 °C with the additional MgO layer on top, at an orientation of 30 ° between the [110] crystallographic axis of the sample to the applied magnetic field. In Figure 3a the signal detected on the longitudinal MOKE magnetometer can be seen. The reversal loop is not symmetric to the applied magnetic field. The signal contains the LMOKE as well as the QMOKE contribution. A step in the magnetization reversal process can also be observed, which is due to the anisotropies described above. An enlarged view on the

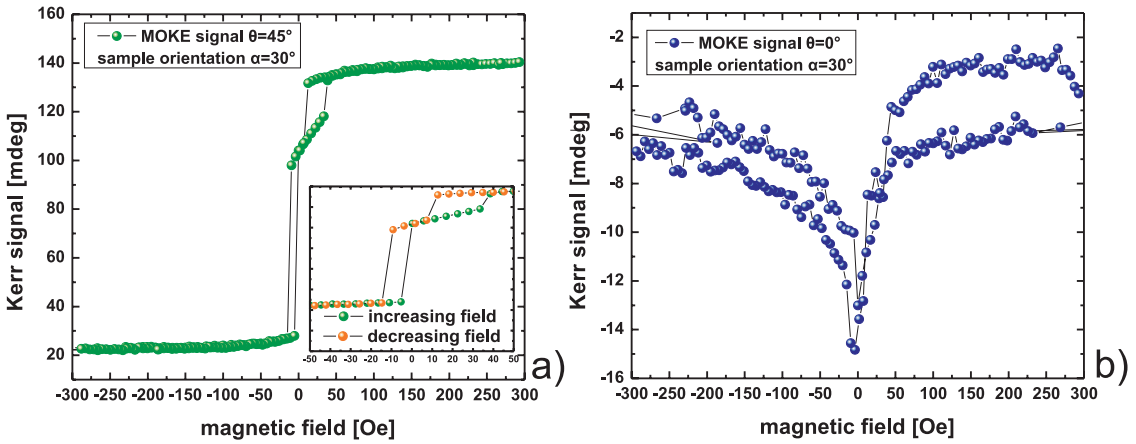

Fig. 3: Magnetization reversal detected a) at an angle of incidence of 45 °. The signal consists of the LMOKE and QMOKE. The inset shows an enlarged view around the coercivity. b) Magnetization reversal detected at an angle of incidence of 0 °. The signal consists only the QMOKE. Both are measured at a sample orientation of 30 °.

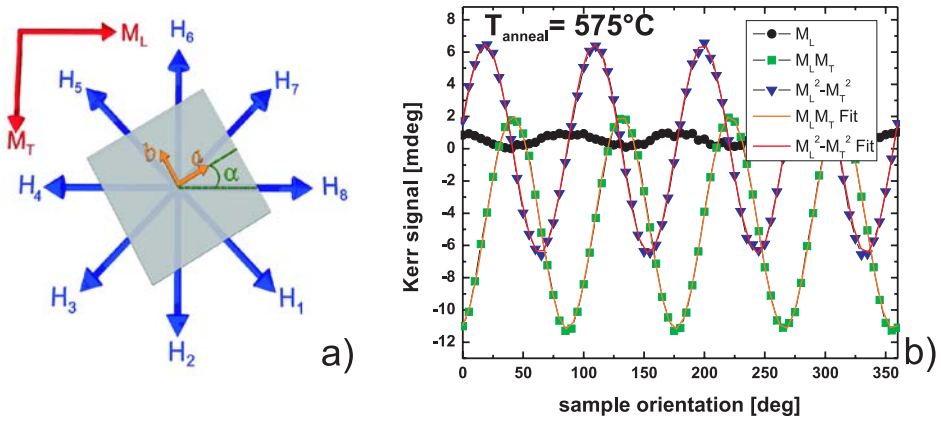

Fig. 4: a) Scheme of the optical geometrie and the applied field directionused for the "8 field method" b) The different QMOKE contributions as a function of the sample orientation for a sample annealed at 575 °C without an additional MgO layer.

signal around the coercive field can be seen in the inset of Fig. 3a. In Figure 3b the signal detected by the detector at normal incidence is shown and it only contains the QMOKE contribution. The QMOKE contribution is about a factor of 10 smaller than the longitudinal one.

For a sample with cubic symmetry the expected Kerr rotation Θ_{Kerr} can be expressed as in Eq. (2) below:

$$\Theta_{\mathrm{Kerr}} = BKM_{\mathrm{L}} + A\left[\left(2G_{44} + \frac{K^2}{\varepsilon}\right)M_L M_T - \frac{\Delta G}{2}\cos(4\alpha)M_{\mathrm{L}}M_{\mathrm{T}}\right] - A\frac{\Delta G}{4}\sin(4\alpha)(M_{\mathrm{L}}^2 - M_{\mathrm{T}}^2) \quad (2)$$

where K is the linear magneto-optical factor, $\Delta G = G_{11} - G_{12} - 2G_{44}$ and the G_{ij} are elements of the quadratic magneto-optic tensor, ε is the complex dielectric constant, α is the angle between the crystal axis of the sample and the plane of incidence and A and B are optical weighting factors. A is proportional to $\sin\theta$, and B to $\cos\theta$. By applying a magnetic field in such a way that one of the quadratic components is vanishing, it is possible to separate the two quadratic contributions. The "8 field method" uses saturation fields in the 0°, 90°, 180° and 270° directions to extract the component proportional to $M_{\mathrm{L}}^2 - M_{\mathrm{T}}^2$, and fields in the directions 45°, 135°, 225° and 315° to extract the component proportional to $M_{\mathrm{L}}M_{\mathrm{T}}$.

Figure 4 shows the different contributions as a function of the sample orientation for the sample annealed at 575 °C without the additional MgO layer. The signal is detected at normal incidence. The solid line is a sine fit, which matches the measured data very well. From the fit, we can determine the amplitude and the offset of the sine function for the different QMOKE contributions. These give information on the ΔG factor in Eq. (2). Applying this method to all the samples of both series we can identify a trend in the QMOKE strength as a function of annealing temperature. Figure 5a shows the results for the series without the additional MgO layer. The amplitudes for the $M_{\mathrm{L}}M_{\mathrm{T}}$ and $M_{\mathrm{L}}^2 - M_{\mathrm{T}}^2$ contribution match very well, as is expected from the model. It seems that both amplitude and offset increase with annealing temperature, except for the sample annealed at 485 °C, where both are significantly higher. This might correspond to the much higher coercive field observed above (see Fig. 2).

For the series with the additional MgO layer the situation is much different (see Fig. 5b). The general trend of increasing QMOKE with the annealing temperature is confirmed. But the absolute values are smaller than in the other series. Obviously the amplitude of the $M_{\mathrm{L}}M_{\mathrm{T}}$ component is

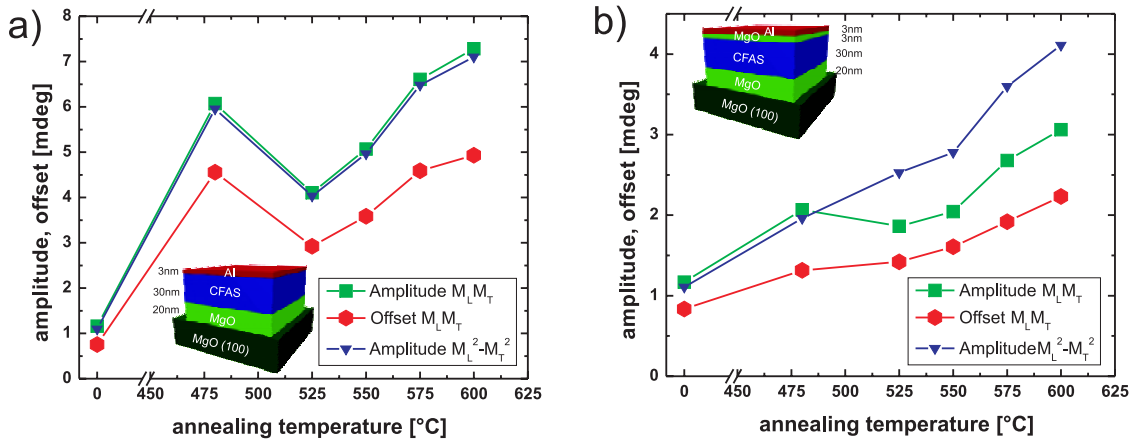

Fig. 5: The different QMOKE contributions as a function of annealing temperature for a) the series without the additional MgO layer and b) with an additional MgO layer.

smaller than the amplitude of the $M_L^2 - M_T^2$ component for the samples annealed above 475 °C. This means that the model for a cubic structure does not fit anymore to these samples, so we can suggest a structural distortion, caused by the additional MgO layer, which would not affect the anisotropy, but the QMOKE.

We have demonstrated that our instrument can give access to magnetic anisotropies and QMOKE of the Heusler alloys. These properties are closely related to the electronic structure of the material. Now we can systematically investigate the correlation between structure and magnetic properties.

The authors would like to thank the group of K. Inomata in Japan for film deposition. Financial support by the DFG Research Unit 559, “New Materials with High Spin Polarization” is gratefully acknowledged. S. Trudel acknowledges support by the Alexander von Humboldt foundation.

References

[1] A. Hubert, R. Schäfer, *Magnetic Domains* Springer, Berlin (1998).
[2] Q.M. Zhong, A.S. Arrott, B. Heinrich, Z. Celinski, J. Magn. Magn. Mater. **104- 107**, 1837 (1992).
[3] S. Yan, R. Schreiber, P. Gr§nberg, R. Schäfer, J. Magn. Magn. Mater. **210**, 309 (2000).
[4] O. Gaier, J. Hamrle, S.J. Hermsdoerfer, H. Schultheiss, B. Hillebrands, Y. Sakuraba, M .Oogane, Y. Ando, J. Appl. Phys. **103**, 103910 (2008).
[5] J. Hamrle, S. Blomeier, O. Gaier, B. Hillebrands, H. Schneider, G. Jakob, K. Postava C. Felser, J. Phys. D **40**, 1563 (2007).
[6] R.M. Osgood III, S.D. Bader, B.Mn. Clemens, R.L. White, H. Matsuyama, J. Magn. Magn. Mater. **182**, 297 (1998).
[7] K.Postava, D. Hrabovsky, J. Pistora, A. R. Fert, S. Visnovsky, T. Yamaguchi, J. Appl. Phys. **91**, 7294 (2002).
[8] S. Trudel, G. Wolf, H. Schultheiss, J. Hamrle, B. Hillebrands, submitted to Rev. Sci. Inst.
[9] F.Y. Yang, C.H. Shang, C.L. Chien, T. Ambrose, J.J. Krebs, G.A. Prinz, V.I. Nikitenko, V.S. Gornakov, A.J. Shapiro, R.D. Shull, Phys. Rev. B **65**, 174410 (2002).

5.19 Depth sensitivity of MOKE and BLS

J. Hamrle and B. Hillebrands[1]

The optical techniques based on magneto-optical effects, such as the magneto-optical Kerr effect (MOKE) and Brillouin light scattering (BLS) spectroscopy, are routinely used for investigations of magnetization dynamics. With this Report, we want to demonstrate how time-resolved MOKE and BLS signals depend on the thickness of the ferromagnetic (FM) layer, as well as on the type of the excited spin-wave mode. Such calculations can serve either for separation of the signal from a single FM layer in case of FM layer stack [4], or for quantitative determination of the energy carried by each spin-wave mode.

As the light travels through the FM layer, the light intensity is attenuated and the phase of the light is delayed. Therefore, sublayers of the FM material situated at different depths of the FM layer provide a different MOKE response to a given magnetization state. Due to the fact that MOKE is a linear effect, the result can be written as a superposition of the single contributions coming from the different depths of the FM layer [1–4]:

$$\Phi_{\mathrm{s/p}}(t) = \int_0^d \left[L_{\mathrm{s/p}}(z) m_L(z) \cos\omega_{\mathrm{sw}} t + P_{\mathrm{s/p}}(z) m_P(z) \sin\omega_{\mathrm{sw}} t \right] \mathrm{d}z \quad , \tag{1}$$

where $\Phi_{\mathrm{s}} = r_{\mathrm{ps}}/r_{\mathrm{ss}}$ and $\Phi_{\mathrm{p}} = -r_{\mathrm{sp}}/r_{\mathrm{pp}}$ are the s- and p- complex Kerr angles, rising from the FM film when the incident light is s and p polarized, respectively. $m_L(z)$ and $m_P(z)$ are the depth profiles of the dynamic magnetizations in the FM film having longitudinal (i.e. in-plane and parallel to the plane of the light incidence) and polar (i.e. out-of-plane) directions, $m_L(z,t) = m_L(z)\cos\omega_{\mathrm{sw}} t$ and $m_P(z,t) = m_P(z)\sin\omega_{\mathrm{sw}} t$, respectively, precessing at spin-wave frequency ω_{sw}. The terms r_{xy}, $x,y = \{\mathrm{s},\mathrm{p}\}$ stand for components of the reflection matrix. $L_{\mathrm{s/p}}(z)$ and $P_{\mathrm{s/p}}(z)$ are the complex MOKE depth sensitivity functions related to longitudinal and polar magnetization, respectively, d being the FM layer thickness.

According to Refs. [9, 11], the BLS intensity $I_{\mathrm{s/p}}^{(\omega_0 \pm \omega_{\mathrm{sw}})}$ of the backscattered light is expressed in a rather similar way as the complex Kerr angle Φ:

$$I_{\mathrm{s/p}}^{(\omega_0 \pm \omega_{\mathrm{sw}})} = I_0 \left| \int_0^d r_{\mathrm{ss/pp}} \left[-L_{\mathrm{s/p}}(z) m_L(z) + P_{\mathrm{s/p}}(z) m_P(z) \right] \mathrm{d}z \right|^2 \quad . \tag{2}$$

Within the depth sensitivity, the main difference between the complex Kerr angle Φ and the BLS intensity $I_{\mathrm{s/p}}^{(\omega_0 \pm \omega_{\mathrm{sw}})}$ is given by the fact that whereas MOKE is a linear combination of $L_{\mathrm{s/p}}$, $P_{\mathrm{s/p}}$ and the magnetization profiles $m_L(z)$, $m_P(z)$, respectively, the BLS intensity is a quadratic form of them.

In case of an optically thick FM layer (i.e. the FM film thickness d is larger than the MOKE probing depth $\Lambda_{\mathrm{MOKE}} = \lambda/(4\pi \mathrm{Im}(N_z))$, λ being vacuum light wavelength and N_z explained just below), $L_{\mathrm{s/p}}(z)$ and $P_{\mathrm{s/p}}(z)$ can be analytically expressed as [2]

$$L_{\mathrm{s/p}}(z) = L_{\mathrm{s/p}}(0) \exp[-4\pi i N_z z/\lambda] \tag{3}$$

$$P_{\mathrm{s/p}}(z) = P_{\mathrm{s/p}}(0) \exp[-4\pi i N_z z/\lambda] \quad , \tag{4}$$

[1] In collaboration with B. Lenk and M. Münzenberg, University of Göttingen, Germany.

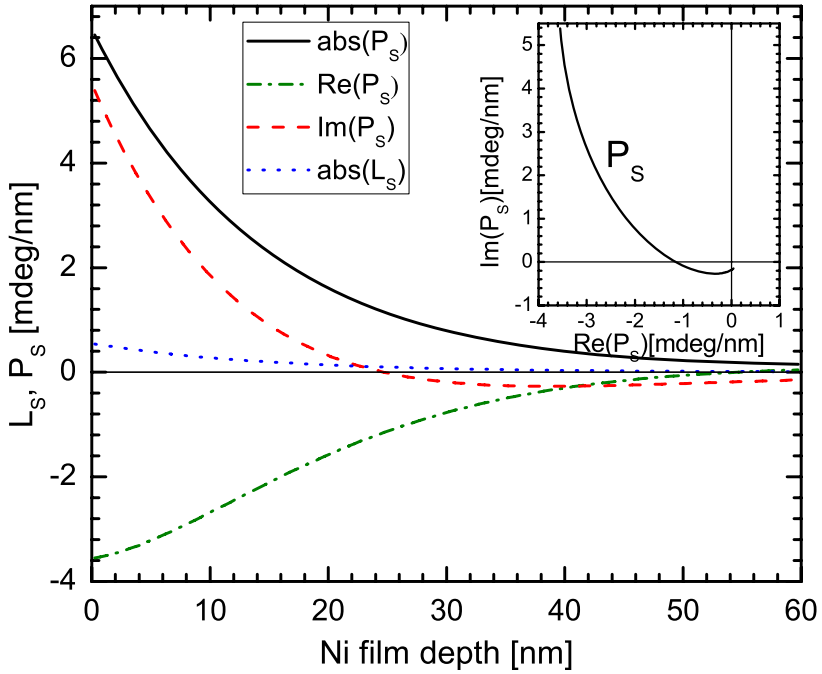

Fig. 1: Depth dependence of the longitudinal and polar depth sensitivity functions L_s, P_s, respectively, inside a 60 nm-thick Ni film. The inset shows the same P_s in the complex plane. Light wavelength and incidence angle are 810 nm and 25°, respectively. See text for details.

where N_z is the normalized wave-vector of light in polar direction, $N_z = \sqrt{(N^{(\mathrm{fm})})^2 - (N^{(\mathrm{air})}\sin\varphi)^2}$, where $N^{(\mathrm{fm})}$ and $N^{(\mathrm{air})}$ are the refractive indices of the FM layer and air, respectively, and φ is the angle of light incidence with respect to the sample normal, respectively. In general, metals provide a large relative optical permeability $\varepsilon_0 \equiv N^2$, N being the refractivity index. Therefore, the angular dependence of N_z can be neglected and hence $N_z \approx N$. For example, for Ni at $\lambda = 810$ nm, N_z is reduced only by 1% when going from $\varphi = 0$ to 90° [4].

An example of $L_{s/p}(z)$ and $P_{s/p}(z)$ is shown in Fig. 1 for the multilayer structure air/Cu(2 nm)/Ni(60 nm)/Cu(5 nm)/Si. The calculations were done using a 4×4 matrix formalism [5], for a light wavelength of $\lambda = 810$ nm and an incidence angle of $\varphi = 25°$. The diagonal permittivity of the used materials are $\varepsilon_0^{(\mathrm{Cu})} = -26.37 + 2.61i$, $\varepsilon_0^{(\mathrm{Ni})} = -13.24 + 22.07i$, $\varepsilon_0^{(\mathrm{Si})} = 13.58 + 0.04i$, the off-diagonal permittivity of Ni being $\varepsilon_{\mathrm{off}}^{(\mathrm{Ni})} = 0.217 - 0.091i$ [12]. As the difference between L_s and L_p (P_s and P_p) is only the starting amplitude and phase of $L_{s/p}(0)$ and $P_{s/p}(0)$, the calculations in Fig. 1 are presented only for L_s and P_s, demonstrating: (i) the polar MOKE (PMOKE) amplitude is about 12× larger than the longitudinal MOKE (LMOKE) amplitude. The reason is that, in general, PMOKE is stronger than LMOKE, followed by relatively small incidence angle used in our example, $\varphi = 25°$. However, even when the maximum LMOKE at an incidence angle of about 60-70° is used, the LMOKE amplitude would increase by a factor of 2, still much smaller than PMOKE. (ii) the analytical expressions of $L_{s/p}$, $P_{s/p}$ (Eq. (3-4)) show that their depth dependence is described by an exponencial decay accompanied by a linear phase shift. Hence, with increasing depth, $|P_{s/p}(z)|$ and $|L_{s/p}(z)|$ exponentially decay, whereas their real and imaginary parts (corresponding to Kerr rotation and Kerr ellipticity) can pass zero or change sign due to the increasing phase shift. This provides a possibility to cancel the MOKE or BLS signal from an arbitrary FM layer in case of a stack of the FM layers [4]. (iii) As follows from Eq. (3-4) and demonstrated in Fig. 1 the MOKE probing length is $\Lambda_{\mathrm{MOKE}} = \lambda/(4\pi\mathrm{Im}(N_z))$, being 14.5 nm for Ni at $\lambda = 810$ nm. Comparing to the penetration depth of light in the same material, $\Lambda_{\mathrm{pen}} = \lambda/(2\pi\mathrm{Im}(N_z))$, the prob-

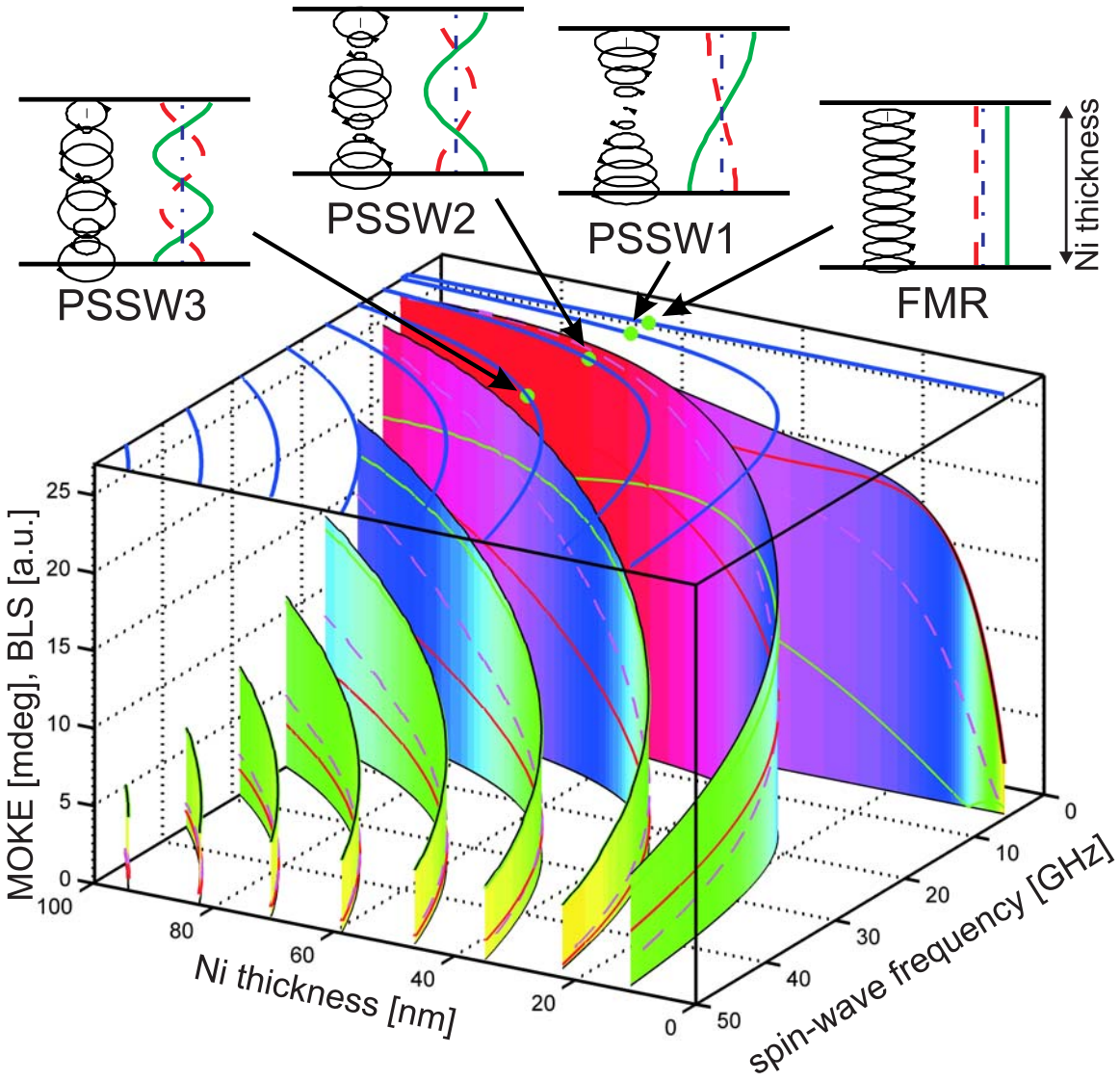

Fig. 2: Calculated MOKE signals ($|\Phi|$: height of the surface plot, Kerr rotation $\theta = \mathrm{Re}(\Phi)$, Kerr ellipticity $\varepsilon = \mathrm{Im}(\Phi)$: solid lines) and the scaled BLS signal (dashed line) as a function of the Ni thickness and the related spin-wave frequencies. For calculation parameters, see text. The top plane of the 3D graph presents the spin-wave dispersion of the Ni film (solid lines). The profiles of the spin-wave amplitudes through a 60-nm-thick Ni film are sketched above the 3D graph for four examples of the spin-wave modes, one FMR and three PSSW modes. Within those profiles, the left part is showing the trajectory of the end-point of the magnetization vector. The right part shows the amplitudes of the dynamic in-plane (solid line) and out-of-plane (dashed line) magnetizations.

ing depth of MOKE Λ_{MOKE} is two times smaller, as the light has to travel to a given sublayer and back. (iv) $L_{\mathrm{s/p}}(z)$, $P_{\mathrm{s/p}}(z)$ are nearly independent on the incidence angle as their angular dependence is governed solely by N_z, whose angular dependence is very weak.

To obtain the MOKE response of the given magnetization state (such as spin waves), the profile of the dynamic magnetizations $m_L(z)$, $m_P(z)$ through the FM film must be calculated first [6–9]. Then, the complex Kerr angle Φ and the BLS intensity $I^{(\omega_0 \pm \omega_{\mathrm{sw}})}$ coming from a given spin-wave mode can be expressed using Eq. (1) and (2), respectively.

As a showcase, we demonstrate the MOKE response to the spinwaves inside the Ni film (Fig. 2). The used magnetic properties of Ni are: saturation magnetization $M_S = 460\,\mathrm{kA/m}$, exchange con-

stant $A = 4.7\,\mathrm{pJ/m}$ (i.e. exchange stiffness $D = 2.46\,\mathrm{meV\,nm^2}$), Landé g-factor $g = 2.1$, out-of-plane anisotropy $K_z = 20\,\mathrm{kJ/m^3}$. The in-plane spin-wave wavevector is $q_{\parallel} = 0$, and the external magnetic field $\mu_0 H = 50\,\mathrm{mT}$ is applied parallel to the plane of incidence. The optical parameters of the Ni film as well as its optical surrounding are described above. The dependence of the MOKE signals on the Ni thickness and the related spin-wave frequencies are presented in Fig. 2 for the homogeneous (ferromagnetic resonance – FMR) mode as well as for several perpendicular standing spin-waves (PSSW) modes. The MOKE signals are expressed as $|\Phi|$, Kerr rotation $\theta = \mathrm{Re}(\Phi)$ and Kerr ellipticity $\varepsilon = \mathrm{Im}(\Phi)$. The amplitude of the in-plane dynamic magnetization of the FMR mode is chosen to be one, $m_L^{(\mathrm{FMR})} = 1$. The amplitudes of the dynamic magnetizations of other spin wave modes are normalized in a way that their energies per unit area are equal [9, 10].

All expressions of the Kerr effects ($|\Phi|$, θ, ε) provide very similar dependencies. In all cases (i) the Kerr effects were calculated for H parallel to the plane of incidence. Hence, the longitudinal contribution to the calculated Kerr effects is zero, as there is no dynamical magnetization in longitudinal direction. However, as discussed above, the longitudinal depth sensitivity function is here about 12-times smaller than the polar one. As spinwave amplitudes are about 1–2-times smaller in the out-of-plane than in the in-plane direction, the polar contribution would be dominant even in the case H perpendicular to the plane of the incidence, where the LMOKE contributes to the outgoing Kerr signal. (ii) The MOKE signals are increasing with increasing Ni thickness and saturate for large Ni thickness (the saturation in Fig. 2 is clearly visible only for the FMR mode and the PSSW1 mode). The saturation roughly appears when the MOKE penetration depth Λ_{MOKE} corresponds to the depth of the unique sign of the dynamic magnetization. For PSSW modes it appears when $1/4$ of the perpendicular spin wavelength $\lambda_{\mathrm{sw},\perp} \approx 2d/n$ (n is integer denoting the PSSW mode order), corresponds to Λ_{MOKE}, $\Lambda_{\mathrm{MOKE}} \approx (1/4)\lambda_{\mathrm{sw},\perp}$. In the case of FMR or Damon Eschbach (DE) mode, the MOKE saturation condition is roughly fulfilled when $\Lambda_{\mathrm{MOKE}} \approx d$. Within our Ni example, $\Lambda_{\mathrm{MOKE}} \approx 15\,\mathrm{nm}$ and hence the MOKE saturation should roughly appear at $d = 15\,\mathrm{nm}$ for the FMR/DE mode and at $d = 30, 60, 90\,\mathrm{nm}$, etc. for PSSW modes with $n = 1, 2, 3$, etc. This is in qualitative agreement with calculations shown in Fig. 2. (iii) the Kerr signals are reduced with increasing number of the PSSW modes for smaller Ni thicknesses. The reason is similar as in the previous case: when 1/4 of the perpendicular spin-wavelength $\lambda_{\mathrm{sw},\perp}$ is shorter than MOKE probing length Λ_{MOKE}, then the MOKE contributions from various depths of the Ni film cancel each other due to sign changes of the dynamic magnetization of the spinwave, reducing the outgoing Kerr signal. In other words, short perpendicular spin-waves (i.e. when $(1/4)\lambda_{\mathrm{sw},\perp} < \Lambda_{\mathrm{MOKE}}$), which appear either for small Ni thickness or PSSW modes with large mode number, provide reduced MOKE signals.

The MOKE data in Fig. 2 are compared with the normalized BLS intensity (dashed line). As the Kerr signals are proportional to $L(z)$, $P(z)$ (Eq. (1)), and the BLS intensity is proportional to a quadratic form of them (Eq. (2)), the behaviour of BLS and MOKE scaled signals are very similar, but the BLS signal is reduced more significantly for smaller Ni thicknesses or for higher orders of PSSW modes.

In conclusion, we have investigated, how signals from magneto-optical dynamic techniques, time-resolved MOKE and BLS, depend on the spin-wave mode and FM layer thickness. As a showcase, we have calculated the complex Kerr angle and BLS signal in Ni film. It is demonstrated that both MOKE and BLS behave in a similar way, reducing their signals with increasing PSSW mode number. With increasing FM layer thickness, the MOKE and BLS signals saturate; however for PSSW modes with higher mode number, the saturation is provided for larger FM layer thicknesses.

References

[1] J. Zak, E.R. Moog, C. Liu, S.D. Bader, J. Magn. Magn. Mater. **88**, L261 (1990).
[2] A. Hubert G. Traeger, J. Magn. Magn. Mater. **124**, 185 (1993).
[3] V. Kamberský, L. Wenzel, A. Hubert, J. Magn. Magn. Mater. **189**, 149 (1998).
[4] J. Hamrle, J. Ferré, M. Nývlt, Š. Višňovský, Phys. Rev. B **66**, 224423 (2002).
[5] Š. Višňovský, Czech. Jour. of Phys. **41**, 663 (1991).
[6] B.A. Kalinikos, A.N. Slavin, J. Phys. C **19**, 7013 (1986).
[7] B. Hillebrands, Phys. Rev. B **41**, 530 (1990).
[8] M. Buchmeier, B.K. Kuanr, R.R. Gareev, D.E. Bürgler, P. Grünberg, Phys. Rev. B **67**, 184404 (2003).
[9] M. Buchmeier, H. Dassow, D.E. Bürgler, C.M. Schneider, Phys. Rev. B **75**, 184436 (2007).
[10] J.F. Cochran, J.R. Dutcher, J. Magn. Magn. Mater. **73**, 299 (1988).
[11] J. Hamrle, O. Gaier, S.-G. Min, B. Hillebrands, Y. Sakuraba, Y. Ando, J. Phys. D: Appl. Phys. **42**, 084005 (2009).
[12] *Handbook of optical constants of solid*, edited by E. Palik (Academic Press Handbook Series, London, 1985).

5.20 An electro-optic modulator-assisted wavevector-resolving Brillouin light scattering setup

T.M. Neumann, T. Schneider, A.A. Serga, and B. Hillebrands

Brillouin light scattering (BLS) spectroscopy is a versatile technique to investigate dynamic magnetic phenomena. Its power is significantly increased by numerous extensions which were added to the basic spectroscopic setup over time.

By introducing time-resolution, it was possible to investigate the evolution of a parametrically excited magnon gas in a ferrite film and observe the formation of a Bose-Einstein condensate of magnons at room temperature [1, 2]. The inclusion of space-resolution led to the discovery of important nonlinear wave phenomena such as soliton and bullet formation [3, 4], the observation of spin-wave tunneling [5] as well as spin-wave quantisation in nanoscaled structures [6].

Other discussed extensions comprise phase- [7] and wavevector resolution [8]. The latter is particularly interesting since the frequency does usually not uniquely identify a wave eigenmode. Due to an often complex dispersion relation the additional knowledge of the wave vector is essential.

For the investigation of spin waves in ferrite films by BLS, wavevector resolution was already introduced in the late 70's [9]. Subsequently, many studies (e.g. [10–12]) have copied the originally presented principle: to the BLS setup in forward scattering geometry a diaphragm is added in the beam path after the sample stage (see Fig. 1). Depending on the shape and position of the hole in the diaphragm, some components of the scattered laser beam which correspond to certain in-plane wavevectors are blocked while others can pass and are detected. The latest success of this technique was the time- and wavevector resolved observation of a parametrically pumped magnon gas after pumping was switched off [13].

It is of crucial importance for an accurate measurement of the in-plane wavevector to calibrate the position of the diaphragm hole. The zero position when the elastically scattered beam passes through the diaphragm can be adjusted by sight, however this procedure is inevitably inaccurate. A second possibility is to calibrate the position based on the measured data: Stokes and anti-Stokes peaks in the BLS spectrum lead to two distinct signals with opposing wavevectors. Their symmetric position with respect to the center can in special cases be used for calibration. However, the intensities of Stokes and anti-Stokes peaks can differ greatly which makes this procedure difficult. Moreover, it is unnecessarily time-consuming since the weaker of the two signal peaks determines the accuracy of the calibration and, therefore, the required measurement time, though in many cases it does not yield any additional physical information about the system under investigation.

The approach presented here uses an intrinsic calibration which is achieved by placing an electro-optic modulator (EOM) in the optical path behind the laser light source. The small amount of modulated, frequency-shifted light plays the role of a reference beam for the wavevector resolution. Since it follows the same path as the unshifted laser light scattered inelastically from the sample but does (in first approximation) not undergo any inelastic scattering in the sample itself, it indicates the position where the in-plane wavevector vanishes for the measurement.

The proposed calibration procedure has two major advantages. First of all, it is applicable even when one of the two signals from Stokes and anti-Stokes scattering is not large enough to be observed. This is in particular the case for surface magnetostatic spin waves. Secondly, it potentially decreases the measurement time since the wavevector scanning does not have to be performed over

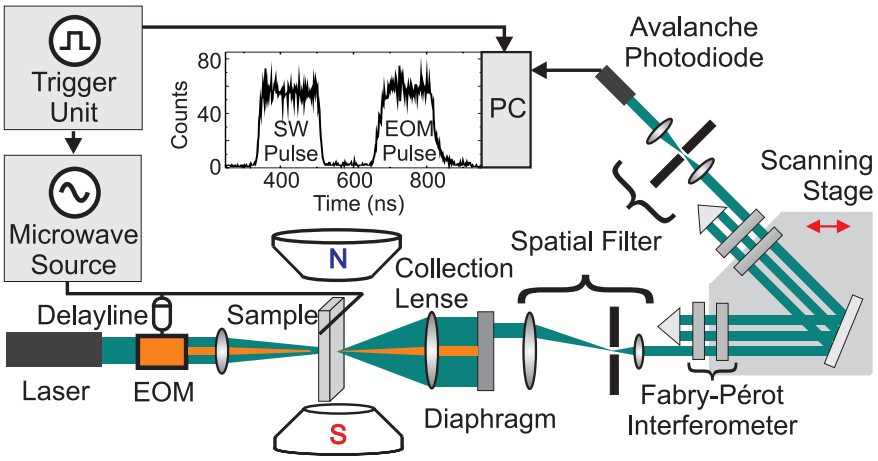

Fig. 1: Sketch of the experimental setup.

the whole range of wavevectors but can (if a symmetry is already known) be restricted to one of the symmetric parts. To confirm the validity of the presented method the in-plane wavevectors of propagating, dipole-dominated spin waves were resolved.

It should be remarked that electro-optic modulators have already been used to realize phase resolution [7] and enhance the frequency resolution [14]. This work adds to their increasing role for the improvement of the Brillouin light scattering setup.

The experimental setup is shown in Fig. 1. The sample under investigation consisted of a 5 µm thick yttrium-iron-garnet (YIG) film which was tangentially magnetized by a magnetic field H (indicated by two pole pieces in Fig. 1). To a microstrip transducer on the surface of the YIG stripe a 200 ns long microwave pulse with 7.132 GHz carrier frequency was supplied with a 1 µs repetition rate. The configuration was chosen in such a way that the microwave pulse excites a packet of backward volume magnetostatic spin waves (BVMSW) [15,16]. Thus, the in-plane wavevector of the excited spin waves has only one well defined, non-zero component in the direction of the bias magnetic field. The measurements discussed below focus on determining this wavevector component and comparing the experimental results with theoretical calculations.

To detect the spin-wave packet light from a single mode, frequency-stabilized 532 nm laser was focused on the sample close to the antenna. The transmitted light was sent to a (3+3)-pass tandem Fabry-Pérot interferometer where the frequency of the light inelastically scattered from the spin waves was resolved. A good description of the underlying BLS setup is found in [17].

The existing BLS setup already includes time- and space resolution in the following way: In order to probe different points of the sample, the sample is mounted on a stage which can be moved by a stepper motor. Time resolution is achieved by measuring the time between the launch of the microwave signal pulse which excites the spin-wave packet and the detection of the scattered photons by the detector. A detailed account is given in [18].

Wavevector resolution was added to the existing setup by placing a diaphragm with a central hole of 0.5 mm diameter in the focal plane behind the collection lens. The diaphragm was mounted on a stage which was horizontally movable by a PC-controlled stepper motor. The stage was moved in steps of 0.08 mm. Since the investigated spin waves possessed only one non-vanishing in-plane component of the wavevector the chosen one-dimensional approach is sufficient for demonstration. To measure both in-plane wavevector components an additional stage for the vertical displacement of the diaphragm will be added. The measurement principle remains, however, unchanged.

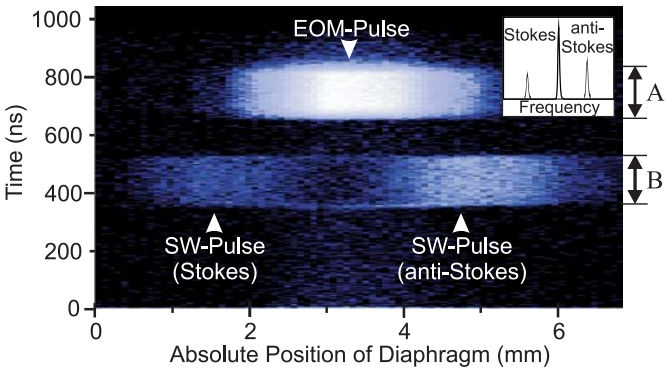

Fig. 2: Time-resolved intensity of the scattered light with respect to the displacement of the diaphragm for a bias magnetic field $H = 1/(4\pi)\,1.870\,\mathrm{kA\cdot m^{-1}}$ and a spin-wave carrier frequency $f = 7.132\,\mathrm{GHz}$. Indicated are the signals from EOM reference pulse in the time interval A as well as from the spin-wave (SW) packet corresponding to the Stokes- and anti-Stokes-peak in the BLS spectrum (sketched in inset) observed in the time interval B.

To calibrate the diaphragm position, an EOM was placed in the beam path in front of the sample (see Fig. 1). It was driven by a 200 ns long pulse from the same microwave source that generated the spin-wave pulse. However, the EOM-pulse was delayed compared to the spin-wave pulse in order to make EOM and spin-wave signal clearly distinguishable in the time-resolved measurements.

Since the same microwave frequency is applied to the EOM and the microstrip transducer which excites the spin waves, the resulting signal peaks in the BLS spectrum coincide. This has two practical advantages. First of all, the frequency interval which is effectively scanned by the interferometer can be small. This reduces the overall measurement time which is particularly important for wavevector resolved measurements. Secondly, the EOM-signal can be used as a frequency reference [14].

Figure 2 shows the intensity of the detected BLS signal relative to the elapsed time and the displacement of the diaphragm from its initial (arbitrary) position. Three signals are clearly distinguishable:

In the time interval marked in Fig. 2 as A the signal from the EOM-pulse is seen. The time interval B contains two signals which both stem from the propagating spin-wave packet. They correspond to the Stokes and anti-Stokes peaks in the BLS spectrum. This was checked by restricting the BLS measurement once to the Stokes and once to the anti-Stokes peak (see inset in Fig. 2). In particular, the signals corresponding to Stokes and anti-Stokes BLS peaks swapped their positions when the laser beam was focused on the other side of the exciting microstrip antenna where the spin-wave packet travels in the opposite direction and the spin-wave wavevector, therefore, changes sign.

To increase the signal to noise ratio the received counts were integrated over the time intervals A and B, respectively. The resulting intensity distribution, which depends only on the diaphragm displacement, is shown in Fig. 3. It is relatively wide because of the comparatively large pin hole in the diaphragm. However, this trade-off was accepted to decrease the measurement time. By fitting the experimental data with a single Gaussian distribution for the EOM-signal and two independent Gaussian distributions (but with the same variance) for the spin-wave signal, the accuracy of the measurement was enhanced. As can be seen from Fig. 3, the fits agree well with the experimental data. The center of the Gaussian profile which fits the EOM-signal was used to calibrate the diaphragm displacement and obtain the $k = 0-$position. Relative to this position the deflection x of the beam which was inelastically scattered on the spin-wave packet was determined.

Measurements were performed for different magnetic fields with the same spin-wave carrier frequency 7.132 GHz. The results are presented in Fig. 4. Figure 4a shows extracts corresponding to the interval B in Fig. 2 which contains the information on the spin-wave wavevector. In accordance with theory an almost linear field dependence is seen [16].

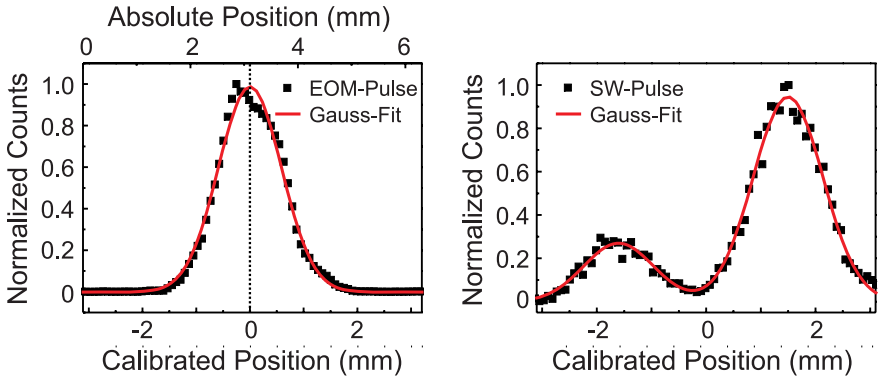

Fig. 3: Dependence of the BLS signal obtained for the EOM pulse and the SW pulse on the diaphragm displacement. The lines are the results of Gauss fits.

In order to unambiguously resolve the signals corresponding to the Stokes and anti-Stokes peaks in the BLS spectrum, separate measurements were conducted by limiting the spectral scanning to one of the two spectral positions (Panel (b)).

From the data, the spin-wave wave number k_{SW} is obtained using the Bragg-condition

$$k_{\mathrm{SW}} = 2 \cdot k_{\mathrm{Laser}} \sin\left(\vartheta/2\right) = 2 \cdot k_{\mathrm{Laser}} \sin\left(\frac{\arctan(x/f)}{2}\right)$$

where $k_{\mathrm{Laser}} = 1.181 \cdot 10^7\,\mathrm{m}^{-1}$ is the wave number of the incoming laser light and ϑ is the angle between the elastically and inelastically scattered light which is determined by the focal length $f = 500\,\mathrm{mm}$ of the collection length and the measured deflection x of the spin-wave signal. The experimentally found spin-wave wavenumbers k_{SW} are combined in Fig. 4c with theoretical calculations based on the Damon-Eshbach formula for the lowest order BVMSW mode [16]. The solid line has been calculated based on the measured field value, a film thickness of 5 µm and a saturation magnetisation $4\pi\mu_0 M_{\mathrm{s}} = 0.175\,\mathrm{T}$. In comparison, the dashed line is the result of a fit, where the film thickness and the magnetic field were taken as fit parameters. The optimal value found for the thickness was 4.2 µm, the magnetic field was adjusted by a shift $\Delta H = -1/(4\pi) \cdot 0.007\,\mathrm{kA \cdot m^{-1}}$ relative to the experimentally measured field H. Both deviations are within reasonable range. The film thickness is not known with sufficient accuracy and may locally vary. The experimentally measured magnetic field does not take into account any contributions from the crystalline anisotropy. If one keeps this in mind, the theoretical curves agree well with experiment overall.

The presented results confirm the validity of the EOM-assisted wavevector resolution measurement procedure. The EOM allows an easy, intrinsic calibration with the same resolution as the actual measurement. The calibration does not rely on any symmetry in the observed peaks and can be performed even when the scanning is restricted to one side of the BLS spectrum. The widely adjustable intensity of the EOM beam guarantees a minimal expenditure of time to obtain a large enough signal for the analysis.

In principle, the EOM beam can be used to calibrate the diaphragm prior to the experiment. Instead, in the presented work the EOM reference was applied parallel to the actual measurement. This is the most natural procedure whenever the pulse regime is required because of other experimental restrictions. The reference EOM beam is applied during the dead time of the cycle so that the overall duration of the experiment is not increased and measurement as well as calibration are completed in a single run.

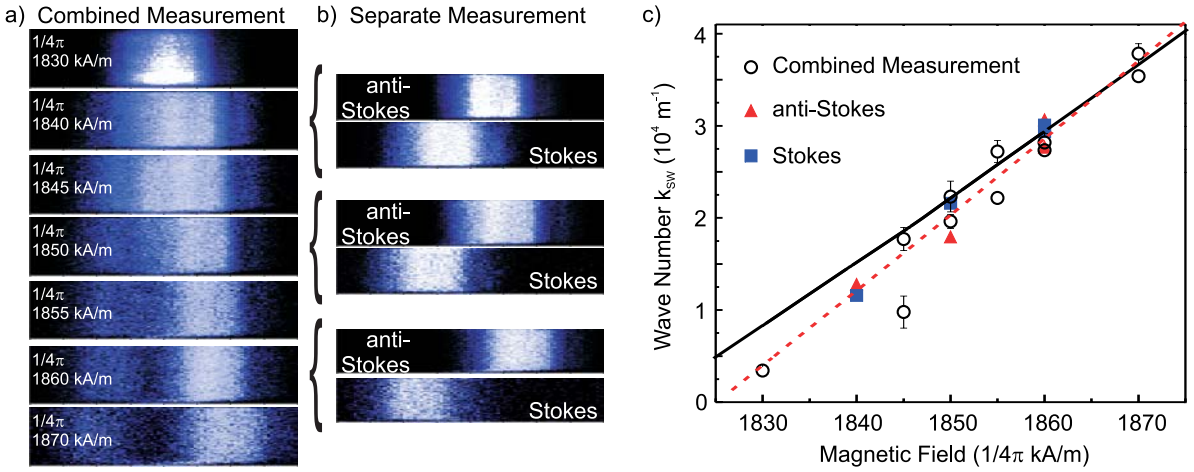

Fig. 4: Dependence of the observed signal on the bias magnetic field indicated in each panel. a) Spatial signal distribution when Stokes and anti-Stokes are measured together (compare to Fig. 2). b) Separately measured Stokes and anti-Stokes signals. c) Experimentally obtained wave numbers in comparison with theoretical calculations without fit parameters (solid line) and with adjusted magnetic field and film thickness (dashed line).

The experiments confirmed the applicability of the diaphragm-based approach to wavevector resolution for the measurement of small wave numbers. The method is not the only way to go in this regime. It is also possible to measure the spin-wave wavelength by using phase resolution [7]. However, this method relies on the scanning of the sample which does, in terms of measurement time not yield any advantages. Moreover, it is only applicable in the case of a single spin wave propagating under homogeneous external conditions - fast temporal or spatial variations of the wave number cannot be resolved. The same draw-backs apply to other interference-based methods using, for instance, inductive probes.

For the diaphragm-approach these limitations do not apply: Since the method relies on the measurement at a single point on the sample, inhomogeneities in the sample do not play any role. As has been seen above, it is even possible to distinguish waves with the same wavenumber modulus but travelling in opposite directions. In combination with the time-resolution it is possible to resolve the wavenumber evolution. Moreover, by exchanging the collection lense with one having a shorter focal length the range of wavevectors which are collected and resolved and measured can be controlled.

In conclusion, we have improved the existing wavevector resolution used in Brillouin light scattering experiments by including an electro-optic modulator as a reference to calibrate the position of the diaphragm hole. The EOM beam makes it possible to determine the position where the in-plane wavevector vanishes with an accuracy comparable to the accuracy of the actual wavevector measurement itself. For experiments conducted in the pulse regime, the proposed method does not increase the measurement time but even cuts it in half under optimum conditions. The applicability of the EOM-based calibration was tested by measuring the wavevectors of a propagating packet of dipole-dominated spin-waves for different bias magnetic fields with time resolution. Comparison with the established theory showed a good agreement.

This work has been financially supported by the Matcor Graduate School of Excellence, the Graduiertenkolleg 792, and the DFG within the SFB/TRR 49.

References

[1] S.O. Demokritov, V.E. Demidov, O. Dzyapko, G.A. Melkov, A.A. Serga, B. Hillebrands, A.N. Slavin, Nature **443**, 430 (2006).
[2] V.E. Demidov, O. Dzyapko, S.O. Demokritov, G.A. Melkov, A.N. Slavin, Phys. Rev. Lett **100**, 047205 (2008).
[3] M. Bauer, O. Büttner, S.O. Demokritov, B. Hillebrands, V. Grimalsky, Yu. Rapoport, A.N. Slavin, Phys. Rev. Lett. **81**, 3769 (1998).
[4] A.A. Serga, M.P. Kostylev, B. Hillebrands, Phys. Rev. Lett. **101**, 137204 (2008).
[5] S.O. Demokritov, A.A. Serga, A. André, V.E. Demidov, M.P. Kostylev, B. Hillebrands, Phys. Rev. Lett. **93**, 047201 (2004).
[6] H. Schultheiss, S. Schäfer, P. Candeloro, B. Leven, B. Hillebrands, A.N. Slavin, Phys. Rev. Lett. **100**, 047204 (2008).
[7] A.A. Serga, T. Schneider, B. Hillebrands, S.O. Demokritov, M.P. Kostylev, Appl. Phys. Lett. **89**, 063506 (2006).
[8] H. Xia, P. Kabos, H.Y. Zhang, P.A. Kolodin, C.E. Patton, Phys. Rev. Lett. **81**, 449 (1998).
[9] V.N. Venitskiĭ, V.V. Eremenko, É.V. Matyushkin, Sov. Phys. JETP **50**, 934 (1979).
[10] W. Wettling, W.D. Wilber, P. Kabos, C.E. Patton, Phys. Rev. Lett. **51**, 1680 (1983).
[11] P. Kabos, G. Wiese, C.E. Patton, Phys. Rev. Lett. **72**, 2093 (1994).
[12] P. Kabos, M. Mendik, G. Wiese, C.E. Patton, Phys. Rev. B. **55**, 11457 (1997).
[13] V.E. Demidov, O. Dzyapko, M. Buchmeier, T. Stockhoff, G. Schmitz, G.A. Melkov, S.O. Demokritov, Phys. Rev. Lett. **101**, 257201 (2008).
[14] S. Caponi, M. Dionigi, D. Fioretto, M. Mattarelli, L. Palmieri, G. Socino, Rev. Sci. Instrum. **72**, 198 (2001).
[15] R.W. Damon, J.R. Eshbach, J. Phys. Chem. Solids **19**, 308 (1961).
[16] M.J. Hurben, C.E. Patton, J. Magn. Magn. Mater.**139**, 263 (1995).
[17] B. Hillebrands, Rev. Sci. Instrum. **70**, 1589 (1999).
[18] O. Büttner, M. Bauer, S.O. Demokritov, B. Hillebrands, Yu.S. Kivshar, V. Grimalsky, Yu. Rapoport, A.N. Slavin, Phys. Rev. B **61** 11576 (2000).

Chapter 6: Publications

Most publications can be downloaded from http://www.physik.uni-kl.de/hillebrands.

6.1 published

1. *A current-controlled dynamic magnonic crystal*
   A.V. Chumak, T. Neumann, A.A. Serga, B. Hillebrands, M.P. Kostylev
   J. Phys. D: Appl. Phys. **42** 205005 (2009).

2. *Direct current control of three magnon scattering processes in spin-valve nanocontacts*
   H. Schultheiss, F. Ciubotaru, A. Laraoui, S.J. Hermsdoerfer, B. Obry, A.A. Serga, X. Janssens, M. van Kampen, L. Lagae, A.N. Slavin, B. Leven, B. Hillebrands
   Phys. Rev. Lett. **103**, 157202 (2009)
   Vir. J. Nan. Sci. & Tech. **20**(16), (2009).

3. *Cluster issue on Heusler compounds and devices*
   C. Felser, B. Hillebrands
   J. Phys. D: Appl. Phys. **42**, 080301 (2009).

4. *Spin-signal propagation in time-dependent noncollinear spin transport*
   Y.-H. Zhu, B. Hillebrands, H.C. Schneider
   Phys. Rev. B **79**, 214412 (2009).

5. *Modeling of microwave-assisted switching in micron-sized magnetic ellipsoids*
   R. Yanes, R. Rozada, F. García-Sánchez, O. Chubykalo-Fesenko, P. Martin Pimentel, B. Leven, B. Hillebrands
   Phys. Rev. B **79**, 224427 (2009).

6. *A spin-wave frequency doubler by domain wall oscillation*
   S.J. Hermsdoerfer, H. Schultheiss, C. Rausch, S. Schaefer, B. Leven, S.-K. Kim, B. Hillebrands
   Appl. Phys. Lett. **94**, 223510 (2009).

7. *An electro-optic modulator-assisted wave vector-resolving Brillouin light scattering setup*
   T. Neumann, T. Schneider, A.A. Serga, B. Hillebrands
   Rev. Sci. Instrum. **80**, 053905 (2009).

8. *Field-induced transition from parallel to perpendicular parametric pumping for a microstrip transducer*
   T. Neumann, A.A. Serga, V.I. Vasyuchka, B. Hillebrands
   Appl. Phys. Lett. **94**, 192502 (2009).

9. *Bose-Einstein condensation of magnons under incoherent pumping*
   A.V. Chumak, G.A. Melkov, V.E. Demidov, O. Dzyapko, V.L. Safonov, S.O. Demokritov
   Phys. Rev. Lett. **102**, 187205 (2009).

10. *Scattering of surface and volume spin waves in a magnonic crystal*
    A.V. Chumak, A.A. Serga, S. Wolff, B. Hillebrands, M.P. Kostylev
    Appl. Phys. Lett. **94**, 172511 (2009).

11. *Design and optimization of one-dimensional ferrite-film based magnonic crystals*
A.V. Chumak, A.A. Serga, S. Wolff, B. Hillebrands, M.P. Kostylev
J. Appl. Phys. **105**, 083906 (2009).

12. *Improvement of structural, electronic, and magnetic properties of Co_2MnSi thin films by He^+-irradiation*
O. Gaier, J. Hamrle, B. Hillebrands, M. Kallmayer, P. Pörsch, G. Schönhense, H.J. Elmers, J. Fassbender, A. Gloskovskii, C.A. Jenkins, C. Felser, E. Ikenaga, Y. Sakuraba, S. Tsunegi, M. Oogane, Y. Ando
Appl. Phys. Lett. **94**, 152508 (2009).

13. *Determination of exchange constants of Heusler compounds by Brillouin light scattering spectroscopy: application to Co_2MnSi*
J. Hamrle, O. Gaier, S.-G. Min, B. Hillebrands, Y. Sakuraba, Y. Ando
J. Phys. D: Appl. Phys. **42**, 084005 (2009).

14. *Brillouin light scattering study of $Co_2Cr_{0.6}Fe_{0.4}Al$ and Co_2FeAl Heusler compounds*
O. Gaier, J. Hamrle, S. Trudel, A. Conca Parra, B. Hillebrands, E. Arbelo, C. Herbort, M. Jourdan
J. Phys. D: Appl. Phys. **42**, 084004 (2009).

15. *Phase sensitive Brillouin scattering measurements with a novel magneto-optic modulator*
F. Fohr, A.A. Serga, T. Schneider, J. Hamrle, B. Hillebrands
Rev. Sci. Instrum. **80**, 043903 (2009).

16. *Magnetic domain-wall motion by propagating spin waves*
D.-S. Han, S.-K. Kim, J.-Y,. Lee, S. J. Hermsdoerfer, H. Schultheiss, B. Leven, B. Hillebrands
Appl. Phys. Lett. **94**, 112502 (2009)
Vir. J. Nan. Sci. & Tech. **19**(13), (2009).

17. *Generation of spin-wave pulse trains by current-controlled magnetic mirrors*
A.A. Serga, T. Neumann, A.V. Chumak, B. Hillebrands
Appl. Phys. Lett. **94**, 112501 (2009).

18. *Brillouin Light Scattering Investigations of Magnetic and Elastic Properties in MBE Grown Trilayer Mo/Co/Au Systems*
R. Gieniusz, T. Blachowicz, A. Maziewski, A Petroutchik, L.T. Baczewski, A. Wawro, J. Hamrle, O. Serga, B. Hillebrands
Acta Physica Polonica A **115**, 213 (2009).

19. *Frequency-dependent reflection of spin waves from a magnetic inhomogeneity induced by a surface direct current*
T. Neumann, A.A. Serga, B. Hillebrands, M.P. Kostylev
Appl. Phys. Lett. **94**, 042503 (2009).

20. *Parametric recovery of a microwave signal using standing spin-wave modes of a magnetic film*
A.V. Chumak, A.A. Serga, G.A. Melkov, A.N. Slavin, V. Tiberkevich, B. Hillebrands
Phys. Rev. B **79**, 014405 (2009).

21. *Probing of a parametrically pumped magnon gas with a packet of non-resonant traveling spin waves*
T. Neumann, A.A. Serga, B. Hillebrands
Appl. Phys. Lett. **93**, 252501 (2008).

22. *Magnetic metal oxide nanocrystals and their applications*
S. Trudel, R.H. Hill
In: Y.B. Hahn, A. Umar (eds) Oxide Nanostructures and Their Applications Vol. 2, American Scientific Publishers, 2009.

23. *Magnetic frustration and spin disorder in isostructural $M(OH_2)_2[Au(CN)_2]_2$ (M = Mn, Fe, Co) coordination polymers containing double aqua-bridged chains: SQUID and μSR studies*
J. Lefebvre, P. Tyagi, S. Trudel, V. Pacradouni, C. Kaiser, J.E. Sonier, D.B. Leznoff
Inorg. Chem. **48**, 55 (2009).

24. *Top-down meets bottom-up: Electron beam induced metalorganic deposition of amorphous iron oxide nanostructures*
S. Trudel, R.H. Hill
Can. J. Chem. **87**, 217 (2009).

6.2 in press

1. *All-optical detection of phase fronts of propagating spin waves in a $Ni_{81}Fe_{19}$ microstripe*
K. Vogt, H. Schultheiss , S.J. Hermsdoerfer , P. Pirro , A.A. Serga , B. Hillebrands
Appl. Phys. Lett., in press.

2. *Exchange stiffness in the Co_2FeSi-based Heusler compound*
O. Gaier, J. Hamrle, S. Trudel, B. Hillebrands, H. Schneider, G. Jakob
J. Phys. D: Appl. Phys., in press.

3. *Tandem magneto-optical Kerr effect magnetometer for the study of quadratic effects*
S. Trudel, G. Wolf, H. Schultheiß, J. Hamrle, B. Hillebrands
Journal of Physics: Conference Series, in press.

6.3 submitted

1. *Spin-wave propagation in a microstructured magnonic crystal*
A.V. Chumak, P. Pirro, A.A. Serga, M.P. Kostylev, R.L. Stamps, H. Schultheiss, K. Vogt, S.J. Hermsdoerfer, B. Laegel, P.A. Beck, B. Hillebrands
submitted to Appl. Phys. Lett..

2. *Magneto-optical investigation of epitaxial non-stoichiometric Co_2MnGe thin films*
S. Trudel, J. Hamrle, B. Hillebrands, T. Taira, M. Yamamoto
submitted to J. Appl. Phys..

3. *Probing quadratic magneto-optical Kerr effects with a tandem dual-beam system*
S. Trudel, G. Wolf, H. Schultheiß, J. Hamrle, B. Hillebrands
submitted to Rev. Sci. Inst..

4. *Structure, exchange stiffness and magnetic anisotropy of $Co_2MnAl_xSi_{1-x}$ Heusler compounds*
   T. Kubota, J. Hamrle, Y. Sakuraba, O. Gaier, M. Oogane, A. Sakuma, B. Hillebrands, K. Takanashi, Y. Ando
   submitted to J. Appl. Phys..

5. *Non-resonant wave front reversal of spin waves used for microwave signal processing*
   V.I. Vasyuchka, G.A. Melkov, A.N. Slavin, A.V. Chumak, V.A. Moiseienko, B. Hillebrands
   submitted to Appl. Phys. Lett..

6. *Reverse Doppler effect in backward spin waves scattered on acoustic waves*
   A.V. Chumak, P. Dhagat, A. Jander, A.A. Serga, B. Hillebrands
   submitted to Phys. Rev. Lett..

7. *Exchange stiffness in Co_2-based Heusler compounds*
   J. Hamrle, S. Trudel, O. Gaier, B. Hillebrands
   submitted to Phys. Rev. B.

6.4 Ph.D. theses

1. *A study of exchange interaction, magnetic anisotropies, and ion beam induced effects in thin films of Co_2-based Heusler compounds*
   Oksana Gaier, TU Kaiserslautern, July 2009.

2. *Phasenaufgelöste Untersuchung der Propagation von Spinwellenpaketen und der Entstehung von Spinwellen-Kaustiken*
   Thomas Schneider, TU Kaiserslautern, June 2009.

Chapter 7: Conferences, Workshops, Schools, Seminars

(shown in chronological order; if not indicated otherwise the contributions were presented by the first author)

7.1 Conferences

7.1.1 Invited talks

B. Hillebrands:
Current induced spin-wave emission from ferromagnetic nano-structures
"Twenty Years of Spintronics: Retrospective and Perspective", Paris, December 2008

B. Hillebrands:
Magnon gases and condensates
DPG Frühjahrstagung, Dresden, March 2009

B. Hillebrands:
Current induced spin wave emission from ferromagnetic nanostructures
INTERMAG Conference 2009, Sacramento, U.S.A., May 2009

B. Hillebrands:
Nanomagnetism - a perspective from the dynamic side
Trends in NanoTechnology (TNT) 2009, Barcelona, September 2009

B. Hillebrands:
Current induced spin-wave emission from ferromagnetic nanostructure
"Advances in Magnetic Nanostructures", Vail/Colorado, October 2009

7.1.2 Contributed talks and posters

C.W. Sandweg, B. Obry, S.J. Hermsdoerfer, S. Schaefer, V. Tiberkevich, B. Leven, A.N. Slavin, B. Hillebrands:
Dissipation of quantized spin waves in nano-scaled magnetic ring structures
MMM, Austin, U.S.A., November 2008

O. Gaier, J. Hamrle, B. Hillebrands, H. Schneider, M. Kallmayer, P. Pörsch, G. Schönhense, H.J. Elmers, J. Fassbender, A. Gloskovskii, C.A. Jenkins, G.H. Fecher, C. Felser, E. Ikenaga, Y. Sakuraba, S. Tsunegi, M. Oogane, Y. Ando:
Tailoring of structural and magnetic properties of Co_2MnSi Heulser compound by He^+ ion irradiation
MMM, Austin, Texas, U.S.A., November 2008

S.J. Hermsdoerfer, C.W. Sandweg, H. Schultheiss, S. Schäfer, B. Leven, B. Hillebrands :
Modification of the thermal spin-wave spectrum in a $Ni_{81}Fe_{19}$ stripe by a domain wall
MMM, Austin, U.S.A., November 2008

J. Hamrle, O. Gaier, S. Trudel, B. Hillebrands, H. Schneider, G. Jakob, M. Jourdan, J. Thöne, G. Fecher, C. Felser, J. Kübler, J. Kudrnovsky, T. Kubota, Y. Sakuraba, M. Oogane, Y. Ando:
Exchange stiffness constant and magnetic ansiotropy in Co_2-based Heusler compounds
Magnetic Research Society Fall Meeting, Boston, U.S.A., December 2008

A.V. Chumak, P. Dhagat, A. Jander, A.A. Serga, B. Hillebrands:
Reverse Doppler effect in spin waves scattered on acoustic waves
Intermag Conference, Sacramento, U.S.A., May 2009

A.V. Chumak, M.P Kostylev, A.A. Serga, S. Wolff, B. Hillebrands:
Nonreciprocal spin wave scattering on a magnonic crystal
Intermag Conference, Sacramento, U.S.A., May 2009

T. Neumann, A.A. Serga, V.I. Vasyuchka, B. Hillebrands:
Field-induced transition from parallel to perpendicular parametric pumping for a microstrip resonator
Intermag Conference, Sacramento, U.S.A., May 2009

O. Serga (T. Neumann):
Probing of a parametrically driven magnon gas with a non-resonant traveling spin wave
Intermag Conference, Sacramento, U.S.A., May 2009

A.V. Chumak, P. Dhagat, A. Jander, A.A. Serga, B. Hillebrands:
Reverse Doppler effect in backward spin waves scattered on acoustic waves
9th International Young Scientists Conference on Applied Physics, Kiev, Ukraine, June 2009

C.W. Sandweg, A.A. Serga, V.I. Vasyuchka, A.V. Chumak, T. Neumann, G.A. Melkov, B. Hillebrands:
Pump-free evolution of a parametrically pumped magnon gas
Spin Waves, St. Petersburg, June 2009

F. Ciubotaru, H. Schultheiss, A. Laraoui, A.A. Serga, X. Janssens, M. van Kampen, L. Lagae, B. Leven, A.N. Slavin, B. Hillebrands:
Current controlled three-magnon-scattering processes in nanopoint contact spin-valves
ICMFS, Berlin, July 2009

F. Fohr, A.A. Serga, T. Schneider, J. Hamrle, B. Hillebrands:
Phase sensitive Brillouin scattering measurements with a novel magneto-optic modulator
ICMFS, Berlin, July 2009

S.J. Hermsdoerfer, H. Schultheiss, C. Rausch, P. Pirro, S. Schäfer, B. Leven, S.-K. Kim, B. Hillebrands:
A spin-wave frequency doubler by oscillating domain walls
ICMFS, Berlin, July 2009

T. Schneider, A.A. Serga, A.V. Chumak, B. Hillebrands, C.W. Sandweg, S. Wolff, M.P. Kostylev, V.S. Tiberkevich, A.N. Slavin:
Diffractionless spin-wave caustics in magnetic films
ICMFS, Berlin, July 2009

H. Schultheiß, B. Obry, C.W. Sandweg, S.J. Hermsdoerfer, B. Leven, B. Hillebrands:
Dissipation and coupling of spin-wave eigenmodes in nano-scaled magnetic ring structures
ICMFS, Berlin, July 2009

A.V. Chumak, P. Dhagat, A. Jander, A.A. Serga, B. Hillebrands:
Inverse Doppler effect in backward spin waves scattered on surface acoustic waves
ICM, Karlsruhe, July 2009

A.V. Chumak, A.A. Serga, T. Neumann, M.P. Kostylev, B. Hillebrands:
Current controlled magnonic crystal
ICM, Karlsruhe, July 2009

J. Hamrle, S. Trudel, O. Gaier, B. Hillebrands, H. Schneider, G. Jakob, Ch. Herbort, E. Arbelo, M. Jourdan, C. Felser, T. Kubota, Y. Sakuraba, M. Oogane, Y. Ando:
Systematization of the exchange stiffness in Co_2-based Heusler compounds
ICM, Karlsruhe, July 2009

C.W. Sandweg, B. Jungfleisch, V.I. Vasyuchka, A.A. Serga, B. Hillebrands:
Two-dimensional wave-vector resolution in Brillouin light scattering spectroscopy
ICM, Karlsruhe, July 2009

S. Schäfer, V. Kegel, A.A. Serga, B. Hillebrands:
Magnon-magnon interaction under parallel parametric pumping in hybridized dispersions
ICM, Karlsruhe, July 2009

T. Schneider, A.A. Serga, A.V. Chumak, B. Hillebrands, C.W. Sandweg, S. Wolff, M.P. Kostylev, V.S. Tiberkevich, A.N. Slavin:
Excitation and propagation of spin-wave caustics
ICM, Karlsruhe, July 2009

S. Trudel, J. Hamrle, O. Gaier, P. Clausen, G. Wolf, B. Hillebrands:
Quadratic magneto-optical Kerr effect in Co_2-based Heusler compound thin films
ICM, Karlsruhe, July 2009

V.I. Vasyuchka, C.W. Sandweg, A.A. Serga, G.A. Melkov, D.V. Slobodyanyuk, B. Hillebrands:
Pumping-free evolution of parametrically pumped magnon gas
ICM, Karlsruhe, July 2009

J. Hamrle, O. Gaier, S. Trudel, B. Hillebrands, H. Schneider, G. Jakob, Ch. Herbort, E. Arbelo, M. Jourdan, C. Felser, T. Kubota, Y. Sakuraba, M. Oogane, Y. Ando:
Exchange stiffness in Co_2-based Heusler compounds
EUROMAT conference, Glasgow, September 2009

7.1.3 Contributions to the DPG Frühjahrstagung

15 contributions: DPG Frühjahrstagung, Dresden, March 2009

7.2 Workshops and Schools

7.2.1 Invited talks

B. Hillebrands:
Brillouin light scattering spectroscopy
MSNOW Workshop, Nancy, France, November 2008

J. Hamrle, O. Gaier, S. Trudel, B. Hillebrands, H. Schneider, G. Jakob, M. Jourdan, G. Fecher, C. Felser, J. Kübler, J. Kudrnovsky, T. Kubota, Y. Sakuraba, M. Oogane, Y. Ando, K. Postava, J. Pištora:
Magneto-optical Kerr effect and exchange stiffness in Co_2-based Heusler compounds
International Workshop "Advances in Spintronic Materials: Theory and Experiment", Duisburg, November 2008

B. Hillebrands:
Spintronik - Chancen und Risiken für die rheinland-pfälzische Wirtschaft
Tag der Technologie 2008 in Rheinland-Pfalz, Mainz, November 2008

J. Hamrle, O. Gaier, S. Trudel, P. Clausen, B. Hillebrands, H. Schneider, G. Jakob, M. Jourdan, C. Felser, T. Kubota, Y. Sakuraba, M. Oogane, Y. Ando, J. Fassbender, K. Postava, J. Pištora:
Quadratic magneto-optical Kerr effect in Co_2-based Heusler compounds
WE-Heraeus Seminar, Bad Honnef, January 2009

B. Hillebrands:
Transport phenomena using spin waves
Workshop "Spin-Calorimetrics", Dresden, May 2009

B. Obry:
Detecting spin waves by Brillouin light scattering microscopy
Joint Workshop DFG Research Unit 559 and JST Strategic Japanese-German Cooperative Program "Nanoelectronics", Diemerstein, July 2009

J. Hamrle:
Exchange stiffness in Co_2-based Heusler compounds
Joint Workshop DFG Research Unit 559 and JST Strategic Japanese-German Cooperative Program "Nanoelectronics ", Diemerstein, July 2009

A.A. Serga:
Parametrically driven magnon gases and condensates
International Seminar and Workshop "Magnonics: From Fundamentals to Applications", Dresden, August 2009

B. Hillebrands:
Fundamentals of spin waves
SPINSWITCH Summer School, Iasi, September 2009

A.A. Serga:
Spin wave logic
SPINSWITCH Summer School, Iasi, September 2009

B. Hillebrands:
Spin dynamics using spin waves
Workshop, Foundation Advanced Technology Institute (ATI), Tokyo, October 2009

7.2.2 Contributed talks and posters

B. Obry, S. Schäfer, H. Schultheiss, C.W. Sandweg, S.J. Hermsdoerfer, V. Tiberkevich, B. Leven, A.N. Slavin, B. Hillebrands:
Dissipation characteristics of quantized spin waves in nano-scaled magnetic ring structures
MSNOW workshop, Nancy, France, November 2008

C. Rausch, S.J. Hermsdoerfer, C.W. Sandweg, H. Schultheiss, S. Schäfer, B. Leven, B. Hillebrands:
Modification of the termal spi-wave spectrum in a $Ni_{81}Fe_{19}$ stripe by a domain wall
MSNOW workshop, Nancy, France, November 2008

H. Schultheiss, A. Laraoui, F. Ciubotaru, M. Manfrini, M. van Kampen, L. Lagae, A.N. Slavin, B. Leven, B. Hillebrands:
Spin-wave radiation and dc current controlled three-magnon-scattering efficiency in a spin-torque nanocontact device
MSNOW workshop, Nancy, France, November 2008

G. Wolf, A. Conca Parra, H. Schultheiss, B. Leven, B. Hillebrands, K. Rott, G. Reiss:
Magneto-optic investigations on the dynamics of the switching behavior of TMR-structures
MSNOW Workshop, Nancy, France, November 2008

J. Hamrle, O. Gaier, S. Trudel, B. Hillebrands, H. Schneider, G. Jakob, M. Jourdan, J. Thöne, G. Fecher, C. Felser, J. Kübler, J. Kudrnovsky, T. Kubota, Y. Sakuraba, M. Oogane, Y. Ando:
Exchange stiffness constant and magnetic anisotropy in Co_2-based Heusler compounds
Magnetic Research Fall Meeting, Boston, U.S.A., December 2008

J. Hamrle, O. Gaier, S. Trudel, B. Hillebrands, H. Schneider, G. Jakob, M. Jourdan, J. Thöne, G. Fecher, C. Felser, J. Kübler, J. Kudrnovsky, T. Kubota, Y. Sakuraba, M. Oogane, Y. Ando:
Experimental values of exchange stiffness in Co_2-based Heusler compounds
Internal workshop "Exchange interaction in Co_2-based Heusler compounds", Kaiserslautern, February 2009

S. Trudel, B. Hillebrands, J. Hamrle, O. Gaier, G. Wolff, P. Clausen:
Quadratic magneto-optical Kerr Effect in Co-based Heusler compounds
Workshop "Exchange interaction in Co_2-based Heusler compounds", Kaiserslautern, February 2009

V. Kegel S. Schäfer, A.A. Serga, B. Hillebrands:
Multiple spin-wave pulse recovery by parallel pumping
Heraeus Sommerschule, Bad Honnef, April 2009

B. Jungfleisch, C.W. Sandweg, V.I. Vasyuchka, A.A. Serga, B. Hillebrands:
2D k-vector selectivity in Brillouin light scattering spectroscopy of microwave excited spin waves
Heraeus Sommerschule, Bad Honnef, April 2009

J. Hamrle, S. Trudel, O. Gaier, B. Hillebrands, H. Schneider, G. Jakob:
Exchange stiffness in Co_2-based Heusler compounds
Workshop "Spin-Calorimetrics", Dresden, May 2009

F. Ciubotaru, H. Schultheiss, A. Laraoui, A.A. Serga, X. Janssens, M. van Kampen, L. Lagae, B. Leven, A.N. Slavin, B. Hillebrands:
Oersted field influence on three-magnon-scattering processes in nanopoint contact spin-valves
SPINSWITCH Summer School, Iasi, September 2009

S. Schäfer, V. Kegel, A.A. Serga, B. Hillebrands:
Probing the relaxation of a high density magnon gas
SFB/TRR 49 Student workshop, Kaiserslautern, September 2009

S. Schäfer, V. Kegel, A.A. Serga, B. Hillebrands:
Spin-wave pulse recovery with variable magnon damping and coherence
SFB/TRR 49 Annual retreat, Oberursel, September 2009

7.3 Meetings

S. Trudel:
Magneto-optical study of high spin polarization Heusler compound thin films
Alexander von Humboldt Network Meeting, Konstanz, February 2009

G. Wolf, T. Sebastian, B. Leven, B. Hillebrands:
Report on HEUSPIN project
Bi-annual project meeting, Wetzlar, April 2009

A. Conca Parra, B. Leven, B. Hillebrands:
Report on MULTIMAG project
Bi-annual project meeting, Mainz, April 2009

G. Wolf, T. Sebastian, B. Leven, B. Hillebrands:
Report on HEUSPIN project
Bi-annual project meeting, Jena, September 2009

A. Conca Parra, A. Ruiz Calaforra, B. Leven, B. Hillebrands:
The memory array for Sensitec
MULTIMAG Special meeting, Mainz, October 2009

F. Fohr, J. Hamrle, H. Schultheiß, A.A. Serga, B. Hillebrands, Y. Fukuma, L. Wang, Y. Otani:
Mapping spin accumulation in spin momentum transfer devices using Brillouin light scattering spectroscopy
Project meeting with RIKEN Institute, Tokyo, Japan, October 2009

7.4 Invited colloquia

A.A. Serga:
Collective effects and instabilities of magnon gases and condensates
SFB/TRR 49 seminar, Universität Frankfurt, December 2008

B. Hillebrands:
Lineare und nichtlineare Optik in neuem Licht: Optik mit Spinwellen
Physikalisches Kolloquium, Universität Konstanz, January 2009

B. Hillebrands:
Nonlinear magnetization dynamics in small magnetic rings and nanocontacts
Core Research and Engineering of Advanced Materials-Interdisciplinary Education Center for Materials Science Seminar, Osaka University, Japan, January 2009

7.5 Seminars

J. Hamrle, O. Gaier, S. Trudel, P. Clausen, B. Hillebrands, H. Schneider, G. Jakob, M. Jourdan, C. Felser, T. Kubota, Y. Sakuraba, M. Oogane, Y. Ando, J. Fassbender, K. Postava, J. Pištora:
Magnetism meets semiconductors: spin phenomena in heterostructures and novel materials
WE-Heraeus-Seminar, Bad Honnef, January 2009

S. Trudel:
Magnetic exchange in Co_2-based Heusler alloys
WE-Heraeus-Seminar, Bad Honnef, January 2009

S. Trudel:
Magnetic thin films: new materials, new possibilities, and unexpected properties
Department of Chemistry, University of Calgary, Canada, March 2009

J. Hamrle, O. Gaier, S. Trudel, P. Clausen, B. Hillebrands, H. Schneider, G. Jakob, M. Jourdan, C. Felser, T. Kubota, Y. Sakuraba, M. Oogane, Y. Ando, K. Postava, J. Pištora:
Quadratic magneto-optical Kerr effect in Co_2-based Heusler compounds
Seminar, Universität Göttingen, April 2009

J. Hamrle, O. Gaier, S. Trudel, P. Clausen, B. Hillebrands, H. Schneider, G. Jakob, M. Jourdan, C. Felser, T. Kubota, Y. Sakuraba, M. Oogane, Y. Ando, K. Postava, J. Pištora:
Quadratic magneto-optical Kerr effect in Co_2-based Heusler compounds
Seminar, Universität Osnabrück, June 2009

A.V. Chumak:
One-dimensional magnonic crystal: design, fabrication and application
International Seminar and Workshop: "Magnonics: From Fundamentals to Applications", Dresden, August 2009

A.V. Chumak, A.A. Serga, G.A. Melkov, V. Tiberkevich, A.N. Slavin, B. Hillebrands:
Parametrically stimulated recovery of microwave signal stored in standing spin-wave modes of a magnetic film
International Seminar and Workshop: "Magnonics: From Fundamentals to Applications", Dresden, August 2009

A.V. Chumak, A.A. Serga, V.I. Vasyuchka, B. Hillebrands:
Parametrical recovery of a spin-wave signal stored in a magnonic crystal
International Seminar and Workshop: "Magnonics: From Fundamentals to Applications", Dresden, August 2009

C.W. Sandweg,B. Jungfleisch, V.I. Vasyuchka, A.A. Serga, B. Hillebrands:
Two-dimensional wave-vector resolution in Brillouin light scattering spectroscopy
International Seminar and Workshop: "Magnonics: From Fundamentals to Applications", Dresden, August 2009

T. Schneider, A.A. Serga, A.V. Chumak, B. Hillebrands, C.W. Sandweg, S. Wolff, M.P. Kostylev, V.S. Tiberkevich, A.N. Slavin:
Non-diffractive spin-wave beams
International Seminar and Workshop: "Magnonics: From Fundamentals to Applications", Dresden, August 2009

A.V. Chumak, A.A. Serga, V.I. Vasyuchka, B. Hillebrands:
Parametrical recovery of a spin-wave signal stored in a magnonic crystal
International Seminar and Workshop: "Magnonics: From Fundamentals to Applications", Dresden, August 2009

G.A. Melkov, V.I. Vasyuchka, A.A. Serga, C.W. Sandweg, D.V. Slobodyanyuk, B. Hillebrands:
Evolution of parametric magnon condensate after pumping is switched off
International Seminar and Workshop: "Magnonics: From Fundamentals to Applications", Dresden, August 2009

B. Hillebrands:
Nanomagnetism investigated by Brillouin light scattering microscopy
Seminar, RIKEN, Tokyo, October 2009

7.6 Contributions of the Institute for Thin Film Technology

L. Kleinen:
Ionenselektive Sensoren für den Einsatz in der Risikobestimmung von Harnsteinbildung
6. Deutsches Biosensor-Symposium, Freiburg, March/April 2009

L. Kleinen:
Multifunctional Plasma Deposited Coatings
exhibition at booth of "Wissenschaftsregion Bonn", Hannover-Messe, April, 2009

L. Kleinen:
Determining the risk of urinary stones by means of a Ca^{2+} field effect chemical sensor
4th International Symposium on Medical, Bio- and Nano-Electronics, Sendai, Japan, May 2009

L. Kleinen:
Plasmadeponierte Schichtsysteme für biomedizinische Anwendungen
Rheinland-Pfalz Woche der Wissenschaft, November 2009

Appendix: Impressions from 2009

Ph.D. defense Dr. Oksana Gaier

Ph.D. defense Dr. Thomas Schneider

Workshop of the FG 559, July 2009
Villa Denis, near Kaiserslautern

Farewell party Dr. Simon Trudel

TECHNISCHE UNIVERSITÄT
KAISERSLAUTERN

Contact:

Prof. Dr. Burkard Hillebrands
Fachbereich Physik
Forschungszentrum OPTIMAS
Technische Universität Kaiserslautern, Germany
P. O. Box 3049
D-67653 Kaiserslautern
Phone: +49-(0)631-205-4228
Fax: +49-(0)631-205-4095
E-mail: hilleb@physik.uni-kl.de
Internet: http://www.physik.uni-kl.de/hillebrands/